

# A Microscopic Description of Elastic Scattering from Unstable Nuclei within a Relativistic Framework

by

Wasiu Akanni Yahya



UNIVERSITEIT  
iYUNIVESITHI  
STELLENBOSCH  
UNIVERSITY

*Dissertation presented for the degree of Doctorate of philosophy in the  
Faculty of Sciences at Stellenbosch University*

100  
1918 - 2018

Supervisors:

Prof. B. I. S. van der Ventel  
Dr. R. A. Bark

March 2018

# Declaration

By submitting this dissertation electronically, I declare that the entirety of the work contained therein is my own, original work, that I am the sole author thereof (save to the extent explicitly otherwise stated), that reproduction and publication thereof by Stellenbosch University will not infringe any third party rights and that I have not previously in its entirety or in part submitted it for obtaining any qualification.

March 2018

Copyright © 2018 Stellenbosch University  
All rights reserved.

# Abstract

## A Microscopic Description of Elastic Scattering from Unstable Nuclei within a Relativistic Framework

W. A. Yahya

*Department of Physics,  
University of Stellenbosch,  
Private Bag X1, Matieland 7602, South Africa.*

Dissertation: PhD

November 2017

In this dissertation, a microscopic study of proton elastic scattering from unstable nuclei at intermediate energies using relativistic formalisms is presented. We have employed both the original relativistic impulse approximation (IA1) and the generalised relativistic impulse approximation (IA2) formalisms to calculate the relativistic optical potentials, with target densities derived from relativistic mean field (RMF) theory using the QHD-II, NL3, and FSUGold parameter sets. Comparisons between the optical potentials computed using both IA1 and IA2 formalisms, and the different RMF Lagrangians are presented for both stable and unstable targets. The comparisons are required to study the effect of using IA1 versus IA2 optical potentials, with different RMF parameter sets, on elastic scattering observables for unstable targets at intermediate energies. We also study the effect of full-folding versus factorized form of the optical potentials on elastic scattering observables. As with the case for stable nuclei, we found that the use of full-folding optical potential improves the scattering observables (especially spin observables) at low intermediate energy (e.g. 200MeV). No discernible difference is found at projectile incident energy of 500 MeV. To check the validity of using localized optical potential, we calculate the scattering observables using non-local potentials by solving the momentum space Dirac equation. The Dirac equation is transformed to two coupled Lippmann-Schwinger equations, which are then numerically solved to obtain the elastic scattering observables. The results are discussed and compared to calculations involving local coordinate-space optical potentials.

# Uittreksel

## 'N Mikroskopiese beskrywing van elastiese verstrooiing van onstabiele kern binne 'n relativistiese raamwerk

W. A. Yahya

*Fisika Departement,  
Universiteit van Stellenbosch,  
Privaatsak X1, Matieland 7602, Suid Afrika.*

Proefskrif: PhD

November 2017

In hierdie proefskrif word 'n mikroskopiese model vir elastiese proton verstrooiing van onstabiele kerne ondersoek deur gebruik te maak van 'n relativistiese formulering. Die NN interaksie word beskryf deur die sogenaamde IA1 en IA2 modelle. Die kernstruktuur word beskryf deur gebruik te maak van drie verskillende relativistiese gemiddelde-veld modelle, naamlik QHDII, NL3 en FSUGold. Die optiese kernpotensiaal word bereken met behulp van die IA1 en IA2 NN interaksies sowel as die drie verskillende kernstruktuur modelle, QHDII, NL3 en FSUGold. Sodoende kan 'n volledige stel verstrooiingswaarneembare bereken word vir elastiese verstrooiing van onstabiele kerne. Die kern optiese potensiaal word ook op twee maniere bereken, naamlik die optimale faktoriseringsmetode en die volle oorvleuelingsmodel. Vir lae energie van die orde van 200 MeV, gee volle oorvleuelingsmodel 'n verbetering in die resultate van die spinwaarneembare. By 'n projektielenergie van ongeveer 500 MeV is daar egter geen beduidende verskil tussen hierdie twee metodes nie. Die Dirac vergelyking in momentum-ruimte word ook opgelos om 'n nie-lokale optiese kernpotensiaal te bereken. Die Dirac vergelyking word herskryf in terme van twee gekoppelde Lippmann-Schwinger vergelykings wat dan opgelos word om die elastiese spinwaarneembare te bepaal. Die resultate van hierdie berekening word dan bespreek en word vergelyk met berekeninge wat gedoen word vir lokale kern optiese potensiale in posisie-ruimte.

# Acknowledgements

All praise is due to ALLAH, the creator of human being, elementary particles, neutron stars, and everything in existence. I say ALHAMDULILLAH for making my PhD journey a success. I will forever be grateful for all the favours of ALLAH upon me. May HE be praised.

I want to appreciate my promoter, Prof. B.I.S. van der Ventel, for his patience and assistance towards the success of my PhD. It was a wonderful experience working with you, as I have learnt a lot from you. My appreciation also goes to my co-promoter, Dr R. A. Bark for his supports, especially with the iThemba LABS top-up. I acknowledge iThemba LABS for the 2017 top-up.

My parents Mr and Mrs Ahmed Yahya have contributed a lot to my life. They are my drivers to this world. I am very happy that you are my parents. I want to acknowledge your support both financially and spiritually throughout my academic career. I say " My Lord, have mercy upon them as they brought me up when I was small". May ALLAH reward you abundantly and grant you AL-JANNATU-LI-FRIDAUS. AAMIN. I also appreciate the entire members of my family for their prayers and supports.

My sincere appreciation also goes to my beloved friend Haruna Abdullahi. He is a GOD-sent, a rare human-being. He stood by me all the way. I appreciate your financial and spiritual supports. May ALLAH Bless you, and grant you success in this life and the hereafter. May ALLAH make us continue our friendship in AL-JANNATU-LI-FRIDAUS. AAMIN.

I acknowledge the various interactions I had with Prof. Shaun Wyngaardt. I say thank you. Many thanks to Dr Ibrahim Taofeeq for introducing me to Stellenbosch University, and to my office mate Dr. Christel Kimene Kaya, as we had lots of discussions related to nuclear physics. I am happy that we were able to successfully defend our PhD. I also appreciate my other colleagues in the department especially Pelerine, Florence, Munirat, and Ishmael.

My appreciation goes to the management of Kwara State University for granting me study leave, and to the head of physics department, Stellenbosch university for his support during the challenging times.

Many thanks to Mr. Stanley February for the pet talks, Ms. Ursala Isaac for the administration, Mr. Cashwool Pool, Ms. Collen April, Botha Tinus for IT support,

and the charismatic Christine who left the department before I completed my PhD. Tinus was always ready to assist with IT problems. I say thanks to you all for contributing in one way or another towards the success of my PhD.

Finally, I want to appreciate my sweetheart, love, companion, and my wife, Uthman Faizat. I acknowledge your supports, prayers, and contributions to our home. I want to let you know that I LOVE YOU SO MUCH. May ALLAH increase our love of each other, and grant us AL-JANNATU-LI-FRIDAUS. I'm sorry that I have not been around for the past three years; it's all for the best. May ALLAH grant us goodness and success. I want to tell my queens KHADEEJAH, SEKEENAH, and ZAINAB, that I'm sorry I have not been around much to play with you. You should know that I love you so much, and that by ALLAH's grace and mercy, we shall "live happily ever after". May ALLAH BLESS all of you and grant you AL-JANNATU-LI-FRIDAUS. AAMIN.

# Contents

<b>Declaration</b>	<b>i</b>
<b>Abstract</b>	<b>ii</b>
<b>Uittreksel</b>	<b>iii</b>
<b>Acknowledgements</b>	<b>iv</b>
<b>Contents</b>	<b>vi</b>
<b>List of Figures</b>	<b>viii</b>
<b>List of Tables</b>	<b>xii</b>
<b>1 Introduction and Motivation</b>	<b>1</b>
1.1 Unstable nuclei . . . . .	4
1.2 Why proton elastic scattering? . . . . .	5
1.3 Outline of Dissertation . . . . .	7
<b>2 Relativistic Mean Field Theory</b>	<b>9</b>
2.1 Background . . . . .	9
2.2 The Lagrangian density . . . . .	11
2.3 Relativistic mean field equations . . . . .	12
2.3.1 Pairing correlations . . . . .	18
2.4 Halo nuclei and skin . . . . .	21
<b>3 Relativistic Optical Potentials</b>	<b>25</b>
3.1 Relativistic kinematics . . . . .	25
3.2 Global Dirac phenomenology . . . . .	26
3.3 Relativistic impulse approximation . . . . .	29
3.4 Generalized relativistic impulse approximation . . . . .	35
3.4.1 Local coordinate space optical potential . . . . .	43
3.4.2 Schrödinger equivalent potentials . . . . .	46
3.4.3 Contributions of sub-classes to IA2 optical potential . . . . .	50
3.5 Full folding versus factorised optical potential . . . . .	51
3.5.1 IA1 . . . . .	51
3.5.2 IA2 . . . . .	55

<i>CONTENTS</i>	vii
<b>4 Solution of the Coordinate Space Dirac Equation</b>	<b>58</b>
4.1 Scattering observables . . . . .	59
4.2 Numerical results and discussions . . . . .	60
4.2.1 Comparison of the RMF models . . . . .	63
4.2.2 IA1 versus IA2 . . . . .	67
4.2.3 Effect of full folding versus optimally factorised optical potential on scattering observables . . . . .	73
<b>5 Dirac Equation in Momentum Space</b>	<b>81</b>
5.1 Partial-wave analysis of the T-matrix . . . . .	83
5.2 Partial-wave analysis of U . . . . .	84
5.3 Partial-wave analysis of the integral equation . . . . .	88
5.4 Solution of the integral equations . . . . .	90
5.4.1 Dealing with the principal value $\mathcal{P}$ . . . . .	90
5.4.2 Discretisation of the integral equations . . . . .	92
5.4.3 Inclusion of Coulomb potential . . . . .	94
5.4.4 Solution at high angular momentum states . . . . .	95
5.5 Results and discussions . . . . .	96
5.5.1 Full folding versus optimal factorization in momentum space . . . . .	99
5.5.2 Effect of using non-local optical potential in IA1 formalism . . . . .	102
<b>6 Conclusion</b>	<b>103</b>
<b>Appendices</b>	<b>106</b>
<b>A</b>	<b>107</b>
A.1 Dirac Matrices . . . . .	107
<b>B</b>	<b>109</b>
B.1 Numerical differentiation of data . . . . .	109
B.2 Numerical integration of data . . . . .	109
B.3 Runge-Kutta-Fehlberg method . . . . .	110
B.4 Noumerov algorithm . . . . .	112
<b>C</b>	<b>114</b>
C.1 Some constants used in IA2 potential . . . . .	114
<b>D</b>	<b>116</b>
D.1 Coulomb functions . . . . .	116
<b>List of References</b>	<b>119</b>

# List of Figures

1.1	Mind map of thesis. . . . .	8
2.1	The upper and lower components wave functions for each state of $^{54}\text{Ca}$ using FSUGold parameter sets. . . . .	15
2.2	$^{48,54,58,60}\text{Ca}$ neutron vector densities. . . . .	18
2.3	Plot of charge density ( $\rho_{ch}(r)$ ) for $^{48,54,58,60}\text{Ca}$ . FBC denotes Fourier-Bessel coefficients. . . . .	19
2.4	$^{48,54,58,60}\text{Ca}$ proton and neutron vector densities plots with NL3 parameter sets. . . . .	20
2.5	Single-particle proton states in $^{48}\text{Ca}$ . Binding energy on the vertical axis is in MeV. . . . .	20
2.6	Single-particle neutron states in $^{48}\text{Ca}$ . Binding energy on the vertical axis is in MeV. . . . .	21
2.7	Single-particle proton states in $^{54}\text{Ca}$ . Binding energy on the vertical axis is in MeV. . . . .	22
2.8	Single-particle neutron states in $^{54}\text{Ca}$ . Binding energy on the vertical axis is in MeV. . . . .	23
2.9	Proton and neutron densities for $^{20,22}\text{C}$ , calculated with NL3 parameter sets. . . . .	24
2.10	Proton and neutron densities for $^{12,14}\text{C}$ , calculated with NL3 parameter sets. . . . .	24
3.1	The scalar and vector global Dirac optical potentials for proton scattering from $^{54}\text{Ca}$ for incident proton energies 65, 100, 200, and 500 MeV. . . . .	28
3.2	IA1 scalar and vector optical potentials for $p+^{48}\text{Ca}$ at $T_{\text{lab}} = 500$ MeV and 200 MeV for QHD-II, NL3, FSUGold RMF models, and Dirac Phenomenology. . . . .	33
3.3	Same as in figure 3.2 except for $p+^{54}\text{Ca}$ . . . . .	34
3.4	IA1 Schrödinger equivalent central and spin orbit potentials for $p+^{48,54}\text{Ca}$ , using the NL3 parameter set, at $T_{\text{lab}} = 200, 500,$ and $800$ MeV. . . . .	34
3.5	Diagrammatic representation of first order optical potential for elastic proton-nucleus scattering. . . . .	37
3.6	Flow chart illustrating how the function "UIA2" calculates the optical potentials in the IA2 formalism. . . . .	44
3.7	IA2 scalar and vector optical potentials for $p+^{48}\text{Ca}$ at $T_{\text{lab}} = 200$ and $500$ MeV for QHD-II, NL3, FSUGold RMF models, and Dirac Phenomenology. . . . .	46

3.8	Same as in figure 3.7 except for $p+^{54}\text{Ca}$ . . . . .	47
3.9	IA2 scalar (S), vector (V), tensor (T), space vector (C), Dirac scalar spin-orbit ( $S_{LS}$ ), and Dirac vector spin-orbit ( $V_{LS}$ ) potentials for $p+^{48}\text{Ca}$ using the NL3 parameter for $T_{\text{lab}} = 200, 500, \text{ and } 800 \text{ MeV}$ . . . . .	48
3.10	Same as in figure 3.9 except for $p+^{54}\text{Ca}$ . . . . .	49
3.11	IA2 Schrödinger equivalent central and spin orbit potentials for $p+^{48,54}\text{Ca}$ , using the NL3 parameter set, at $T_{\text{lab}} = 200, 500, \text{ and } 800 \text{ MeV}$ . The solid lines are real parts while dashed lines denote imaginary parts. . . . .	50
3.12	Contributions of the IA2 F subclasses to $p+^{40}\text{Ca}$ (QHD II model) at $T_{\text{lab}} = 200 \text{ MeV}$ . . . . .	52
3.13	Contributions of the IA2 F subclasses to $p+^{54}\text{Ca}$ (NL3 model) at $T_{\text{lab}} = 200 \text{ MeV}$ . . . . .	53
3.14	Full-folding versus factorised scalar and vector optical potentials in the IA2 formalism for elastic scattering of $p+^{48}\text{Ca}$ (NL3 model) at $T_{\text{lab}} = 200$ and $500 \text{ MeV}$ . The localised forms of the optical potentials were used. The real parts are indicated with solid lines while imaginary parts are dashed lines. The full folding ("Full fold") results are shown in blue lines while the optimally factorised ("Opt fact") results are indicated with red lines. . . . .	56
3.15	Same as in figure 3.14 except for $p+^{54}\text{Ca}$ . . . . .	57
4.1	Flow chart illustrating how the function SCATOBS calculates the scattering observables. . . . .	61
4.2	Scattering cross section, analysing power, and spin rotation function for the $^{40,44,48,52,54,58,60}\text{Ca}$ isotopes at $T_{\text{lab}} = 200 \text{ MeV}$ using the NL3 parameter set and IA2 optical potentials. . . . .	62
4.3	Scattering cross section calculations showing comparison of the different Lagrangian densities for proton scattering from $^{48,54,58,60}\text{Ca}$ at $T_{\text{lab}} = 200 \text{ MeV}$ using IA2 optical potentials. . . . .	64
4.4	Analysing power calculations showing comparison of the different Lagrangian densities for proton scattering from $^{48,54,58,60}\text{Ca}$ at $T_{\text{lab}} = 200 \text{ MeV}$ . . . . .	65
4.5	Spin rotation parameter calculations showing comparison of the different Lagrangian densities for proton scattering from $^{48,54,58,60}\text{Ca}$ at $T_{\text{lab}} = 200 \text{ MeV}$ . . . . .	66
4.6	Scattering cross section calculations showing comparison of the RMF models for $^{48,54,58,60}\text{Ca}$ at $T_{\text{lab}} = 500 \text{ MeV}$ . . . . .	66
4.7	Analysing power calculations showing comparison of the RMF models for $^{48,54,58,60}\text{Ca}$ at $T_{\text{lab}} = 500 \text{ MeV}$ . . . . .	67
4.8	Spin rotation parameter calculations showing comparison of the RMF models for $^{48,54,58,60}\text{Ca}$ at $T_{\text{lab}} = 500 \text{ MeV}$ . . . . .	68
4.9	Scattering cross section calculations showing comparison of the RMF models for $^{48,54,58,60}\text{Ca}$ at $T_{\text{lab}} = 800 \text{ MeV}$ . . . . .	68
4.10	Analysing power calculations showing comparison of the RMF models for $^{48,54,58,60}\text{Ca}$ at $T_{\text{lab}} = 800 \text{ MeV}$ . . . . .	69
4.11	Spin rotation parameter calculations showing comparison of the RMF models for $^{48,54,58,60}\text{Ca}$ at $T_{\text{lab}} = 800 \text{ MeV}$ . . . . .	69

4.12	Comparison of the IA1, IA2, and global Dirac phenomenology scattering observables for $^{40}\text{Ca}$ target at $T_{\text{lab}} = 200$ MeV. . . . .	70
4.13	Comparison of the IA1, IA2, and global Dirac phenomenology scattering observables for $^{40}\text{Ca}$ target at $T_{\text{lab}} = 500$ MeV. . . . .	71
4.14	Comparison of the IA1, IA2, and global Dirac phenomenology scattering observables for $^{40}\text{Ca}$ target at $T_{\text{lab}} = 800$ MeV. . . . .	72
4.15	Comparison of the IA1, IA2, and global Dirac phenomenology scattering observables for $^{48}\text{Ca}$ target at $T_{\text{lab}} = 200$ MeV. . . . .	73
4.16	Comparison of the IA1, IA2, and global Dirac phenomenology scattering observables for $^{48}\text{Ca}$ target at $T_{\text{lab}} = 500$ MeV. . . . .	74
4.17	Comparison of the IA1, IA2, and global Dirac phenomenology scattering observables for $^{48}\text{Ca}$ target at $T_{\text{lab}} = 800$ MeV. . . . .	75
4.18	Comparison of the IA1, IA2, and global Dirac phenomenology scattering observables for $^{54}\text{Ca}$ target at $T_{\text{lab}} = 200$ MeV. . . . .	75
4.19	Comparison of the IA1, IA2, and global Dirac phenomenology scattering observables for $^{54}\text{Ca}$ target at $T_{\text{lab}} = 500$ MeV. . . . .	76
4.20	Comparison of the IA1, IA2, and global Dirac phenomenology scattering observables for $^{58}\text{Ca}$ target at $T_{\text{lab}} = 200$ MeV. . . . .	76
4.21	Comparison of the IA1, IA2, and global Dirac phenomenology scattering observables for $^{58}\text{Ca}$ target at $T_{\text{lab}} = 500$ MeV. . . . .	77
4.22	Effect of full folding versus optimally factorised optical potential on scattering observables for proton scattering from $^{48}\text{Ca}$ target at $T_{\text{lab}} = 200$ MeV. . . . .	77
4.23	Effect of full folding versus optimally factorised optical potential on scattering observables for proton scattering from $^{48}\text{Ca}$ target at $T_{\text{lab}} = 500$ MeV. . . . .	78
4.24	Effect of full folding versus optimally factorised optical potential on scattering observables for proton scattering from $^{54}\text{Ca}$ target at $T_{\text{lab}} = 200$ MeV. . . . .	78
4.25	Effect of full folding versus optimally factorised optical potential on scattering observables for proton scattering from $^{54}\text{Ca}$ target at $T_{\text{lab}} = 500$ MeV. . . . .	79
4.26	Effect of full folding versus optimally factorised optical potential on scattering observables for proton scattering from $^{58}\text{Ca}$ target at $T_{\text{lab}} = 200$ MeV. . . . .	79
4.27	Effect of full folding versus optimally factorised optical potential on scattering observables for proton scattering from $^{58}\text{Ca}$ target at $T_{\text{lab}} = 500$ MeV. . . . .	80
5.1	Flow chart illustrating how the function <code>lippschwinger</code> calculates the scattering observables. . . . .	97
5.2	Scattering cross section calculated in position and momentum space for $^{40,48,54,58}\text{Ca}$ targets at $T_{\text{lab}} = 200$ MeV. . . . .	98
5.3	Same as in figure 5.2 but for $T_{\text{lab}} = 500$ MeV. . . . .	99
5.4	Analyzing power calculated in position space and momentum space for $^{40,48,54,58}\text{Ca}$ targets at $T_{\text{lab}} = 200$ MeV. . . . .	99
5.5	Same as in figure 5.4 but for $T_{\text{lab}} = 500$ MeV. . . . .	100

## LIST OF FIGURES

xi

5.6	Spin rotation calculated in position and momentum space for $^{40,48,54,58}\text{Ca}$ targets at $T_{\text{lab}} = 200$ MeV. . . . .	100
5.7	Same as in figure 5.6 but for $T_{\text{lab}} = 500$ MeV. . . . .	101
5.8	Elastic scattering observables calculated in momentum space using full-folding optical potential (in blue dashed lines) and optimally factorised one (in red dashed line) for $p+^{48}\text{Ca}$ target at $T_{\text{lab}} = 200$ MeV. . . . .	101
5.9	Elastic scattering observables calculated in momentum space using full-folding optical potential (in blue dashed lines) and optimally factorised one (in red dashed line) for $p+^{48}\text{Ca}$ target at $T_{\text{lab}} = 200$ MeV. . . . .	102

# List of Tables

2.1	Parameter sets for the four relativistic mean field models used in this work	13
2.2	Root-mean-square charge radius, proton and neutron root-mean-square radii of some closed shell Calcium isotopes. . . . .	17
3.1	Kinematic covariants $K_n$ ( $n = 1 \cdots 13$ ). $\tilde{S} = \frac{1}{4} (K_1 + K_2 + K_3 - K_4 + \frac{1}{2}K_5)$ , where $K_1 \equiv S$ , $K_2 \equiv P$ , $K_3 \equiv V$ , $K_4 \equiv A$ , $K_5 \equiv T$ . . . . .	39
3.2	The rho–spin sectors and independent amplitudes for each subclass with the constraint conditions charge symmetry, time–reversal, and on–mass–shell. . . . .	40
3.3	Relation between the 13 invariant amplitudes $F_n^{\rho'_1 \rho'_2 \rho_1 \rho_2}$ and nine symmetrized amplitudes $f_n^{\rho'_1 \rho'_2 \rho_1 \rho_2}$ with $\rho'_1 \rho'_2 \rho_1 \rho_2 \equiv \rho$ . . . . .	41
3.4	Table showing contributions of the IA2 $\hat{F}$ sub-classes to the scalar and vector potentials for $p+^{40}\text{Ca}$ at $T_{\text{lab}} = 200$ MeV. . . . .	51
3.5	Table showing contributions of the IA2 $\hat{F}$ sub-classes to the scalar and vector potentials for $p+^{54}\text{Ca}$ at $T_{\text{lab}} = 200$ MeV. . . . .	52

# Chapter 1

## Introduction and Motivation

Traditionally, elastic and quasielastic scattering calculations in nuclear physics were performed using the Schrödinger equation, with nonrelativistic phenomenological and microscopical potentials [1–3]. One of the fundamental assumptions was the use of the impulse approximation where in-medium amplitudes are replaced with free on-shell nucleon-nucleon (NN) amplitudes, which is accurate when the projectile beam energy is much larger than the target nucleon binding energy. The nonrelativistic formalism including medium effects, such as Pauli blocking and binding energy, was successful at energies lower than  $\sim 300$  MeV, while nonrelativistic impulse approximation including target nucleon correlations and electromagnetic spin-orbit corrections was able to successfully describe proton-nucleus elastic scattering data at energies equal to 800 MeV and above [2]. Despite the inclusion of off-shell effects, full folding integration, and higher order multiple scattering to the non-relativistic approach, the model did not satisfactorily describe the spin observables for proton elastic scattering from  $^{40}\text{Ca}$  at incident laboratory energy of 500 MeV [4–6].

The first calculations based on a relativistic descriptions of nuclear scattering processes was presented by Clark and collaborators [7–10]. They used the Dirac equation and phenomenological potentials to describe proton-nucleus elastic scattering at proton incident energies up to 1GeV. The Dirac phenomenological potential strengths were shown to be consistent with nucleon self-energies obtained using relativistic models of infinite nuclear matter [11–14]. Good fits to differential cross section data were obtained. Unlike the nonrelativistic model phenomenology the Dirac phenomenology, with large scalar and vector potentials, was shown to successfully predict the spin rotation parameter  $Q$ , whenever the cross section and analysing power data were accurately predicted [15–17]. In an attempt to obtain a formal, relativistic scattering theory, Celenza et al. [18] proposed a " $t\rho$ " form for the leading term in a relativistic optical potential, and referred to this as a relativistic impulse approximation model, even though the explicit forms for the NN invariant amplitudes were not presented [16]. The contributions of virtual negative energy projectile states to proton-nucleus scattering is quite significant; this is only present in relativistic formalism. At energies lower than  $\sim 300\text{MeV}$ , Pauli-blocking, target-nucleon correlations, binding energy, and treatment of non-locality are significant [16, 19, 20]. On the other hand, at very high energy ( $\geq 1\text{GeV}$ ), there is possibility of

meson production, which can lead to excitation of resonances in the target nucleons [1, 21]. Pion production is large at NN laboratory energy of around 600 MeV due to  $\Delta$  isobar.

Following the success of the Dirac phenomenology in predicting the cross section, spin rotation, and analysing power data [22], a five-term parametrization of the nucleon-nucleon scattering operator was introduced by McNeil, Ray and Wallace (MRW) in 1983 [23]. A relativistic scattering model, called the relativistic impulse approximation, that used the MRW five-term, Lorentz invariant nucleon-nucleon operator was later introduced [24, 25], and it successfully predicted proton-nucleus data at 500 MeV and 800 MeV. In the relativistic impulse approximation, the projectile particle interacts with the target through one-boson-exchange while the other nucleons act as spectators, and the NN amplitudes were obtained from fits to scattering data based on single-boson-exchange models. In this formalism (now called IA1), the scalar and vector optical potentials have direct relations with the Lorentz properties of the mesons mediating the strong nuclear force.

The original relativistic impulse approximation (IA1) is based on making use of five Fermi covariants (i.e. scalar, pseudoscalar, vector, axial vector, and tensor) to extend positive-energy NN amplitudes into operators in the full Dirac space of two nucleons. The IA1 formalism successfully predicts the spin observables in proton-nucleus (p-A) elastic scattering above about 300 MeV [25]. At low projectile proton energies however, the IA1 model overestimated both scalar and vector optical potentials. This is due to the fact that pion exchange contributions are forced to be pseudoscalar, whereas, at low energy, pair contributions are large. As shown in Ref. [26], the relativistic formalism of p-A elastic scattering differs from its nonrelativistic counterpart due to pair contributions. The relativistic formalism implicitly incorporates virtual  $N\bar{N}$  pair effects. There is an ambiguity, however in the IA1 approach of predicting virtual pair effects because IA1 used just five Fermi covariants to extend physical NN data to the full Dirac space [27]. The IA1 formalism also did not include exchange contributions. Explicit incorporation of exchange to the relativistic impulse approximation was first introduced in Refs. [19, 20].

In Ref. [28], the authors studied the validity of the relativistic impulse approximation for elastic proton-nucleus scattering at kinetic energies below 200 MeV. At energies below 200 MeV, medium effects, Pauli blocking, and multiple scattering have significant contributions. At these low energies, correction to the optical potentials for medium modifications from Pauli blocking is often done by performing relativistic Brueckner theory calculations via a one-boson-exchange potential [19, 20, 29]. To address the problem of the IA1 at low incident projectile energy, the generalised relativistic impulse approximation was presented by Tjon and Wallace [30, 31]. In the generalised relativistic impulse approximation (called IA2) formalism, the relativistic optical potential for proton elastic scattering is calculated using a complete set of Lorentz-invariant amplitudes. In Ref. [30], a relativistic meson exchange model was used to compute the nucleon-nucleon invariant amplitudes for on-mass-shell kinematics. The resulting amplitudes were then fit by sums of Yukawa terms. They also presented an analysis of the complete sets of Feynman invariant amplitudes which were then employed to construct the IA2 optical potentials. In this general form

for the nucleon–nucleon invariant scattering operator, transitions from positive to negative energies were dynamically determined from the meson exchange model.

Off-shell effects, introduced due to the momentum dependence of the optical potential, for proton elastic scattering from stable nuclei have been investigated using the IA2 formalism and the contributions were found to be minor [32]. Multiple scattering contributions to the IA2 optical potential have also been studied in low and intermediate energy region in Ref. [33]. The author investigated the second-order multiple scattering contributions by studying proton scattering from  $^{40}\text{Ca}$  at 100, 200, 500 and 800 MeV, and found an increase in the strength of both real scalar and vector optical potentials, with a reduction in the imaginary scalar and vector potentials. The largest multiple scattering contribution was found at 100 MeV. The multiple scattering contributions to the elastic scattering observables show some improvement in reproducing experimental data at large angles and at low energies  $\leq 100$  MeV only. IA2 formalism has been used to study proton elastic scattering from unstable isotopes  $^{60-74}\text{Ca}$  [34],  $^{6,8}\text{He}$  [35], and  $^{8-22}\text{C}$  [36].

The success of relativistic impulse approximation in the description of proton-nucleus elastic scattering data led to its use in quasielastic proton-nucleus scattering using plane waves (RPWIA) [37–43] and distorted-waves (RDWIA) [21, 44–49]. In the original relativistic impulse approximation, the projectile is treated using plane waves, while the target is treated as a free Fermi gas. In an attempt to see the relativistic effects on nuclear structure via quasielastic scattering, the relativistic plane-wave impulse approximation was introduced in Refs. [44, 50], where they assumed a Fermi model for the target. Cross sections and spin observables have been obtained for quasielastic proton-nucleus scattering and accurate results were obtained when compared with experiment, which confirmed relativistic effects. In Ref. [43], the authors studied the effects of using IA2 amplitudes on spin observables compared with using the five-term IA1 amplitudes. They found that certain spin observables discriminate between the two representations. The RDWIA was employed for the calculation of proton-nucleus quasielastic scattering using eikonal approximations to introduce distortions [47, 48]. Refs. [21, 46] included distortions through a full partial-wave expansion of the wave functions. In RPWIA, both projectile and ejectile particles are described using relativistic plane-waves, while RDWIA incorporates final state interaction (FSI) effects through the distorted-wave functions of the ejectiles [45]. In RPWIA, relativistic effects are incorporated via the effective nucleon mass, but in relativistic distorted-wave impulse approximation, relativistic effects are included by obtaining the wave functions of both the projectile and ejectile as solutions of Dirac equation containing relativistic potentials [21]. In Ref. [45], neutrino-induced strangeness associated production on nuclei was studied within the frameworks of RPWIA and RDWIA. The relativistic distorted wave impulse approximation analysis using the full IA2 formalism remains to be studied. The various studies stated above using RPWIA and RDWIA focussed on stable nuclei. It will be interesting to apply both of these formalisms to the study of unstable nuclei.

## 1.1 Unstable nuclei

A stable nucleus has the right amount of neutrons and protons such that the attractive nuclear force between the nucleons overcomes the Coulomb repulsive force that tends to pull the protons apart. On the other hand, the attractive nuclear force in an unstable nucleus does not provide the required amount of binding energy to hold the nucleus together. On a neutron-proton plot, the stable nuclei lie along the line of stability. The unstable nuclei, however, lie above and below the line of stability. Those that lie below the line of stability are said to be proton rich, while those above this line are said to be neutron rich.

The availability of high-intensity radioactive ion beams (RIB) has made elastic and inelastic proton scattering from unstable nuclei available to study and the old theories of nuclear physics are now being tested, the limits of nuclear stability are being probed, and surprising results have been obtained thus far. Major surprises found in low-energy nuclear structure are the disappearance of the normal shell closures observed near the stability valley, appearance of new magic numbers, exotic features of nuclear structure such as nuclear halos and skins, and new regions of deformation [51]. Structure and reaction studies of unstable nuclei will have great impact on astrophysics because they are known to play an important role in nucleosynthesis. These RIB facilities, will make available large amount of unstable nuclei data, and will enhance the study of unstable nuclei via electron and proton scattering.

About 3000 isotopes have been identified so far, including 2,700 radioactive ones and theory predicts that about 7000 isotopes might exist between the drip-lines. More than 100 new unstable isotopes were discovered in a single year, for the first time in 2010 [52]. The limits of the nuclear landscape are set by the drip-lines. The drip-lines define the regions where additional neutron or proton would make the nucleus unbound, and the neutron or proton "drips" out of the nuclide. Because the Coulomb force increases in effect as the proton to neutron ratio increases, the proton drip-line lies much closer to the valley of stability compared to the neutron drip-line. For neutron (proton) rich nuclei,  $\beta^-$  ( $\beta^+$ ) decay is energetically favourable. Due to the pairing interaction, there are more stable even-even nuclei than stable odd-odd nuclei or stable odd-A nuclei [53]. Study of unstable nuclei will allow us to test, refine, and develop existing models for nuclear structure. The study of unstable nuclei can allow many questions to be explored:

- (i) what are the limits of nuclear existence?
- (ii) how many protons and neutrons can form a bound nucleus?
- (iii) what are the properties of very short-lived nuclei?

The success of the first application of radioactive ion (RI) beams to measure interaction cross section of light unstable nuclei triggered the construction of new RI beam facilities that could provide high intensity beams [54]. There are two main techniques of producing and accelerating radioactive beams: Isotope Separation On-Line (ISOL) and In-Flight Fragmentation (IFF). The ISOL technique, which

is suitable for low energy experiments because the ions are produced at rest, was invented over 60 years ago in Copenhagen [55], and later migrated to CERN where a proton drive beam was available at the Syncho-Cyclotron [56]. In this method, radioactive nuclei are produced in thick targets with primary beams of protons. The residual nuclei are thermalised and ionised in an ion source. The collected ions are mass analysed, and accelerated to the energy required by the experiment with the radioactive projectiles [57, 58]. Notable among the RIB facilities that make use of the ISOL method are Louvain-la-Neuve (Belgium), the *Système de Production d'Ions Radioactifs en Ligne* (SPIRAL, France), Alto (France), ISAC (at TRIUMF, Canada), and REX ISOLDE (CERN, Switzerland/France). In the in-flight fragmentation technique, high energy heavy ion beam impinges on a thin target. The residual nuclei are moved to the experimental setup after charge, momentum, and mass selection in a fragment separator [58, 59]. Some of the RIB facilities that make use of fragmentation technique are Lawrence Berkeley Laboratory (LBL, USA), GANIL (France), RIKEN (Japan), NSCL (Michigan State University, USA), GSI (Darmstadt, Germany), and Institute of Modern Physics (IMP, China). The above mentioned radioactive ion beam facilities are already in existence.

There are plans (most are under constructions) to build RIB facilities that would produce higher intensity beams of nuclei much farther from the stability valley. Some of them that would make use of the ISOL technique are the *Système de Production d'Ions Radioactifs en Ligne*, generation 2 (SPIRAL 2, France), Selective Production of Exotic Species (SPES, at LNL Italy), High Intensity and Energy ISOLDE (HIE-ISOLDE at CERN Switzerland/France), Advanced Rare Isotope Laboratory (ARIEL at TRIUMF Canada), European Isotope On-line Radioactive Ion Beam Facility (EUROSOL, in Europe), Beijing ISOL in China, and Advanced National Facility for Unstable and Rare Isotope Beams (ANURIB Kolkata, India). Radioactive Ion Beam Factory (RIBF at RIKEN Japan), Facility for Antiproton and Ion Research (FAIR, Germany), Facility for Rare Isotope Beams (FRIB at MSU, USA), High Intensity Heavy Ion Accelerator Facility (HIAF China), and RAON facility in Korea would be Fragmentation based. Among the "new generation" RIB facilities, only RIKEN RIBF is currently in operation. FAIR is planned to start partially in 2018, FRIB is expected to be completed in 2020 while HIAF should be ready by 2019 [51]. These (new generation) facilities would provide RI beams of high intensity, variety and quality. Locally, the iThemba Labs accelerator facility is developing a proposal to produce beams of radioactive ions for nuclear and material research.

## 1.2 Why proton elastic scattering?

One of the reaction processes to study both stable and unstable nuclei is elastic scattering. Employing electron and proton scattering, one can obtain information on the neutron ground state density and transition density distributions [60, 61]. At intermediate energy, a good tool to probe nucleon density distributions is proton elastic scattering, because of its larger mean free path in the nuclear medium. The mean free path of protons in nuclear matter at intermediate energy is large enough to penetrate into the nucleus, thus providing some sensitivity to the nuclear interior. The nuclear reaction mechanism becomes simpler at intermediate energies since the

velocity of the projectile is much faster than the Fermi motion of the bound nucleons [51, 62–64]. A considerable number of works have therefore been devoted to elastic proton scattering to study interactions and nuclear structures in the nuclear interior. It has been stated that the best energy region to deduce the density distribution in nuclei is between 200 MeV and 400 MeV per nucleon, where the mean free path of the nucleon in nuclei is expected to be large and the scattering does not suffer much from the meson production. The new facility at RIKEN (RIBF) will be able to supply the sufficient unstable nuclear beam in this energy region. In fact, the nucleon density distribution of unstable radioactive ions has been planned to be studied at RIBF by proton scattering in inverse kinematics, where an energetic radioactive ion beam of about 300 MeV/nucleon scatters off a proton at rest.

Although electron scattering is a very good technique to measure stable nuclei densities, it is not easy to apply in the case of unstable nuclei [65]. Elastic proton scattering gives information on the nuclear matter distributions and the effective  $NN$  potentials. Inelastic scattering is important to scan new regions of deformation. Proton scattering experiments on unstable nuclei are often performed in inverse kinematics, where the radioactive beam strikes a target that contains the protons. This is because the lifetime of unstable nuclei are too short to prepare as targets in most cases. In direct kinematics the light particle (in our case, proton) is accelerated onto the stationary heavy target, while in inverse kinematics the heavy particle is accelerated, and the light particle (proton) serves as the target. Very good sensitivity and high resolution are required for experiments in inverse kinematics in order to detect rare events with high efficiency and to have the maximum information possible with low statistics [66]. It is sometimes experimentally difficult to detect the heavy fragment in inverse kinematics because of the short lifetime of unstable nuclei. Hence, the energy and angle of the recoiling protons are therefore measured for this type of reaction, from which the scattering angle and excitation energy can be deduced. It should be noted that in inverse kinematics, the centre of mass scattering angles  $\theta_{cm}$  of interest are larger compared to direct kinematics case where typically the angles of interest  $\theta_{cm} \lesssim 30^\circ$ . This is one of the challenges involved in performing scattering experiment with unstable nuclei.

Proton elastic and inelastic scattering study of proton-rich  $^{30}\text{S}$  and  $^{34}\text{Ar}$  isotopes at 53 MeV/A and 47MeV/A have been performed and presented in Ref. [63]. Secondary beams from the MUST silicon detector array and GANIL facility were used in the experiment. It was found from the study that there was no indication of a proton skin in the two nuclei. Angular distributions of proton elastic scattering at 277–300 MeV per nucleon on  $^9\text{C}$  was studied in Ref. [67]. The experiment was performed in inverse kinematics at GSI Darmstadt, and relativistic impulse approximation was used to analyse the angular distribution. The recoil angle and recoil energy of the proton were measured using the recoil proton spectrometer they developed. At the same facility,  $^6\text{He}$ ,  $^8\text{He}$ ,  $^6\text{Li}$ ,  $^8\text{Li}$ ,  $^9\text{Li}$  and  $^{11}\text{Li}$  have been studied at intermediate energies [68]. At GANIL RIB facility, proton elastic and inelastic scattering on some proton-rich Argon and Sulphur isotopes have been studied at 47 MeV/u and 53 MeV/u, respectively [62, 63].

### 1.3 Outline of Dissertation

In this research, proton elastic scattering from unstable nuclei at intermediate projectile laboratory energy is studied using the relativistic impulse approximation (IA1) and generalised relativistic impulse approximation (IA2) formalisms. To calculate the elastic scattering spin observables needed to study these nuclei, one requires the Lorentz invariant nucleon–nucleon (NN) amplitudes and the bound state wave functions of the target nuclei. The bound state wave functions are calculated using relativistic mean field theory with the QHD I, QHD II, NL3, and FSUGold parameter sets. QHD stands for quantum hadrodynamics, "NL" means non-linear, and FSUGold means Florida state University Gold. These models are described fully in chapter 2. The nucleon–nucleon amplitudes to be employed are those used in the IA1 and IA2 formalisms. It is an open question as to what effect the use of IA1 versus IA2 will have in the study of scattering experiments from unstable nuclei. This work will be able to make a significant contribution in terms of understanding this fundamental question concerning the NN interaction. The final step in this project will be the calculation of the complete set of spin observables, namely the unpolarized cross section, the analysing power and the spin rotation function.

There are a number of open questions which this project will attempt to answer:

1. Can reaction studies from unstable nuclei provide a better discriminator in the choice between the IA1 and IA2 representations of the nucleon-nucleon invariant amplitudes?
2. What is the effect of using full-folding optical potential on the scattering observables compared to using factorised form of the optical potential?
3. Can the use of non-local optical potential give better description of the scattering observables compared to the localised form of the optical potential.
4. What is the effect of using the different forms of the Lagrangian densities, namely QHDI, QHDII, NL3 and FSUGold?

The results of this research such as the calculation of relativistic distorted waves for scattering from unstable nuclei will be of direct use in the calculation of exclusive ( $\mathbf{p}, 2\mathbf{p}$ ) scattering from such nuclei and will inform the scientific case for the iThemba LABS radioactive beam project.

The outline of the thesis is given as follows. In Chapter 2, the relativistic mean field models employed in this research are presented. The calculated bound state wave functions (and hence densities) are required as inputs in Chapter 3 where the relativistic optical potentials are calculated using IA1 and IA2 formalisms. Chapter 3 also contains comparisons of the optical potentials calculated using relativistic mean field densities with the QHD II, NL3, and FSUGold parameter sets. Chapter 4 contains calculations of the elastic scattering observables namely the differential cross section, analysing power, and spin rotation function. These scattering observables are obtained by solving the coordinate space Dirac equation with the localised IA1 and

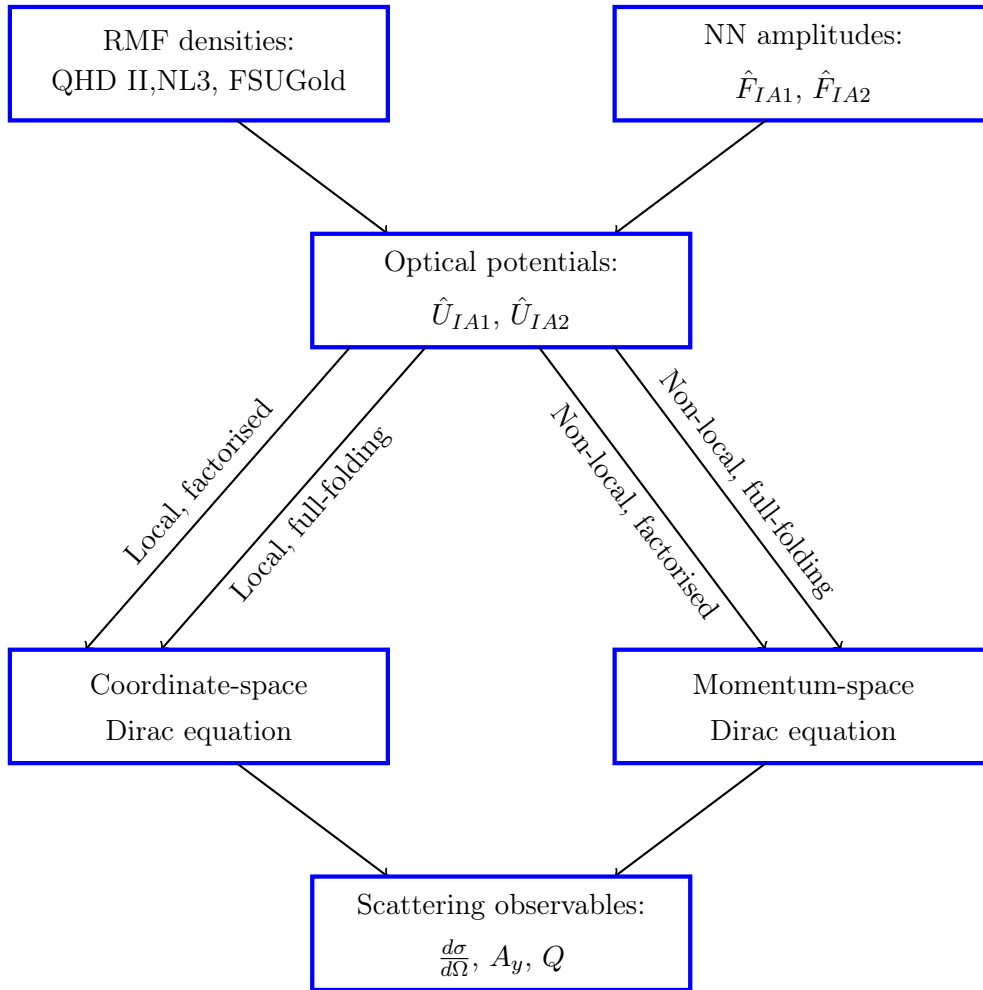


**Figure 1.1:** *Mind map of thesis.*

IA2 optical potentials calculated in Chapter 3. In this same chapter, the scattering observables calculated using the different RMF models, and employing both IA1 and IA2 formalisms will be compared. The scattering observables obtained using the factorised optical potentials will then be compared with the results obtained using the full-folding optical potentials. In Chapter 5, the scattering observables are calculated by solving the momentum space Dirac equation. This will enable one to obtain the scattering observables using non-local optical potentials. The results obtained using both local and non-local optical potentials will then be compared. Figure 1.1 shows the mind map of the thesis.

## Chapter 2

# Relativistic Mean Field Theory

Relativistic mean field (RMF) theory has been used as a tool to investigate the structure of the nucleus, and it has been able to successfully describe ground-state properties (such as radius, binding energy, spin-orbit splitting, deformation, and neutron halo) of both stable nuclei and nuclei away from the stability line, with very limited number of parameters [65, 69, 70]. In this theory, nucleons are treated as point-like particles which are described by Dirac spinors interacting through mesons exchange [69, 71]. The RMF theory has been utilized at normal densities and also for finite closed-shell nuclei [72]. These investigations reveal that the  $\sigma$  and  $\omega$  mesons with adjustable coupling constants and masses yield large scalar (S) and vector (V) potentials (consistent with Dirac phenomenology) which provide a good description of nuclear saturation and charge densities of closed-shell nuclei [73]. The goal of this chapter is to calculate ground state properties of unstable nuclei, such as binding energies, root mean square proton, neutron, and charge radii, scalar and vector densities using relativistic mean field theory.

### 2.1 Background

The description of nuclear matter based on the exchange of mesons was first introduced by Walecka [74], and the formalism is called quantum hadrodynamics. Quantum hadrodynamics (QHD) describes the nuclear many-body problem as a relativistic system of mesons and baryons [75]. It ensures the incorporation of the nuclear structure effects in a fully relativistic way via the bound state wave function of the nucleon. The model is consistent with QCD symmetries, that is, parity invariance, lorentz invariance, isospin and chiral symmetry, and electromagnetic gauge invariance. The first QHD model (QHD-I) was applied to spherical closed-shell nuclei. In the QHD-I (or  $\sigma\omega$  model), the model describes nuclear matter as resulting from interactions between nucleons (baryons) in the nucleus through exchange of neutral scalar ( $\sigma$ ) and vector ( $\omega$ ) mesons. The scalar meson results in a strong attractive central force and a spin orbit force in the nucleon-nucleon interaction. The vector meson on the other hand results in a strong repulsive central force and a spin-orbit force. The  $\sigma$  and  $\omega$  mesons carry both isospin zero. The  $\omega$  meson has been observed in nature as a resonance at  $m_\omega = 783\text{MeV}$  [76]. The free parameters in the QHD-I model are the scalar coupling constant  $g_\sigma$ , the vector coupling constant

$g_\omega$ , and the mass of the scalar meson  $m_\sigma$ . This model gives a value of the nuclear matter compressibility (K) that is too high (560 MeV against experimental value  $210 \pm 30$  MeV [77]). An inclusion of the self-couplings of the scalar meson field to the Lagrangian density made the QHD I to better reproduce the nuclear matter compressibility [78].

For nuclei with large neutron excess, a meson carrying isospin 1, the  $\rho$ - meson is needed; this led to the introduction of the QHD-II parametrization by Serot and Walecka [72]. The QHD-II parametrization incorporates (in addition to the  $\sigma$  and  $\omega$  mesons) the charged vector  $\rho$  meson, charged pseudoscalar  $\pi$  meson, electromagnetic interaction through the photon field  $A^\mu$  to account for the Coulomb repulsion between protons in nuclei. The inclusion of the  $\rho$ -meson is to distinguish between the baryons (protons and neutrons) [79]. The  $\rho$ - meson is observed in nature as a resonance at  $m_\rho = 763\text{MeV}$  [76]. The inclusion of the  $\rho$  meson and the nonlinear self-couplings of the scalar  $\sigma$  meson made the QHD model to be applicable to open-shell spherical nuclei, light deformed nuclei, and heavy deformed nuclei in the rare earth region [73]. The couplings are determined by fitting calculated properties of nuclei and nuclear matter to the experimentally observed values.

Among the first QHD models that contained non-linear terms are the NL1 [80] and NL-SH [81] parametrizations. The NL-SH parametrization was formulated to improve the existing QHD model so as to better describe neutron radii of neutron-rich nuclei [81]. The NL1 parametrization gives good results for charge radii and binding energy, and also a good description of the super-deformed bands [70]. It, however, gives less satisfactory results for nuclei away from the stability line, and it underestimates nuclear matter incompressibility ( $K = 212$  MeV). Although, the NL-SH parametrization gives a better description of deformation properties than the NL1 parametrization, it also fails to give satisfactory results for nuclei far away from the stability line. Moreover, it overestimates nuclear matter incompressibility [70]. Two other parameter sets (TM1 and TM2) were introduced in Ref. [82] by including self-coupling in the  $\omega$  meson field to the QHD Lagrangian density. The TM1 (TM2) parametrization was introduced to obtain good agreement with light (heavy) unstable nuclei. An improvement on the TM1 parameter set is the PK1 parameter set, obtained by fitting some ground state properties of a wide range of heavy nuclei. The PK1 parameter set is able to better reproduce the nuclear symmetry energy and compressibility [83].

Two other extensions to the QHD-I model (that incorporate nonlinear terms) are the NL3 and FSUGold parametrizations. The NL3 parametrization was introduced in Ref. [70] to provide an improved set of Lagrangian parameters, that cured the deficiencies of the previous parametrizations. This parametrization is able to improve the predicted value of the compressibility (K), and it has been successfully used to describe ground state properties of both stable nuclei and nuclei away from the stability line, with values very close to experimental ones. The parameter sets were obtained by fitting the predicted values of binding energy, neutron radii, and

charge radii of spherical nuclei to the observed values of nuclei far from the valley of beta stability [70]. In the FSUGold model [84], a coupling between the  $\omega$  meson field and the  $\rho$  meson field was introduced. This was done to better describe the density dependence of the nuclear asymmetry energy without changing the saturation properties of nuclear matter. The parameter sets of this model were obtained by fitting charge radii and binding energies of some magic nuclei to the calculated properties. The model produces an equation of state which is softer for symmetric nuclear matter compared with the NL3 parameter set. The FSUGold parameter set gives a compression modulus of  $K = 230 \text{ MeV}$  for symmetric nuclear matter while the NL3 parametrization gives  $K = 271 \text{ MeV}$ . The addition of two extra parameters  $\zeta$  and  $\Lambda_V$  in the FSUGold make the predictions of this model close to experiment. The parameter  $\zeta$  reduces the value of  $K$  while the parameter  $\Lambda_V$  is used to soften the symmetry energy [84, 85]. As mentioned in Ref. [86], the models that have the softest symmetry energy are always the ones to first drip neutrons. In this chapter, four models (QHD-I, QHD-II, NL3, and FSUGold) will be used to calculate the ground state properties of unstable nuclei.

## 2.2 The Lagrangian density

The QHD model starts with the quantum field theory Lagrangian density describing nucleons interacting through various meson fields. A general Lagrangian density can be written as [84]:

$$\begin{aligned} \mathcal{L} = & \bar{\psi} \left[ \gamma^\mu \left( i\partial_\mu - g_\omega \omega_\mu - \frac{g_\rho}{2} \boldsymbol{\tau} \cdot \boldsymbol{\rho}_\mu - \frac{e}{2} (1 + \tau_3) A_\mu \right) \right. \\ & - (M - g_\sigma \sigma) \left. \right] \psi + \frac{1}{2} \partial^\mu \sigma \partial_\mu \sigma - \frac{1}{2} m_\sigma^2 \sigma^2 - \frac{1}{4} \Omega^{\mu\nu} \Omega_{\mu\nu} \\ & + \frac{1}{2} m_\omega^2 \omega^\mu \omega_\mu - \frac{1}{4} \mathbf{B}^{\mu\nu} \cdot \mathbf{B}_{\mu\nu} + \frac{1}{2} m_\rho^2 \boldsymbol{\rho}^\mu \cdot \boldsymbol{\rho}_\mu - \frac{1}{4} F^{\mu\nu} F_{\mu\nu} \\ & - U(\sigma, \omega^\mu, \boldsymbol{\rho}^\mu). \end{aligned} \quad (2.2.1)$$

Here,  $\psi$  is the Dirac spinor for the nucleon with mass  $M$ , and  $A_\mu$  is the electromagnetic field responsible for the Coulomb interaction. The nucleon interacts via exchange of various mesons and a photon.  $\sigma$  and  $\omega$  are the isoscalar-scalar and the isoscalar-vector mesons, which provide an intermediate range attraction and a short range repulsion, respectively.  $\rho$  is the isovector-vector meson and provides the isovector part of the nuclear interaction, and becomes important for the description of nuclei that have number of neutrons not equal to number of protons.  $m_\sigma$ ,  $m_\omega$ , and  $m_\rho$  are the masses of the  $\sigma$ ,  $\omega$ , and  $\rho$  mesons, respectively.  $g_\sigma$ ,  $g_\omega$ ,  $g_\rho$  and  $e^2/4\pi$  are the coupling constants for the  $\sigma$ ,  $\omega$  and  $\rho$  mesons and for the photon, respectively. The isospin Pauli matrices are written as  $\boldsymbol{\tau}$ , with  $\tau_3$  being the third component of  $\boldsymbol{\tau}$ . The nonlinear self-interaction term  $U(\sigma, \omega^\mu, \boldsymbol{\rho}^\mu)$  is incorporated via [84, 86]

$$U(\sigma, \omega^\mu, \boldsymbol{\rho}^\mu) = \frac{\eta}{3!} (g_\sigma \sigma)^3 + \frac{\lambda}{4!} (g_\sigma \sigma)^4 - \frac{\zeta}{4!} (g_\omega^2 \omega_\mu \omega^\mu)^2 - \Lambda_\omega (g_\rho^2 \mathbf{b}_\mu \cdot \mathbf{b}^\mu) (g_\omega^2 \omega_\mu \omega^\mu), \quad (2.2.2)$$

where  $\eta$ ,  $\lambda$ , and  $\zeta$  are isoscalar-meson self-interactions. They are used to soften the equation of state of symmetric nuclear matter.  $\Lambda_\omega$  is the mixed isoscalar-isovector coupling, which modifies the density dependence of the symmetric energy [84].

The field tensors for the vector mesons and electromagnetic field are

$$\begin{aligned}\Omega^{\mu\nu} &= \partial^\mu \omega^\nu - \partial^\nu \omega^\mu \\ \mathbf{B}^{\mu\nu} &= \partial^\mu \boldsymbol{\rho}^\nu - \partial^\nu \boldsymbol{\rho}^\mu \\ F^{\mu\nu} &= \partial^\mu A^\nu - \partial^\nu A^\mu.\end{aligned}\tag{2.2.3}$$

The equations of motion for baryons and mesons can now be derived from the Lagrangian density  $\mathcal{L}$  and Euler-Lagrangian equation:

$$\frac{\partial \mathcal{L}}{\partial \phi(x)} - \partial_\mu \left( \frac{\partial \mathcal{L}}{\partial (\partial_\mu \phi)} \right) = 0.\tag{2.2.4}$$

For baryons, the equation of motion is the Dirac equation:

$$[\gamma^\mu (i\partial_\mu - V_\mu) - (M - S)] \psi = 0,\tag{2.2.5}$$

where the scalar and vector potentials are defined in terms of the meson fields as

$$S = g_\sigma \sigma,\tag{2.2.6}$$

and

$$V_\mu = g_\omega \omega_\mu + g_\rho \boldsymbol{\tau} \cdot \boldsymbol{\rho}_\mu + \frac{e}{2} (1 + \tau_3) A_\mu.\tag{2.2.7}$$

For mesons and photon, the field equations are:

$$(\partial^\mu \partial_\mu + m_\sigma^2) \sigma = -g_\sigma \bar{\psi} \psi - \eta \sigma^2 - \lambda \sigma^3,\tag{2.2.8}$$

$$\partial_\nu \Omega^{\mu\nu} + m_\omega^2 \omega^\mu = g_\omega \bar{\psi} \gamma^\mu \psi\tag{2.2.9}$$

$$\partial_\nu \mathbf{B}^{\mu\nu} + m_\rho^2 \boldsymbol{\rho}^\mu = g_\rho \bar{\psi} \gamma^\mu \boldsymbol{\tau} \psi + g_\rho (\boldsymbol{\rho}_\nu \times \mathbf{B}^{\mu\nu}),\tag{2.2.10}$$

$$\partial_\nu F^{\mu\nu} = e \bar{\psi} \gamma^\mu \frac{1 + \tau_3}{2} \psi.\tag{2.2.11}$$

Table 2.1 shows the parameter sets for the four relativistic mean field models used in this work: QHD-I, QHD-II, NL3 and FSUGold. All the masses are given in MeV, and the parameter sets are those of the Walecka convention. For a comparison with the Ring convention, see Ref. [87].

## 2.3 Relativistic mean field equations

In RMF theory, meson field operators are replaced by their expectation values (i.e., classical fields) [72, 75]. For static, spherically symmetric system [86]:

$$\begin{aligned}\sigma(x) &\rightarrow \langle \sigma(x) \rangle = \sigma_0(r), \\ \omega^\mu(x) &\rightarrow \langle \omega^\mu(x) \rangle = g^{\mu 0} \omega_0(r), \\ \boldsymbol{\rho}_i^\mu(x) &\rightarrow \langle \boldsymbol{\rho}_i^\mu(x) \rangle = g^{\mu 0} \delta_{\alpha 3} \rho_0(r), \\ A^\mu(x) &\rightarrow \langle A^\mu(x) \rangle = g^{\mu 0} A_0(r).\end{aligned}\tag{2.3.1}$$

where  $r \equiv |\mathbf{x}|$ . For static spherically symmetric nuclei, only the fourth component of the vector fields (i.e.,  $\omega_0$ ,  $\rho^0$ , and  $A^0$ ) are non-vanishing. Charge conservation also

**Table 2.1:** Parameter sets for the four relativistic mean field models used in this work. The parameters  $\eta$ ,  $m_\sigma$ ,  $m_\omega$ ,  $\omega_\rho$  are all given in MeV. Mass of nucleon  $M$  is fixed at 939 MeV.

Model	QHD-I	QHD-II	NL3	FSUGold
$g_\sigma^2$	109.63	109.63	104.3871	112.1996
$g_\omega^2$	190.43	190.43	165.5854	204.5469
$g_\rho^2$	0.0	65.23	79.60	138.4701
$\eta$	0.0	0.0	3.8599	1.4203
$\lambda$	0.0	0.0	-0.01591	0.02376
$\zeta$	0.0	0.0	0.0	0.06
$\Lambda_\omega$	0.0	0.0	0.0	0.03
$m_\sigma$	520	520	508.194	491.5
$m_\omega$	783	783	782.501	782.50
$m_\rho$	0.0	770	763.00	763.0

ensures that only the third-component ( $\rho_{03}$ ) of the isovector  $\boldsymbol{\rho}^0$  has a contribution to the interaction. The baryon sources are replaced by their ground state normal-ordered expectation values:

$$\begin{aligned}
\bar{\psi}\mathbf{1}\psi &\rightarrow \langle : \bar{\psi}\mathbf{1}\psi : \rangle = \rho_s(r), \\
\bar{\psi}\gamma^\mu\psi &\rightarrow \langle : \bar{\psi}\gamma^\mu\psi : \rangle = g^{\mu 0}\rho_v(r), \\
\bar{\psi}\gamma^\mu\tau_\alpha\psi &\rightarrow \langle : \bar{\psi}\gamma^\mu\tau_\alpha\psi : \rangle = g^{\mu 0}\delta_{\alpha 3}\rho_3(r), \\
\bar{\psi}\gamma^\mu\tau_p\psi &\rightarrow \langle : \bar{\psi}\gamma^\mu\tau_p\psi : \rangle = g^{\mu 0}\rho_p(r).
\end{aligned} \tag{2.3.2}$$

In equation (2.3.2),  $\tau_p = (1 + \tau_3)/2$  denotes the proton isospin projection operator,  $\rho_s(r)$  is the Lorentz-scalar density,  $\rho_v$  is the vector density. The isovector density, which is the difference between proton density and neutron density, is denoted by  $\rho_3(r)$ . The baryon sources give meson fields that satisfy coupled, nonlinear Klein-Gordon equations given by

$$\begin{aligned}
\left(\frac{d^2}{dr^2} + \frac{2}{r}\frac{d}{dr} - m_\sigma^2\right)g_\sigma\sigma_0(r) - g_\sigma^2\left(\frac{\eta}{2}g_\sigma^2\sigma_0^2(r) + \frac{\lambda}{6}g_\sigma^3\sigma_0^3(r)\right) \\
- 2\Lambda_\sigma g_\rho^2\rho_0^2(r)g_\sigma\sigma_0(r) = -g_\sigma^2\rho_s(r),
\end{aligned} \tag{2.3.3a}$$

$$\begin{aligned}
\left(\frac{d^2}{dr^2} + \frac{2}{r}\frac{d}{dr} - m_\omega^2\right)g_\omega\omega_0(r) - g_\omega^2\left(\frac{\zeta}{6}g_\omega^3\omega_0^3(r)\right) \\
+ 2\Lambda_\omega g_\rho^2\rho_0^2(r)g_\omega\omega_0(r) = -g_\omega^2\rho_\omega(r),
\end{aligned} \tag{2.3.3b}$$

$$\left(\frac{d^2}{dr^2} + \frac{2}{r}\frac{d}{dr} - m_\rho^2\right)g_\rho\rho_0(r) - 2g_\rho^2(\Lambda_\omega g_\omega^2\omega_0^2(r))g_\rho\rho_0(r) = -\frac{g_\rho^2}{2}\rho_3(r). \tag{2.3.3c}$$

The solution of the photon field is reduced to [88]

$$A_0(r) = e \left( \frac{1}{r} \int_0^r dx x^2 \rho_p(x) + \int_r^\infty dx x \rho_p(x) \right). \quad (2.3.4)$$

The solution of the Dirac equation can be written in terms of two-component upper and lower parts. The positive energy spinors can be written as [29, 86]

$$u_\alpha(\mathbf{x}) \equiv u_{n\kappa mt}(\mathbf{x}) = \frac{1}{r} \begin{pmatrix} g_{n\kappa t}(r) \mathcal{Y}_{\kappa m}(\hat{r}) \\ i f_{n\kappa t}(r) \mathcal{Y}_{-\kappa m}(\hat{r}) \end{pmatrix}, \quad (2.3.5)$$

where the angular and spin solutions are the spherical harmonics:

$$\mathcal{Y}_{\ell jm}(\hat{r}) = \sum_{s_z = \pm \frac{1}{2}} \langle \ell, \frac{1}{2}, m_\ell, m_s | jm \rangle Y_{\ell, m_\ell}(\hat{r}) \chi_{m_s}, \quad (2.3.6)$$

and

$$j = |\kappa| - \frac{1}{2}, \quad \ell = \begin{cases} \kappa & \text{if } \kappa > 0 \\ -1 - \kappa & \text{if } \kappa < 0 \end{cases}. \quad (2.3.7)$$

$Y_{\ell, m-s_z}(\hat{r})$  is the spherical harmonic, the two-component Pauli spinor  $\chi_{m_s}$  is given as

$$\chi_{m_s} = \begin{cases} \begin{pmatrix} 1 \\ 0 \end{pmatrix}, & m_s = \frac{1}{2} \\ \begin{pmatrix} 0 \\ 1 \end{pmatrix}, & m_s = -\frac{1}{2} \end{cases}, \quad (2.3.8)$$

and  $g(r)$  and  $f(r)$ , which should not be confused with the mesons coupling constants, denote here the radial parts of the upper and lower components of the bound state wave function, with the normalization

$$\int dr r^2 [g^2(r) + f^2(r)] = 1. \quad (2.3.9)$$

The Dirac equation then satisfies first-order coupled differential equations

$$\begin{aligned} \left( \frac{d}{dr} + \frac{\kappa}{r} \right) g_\alpha(r) - (E_\alpha + M - g_\sigma \sigma_0(r) - g_\omega \omega_0(r) \\ \mp \frac{1}{2} g_\rho \rho_0 - e \begin{pmatrix} 1 \\ 0 \end{pmatrix} A_0(r)) f_\alpha(r) = 0, \end{aligned} \quad (2.3.10a)$$

$$\begin{aligned} \left( \frac{d}{dr} - \frac{\kappa}{r} \right) f_\alpha(r) + (E_\alpha - M + g_\sigma \sigma_0(r) - g_\omega \omega_0(r) \\ \mp \frac{1}{2} g_\rho \rho_0 - e \begin{pmatrix} 1 \\ 0 \end{pmatrix} A_0(r)) g_\alpha(r) = 0. \end{aligned} \quad (2.3.10b)$$

Equations (2.3.3) and (2.3.10) form a system of coupled differential equations also known as the relativistic Hartree equations, which are numerically solved by a self-consistent iteration scheme using the parameter sets from the various RMF

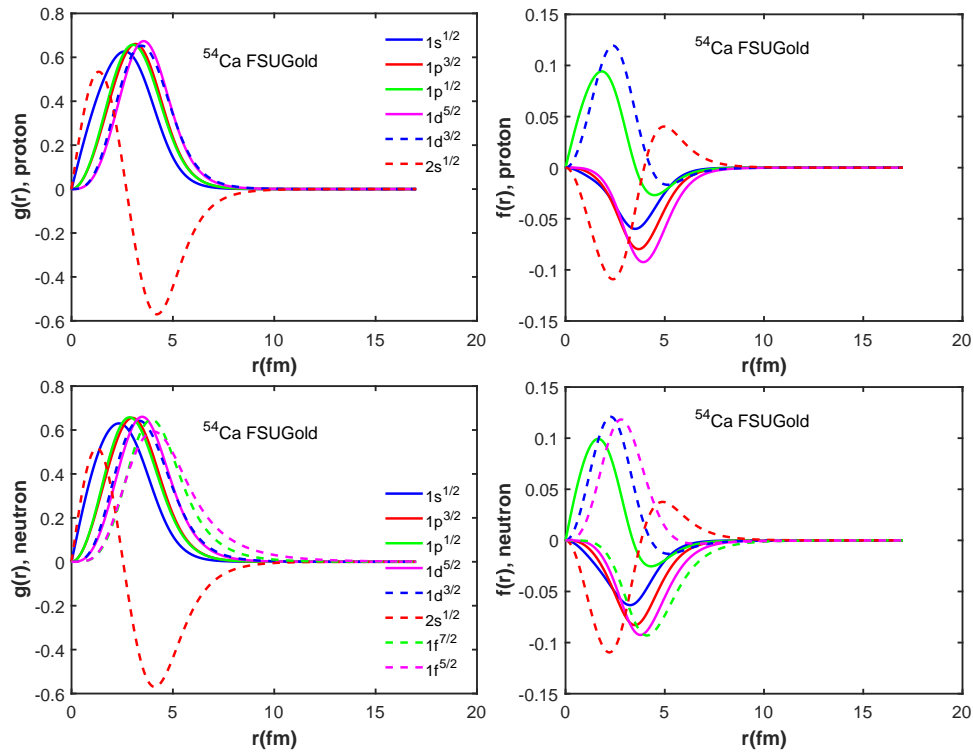


**Figure 2.1:** The upper and lower components wave functions for each state of  $^{54}\text{Ca}$  using FSUGold parameter sets.

models to obtain the ground-state properties of the system. The self-consistent process begins with Woods–Saxon shaped meson fields to generate bound-state energies and corresponding wave functions for the single-particle states. The scalar and vector densities computed from these wave functions are used as sources for the meson–field equations, thereby generating new meson–fields via Green’s function techniques. This iterative scheme continues until one achieves self-consistency (that is convergence) [86]. The plots in Figure 2.1 show the upper and lower components wave functions for each state of  $^{48}\text{Ca}$  using FSUGold parameter set.

In equation (2.3.10), the lower and upper numbers represent neutrons and protons, respectively. For closed-shell nuclei, the scalar density, vector (baryon) density, isovector density, and charge density are given, respectively, by [29, 71, 89]:

$$\begin{aligned} \rho_S(r) &= \sum_{\alpha}^{occ} \bar{u}_{\alpha}(\mathbf{x}) u_{\alpha}(\mathbf{x}) \\ &= \sum_{\alpha}^{occ} \left( \frac{2j_{\alpha} + 1}{4\pi r^2} \right) [g_{\alpha}^2(r) - f_{\alpha}^2(r)], \end{aligned} \quad (2.3.11)$$

$$\begin{aligned}
\rho_V(r) &= \sum_{\alpha}^{occ} \bar{u}_{\alpha}(\mathbf{x}) \gamma^0 u_{\alpha}(\mathbf{x}) \\
&= \sum_{\alpha}^{occ} \left( \frac{2j_{\alpha} + 1}{4\pi r^2} \right) [g_{\alpha}^2(r) + f_{\alpha}^2(r)], \tag{2.3.12}
\end{aligned}$$

$$\begin{aligned}
\rho_3(r) &= \sum_{\alpha}^{occ} u_{\alpha}^{\dagger}(\mathbf{r}) \tau u_{\alpha}(\mathbf{r}) \\
&= \sum_{\alpha}^{occ} \tau_{3\alpha} \left( \frac{2j_{\alpha} + 1}{4\pi r^2} \right) [g_{\alpha}^2(r) + f_{\alpha}^2(r)] \\
&= \rho_{V,p}(r) - \rho_{V,n}(r), \tag{2.3.13}
\end{aligned}$$

$$\begin{aligned}
\rho_{ch}(r) &= \sum_{\alpha}^{occ} u_{\alpha}^{\dagger}(\mathbf{r}) \frac{1 + \tau_{3\alpha}}{2} u_{\alpha}(\mathbf{r}) \\
&= \sum_{\alpha}^{occ} \frac{1 + \tau_{3\alpha}}{2} \left( \frac{2j_{\alpha} + 1}{4\pi r^2} \right) [g_{\alpha}^2(r) + f_{\alpha}^2(r)], \tag{2.3.14}
\end{aligned}$$

where the relation

$$\sum_{m=-j}^j \mathcal{Y}_{\kappa m}^{\dagger} \mathcal{Y}_{\kappa' m} = \left( \frac{2j + 1}{4\pi} \right) \delta_{\kappa\kappa'} \tag{2.3.15}$$

has been used. Also the sums in equations (2.3.11) – (2.3.14) are taken over all the occupied (occ) states.

The proton root-mean-square (rms) matter radius is computed using

$$r = [\langle r^2 \rangle]^{\frac{1}{2}} = \left[ \frac{1}{Z} \int d\tau r^2 \rho_{V,p}(r) \right]^{\frac{1}{2}}, \tag{2.3.16}$$

where  $Z$  denotes the number of protons in the nucleus. Similarly, for charge root-mean-square radius,

$$r_{ch} = [\langle r_{ch}^2 \rangle]^{\frac{1}{2}} = \left[ \frac{1}{Z} \int d\tau r^2 \rho_{ch}(r) \right]^{\frac{1}{2}}, \tag{2.3.17}$$

The root-mean square radii computed using QHDII, NL3, and FSUGold parameter sets, are shown and compared with experimental data, where available, in Table 2.2. There is satisfactory agreement with experiment at the 1% level. The experimental data for  $^{40,48}\text{Ca}$ ,  $^{98}\text{Zr}$ , and  $^{132}\text{Sn}$  are taken from Ref. [90] while the theoretical result for  $^{54}\text{Ca}$  is taken from Ref. [91].

The neutron vector densities are shown in figure 2.2 for  $^{48,54,58,60}\text{Ca}$ , using the four RMF models, for comparison. In Figure 2.3, the plots of the charge densities, calculated for  $^{48,54,58,60}\text{Ca}$ , using the four RMF models are shown. The results

**Table 2.2:** Root-mean-square charge radius, proton and neutron root-mean-square radii of some closed shell Calcium isotopes.

Nucleus	Observable	QHD-II	NL3	FSUGold	Experiment
$^{40}\text{Ca}$	$r_p$	3.3863	3.3770	3.3863	
	$r_n$	3.3315	3.3285	3.3315	
	$\Delta r = r_n - r_p$	-0.05487	-0.04858	-0.0513	
	$r_{ch}$	3.4795	3.4705	3.4795	3.4776 [90]
$^{48}\text{Ca}$	$r_p$	3.3747	3.3789	3.3659	
	$r_n$	3.5875	3.6046	3.5632	
	$\Delta r = r_n - r_p$	0.21276	0.22572	0.1973	
	$r_{ch}$	3.4682	3.4723	3.4597	3.4771 [90]
$^{54}\text{Ca}$	$r_p$	3.4585	3.5037	3.4834	
	$r_n$	3.8746	3.9008	3.8249	
	$\Delta r = r_n - r_p$	0.41604	0.39704	0.3414	
	$r_{ch}$	3.5498	3.5939	3.5741	3.5640 [91]
$^{58}\text{Ca}$	$r_p$	3.4945	3.5317	3.5191	
	$r_n$	4.0474	4.0668	3.9950	
	$\Delta r = r_n - r_p$	0.55295	0.53514	0.47589	
	$r_{ch}$	3.5849	3.6212	3.6089	
$^{60}\text{Ca}$	$r_p$	3.5137	3.5513	3.5407	
	$r_n$	4.1442	4.1591	4.0841	
	$\Delta r = r_n - r_p$	0.63052	0.60779	0.54339	
	$r_{ch}$	3.6036	3.6403	3.6300	
$^{98}\text{Zr}$	$r_p$		4.3032	4.2836	
	$r_n$		4.5415	4.4716	
	$\Delta r = r_n - r_p$		0.23826	0.18796	
	$r_{ch}$		4.3769	4.3577	4.4012 [90]
$^{132}\text{Sn}$	$r_p$		4.6435	4.6542	
	$r_n$		4.9891	4.9251	
	$\Delta r = r_n - r_p$		0.34558	0.27090	
	$r_{ch}$		4.7119	4.7225	4.7093 [90]

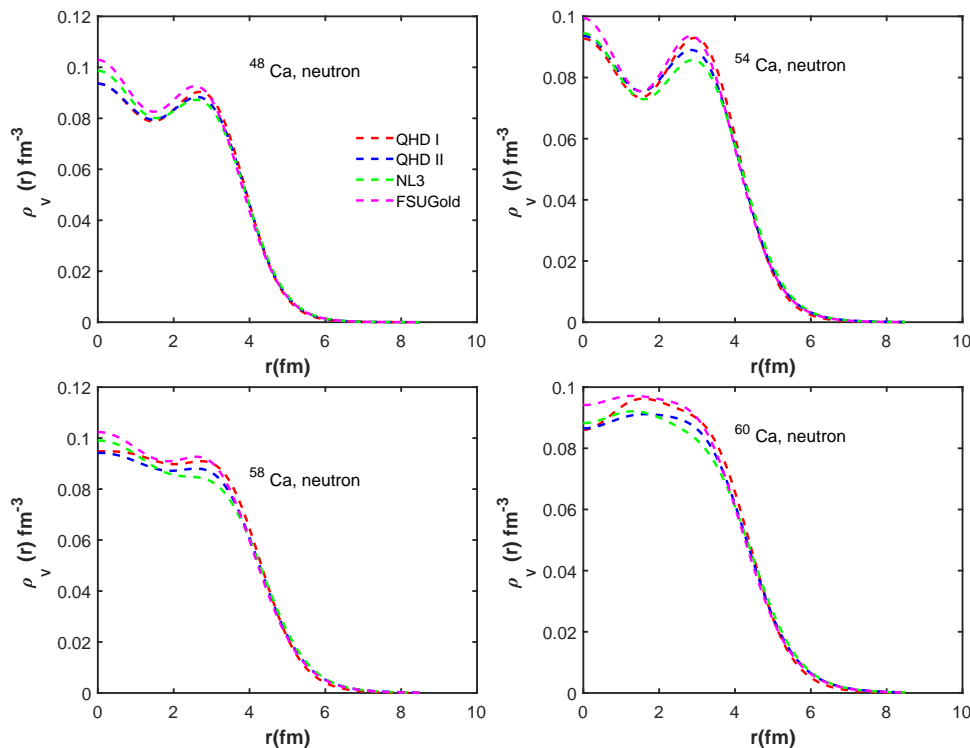


**Figure 2.2:**  $^{48,54,58,60}\text{Ca}$  neutron vector densities.

obtained for the case of  $^{48}\text{Ca}$  is compared with empirical charge density distributions (Fourier-Bessel coefficients) obtained using the data from Ref. [90]. Figure 2.4 shows plots of proton and neutron vector densities for  $^{48,54,58,60}\text{Ca}$ , using the NL3 parametrization. There is increase in the difference between proton and neutron densities as neutron number increases.

Figures 2.5–2.8 show the proton and neutron single-particle states in  $^{48,54}\text{Ca}$ , using the QHD-I, QHD-II, NL3, and FSUGold parametrizations. In figure 2.6, a level inversion occurs with the  $1d_{3/2}$  state coming below the  $2s_{1/2}$ , in all the four RMF models. Similar situation can be observed in figure 2.8 for  $^{54}\text{Ca}$ .

### 2.3.1 Pairing correlations

Pairing correlations are as a result of short range part of the nucleon-nucleon interaction, and they play a crucial role in open shell nuclei [92]. To account for pairing for open shell nuclei, the occupation numbers  $n_\alpha$  have to be introduced to the sums in equations (2.3.11)–(2.3.14). Without pairing,  $n_\alpha = 1$  for occupied levels and zero for unoccupied levels. The BCS (Bardeen-Cooper-Schrieffer) approach under constant gap approximation is often used with RMF theory to deal with pairing correlations [69, 80]. The conventional BCS theory does not, however, properly include contribution of continuum states; this made it not suitable for exotic nuclei. By quantizing continuum states and making use of the relativistic Hartree Bogoliubov formalism [93], the relativistic continuum Hartree Bogoliubov theory was developed [94–96]. See [92] for a review of the relativistic continuum Hartree Bogoliubov theory applied

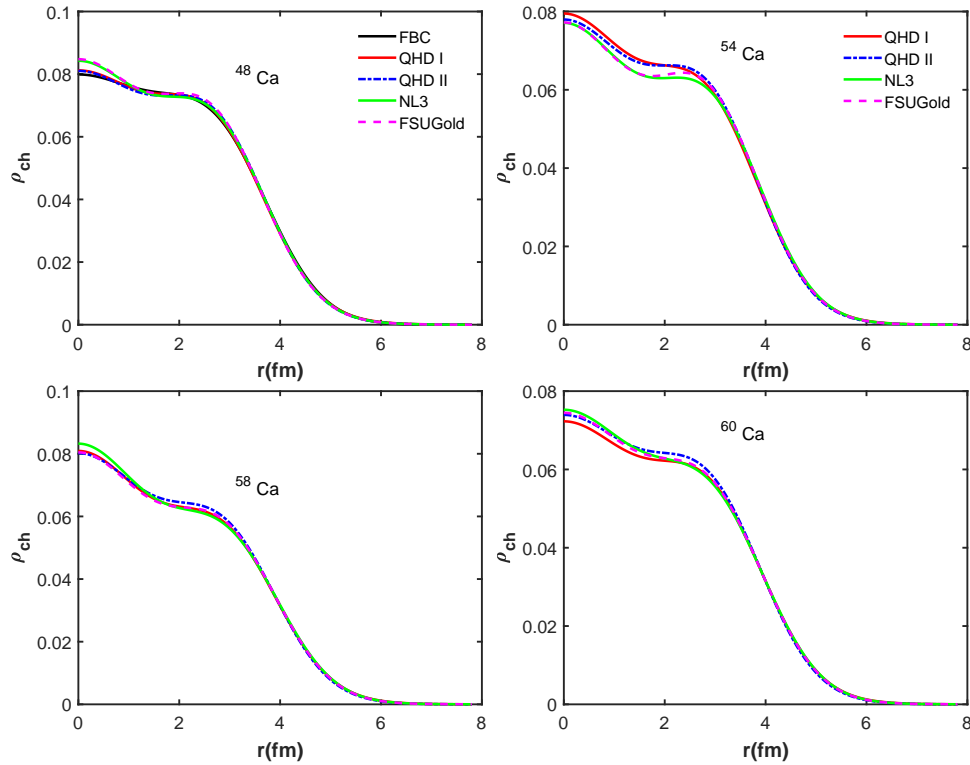


**Figure 2.3:** Plot of charge density ( $\rho_{ch}(r)$ ) for  $^{48,54,58,60}\text{Ca}$ . FBC denotes Fourier-Bessel coefficients.

to ground state properties of exotic nuclei. In the BCS approach, the occupation numbers are calculated using the constant gap approximation via [71, 73, 82]:

$$n_{\alpha} = \frac{1}{2} \left( 1 - \frac{\epsilon_{\alpha} - \lambda}{\sqrt{(\epsilon_{\alpha} - \lambda)^2 + \Delta^2}} \right), \quad (2.3.18)$$

where  $\epsilon_{\alpha}$  is the single-particle energy. This is an approximation for exotic nuclei which are far from the valley of stability. The occupation probability  $v_{\alpha}^2 = n_{\alpha}$ , and the unoccupation probability  $u_{\alpha}^2 = 1 - v_{\alpha}^2$ . The constant gap parameter can be calculated using the following five-point formula [97]:

$$\Delta = \frac{-1}{8} [M(N+2) - 4M(N+1) + 6M(N) - 4M(N-1) + M(N-2)], \quad (2.3.19)$$

where  $M(N)$  is the atomic mass of a nucleus with  $N$  neutrons and  $Z$  protons. The Fermi energy  $\lambda$  for protons (neutrons) is calculated from

$$\sum_{\alpha} n_{\alpha} = Z(N), \quad (2.3.20)$$

and the sum is taken over proton (neutron) states.

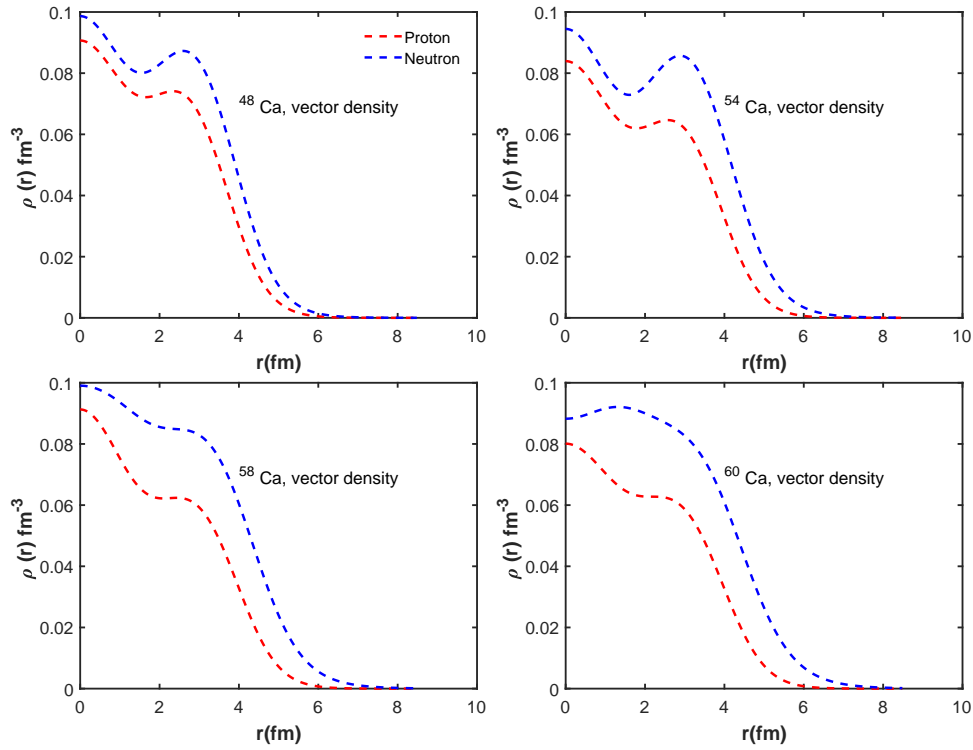


**Figure 2.4:**  $^{48,54,58,60}\text{Ca}$  proton and neutron vector densities plots with NL3 parameter sets.

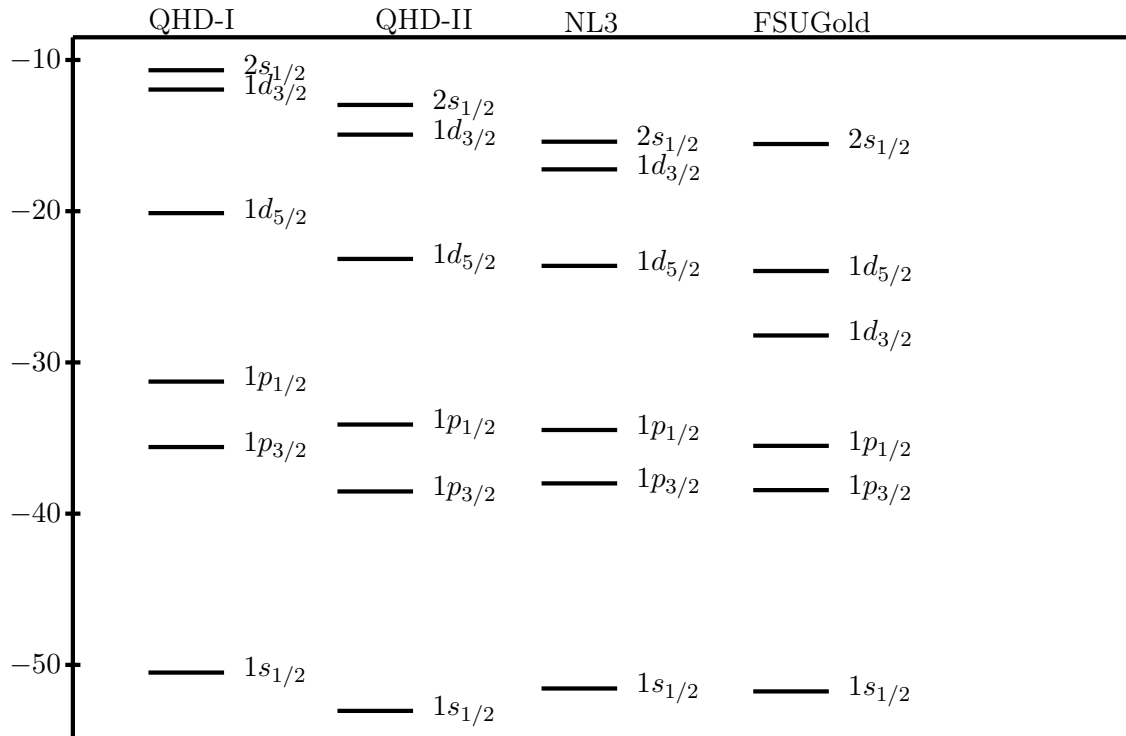


**Figure 2.5:** Single-particle proton states in  $^{48}\text{Ca}$ . Binding energy on the vertical axis is in MeV.

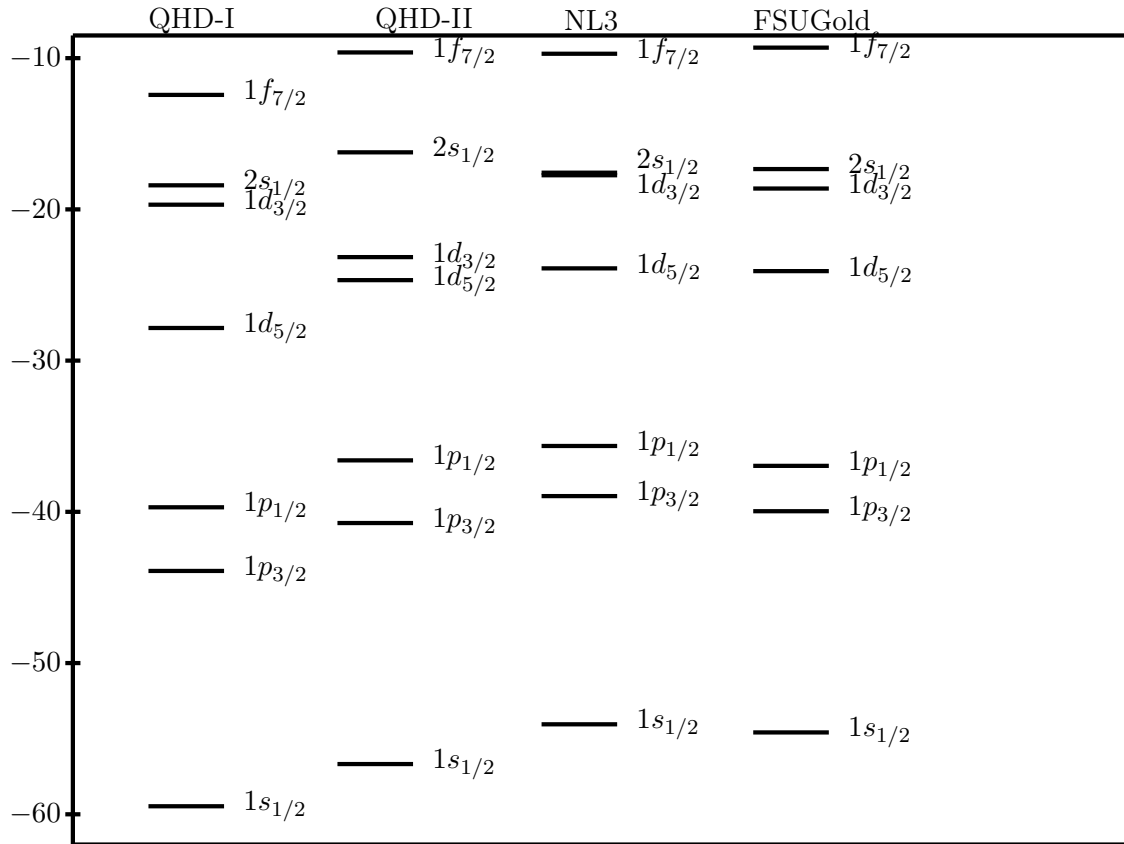


**Figure 2.6:** Single-particle neutron states in  $^{48}\text{Ca}$ . Binding energy on the vertical axis is in MeV.

## 2.4 Halo nuclei and skin

Usually, halo is considered as a long low density tail in the nuclear matter distribution, whereas skin means a significant difference between root mean square radius values for protons and neutrons. In fact the new era of study of nuclei started when unstable nuclei (halos) with very large interaction cross sections were discovered by Tanihata and his collaborators [98]. Even though same nuclei are sometimes considered as halo or skin by different authors, some rules to distinguish them were given in Ref. [99]. Halo nuclei have radii larger than predicted from the usual  $A^{1/3}$  systematic. They have density distributions reaching further out than usual, and show narrower momentum distributions of the break up fragments of the halo nuclei. In the neutron skin

$$\frac{\rho_n(r)}{\rho_p(r)} > 4. \quad (2.4.1)$$

Neutron skin should contain a significant number of neutrons, contrary to the case of neutron halo, i.e., for neutron skin

$$\frac{\rho_n(r \sim R_A)}{\rho_n(r = 0)} > 0.01. \quad (2.4.2)$$

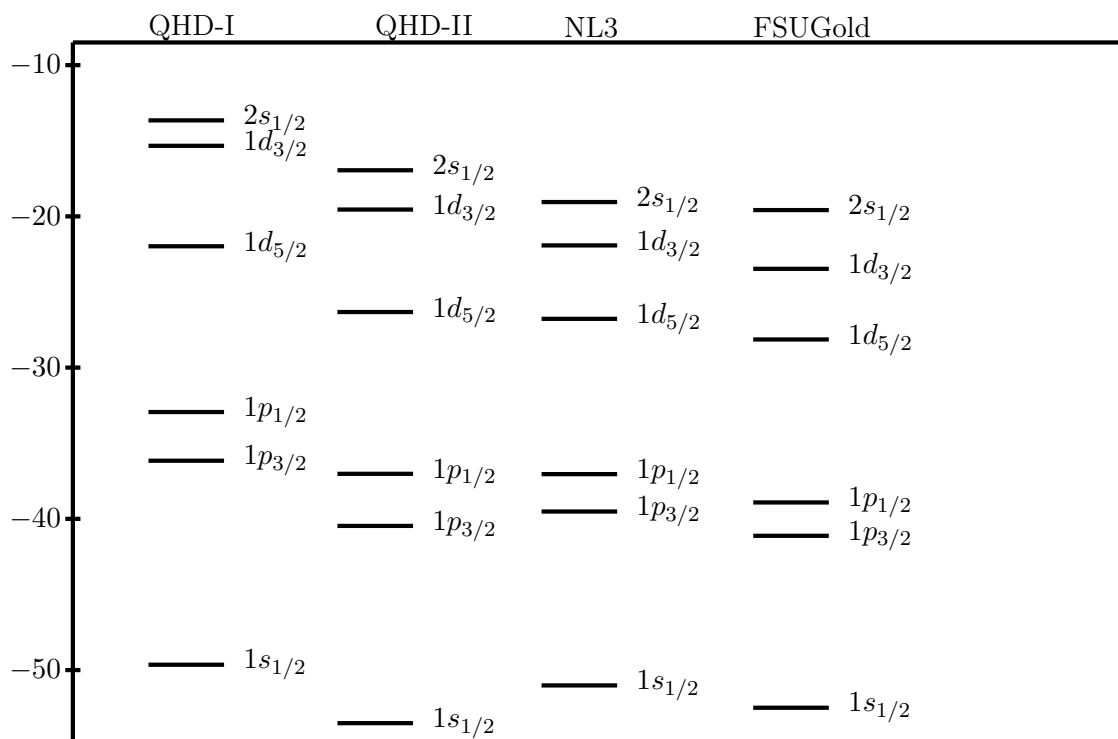


**Figure 2.7:** Single-particle proton states in  $^{54}\text{Ca}$ . Binding energy on the vertical axis is in MeV.

The difference between neutron and proton radii should be large enough i.e.,  $\delta R = R_n - R_p > 1\text{fm}$ . It was shown in Ref. [99] that neutron skin does not directly depend on the number of excess neutrons but rather on how far the nucleus is away from the  $\beta$  stability line.  $^{48}\text{Ca}$  and  $^{208}\text{Pb}$  are believed to have neutron skin.

Some nuclei with (possible) proton halo are  $^{17}\text{Ne}$ ,  $^{17}\text{F}$ ,  $^8\text{B}$ . Those with neutron halo are  $^{14}\text{N}$ ,  $^{11}\text{Be}$ ,  $^{15}\text{C}$ ,  $^{19}\text{C}$ ,  $^6\text{He}$ ,  $^{11}\text{Li}$ ,  $^{14}\text{Be}$ ,  $^{17}\text{B}$ , where the first four nuclei have one-neutron halo, while the last four have two-neutron halo. In a three-body picture ( $A + n + n$ , i.e., core nuclide  $A$  and two neutrons), a so-called Borromean state can exist. The Borromean state is a bound three-body system in which none of the two-body subsystems form a bound state.  $^6\text{He}$ ,  $^{11}\text{Li}$ ,  $^{14}\text{Be}$ , and  $^{17}\text{B}$  are Borromean nuclei. When the two-body system are bound and one is unbound, that is sometimes referred to as a "Samba" configuration. It is possible that  $^{22}\text{C}$  is an example of a "Samba" system, which is composed of two-neutron halo and a  $^{18}\text{C}$  core. Ref. [100] gives details of these weakly bound three-body systems and others such as "Tango" nuclei. Detailed study of these types of exotic nuclei are given in [101–105]. In Ref. [65], the ground state properties of some even–even carbon and beryllium nuclei were studied using relativistic mean field theory. A two–neutron halo was observed in  $^{14}\text{Be}$  (which is the drip-line nucleus for beryllium nuclei), but surprisingly not for  $^{22}\text{C}$  (which is the drip-line nucleus for carbon nuclei). For carbon nuclei, a new magic number was observed for  $N = 16$ .

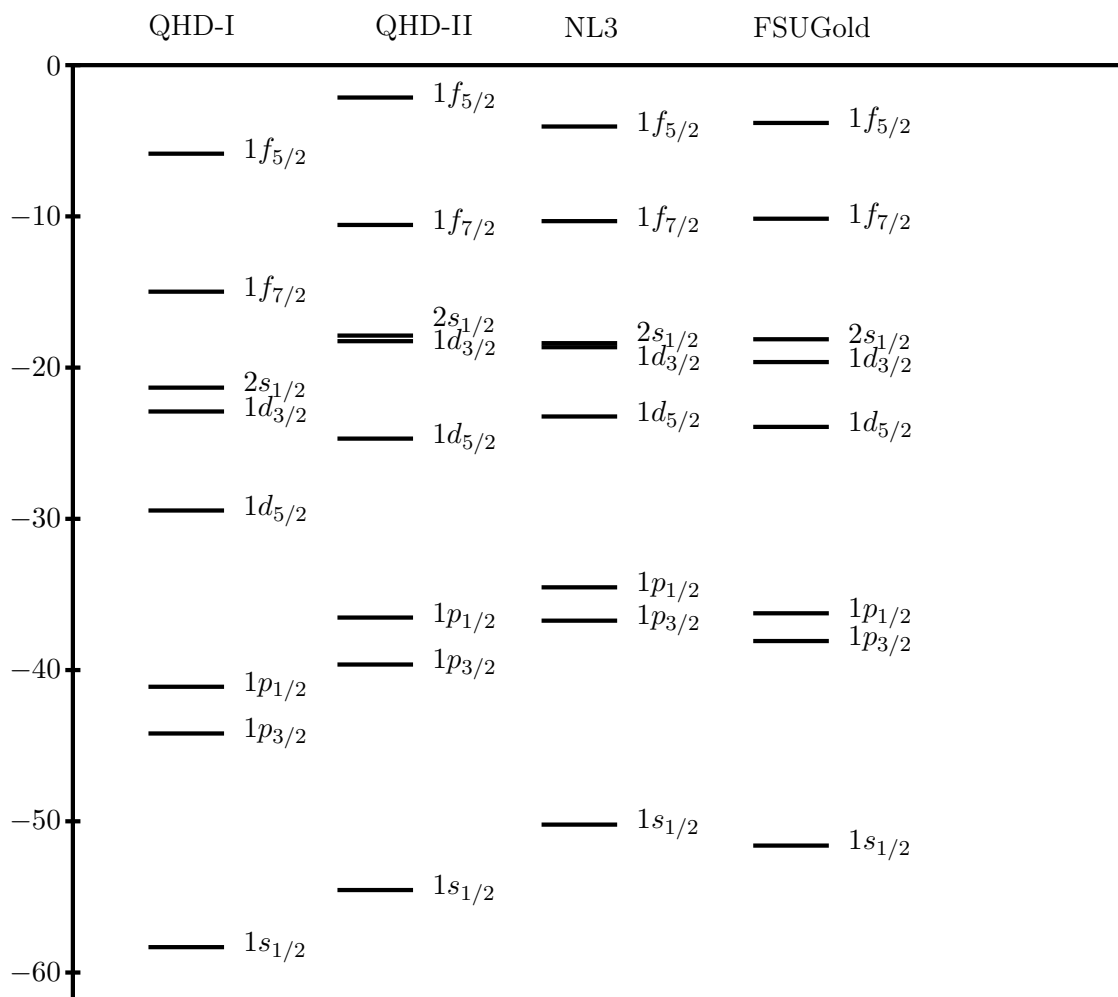


**Figure 2.8:** Single-particle neutron states in  $^{54}\text{Ca}$ . Binding energy on the vertical axis is in MeV.

Figure 2.9 shows plots of the proton and neutron vector densities for  $^{20,22}\text{C}$ , calculated using the NL3 parameter sets. The two plots show that there is no much difference between the neutron density distributions of the two Carbon nuclei ( $^{20,22}\text{C}$ ). This means that (as observed also in Ref. [65]) there is no two neutron halo in  $^{22}\text{C}$ . In contrast, figure 2.10 shows that there is a two-neutron halo in  $^{14}\text{Be}$ , as there is a significant difference between the neutron and proton densities.

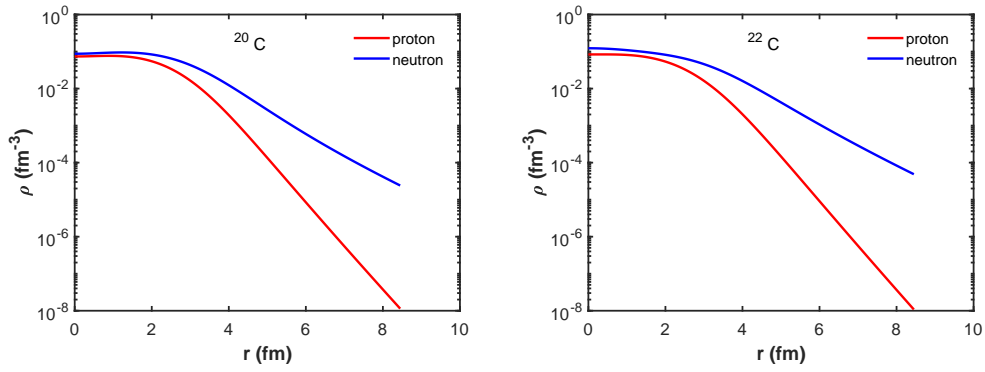


Figure 2.9: Proton and neutron densities for  $^{20,22}\text{C}$ , calculated with NL3 parameter sets.

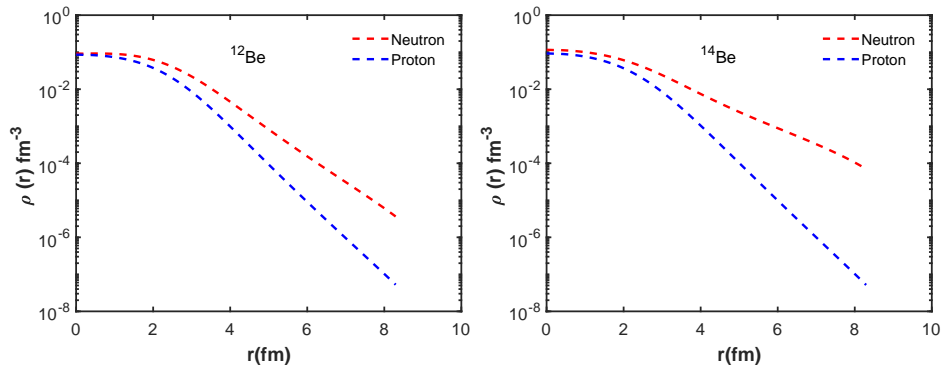


Figure 2.10: Proton and neutron densities for  $^{12,14}\text{C}$ , calculated with NL3 parameter sets.

## Chapter 3

# Relativistic Optical Potentials

In this chapter, the relativistic optical potentials for elastic proton scattering from unstable nuclei are calculated using Dirac phenomenology, the original relativistic impulse approximation (IA1) and the generalised relativistic impulse approximation (IA2). The results obtained using these formalisms are compared and studied. The use of different RMF models (QHD II, NL3, and FSUGold) are compared. The effect of medium modifications due to Pauli blocking are also studied for various incident projectile laboratory energies. To proceed, we start with relativistic kinematics for elastic scattering.

### 3.1 Relativistic kinematics

We will describe, here, the nucleon–nucleus elastic scattering kinematics. It is assumed that the collision between the proton (nucleon) and the nucleus takes place in a scattering plane where the beam is along the  $z$ -axis. The target nucleus has spin-zero, while the projectile proton has spin one-half ( $\frac{1}{2}$ ). The starting point is the laboratory kinetic energy of the projectile ( $T_{\text{lab}}$ ), from which the total energy in the laboratory (lab) frame can be calculated:

$$E_{\text{lab}} = T_{\text{lab}} + m_P, \quad (3.1.1)$$

where  $m_P$  is the mass of the projectile particle (proton in this case), and we have set  $\hbar = c = 1$ . The momentum of the projectile in the lab frame is calculated using

$$k_{\text{lab}} = [E_{\text{lab}}^2 - m_P^2]^{\frac{1}{2}}. \quad (3.1.2)$$

The invariant Mandelstam variable  $s$  is then obtained from

$$s = m_P^2 + m_T^2 + 2m_T E_{\text{lab}}, \quad (3.1.3)$$

where  $m_T$  is the mass of the target nucleus. The momentum in the centre of mass frame is calculated via the relation with the projectile momentum in lab frame:

$$k_{\text{cm}} = \frac{k_{\text{lab}} m_T}{\sqrt{s}}, \quad (3.1.4)$$

and the total energy of the projectile in the centre-of-mass frame is calculated using

$$E_{\text{cm}} = [k_{\text{cm}}^2 - m_p^2]^{\frac{1}{2}}. \quad (3.1.5)$$

Similar expression can be written for the total energy of the target in the centre-of-mass frame. Given the centre-of-mass frame scattering angle  $\theta_{\text{cm}}$ , the momentum transferred to the target is obtained from the relation

$$q = 2k_{\text{cm}} \sin(\theta_{\text{cm}}/2). \quad (3.1.6)$$

Equations (3.1.1) through (3.1.6) describe the relativistic proton-nucleus elastic scattering kinematics to be used in this work.

## 3.2 Global Dirac phenomenology

An optical model based on the Dirac equation (Dirac Phenomenology) was developed for nucleon-nucleus elastic scattering in Ref. [7, 9, 10, 106]. In this model, the relativistic optical potential contains both Lorentz scalar and Lorentz vector potentials. The Dirac phenomenology has twelve adjustable parameters, which is the same number as for non-relativistic (Schrödinger) phenomenology. The real part of the scalar and vector optical potentials are consistent with the relativistic one-boson-exchange model of NN scattering.

The lack of spin observables data made the Dirac phenomenology to be initially viewed with some skepticism. The availability of experimental data coupled with the inability of the Schrödinger approach to reproduce these data led to the success (and acceptance) of Dirac phenomenology to describe nucleon-nucleus scattering. Since then the Dirac approach has been used to successfully describe proton-nucleus (and also neutron-nucleus scattering) data for many spin zero targets. It was observed that the Dirac approach was able to better reproduce experimental (especially spin observables) data compared with the Schrödinger approach [107]. Notable among these data is the proton elastic scattering on  $^{40}\text{Ca}$  at incident projectile energy of 497.5 MeV; the Dirac model was able to reproduce the data while the Schrödinger model was not [107].

Global fitting approaches were later introduced to obtain the relativistic optical model potentials. In Refs. [108–110], the authors presented global Dirac optical model fits to proton elastic scattering data, by considering only energy dependence of the potential parameters. Sequel to this, an approach was presented that contained both energy (E) and mass number (A) dependence of the potential parameters. For instance, in Ref. [111], the authors introduced a global parametrization of global optical model potentials. In this model, the potential parameters depend both on energy (between 65 MeV and 1040 MeV) and mass ( $40 \leq A \leq 208$ ) of the target nucleus. In Dirac phenomenology, the scalar and vector potentials have large values; this has been attributed to nucleon quark degrees of freedom [112]. The global Dirac optical model potential parameters presented in Ref. [112] contained parameters for a larger energy range and for both light medium and heavy nuclei. In this section we present the global Dirac optical model potentials introduced in Ref. [111].

The general form of the vector and scalar optical potentials can be written as [111]:

$$V(r, E) = V_v(E)f_v(r, E) + i [W_v(E)g_v(r, E) + W_{vsp}(E)h_v(r, E)], \quad (3.2.1)$$

$$S(r, E) = V_s(E)f_s(r, E) + i [W_s(E)g_s(r, E) + W_{ssp}(E)h_s(r, E)]. \quad (3.2.2)$$

Here,  $V_v$  is the real vector potential,  $V_s$  the real scalar potential,  $W_v$  the imaginary vector potential,  $W_s$  the imaginary scalar potential,  $f(r, E)$  the real volume form factor,  $g(r, E)$  the imaginary volume form factor,  $W_{vsp}$  and  $W_{ssp}$  are the imaginary surface potentials, while  $h_v$  and  $h_s$  are the surface form factors. The surface terms were included to extend the model to low energies.

Recoil effects are incorporated via the Cooper-Jennings procedure [113]. This results in multiplying the scalar and vector optical potentials by the Cooper-Jenning recoil factors  $R_s$  and  $R_v$ , respectively. The two factors  $R_s$  and  $R_v$  are given, respectively, by [111, 112]:

$$R_s = \frac{E_T}{\sqrt{s}}, \quad (3.2.3)$$

$$R_v = \frac{W_T}{\sqrt{s}}, \quad (3.2.4)$$

where  $E_T$  is the total energy of the target nucleus in the centre of mass frame and  $W_T$  is the target nucleus mass. The real and imaginary parts of the vector potentials are given, respectively, by:

$$V_v(r, E, A) = R_v \left( \sum_{m=0}^3 \frac{V_m}{E^m} \right) f(r, R_1, z_1), \quad (3.2.5)$$

and

$$\begin{aligned} W_v(r, E, A) = & R_v \left( \sum_{m=0}^3 \frac{W_m}{E^m} \right) f(r, R_2, z_2) \\ & + R_v W_{sp} \exp(-\lambda E) z_3 \frac{d f(r, R_3, z_3)}{d R_3}. \end{aligned} \quad (3.2.6)$$

In the same vein, the real and imaginary scalar potentials are given, respectively, by:

$$V_s(r, E, A) = R_s \left( \sum_{m=0}^3 \frac{V_m}{E^m} \right) f(r, R_1, z_1), \quad (3.2.7)$$

and

$$\begin{aligned} W_s(r, E, A) = & R_s \left( \sum_{m=0}^3 \frac{W_m}{E^m} \right) f(r, R_2, z_2) \\ & + R_s W_{sp} \exp(-\lambda E) z_3 \frac{d f(r, R_3, z_3)}{d R_3}, \end{aligned} \quad (3.2.8)$$

where  $E$  is the incident proton centre of mass total energy in MeV divided by 1000 MeV, and the volume form factors  $f(r, E, z)$  are symmetrized Woods-Saxon (SWS) written as

$$f(r, E, z) = \frac{1}{\{1 + \exp[(r - R)/z]\} \{1 + \exp[-(r + R)/z]\}}. \quad (3.2.9)$$

The geometry parameters  $R_i$  and  $z_i$  are given by

$$R_i = A^{1/3} \left( \sum_{m=0}^2 \frac{r_{mi}}{A^m} \right) + \frac{r_{3i}}{E} + \frac{r_{4i}}{E^2} + \frac{r_{5i}}{E^3} \quad (3.2.10)$$

and

$$z_i = \left( \sum_{m=0}^2 \frac{a_{mi}}{A^m} \right) + \frac{a_{3i}}{E} + \frac{a_{4i}}{E^2} + \frac{a_{5i}}{E^3}. \quad (3.2.11)$$

where  $i = 1, 2$ , and  $3$ . The surface term geometry parameters are assumed to depend on  $A$  (only) and independent of  $E$ . The global optical potential parameters  $\lambda$ ,  $V_m$ ,  $W_m$ ,  $r_{mi}$ ,  $a_{mi}$  employed in this work are tabulated in Table II of Ref. [111].

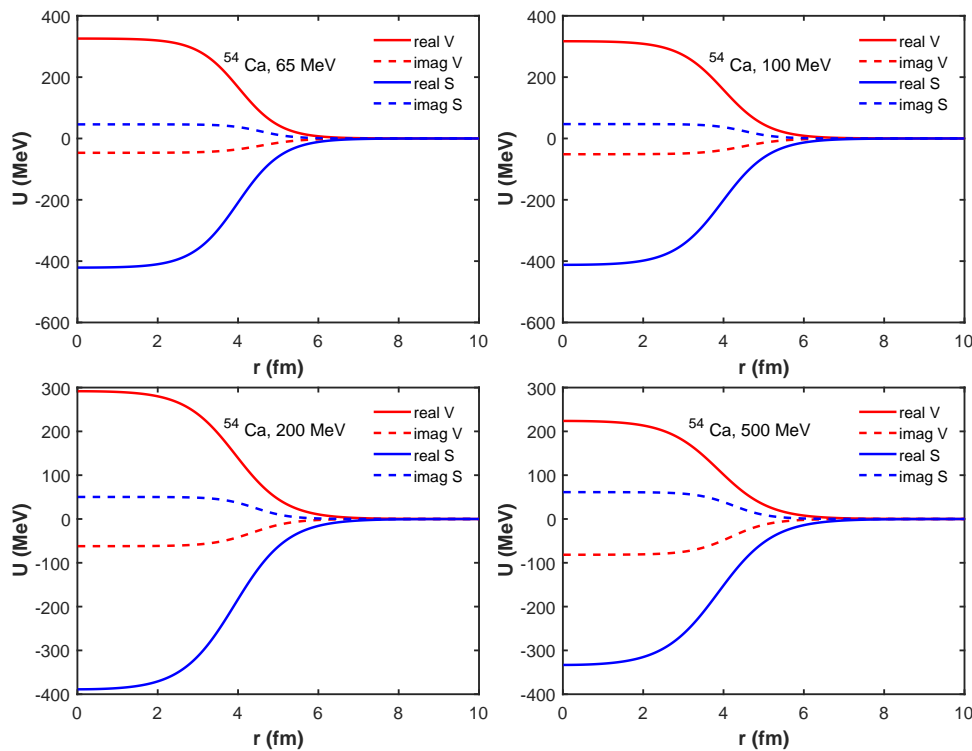


**Figure 3.1:** The scalar and vector global Dirac optical potentials for proton scattering from  $^{54}\text{Ca}$  for incident proton energies 65, 100, 200, and 500 MeV.

The scalar and vector global Dirac optical potentials for proton scattering from  $^{54}\text{Ca}$  are shown in figure 3.1 for incident proton energies 65, 100, 200, and 500 MeV. The solid lines are the real parts while the dashed lines are the imaginary parts.

### 3.3 Relativistic impulse approximation

In the impulse approximation framework, only a single nucleon inside a target nucleus interacts with the incident projectile particle, while the remaining bound nucleons act as spectators, and it is assumed that the projectile energy is higher than the binding energy of the target [114]. Nonrelativistic microscopic models initially were used to describe intermediate energy proton–nucleus ( $p - A$ ) elastic scattering phenomena through the use of Schrödinger equation formalism but including relativistic kinematics. For energy less than 300 MeV, the nonrelativistic models with Pauli blocking and binding energy effects included in projectile–target–nucleon scattering states (i.e., medium effects) led to good descriptions of  $p - A$  data [2]. Nonrelativistic impulse approximation (NRIA) models were also able to successfully describe  $p - A$  elastic scattering at higher energies ( $\geq 800$  MeV), even without including nuclear medium effects, but second-order terms and electromagnetic spin-orbit corrections are included. The results of the nonrelativistic models were however, not satisfactory for  $^{40}\text{Ca}$  target at  $T_{\text{lab}} = 500$  MeV [2]. For this reason, a relativistic impulse approximation (RIA) folding model for the proton–nucleus Dirac equation optical potential was constructed and it was shown to successfully give a good description of the 500 MeV data [2, 24, 25, 115]. The RIA has been proved to be successful in describing scattering of an energetic particle from nuclei (especially stable ones) provided that the momentum transfer to the target nucleus is relatively small compared to the momenta transfer to the ejectile particles. The nonrelativistic impulse approximation approach of obtaining optical potential is not able to successfully explain spin observables for  $p$ - $A$  scattering for energies from 400 MeV to 1000MeV [116], while the RIA was found to give a remarkably excellent fit to  $p$ - $^{40}\text{Ca}$  data at energy of 500 – 800 MeV, without any adjustable parameters. The success of the RIA has been attributed to the use of relativistic density matrix of the target nucleus and incorporation of a term describing projectile propagation in negative energy states [116].

The optical potential in the original RIA is calculated by folding the NN invariant scalar and vector amplitudes with the target scalar and vector densities, respectively; the contribution of the tensor optical potential is very small in the RIA [25]. The RIA uses the Dirac equation to describe the motion of the projectile in the field of the target nucleus. In Ref. [25], it was found that the RIA differential cross sections were too large and the analysing powers too small at energies 181 MeV and 300 MeV. However, at 400 MeV the results agreed well with experimental data, and it was found that the best agreement was at 500 MeV. They found that the original RIA predictions were satisfactory at energies above 400 MeV; the nonrelativistic approach was only able to successfully predict the differential cross section data at energies above 800MeV. At low energy, however, where nuclear-medium effects are important, the RIA results were too large. To apply RIA to lower energies, modifications due to exchange and Pauli-blocking effects have to be included [20, 29]. The RIA optical potentials were found to be consistent with phenomenological ones for kinetic energies above about 300 MeV. It was found that the RIA gives unsatisfactory results at projectile incident energies lower than 200 MeV. The failure of the original RIA at low energy has been attributed to medium effects. Neutron total cross section has

also been calculated using the RIA formalism [117], and the tensor contribution to the optical potential has been found to be noticeable only at high energy and for heavy nuclei [118].

In Ref. [64], the authors studied the use of proton elastic scattering at high and intermediate energies to extract information about density distributions of unstable nuclei using relativistic impulse approximation (RIA) and Glauber model for proton scattering. They found that the RIA was able to better describe the spin observables of the unstable nuclei (they studied) than the Glauber model.

To obtain the expressions for the relativistic optical potentials in the IA1 formalism, we start with the semi-relativistic model developed by Ray and Hoffmann [2, 16]. This model, which treats the projectile relativistically and the target non-relativistically, starts with the following semi-relativistic equation of motion for proton-nucleus system:

$$\left[ \boldsymbol{\alpha}_1 \cdot \mathbf{p} + \beta_1 \left( m_p + \sum_{i=1}^A v_{pi} \right) + H_A \right] \Psi = E\Psi, \quad (3.3.1)$$

where  $\boldsymbol{\alpha}_1$  and  $\beta_1$  are the  $4 \times 4$  Dirac matrices (see Appendix A) which act on the projectile wave function,  $i$  runs from 1 to  $A$ , the number of nucleons in the target,  $m_p$  is the projectile mass,  $v_{pi}$  denotes the projectile (1)-target nucleon ( $i$ ) interaction,  $\mathbf{p}$  is the momentum operator,  $H_A$  is the non-relativistic, many-body target nucleus Hamiltonian. We neglect the kinetic energy operator of the target, and define the proton-nucleus propagator as

$$G(E) = (\gamma_1^0 - \boldsymbol{\gamma}_1 \cdot \mathbf{p} - m_p - \gamma_1^0 H_A + i\epsilon)^{-1}, \quad (3.3.2)$$

where  $\gamma_1^0$  and  $\boldsymbol{\gamma}_1$  are the Dirac gamma matrices for particle 1 (the projectile). This leads to a many-body Lippmann-Schwinger-type equation given by

$$T = v_{pi} + v_{pi}G(E)T. \quad (3.3.3)$$

If antisymmetric intermediate target states are selected, equation (3.3.3) transforms to

$$T = Av + AvGRT. \quad (3.3.4)$$

Here  $v$  is the average  $p-A$  nucleon interaction, and  $\mathcal{R}$  projects antisymmetric target nucleus states. A semi-relativistic effective operator, similar to Kerman-MacManus-Thaler operator or Watson operator can then be defined as

$$\tau = v + vGQ\tau. \quad (3.3.5)$$

The projection operators  $P$  and  $Q$  span the full Dirac basis,  $P \equiv |\Phi_0\rangle\langle\Phi_0|$  projects the elastic channel, and  $\mathcal{R} = P + Q$ . For proton-nucleus elastic scattering, the semi-relativistic optical potential is introduced through

$$PTP = U + UGPTP, \quad (3.3.6)$$

where  $U$  is the optical potential and it is related to  $\tau$  through

$$U = AP\tau P + A(A-1)P\tau QGQ\tau P + \dots, \quad (3.3.7)$$

similar to non-relativistic multiple scattering theory. Proton–nucleus scattering observables are obtained by solving the one–body Dirac equation

$$(\not{p} - m_p - \gamma_1^0 - U) \phi(\mathbf{r}) = 0, \quad (3.3.8)$$

where  $P\Psi = \phi(\mathbf{r})\Phi_0$ , and  $\Phi_0$  is the ground state antisymmetric target wave function. The above formalism has treated the target nucleus non-relativistically. Since one of the nucleons (in the NN centre of momentum system) is required to be treated relativistically, the non-relativistic target wave function  $\Phi_0$  is replaced with a relativistic wave function  $\tilde{\Phi}_0$ . Also, the free NN scattering t–matrix  $\mathcal{F}$  replaces the effective operator  $\tau$ . The first–order optical potential used in equation (3.3.8) is given as

$$U^{(1)}(q) = -\frac{4\pi ik}{m} \sum_{\beta} \sum_{i=1}^A \left\langle \tilde{\Phi}_0 | \hat{\mathcal{F}}_{\beta} | \tilde{\Phi}_0 \right\rangle. \quad (3.3.9)$$

Here  $\tilde{\Phi}_0$  denotes a relativistic Hartree-Fock or relativistic mean field bound state wave function for the target nucleus,  $k$  is the p-A centre-of-mass frame three-momentum,  $m$  is the projectile mass, and the momentum transfer  $\mathbf{q} = \mathbf{k} - \mathbf{k}'$ . The ground state wave function is typically a Hartree product of single–particle four component wave function  $\phi_{\alpha}$ , with the states labelled  $\alpha$ . The sums over  $\alpha$  run over all the occupied single-particle states in the nucleus. The relativistic Lorentz invariant NN amplitude in the IA1 formalism are given by [19, 20, 23]:

$$\begin{aligned} \hat{\mathcal{F}} = & \mathcal{F}_S (\mathbb{I}_4 \otimes \mathbb{I}_4) + \mathcal{F}_P (\gamma_{(1)}^5 \otimes \gamma_{(2)}^5) + \mathcal{F}_V (\gamma_{(1)}^{\mu} \otimes \gamma_{(2)\mu}) \\ & + \mathcal{F}_A (\gamma_{(1)}^5 \gamma_{(1)}^{\mu} \otimes \gamma_{(2)}^5 \gamma_{(2)\mu}) + \mathcal{F}_T (\sigma_1^{\mu\nu} \otimes \sigma_{(2)\mu\nu}), \end{aligned} \quad (3.3.10)$$

or in the short form

$$\hat{\mathcal{F}}(s, t) = \sum_{\beta} \mathcal{F}_{\beta} \lambda^{\beta} \otimes \lambda_{\beta}. \quad (3.3.11)$$

The subscripts "1" and "2" indicate the action on the projectile (proton) and target nucleus, respectively. The five complex amplitudes for scalar (S), vector (V), tensor (T), pseudoscalar (P), and axial vector (A) interactions are determined directly from the NN phase shifts which parametrize the physical NN scattering data [23]. They depend on the square of the momentum transfer  $q^2$  and the Mandelstam invariant parameter  $s$ . The relativistic (IA1) NN invariant amplitudes used in this work are those described in Ref. [23].

As explained in Ref. [115], for a spin-saturated nucleus, the matrix element involves a trace over struck-nucleon spins which eliminates all but the scalar ( $F_S$ ), time component of vector ( $\gamma^0 F_V$ ) terms and a small tensor term from the Dirac scattering amplitude shown above. The optical potential takes care of the multiple-scattering effect. The first-order optical potential in the IA1 formalism is then given as:

$$U^{(1)}(q) = -\frac{4\pi ik}{m} [F_S(q)\rho_S(q) + \gamma^0 F_V(q)\rho_V(q) - 2i\boldsymbol{\alpha}_1 \cdot \hat{r} F_T(q)\rho_T(q)], \quad (3.3.12)$$

where the scalar, vector, and tensor form factors are given, respectively, by

$$\rho_S(q) = 4\pi \int_0^{\infty} r^2 j_0(qr) \rho_S(r) dr, \quad (3.3.13)$$

$$\rho_V(q) = 4\pi \int_0^\infty r^2 j_0(qr) \rho_V(r) dr, \quad (3.3.14)$$

$$\rho_T(q) = 4\pi \int_0^\infty r^2 j_1(qr) \rho_T(r) dr. \quad (3.3.15)$$

Here,  $j_0$  and  $j_1$  are the spherical Bessel function of the first kind, and the scalar, vector, and tensor densities are given by

$$\rho_S(r) = \sum_{\alpha}^{occ} \left( \frac{2j_{\alpha} + 1}{4\pi r^2} \right) [g_{\alpha}^2(r) - f_{\alpha}^2(r)], \quad (3.3.16)$$

$$\rho_V(r) = \sum_{\alpha}^{occ} \left( \frac{2j_{\alpha} + 1}{4\pi r^2} \right) [g_{\alpha}^2(r) + f_{\alpha}^2(r)], \quad (3.3.17)$$

$$\rho_T(r) = \sum_{\alpha}^{occ} \left( \frac{2j_{\alpha} + 1}{4\pi r^2} \right) 2g_{\alpha}(r) f_{\alpha}(r), \quad (3.3.18)$$

where the sums run over all the occupied single-particle states in the nucleus. The on-shell  $t\rho$  form of the RIA optical potential in coordinate space is obtained from the Fourier transform of the momentum space optical potential given in equation (3.3.12) as:

$$U^{(1)}(r) = S(r) + \gamma_1^0 V(r) - 2i\alpha_1 \cdot \hat{r} T(r), \quad (3.3.19)$$

where the subscript "1" in  $\alpha_1$  and  $\gamma_1^0$  indicates that both act on the incident proton and the coordinate space scalar (S(r)), vector (V(r)), and tensor (T(r)) IA1 optical potentials are given, respectively, by [16]

$$S(r) = -\frac{4\pi ik}{m} \sum_{t=p,n} \frac{1}{2\pi^2} \int_0^\infty dq q^2 j_0(qr) \mathcal{F}_{t,S}(q) \rho_{t,S}(q), \quad (3.3.20)$$

$$V(r) = -\frac{4\pi ik}{m} \sum_{t=p,n} \frac{1}{2\pi^2} \int_0^\infty dq q^2 j_0(qr) \mathcal{F}_{t,V}(q) \rho_{t,V}(q), \quad (3.3.21)$$

$$T(r) = -\frac{4\pi ik}{m} \sum_{t=p,n} \frac{1}{2\pi^2} \left[ r \int_0^\infty dq q^2 j_0(qr) \mathcal{F}_{t,T}(q) \rho_{t,T}(q) + \int_0^\infty dq q^2 j_1(qr) \frac{d\mathcal{F}_{t,T}(q)}{dq} \rho_{t,T}(q) \right], \quad (3.3.22)$$

It should be noted that off-shell effects and nuclear-medium modifications of the  $NN$  interaction were neglected in the original RIA. Proton scattering on some nuclei such as  $^{40}\text{Ca}$  and  $^{208}\text{Pb}$  were successful at laboratory energy 500 MeV and 800 MeV [23, 115]. The RIA results were however not successful at low energy ( $\lesssim 200\text{MeV}$ ).

The scalar and vector optical potentials calculated using the IA1 formalism for proton scattering from  $^{48}\text{Ca}$  are shown in figure 3.2 for incident proton energies of

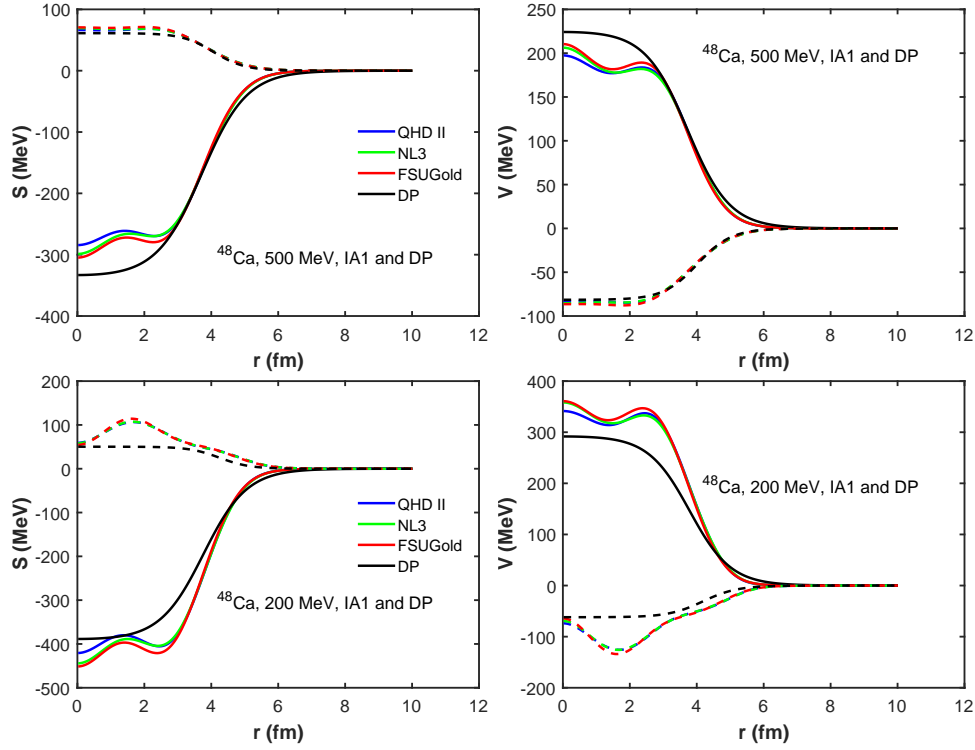


**Figure 3.2:** IA1 scalar and vector optical potentials for  $p+^{48}\text{Ca}$  at  $T_{\text{lab}} = 500 \text{ MeV}$  and  $200 \text{ MeV}$  for QHD-II, NL3, FSUGold RMF models, and Dirac Phenomenology. The blue line denotes QHD II, green line denotes NL3 and red line denotes FSUGold. The potential calculated using Dirac phenomenology is indicated by black line. The solid lines are the real parts while the dashed lines are the imaginary parts.

500 MeV and 200 MeV. The solid lines are the real parts while the dashed lines are the imaginary parts. The figure shows comparisons of the different RMF models and Dirac phenomenology. The FSUGold parameter set gives the strongest scalar and vector potentials, while the QHD II model gives the weakest scalar and vector potentials at  $T_{\text{lab}} = 200 \text{ MeV}$  and  $500 \text{ MeV}$ . At incident projectile energy of 500 MeV, the strengths of the real parts of Dirac phenomenology scalar and vector potentials are stronger than those of IA1 potentials. At incident proton energy of 200 MeV, however, the strengths of the IA1 potentials are stronger than those of Dirac phenomenology; the IA1 formalism gives large scalar and vector potentials at low energy. The overly strong scalar and vector potentials at low energy in the IA1 formalism has been attributed to the implicit incorporation of pseudoscalar pion coupling. Similar observations are seen in figure 3.3 for proton scattering from the unstable  $^{54}\text{Ca}$  nucleus at 500 MeV and 200 MeV. In the IA1 formalism, the Schrödinger equivalent central and spin orbit potentials required to solve the coordinate space Dirac equation (in order to obtain the scattering observables) are written as

$$U_c(r) = \frac{1}{2E} \left[ 2mS(r) + 2EV(r) + S^2(r) - V^2(r) - 2V_cV(r) + \left( T^2 - \frac{T}{A} \frac{dA}{dr} + \frac{2T}{r} + \frac{dT}{dr} \right) + 2EU_{\text{Darwin}} \right], \quad (3.3.23)$$

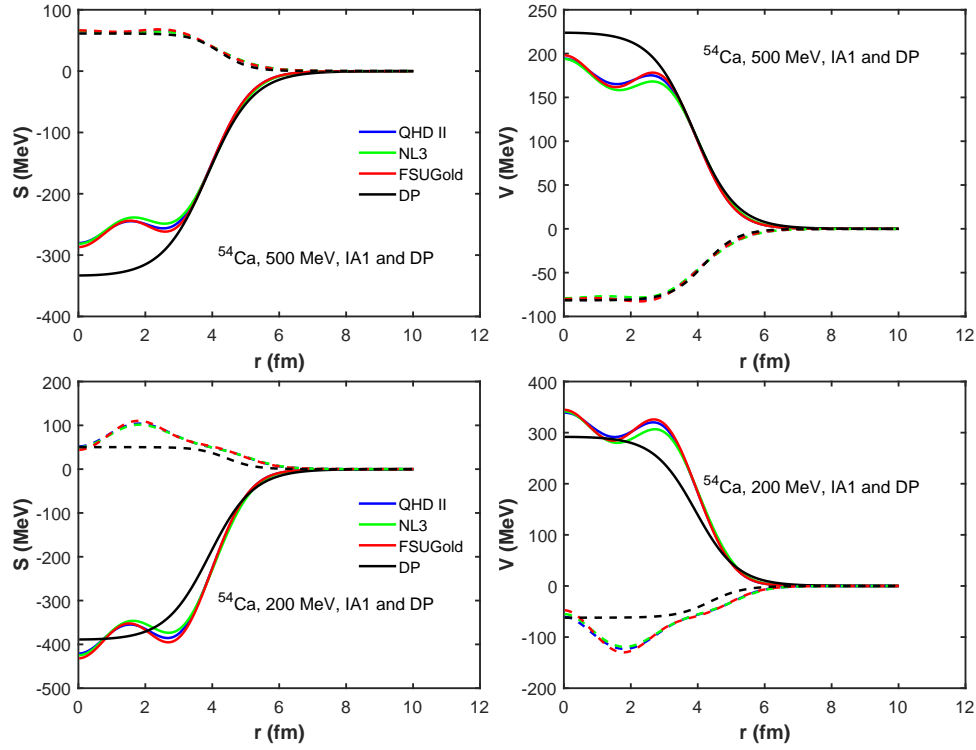


**Figure 3.3:** Same as in figure 3.2 except for  $p+^{54}\text{Ca}$ .

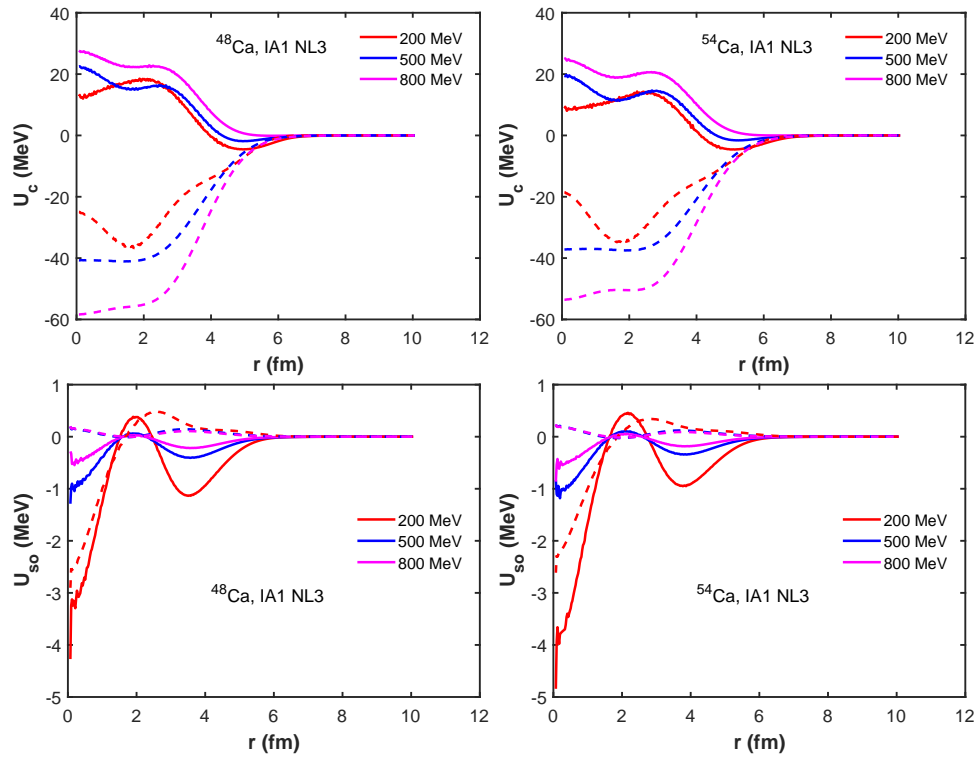


**Figure 3.4:** IA1 Schrödinger equivalent central and spin orbit potentials for  $p+^{48,54}\text{Ca}$ , using the NL3 parameter set, at  $T_{\text{lab}} = 200, 500,$  and  $800$  MeV. The solid lines are real parts while dashed lines denote imaginary parts.

and

$$U_{\text{so}}(r) = \frac{1}{2E} \left( -\frac{1}{rA} \frac{dA}{dr} + \frac{2T}{r} \right), \quad (3.3.24)$$

where

$$U_{\text{Darwin}}(r) = \frac{1}{2E} \left[ -\frac{1}{2r^2A} \frac{d}{dr} \left( r^2 \frac{dA}{dr} \right) + \frac{3}{4A^2} \left( \frac{dA}{dr} \right)^2 \right] \quad (3.3.25)$$

and

$$A(r) = \frac{1}{E + m} (m + S(r) + E - V(r) - V_c), \quad (3.3.26)$$

$V_c$  is the Coulomb potential and  $m$  is the mass of the projectile. In figure 3.4, the plots of the Schrödinger equivalent central and spin orbit potentials are shown for proton elastic scattering from  $^{48,54}\text{Ca}$  at incident projectile energies 200, 500, and 800 MeV using the NL3 parameter set. The top left panel contains the central potential for  $p+^{48}\text{Ca}$ , while the right panel contains central potential for  $p+^{54}\text{Ca}$ . The bottom left panel shows the spin-orbit potential for  $p+^{48}\text{Ca}$ , while the bottom right panel shows the spin-orbit potential for  $p+^{54}\text{Ca}$ . The solid lines are real parts while the dashed lines are imaginary parts. The strengths of the central potentials increase with increase in incident projectile energy for  $p+^{48,54}\text{Ca}$ . The real parts of the spin-orbit potentials decrease as incident projectile energy increases.

### 3.4 Generalized relativistic impulse approximation

The original RIA (i.e. IA1) made use of just five Fermi covariants (S, V, T, P, A) to extend NN amplitudes into full Dirac space. The five invariant amplitudes in IA1 are obtained from positive energy NN scattering data, such as phase shifts. At low energy, the IA1 formalism produces large scalar and vector optical potentials because it assumes pion exchange contributions to be pseudoscalar instead of pseudovector. At low energy, there is also significant pair contributions to p-A scattering. In Ref. [27], the authors replaced the pseudoscalar covariants by pseudovector covariants; this led to reduction in the scalar and vector potential strengths at low energy and the pair contributions also significantly reduced.

In this section, the generalised relativistic impulse approximation (called IA2) for elastic proton scattering, introduced by Tjon and Wallace [31] is presented. In this formalism, the relativistic optical potential is constructed by making use of the symmetric Lorentz-invariant nucleon-nucleon amplitudes of Ref. [30]. This was done to address the problems associated with the use of IA1 formalism in describing elastic proton scattering at low energy.

Following Refs. [31], we start with the fixed energy Dirac equation for a projectile proton scattering from a target nucleus:

$$\left[ \not{p} - m - \hat{U}(\mathbf{r}) \right] \psi(\mathbf{r}) = 0. \quad (3.4.1)$$

Here,  $\not{p} = \gamma_\mu p^\mu$ ,  $p^\mu = (E, \mathbf{p})$  and the energy  $E = (\hat{p}^2 + m^2)^{\frac{1}{2}}$  and  $\hat{p}$  is the on-shell momentum. The relativistic optical potential including correlation term can be

written as [33]:

$$\hat{U}(\mathbf{r}) = \sum_{i=1}^A \langle \tilde{\Phi}_0 | \mathcal{F}_i | \tilde{\Phi}_0 \rangle + A(A-1) \left[ \frac{1}{A(A-1)} \sum_{i \neq j} \sum_j \langle \tilde{\Phi}_0 | \mathcal{F}_i \tilde{G} \mathcal{F}_j | \tilde{\Phi}_0 \rangle - \frac{1}{A^2} \left\langle \tilde{\Phi}_0 \left| \sum_i \mathcal{F}_i \right| \tilde{\Phi}_0 \right\rangle \tilde{G} \left\langle \tilde{\Phi}_0 \left| \sum_j \mathcal{F}_j \right| \tilde{\Phi}_0 \right\rangle \right], \quad (3.4.2)$$

where  $\tilde{\Phi}_0$  is the relativistic ground state target nucleus wave function, and  $\tilde{G}$  denotes the Dirac propagator for the intermediate projectile proton and it is given by

$$\tilde{G} = (\not{p} - m - \gamma^0 \tilde{E}_A + i\epsilon)^{-1}. \quad (3.4.3)$$

Here,  $\tilde{E}_A$  is the average intermediate excitation energy of the target nucleus [119]. Only the first term in equation (3.4.2) will be considered in this section. The second term contains correlation corrections, and it has been shown to have very small contributions [35]. Following Ref. [31] and figure (3.5), the first order relativistic optical potential is given in momentum space by

$$\hat{U}(\mathbf{k}', \mathbf{k}) = \frac{-4\pi i k_{\text{lab}}}{m} \sum_a \int \frac{d^3 P}{(2\pi)^3} \bar{\psi}_a(\mathbf{P} + \frac{1}{2}\mathbf{q}) \hat{\mathcal{F}}(k, P - \frac{1}{2}q; k', P + \frac{1}{2}q) \psi_a(\mathbf{P} - \frac{1}{2}\mathbf{q}), \quad (3.4.4)$$

where all occupied (proton or neutron single particle) states are included over  $a$  and  $q = k - k'$  is the momentum transfer. The invariant NN amplitude  $\hat{\mathcal{F}}$  in equation (3.4.4) is related to the Feynman amplitude  $\hat{\mathcal{M}}$  through

$$\hat{\mathcal{M}}(k, P - \frac{1}{2}q; k', P + \frac{1}{2}q) = \frac{4\pi i k_{\text{lab}}}{m} \hat{\mathcal{F}}(k, P - \frac{1}{2}q; k', P + \frac{1}{2}q). \quad (3.4.5)$$

The  $4 \times 4$  relativistic nuclear density matrix  $\hat{\rho}(\mathbf{P}, \mathbf{q})$  is defined in the Dirac space of particle 2 (denoted using subscript 2) as:

$$\hat{\rho}(\mathbf{P}, \mathbf{q}) \equiv 4 \sum_a \psi_a(\mathbf{P} - \frac{1}{2}\mathbf{q}) \bar{\psi}_a(\mathbf{P} + \frac{1}{2}\mathbf{q}). \quad (3.4.6)$$

Using equations (3.4.5) and (3.4.6) in equation (3.4.4) results in the optical potential being written as

$$\hat{U}(\mathbf{k}', \mathbf{k}) = -\frac{1}{4} \text{Tr}_2 \left[ \int \frac{d^3 P}{(2\pi)^3} \hat{\mathcal{M}}(k, P - \frac{1}{2}q; k', P + \frac{1}{2}q) \hat{\rho}(\mathbf{P}, \mathbf{q}) \right], \quad (3.4.7)$$

where the trace is with respect to the Dirac space of the target nucleon (particle 2). In order to distinguish between neutron and proton contributions, one writes equation (3.4.7) as

$$\hat{U}(\mathbf{k}', \mathbf{k}) = -\frac{1}{4} \text{Tr}_2 \left[ \int \frac{d^3 P}{(2\pi)^3} \hat{\mathcal{M}}_{pp}(k, P - \frac{1}{2}q; k', P + \frac{1}{2}q) \hat{\rho}_p(\mathbf{P}, \mathbf{q}) \right] - \frac{1}{4} \text{Tr}_2 \left[ \int \frac{d^3 P}{(2\pi)^3} \hat{\mathcal{M}}_{pn}(k, P - \frac{1}{2}q; k', P + \frac{1}{2}q) \hat{\rho}_n(\mathbf{P}, \mathbf{q}) \right], \quad (3.4.8)$$

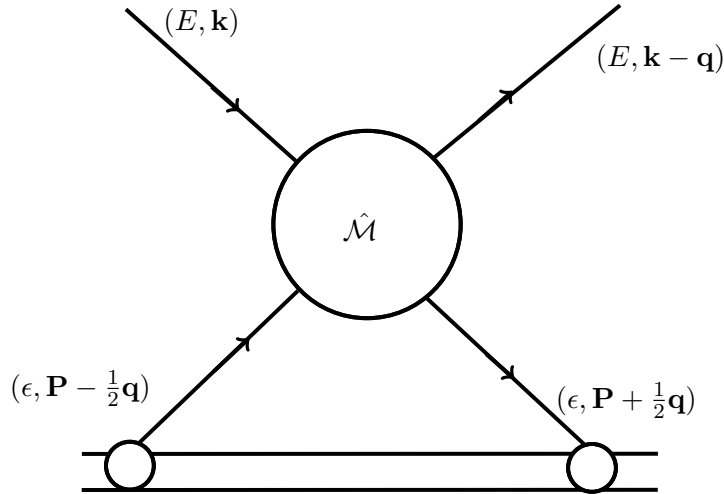


**Figure 3.5:** Diagrammatic representation of first order optical potential for elastic proton-nucleus scattering.

where  $\hat{\rho}_p$  and  $\hat{\rho}_n$  are, respectively, protons and neutrons density matrices.

Applying optimal factorization (i.e. evaluating the NN amplitude at  $\mathbf{P} = 0$  as it is often assumed that the NN amplitude generally varies slowly compared to the nuclear wave function.), the optical potential in equation (3.4.7) becomes (the so-called  $t\rho$  form):

$$\begin{aligned} \hat{U}(\mathbf{k}', \mathbf{k}) = & -\frac{1}{4} \text{Tr}_2 \left[ \hat{\mathcal{M}}_{pp} \left( k, \frac{1}{2}q; k', \frac{1}{2}q \right) \hat{\rho}_p(\mathbf{q}) \right] \\ & -\frac{1}{4} \text{Tr}_2 \left[ \hat{\mathcal{M}}_{pn} \left( k, \frac{1}{2}q; k', \frac{1}{2}q \right) \hat{\rho}_n(\mathbf{q}) \right], \end{aligned} \quad (3.4.9)$$

where the nuclear density form factor is written as

$$\hat{\rho}(\mathbf{q}) = \rho_S(q) + \gamma_2^0 \rho_V(q) - \frac{\boldsymbol{\alpha}_2 \cdot \mathbf{q}}{2m} \rho_T(q) \quad (3.4.10)$$

and the scalar, vector, and tensor form factors are given, respectively, by [31]

$$\begin{aligned} \rho_S(q) &= 4\pi \int_0^\infty dr r^2 \rho_S(r) j_0, \\ \rho_V(q) &= 4\pi \int_0^\infty dr r^2 \rho_V(r) j_0, \\ \rho_T(q) &= 4\pi m \int_0^\infty dr r^2 \rho_T(r) \frac{j_1}{q}. \end{aligned} \quad (3.4.11)$$

The scalar density  $\rho_S(r)$  and vector density  $\rho_V(r)$  have been given in equations (3.3.16) and (3.3.17). The tensor density, written slightly differently from IA1 tensor density, is given as

$$\rho_T(r) = \sum_{\alpha}^{\text{occ}} \left( \frac{2j_{\alpha} + 1}{4\pi r^2} \right) [4g_{\alpha}(r) f_{\alpha}(r)] \quad (3.4.12)$$

In the IA2 formalism, the full NN amplitude is expanded in terms of covariant projection operators  $\Lambda_{\rho_i}$  to separate positive and negative-energy sectors of the Dirac space

$$\hat{F}(k_1, k_2; k'_1, k'_2) = \sum_{\rho'_1 \rho'_2 \rho_1 \rho_2} \left[ \Lambda_{\rho'_1}(\mathbf{k}'_1) \otimes \Lambda_{\rho'_2}(\mathbf{k}'_2) \right] \hat{F}^{\rho'_1 \rho'_2 \rho_1 \rho_2} [\Lambda_{\rho_1}(\mathbf{k}_1) \otimes \Lambda_{\rho_2}(\mathbf{k}_2)]. \quad (3.4.13)$$

This can be written in terms of the kinematic covariants  $K_n$  ( $n = 1 \cdots 13$ ) as

$$\hat{F} = \sum_{\rho'_1 \rho'_2 \rho_1 \rho_2} \sum_{n=1}^{13} F_n^{\rho'_1 \rho'_2 \rho_1 \rho_2} \left[ \Lambda_{\rho'_1}(\mathbf{k}'_1) \otimes \Lambda_{\rho'_2}(\mathbf{k}'_2) \right] K_n [\Lambda_{\rho_1}(\mathbf{k}_1) \otimes \Lambda_{\rho_2}(\mathbf{k}_2)], \quad (3.4.14)$$

where  $\rho(\rho')$  = + for positive energy initial (final) state or – for negative energy initial (final) state,  $\rho_1$  is for projectile particle and  $\rho_2$  for target struck nucleon. The kinematic covariants  $K_n$  are given in Table (3.1). It should be noted that  $\hat{F}_{\text{IA2}}^{11} \neq \hat{F}_{\text{IA1}}$  due to the presence of projection operators in the IA2  $\hat{F}$ . The covariant energy projection operators

$$\Lambda_{\pm}(\mathbf{k}) = \frac{\pm(E\gamma^0 - \boldsymbol{\gamma} \cdot \mathbf{k}) + m}{2m} \quad (3.4.15)$$

allow the separation of the positive and negative energy sectors of the Dirac space. The four momenta  $Q_{ij,\mu}$  given in Table 3.1 are expressed as

$$Q_{ij,\mu} = \frac{(k'_i + k_j)_\mu}{2m}, \quad (3.4.16)$$

where  $i = 1$  (for nucleon 1, which is the projectile),  $i = 2$  (for nucleon 2, which is the target struck nucleon). If optimal factorization ( $\mathbf{P} = 0$ ) is used for the optical potential, the four momenta  $Q_{ij,\mu}$  are given by:

$$\begin{aligned} Q_{11} &= \left[ \frac{E(\mathbf{k}') + E(\mathbf{k})}{2m}, \frac{1}{m} (\mathbf{k} - \frac{1}{2}\mathbf{q}) \right], \\ Q_{12} &= \left[ \frac{E(\mathbf{k}') + E(\frac{1}{2}\mathbf{q})}{2m}, \frac{1}{2m} (\mathbf{k} - \frac{3}{2}\mathbf{q}) \right], \\ Q_{21} &= \left[ \frac{E(\mathbf{k}) + E(\frac{1}{2}\mathbf{q})}{2m}, \frac{1}{2m} (\mathbf{k} + \frac{1}{2}\mathbf{q}) \right], \\ Q_{22} &= \left[ \frac{E(\frac{1}{2}\mathbf{q})}{2m}, 0 \right]. \end{aligned} \quad (3.4.17)$$

The invariant amplitudes  $\hat{F}^{\rho'_1 \rho'_2 \rho_1 \rho_2}$  act only within a specific  $\rho$ -spin sector. The full NN amplitude  $\hat{F}$  is a  $4 \times 4 \otimes 4 \times 4 = 16 \times 16$  matrix, and has 256 independent elements. Imposing charge symmetry, parity invariance, and time reversal invariance reduces the 256 elements to 56 for off-mass-shell, 50 for quasipotential, and 44 for on-mass-shell kinematics, for each isospin [31]. In Table (3.1),  $\tilde{S}$  is the Fierz exchange operator for two-particle Dirac states, and the properties have been given in Ref [31].

**Table 3.1:** Kinematic covariants  $K_n$  ( $n = 1 \dots 13$ ).  $\tilde{S} = \frac{1}{4}(K_1 + K_2 + K_3 - K_4 + \frac{1}{2}K_5)$ , where  $K_1 \equiv S$ ,  $K_2 \equiv P$ ,  $K_3 \equiv V$ ,  $K_4 \equiv A$ ,  $K_5 \equiv T$ .

$n$	$K_n$	$n$	$K_n$
1	$S = \mathbb{I}_4 \otimes \mathbb{I}_4$	8	$(\gamma^5 \otimes \gamma^5 \gamma_\mu) Q_{11,\mu}$
2	$P = \gamma^5 \otimes \gamma^5$	9	$(\gamma^5 \gamma^\mu \otimes \gamma^5) Q_{22,\mu}$
3	$V = \gamma^\mu \otimes \gamma_\mu$	10	$(\mathbb{I}_4 \otimes \gamma_\mu) Q_{12,\mu} \tilde{S}$
4	$A = \gamma^5 \gamma^\mu \otimes \gamma^5 \gamma_\mu$	11	$(\gamma^\mu \otimes \mathbb{I}_4) Q_{21,\mu} \tilde{S}$
5	$T = \sigma^{\mu\nu} \otimes \sigma_{\mu\nu}$	12	$(\gamma^5 \otimes \gamma^5 \gamma_\mu) Q_{12,\mu} \tilde{S}$
6	$(\mathbb{I}_4 \otimes \gamma_\mu) Q_{11,\mu}$	13	$(\gamma^5 \gamma^\mu \otimes \gamma^5) Q_{21,\mu} \tilde{S}$
7	$(\gamma^\mu \otimes \mathbb{I}_4) Q_{22,\mu}$		

In Table (3.2), the numbers in parenthesis in the last column denote the number of non-vanishing independent on-mass-shell amplitudes  $f_n^{ij}$  that contribute to the invariant amplitude  $\hat{F}^{ij}$ . The 13 invariant amplitudes  $F_n^{\rho_1 \rho_2 \rho_1 \rho_2}$  are constructed from the nine symmetrized amplitudes  $f_n^{\rho_1 \rho_2 \rho_1 \rho_2}$  of Ref. [30] as shown in Table (3.3). See also Table II of Ref. [31]. Each of the symmetrized amplitudes  $f_n^\rho$  is even or odd with respect to  $\theta \rightarrow \pi - \theta$  transformations, and are parametrized according to

$$f_n^\rho = \frac{m}{4\pi i k_{\text{lab}}} [\mathcal{M}_n^\rho(t) + \sigma_n^\rho \mathcal{M}_n^\rho(u)], \quad (3.4.18)$$

where  $\sigma_n^\rho = \pm 1$ ,  $s, t$  are Mandelstam variables,  $\mathcal{M}_n^\rho(t)$  and  $\mathcal{M}_n^\rho(u)$  denote sum of Yukawa terms as given by:

$$\begin{aligned} \mathcal{M}_n^\rho(t) &= \sum_{m=1}^4 \frac{(g_{nm}^\rho)^2}{\mu_m^2 - t} \frac{\Lambda^2}{\Lambda^2 - t}, \\ \mathcal{M}_n^\rho(u) &= \sum_{m=1}^4 \frac{(g_{nm}^\rho)^2}{\mu_m^2 - u} \frac{\Lambda^2}{\Lambda^2 - u}. \end{aligned} \quad (3.4.19)$$

The values of the symmetry parameters  $\sigma_n^\rho$ , coupling constants  $(g_{nm}^\rho)^2/4\pi$ , cut-off mass  $\Lambda$ , and masses  $\mu_m$  are given in Tables IV–XI of Ref. [30] for  $T_{\text{lab}} = 200, 500, 800$  MeV.

Using equations (3.4.5) and (3.4.13), the Feynman amplitude  $\hat{\mathcal{M}}$  can be expanded as:

$$\begin{aligned} \hat{\mathcal{M}}(k_1, k_2; k'_1, k'_2) &= \sum_{\rho'_1 \rho'_2 \rho_1 \rho_2} \left[ \Lambda_{\rho'_1}(\mathbf{k}'_1) \otimes \Lambda_{\rho'_2}(\mathbf{k}'_2) \right] \left( \sum_{n=1}^{13} \mathcal{M}_n^{\rho'_1 \rho'_2 \rho_1 \rho_2} [a_1] K_n \right) \\ &\quad \times [\Lambda_{\rho_1}(\mathbf{k}_1) \otimes \Lambda_{\rho_2}(\mathbf{k}_2)]. \end{aligned} \quad (3.4.20)$$

**Table 3.2:** *The rho-spin sectors and independent amplitudes for each subclass with the constraint conditions charge symmetry, time-reversal, and on-mass-shell.*

rho-spin sector $\hat{F}^{ij}$	rho-spin labels $\rho'_1\rho'_2, \rho_1\rho_2$	value of $\eta_{ij}$	nonvanishing independent on-mass-shell amplitudes
$\hat{F}^{11}$	++, ++	+	$f_n^{11}, n = 1 - 5$ (5)
$\hat{F}^{12}$	+-, ++	+	$f_n^{12}, n = 1 - 5, 7 - 9$ (8)
$\hat{F}^{21}$	-+, ++	+	(0)
$\hat{F}^{13}$	++, +-	-	(0)
$\hat{F}^{31}$	++, -+	-	(0)
$\hat{F}^{14}$	+-, +-	+	$f_n^{14}, n = 1 - 6$ (6)
$\hat{F}^{41}$	-+, -+	+	(0)
$\hat{F}^{23}$	-+, +-	-	$f_n^{23}, n = 1 - 6$ (6)
$\hat{F}^{32}$	+-, -+	-	(0)
$\hat{F}^{22}$	--, ++	+	$f_n^{22}, n = 1 - 6$ (6)
$\hat{F}^{33}$	++, --	-	(0)
$\hat{F}^{24}$	--, +-	+	$f_n^{24}, n = 1 - 5, 7 - 9$ (8)
$\hat{F}^{42}$	--, -+	+	(0)
$\hat{F}^{34}$	+-, --	-	(0)
$\hat{F}^{43}$	-+, --	-	(0)
$\hat{F}^{44}$	--, --	+	$f_n^{44}, n = 1 - 5$ (5)
Total			44

**Table 3.3:** Relation between the 13 invariant amplitudes  $F_n^{\rho'_1 \rho'_2 \rho_1 \rho_2}$  and nine symmetrized amplitudes  $f_n^{\rho'_1 \rho'_2 \rho_1 \rho_2}$  with  $\rho'_1 \rho'_2 \rho_1 \rho_2 \equiv \rho$ .

$n$	$F_n^{\rho'_1 \rho'_2 \rho_1 \rho_2} \equiv F_n^\rho$
1	$\frac{3}{4}f_1^\rho + \frac{3}{2}f_2^\rho - f_3^\rho + f_4^\rho - \frac{1}{4}f_5^\rho$
2	$-\frac{1}{4}f_1^\rho + \frac{3}{2}f_2^\rho + f_3^\rho - f_4^\rho + \frac{3}{4}f_5^\rho$
3	$-\frac{1}{4}f_1^\rho - \frac{1}{2}f_3^\rho + \frac{1}{4}f_4^\rho + \frac{1}{4}f_5^\rho$
4	$\frac{1}{4}f_1^\rho - \frac{3}{2}f_3^\rho - \frac{1}{2}f_4^\rho - \frac{1}{4}f_5^\rho$
5	$-\frac{1}{8}f_1^\rho + \frac{1}{4}f_2^\rho - \frac{1}{8}f_5^\rho$
6	$f_6^\rho + f_7^\rho$
7	$f_6^\rho - f_7^\rho$
8	$\eta_{ij}f_8^\rho + \eta_{ij}f_9^\rho$
9	$\eta_{ij}f_8^\rho - \eta_{ij}f_9^\rho$
10	$f_6^\rho - \eta_{ij}f_7^\rho$
11	$f_6^\rho + \eta_{ij}f_7^\rho$
12	$\eta_{ij}f_8^\rho + f_9^\rho$
13	$\eta_{ij}f_8^\rho - f_9^\rho$

Here,  $\mathcal{M}_n^{\rho'_1 \rho'_2 \rho_1 \rho_2}[a_1]$  is given by

$$\mathcal{M}_n^{\rho'_1 \rho'_2 \rho_1 \rho_2}[a_1] = \frac{4\pi i k_{\text{lab}}}{m} \mathcal{F}_n^{\rho'_1 \rho'_2 \rho_1 \rho_2}[a_1], \quad (3.4.21)$$

and the set  $[a_1]$  needed for on-mass-shell kinematics are  $s = (k_1 + k_2)^2$ ,  $t = (k_1 - k_2)^2$ , and  $u = (k_1 + k'_2)^2$ . The full set is given in Table III of Ref. [30].

The optical potential given in equation (3.4.9) then becomes after some manipulations:

$$\hat{U}(\mathbf{k}', \mathbf{k}) = \sum_{\nu=1}^8 \sum_{\rho'_1 \rho_1} \sum_{m=1}^8 U_m^{\rho'_1 \rho_1}(\mathbf{k}', \mathbf{k}) D_{m\nu}^{\rho'_1 \rho_1} \hat{\chi}_\nu(\mathbf{q}). \quad (3.4.22)$$

where

$$D_{m\nu}^{\rho'_1 \rho_1} = \sum_{\kappa=1}^8 \left[ \rho_1 \frac{E(\mathbf{k})}{2m} \phi_{\kappa 2\nu} - \frac{1}{2} \rho_1 \phi_{\kappa 6\nu} + \frac{1}{2} \phi_{\kappa 1\nu} \right] \\ \times \left[ \rho'_1 \frac{E(\mathbf{k}')}{2m} \phi_{2m\kappa} - \frac{1}{2} \rho'_1 \phi_{6m\kappa} + \frac{1}{2} \rho'_1 \phi_{4m\kappa} + \phi_{1m\kappa} \right], \quad (3.4.23)$$

and

$$U_m^{\rho'_1 \rho_1}(\mathbf{k}', \mathbf{k}) = - \sum_{\rho'_2 \rho_2} \sum_{n=1}^{13} \sum_{k=1}^4 \mathcal{M}_n^{\rho'_1 \rho'_2 \rho_1 \rho_2}[a_1] \rho_k^{\rho_2 \rho'_2}(q) C_{nk}^m. \quad (3.4.24)$$

The covariant operators  $\hat{\chi}_\nu(\mathbf{q})$  are given by

$$\hat{\chi}_\nu(\mathbf{q}) = \left\{ 1, \gamma^0, \frac{-\boldsymbol{\alpha} \cdot \mathbf{q}}{m}, \frac{\boldsymbol{\gamma} \cdot \mathbf{q}}{m}, \frac{\boldsymbol{\alpha} \cdot \mathbf{k}}{m}, \frac{\boldsymbol{\gamma} \cdot \mathbf{k}}{m}, \frac{(\boldsymbol{\alpha} \cdot \mathbf{k})(\boldsymbol{\alpha} \cdot \mathbf{q})}{m^2}, \frac{(\boldsymbol{\gamma} \cdot \mathbf{k})(\boldsymbol{\alpha} \cdot \mathbf{q})}{m^2} \right\}. \quad (3.4.25)$$

For closed-shell nuclei, only  $\hat{\chi}_1$  to  $\hat{\chi}_4$  contribute to  $\hat{\chi}_\nu$ . The nonzero values of  $C_{nk}^m$  and  $\phi_{ijk}$  are given in Appendix C, and the form factors  $\rho_k^{\rho_2\rho'_2}(q)$  for  $k = 1$  to 4 are [31]:

$$\begin{aligned} \rho_1^{\rho_2\rho'_2}(q) &= \frac{1}{4} [\rho_2\rho'_2(\delta^2 + b^2) + 1] \rho_S(q) + \frac{1}{4}(\rho_2 + \rho'_2)\delta\rho_V(q) - \frac{1}{2}\rho_2\rho'_2b^2\delta\rho_T(q), \\ \rho_2^{\rho_2\rho'_2}(q) &= \frac{1}{4}(\rho_2 + \rho'_2)\delta\rho_S(q) + \frac{1}{4}(\rho_2\rho'_2 + 1)\rho_V(q) - \frac{1}{4}(\rho_2 + \rho'_2)b^2\rho_T(q), \\ \rho_3^{\rho_2\rho'_2}(q) &= \frac{1}{4}\rho_2\rho'_2\delta\rho_T(q) + \frac{1}{8}(\rho_2 + \rho'_2)\rho_V(q) - \frac{1}{8}[1 - \rho_2\rho'_2(b^2 + \delta^2)]\rho_T(q), \\ \rho_4^{\rho_2\rho'_2}(q) &= \frac{1}{8}(\rho_2 - \rho'_2)[\rho_S(q) - \delta\rho_T(q)], \end{aligned} \quad (3.4.26)$$

where  $b^2 = q^2/(4m^2)$  and  $\delta = (1 + b^2)^{\frac{1}{2}}$ .

Defining the average momenta  $\mathbf{k}_a = (\mathbf{k} + \mathbf{k}')/2$  and the momentum transfer  $\mathbf{q} = \mathbf{k} - \mathbf{k}'$ , enables the optical potential in the IA2 formalism to be written in the usual form

$$\begin{aligned} \hat{U}(\mathbf{k}', \mathbf{k}) &= S + \gamma_1^0 V - \frac{\boldsymbol{\alpha}_1 \cdot \mathbf{q}}{m} T + \left( \frac{-E\gamma_1^0 + \boldsymbol{\gamma}_1 \cdot \mathbf{k}_a + m}{m} \right) C \\ &+ \frac{\boldsymbol{\gamma}_1 \cdot \mathbf{q}}{m} D + \frac{\boldsymbol{\alpha}_1 \cdot \mathbf{k}_a}{m} F + i \frac{\boldsymbol{\sigma}_1 \cdot (\mathbf{q} \times \mathbf{k}_a)}{m^2} [S_{LS} + \gamma_1^0 V_{LS}], \end{aligned} \quad (3.4.27)$$

where the non-local potentials

$$S = U_1 + \left[ \frac{\mathbf{k}_a \cdot \mathbf{q}}{m^2} + \frac{\mathbf{q}^2}{2m^2} \right] U_7 - U_6, \quad (3.4.28)$$

$$V = U_2 + \left[ \frac{\mathbf{k}_a \cdot \mathbf{q}}{m^2} + \frac{\mathbf{q}^2}{2m^2} \right] U_8 + \frac{E}{m} U_6, \quad (3.4.29)$$

$$T = U_3 - \frac{1}{2} U_5, \quad (3.4.30)$$

$$C = U_6, \quad (3.4.31)$$

$$D = U_4 + \frac{1}{2} U_6, \quad (3.4.32)$$

$$F = U_5, \quad (3.4.33)$$

$$S_{LS} = -U_7, \quad (3.4.34)$$

$$V_{LS} = -U_8, . \quad (3.4.35)$$

The two potentials D and F associated with time-reversal odd operators vanish for on-mass-shell NN amplitudes used in the calculation of the optical potentials in this work. S, V, T, C,  $S_{LS}$ ,  $V_{LS}$  are, respectively, the scalar, time component of vector, tensor, space-vector, scalar spin-orbit, and vector spin-orbit potentials. Each of the potentials is a non-local function of  $\mathbf{k}$  and  $\mathbf{k}'$ . It should be noted that the first order optical potential in the IA1 formalism does not contain Dirac spin-orbit potentials.

### 3.4.1 Local coordinate space optical potential

Local form of the optical potentials have been found to be accurate at high energy for nucleon–nucleus elastic scattering due to the diffractive nature of the scattering. In the Dirac optical potential derived above, nonlocalities are present due to projection operators and covariants, as they depend on  $\mathbf{k}$  and  $\mathbf{k}'$ . These are localised by assuming that the momentum operator  $\mathbf{k}$  stays near the asymptotic value  $\hat{\mathbf{k}}$ , i.e.  $\mathbf{k} \approx \hat{\mathbf{k}}$ . This enables  $E(\mathbf{k})$  and  $E(\mathbf{k}')$  to be replaced by  $E = E(\hat{\mathbf{k}})$ . Also

$$\frac{\mathbf{k}}{m} \approx \frac{\hat{\mathbf{k}}}{m}, \quad \frac{\mathbf{k}_a \cdot \mathbf{q}}{m} = \frac{\mathbf{k}^2 - \mathbf{k}'^2}{2m} \approx 0. \quad (3.4.36)$$

The momentum space Dirac equation containing the optical potential is given by

$$[\gamma^0 E - \boldsymbol{\gamma} \cdot \mathbf{k}' - m] \Psi(\mathbf{k}') - \frac{1}{(2\pi)^3} \int d^3k \hat{U}(\mathbf{k}', \mathbf{k}) \Psi(\mathbf{k}) = 0, \quad (3.4.37)$$

where  $\Psi(\mathbf{k}')$  is obtained by taking the Fourier transform of the coordinate space wave function:

$$\Psi(\mathbf{k}') = \int d^3r e^{-i\mathbf{k}' \cdot \mathbf{r}} \Psi(\mathbf{r}). \quad (3.4.38)$$

Substituting equation (3.4.38) into equation (3.4.37), and using

$$\mathbf{k}\Psi(\mathbf{r}) \rightarrow -i\nabla\Psi(\mathbf{r}), \quad \mathbf{k}_a\Psi(\mathbf{r}) \rightarrow \left(-i\nabla - \frac{1}{2}\mathbf{q}\right)\Psi(\mathbf{r}) \quad (3.4.39)$$

enables the localised coordinate space Dirac equation to be written as

$$\left[E\gamma^0 + i\boldsymbol{\gamma} \cdot \nabla - m - \hat{U}(\mathbf{r})\right] \Psi(\mathbf{r}) = 0, \quad (3.4.40)$$

where

$$\begin{aligned} \hat{U}(\mathbf{r}) = & S(r) + \gamma^0 V(r) - i \frac{\boldsymbol{\alpha} \cdot \hat{\mathbf{r}}}{m} \frac{dT(r)}{dr} + \frac{C(r)}{m} (-E\gamma^0 - i\boldsymbol{\gamma} \cdot \nabla + m) \\ & - i \frac{\boldsymbol{\gamma} \cdot \nabla C(r)}{2m} - \left[ \frac{dS_{LS}(r)}{dr} + \gamma^0 \frac{dV_{LS}(r)}{dr} \right] \frac{\boldsymbol{\sigma} \cdot (-i\mathbf{r} \times \nabla)}{m^2 r}. \end{aligned} \quad (3.4.41)$$

The local functions  $S(r)$ ,  $V(r)$ , and  $C(r)$  are obtained using

$$f(r) = \frac{1}{2\pi^2} \int dq q^2 j_0(qr) f(q), \quad (3.4.42)$$

where  $f(r)$  denotes  $S(r)$ ,  $V(r)$  or  $C(r)$ . The other functions are obtained using [33, 34]

$$\frac{df}{dr} = \frac{1}{2\pi^2} \int dq q^3 j_1(qr) f(q), \quad (3.4.43)$$

where  $\frac{df}{dr}$  represents  $\frac{dT}{dr}$ ,  $\frac{dS_{LS}(r)}{dr}$ , or  $\frac{dV_{LS}(r)}{dr}$ ,  $j_0(qr)$  and  $j_1(qr)$  are the spherical bessel functions.

Using the transformation

$$\Psi(\mathbf{r}) = \left(1 + \frac{C(r)}{m}\right)^{\frac{1}{2}} \tilde{\Psi}(\mathbf{r}), \quad (3.4.44)$$

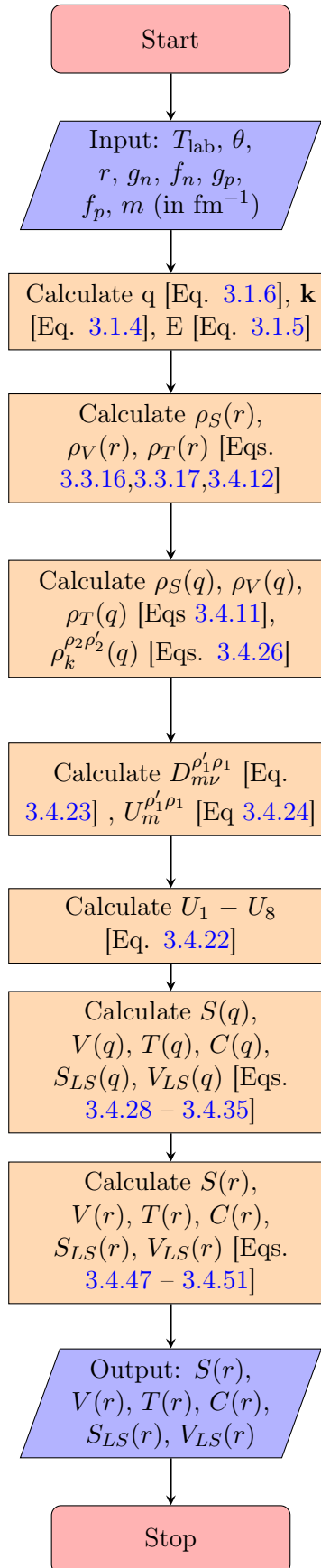


**Figure 3.6:** Flow chart illustrating how the function "UIA2" calculates the optical potentials in the IA2 formalism.

the Dirac equation is obtained in a simpler form in which the optical potential contains five terms:

$$\left[ E\gamma^0 + i\boldsymbol{\gamma} \cdot \boldsymbol{\nabla} - m - \tilde{U}(\mathbf{r}) \right] \tilde{\Psi}(\mathbf{r}) = 0, \quad (3.4.45)$$

in which case the optical potential  $\tilde{U}(\mathbf{r})$  is given by [31]:

$$\tilde{U}(\mathbf{r}) = \tilde{S}(r) + \gamma^0 \tilde{V}(r) - i\boldsymbol{\alpha} \cdot \hat{\mathbf{r}} \tilde{T}(r) - \left[ \tilde{S}_{LS}(r) + \gamma^0 \tilde{V}_{LS}(r) \right] [\boldsymbol{\alpha} \cdot (-i\mathbf{r} \times \boldsymbol{\nabla})]. \quad (3.4.46)$$

Here,

$$\tilde{S}(r) = \frac{S(r)}{1 + C(r)/m}, \quad (3.4.47)$$

$$\tilde{V}(r) = \frac{V(r)}{1 + C(r)/m}, \quad (3.4.48)$$

$$\tilde{T}(r) = \left( \frac{1}{m + C(r)} \right) \frac{dT(r)}{dr}, \quad (3.4.49)$$

$$\tilde{S}_{LS}(r) = \left( \frac{1}{mr[m + C(r)]} \right) \frac{dS_{LS}(r)}{dr}, \quad (3.4.50)$$

$$\tilde{V}_{LS}(r) = \left( \frac{1}{mr[m + C(r)]} \right) \frac{dV_{LS}(r)}{dr}, \quad (3.4.51)$$

Figure 3.6 shows the flow chart illustrating the step-by-step procedure to calculate the local relativistic optical potentials in the IA2 formalism. The functions "Cmnk(m,n,k,p,q,mass)" and "phi\_ijk(i,j,k,p,q,mass)" have been written to calculate  $C_{nk}^m$  and  $\phi_{ijk}$ , respectively. The MATLAB function "UIA2" takes as inputs the incident proton laboratory energy  $T_{lab}$ , the scattering angle in the centre of mass frame  $\theta$ , and the upper and lower components wave functions ( $g$  and  $f$  obtained in Chapter 2). The local optical potentials are then calculated as displayed in the flow chart.

In figure 3.7, the optical potentials calculated for proton elastic scattering from  $^{48}\text{Ca}$  using the QHD II, NL3, and FSUGold parameter sets (in the case of IA1 and IA2) and Dirac phenomenology at  $T_{lab} = 200$  and 500 MeV are compared. The QHD II is shown in blue colour, NL3 in green, and FSUGold in red. The potentials calculated using Dirac phenomenology are in black. The solid lines are the real parts while the dashed lines are the imaginary parts of the optical potentials. The top left graph denotes the IA2 scalar potential at incident projectile energy of 500 MeV, the top right graph is the vector potential. The bottom plots are for incident proton energy of 200 MeV. From figure 3.7, one can observe that the strengths of the IA2 scalar and vector potentials are lower than that obtained via Dirac phenomenology. The strengths of the scalar and vector optical potentials (especially the imaginary parts) obtained through IA1 formalism are closer to the Dirac phenomenology (as shown above); that is the strengths of the IA1 potentials are stronger than that of the IA2 potentials for both stable and unstable nuclei. From the plots at  $T_{lab} = 200\text{MeV}$ , the IA2 scalar and vector potentials are lower than Dirac phenomenological potentials. The scalar and vector potentials obtained from

IA1 formalism are however greater than that obtained from Dirac phenomenology. Figure 3.8 shows the case of  $p+^{54}\text{Ca}$  at  $T_{\text{lab}} = 500$  and 200 MeV, respectively. There is similar behaviour with that of  $p+^{48}\text{Ca}$ .

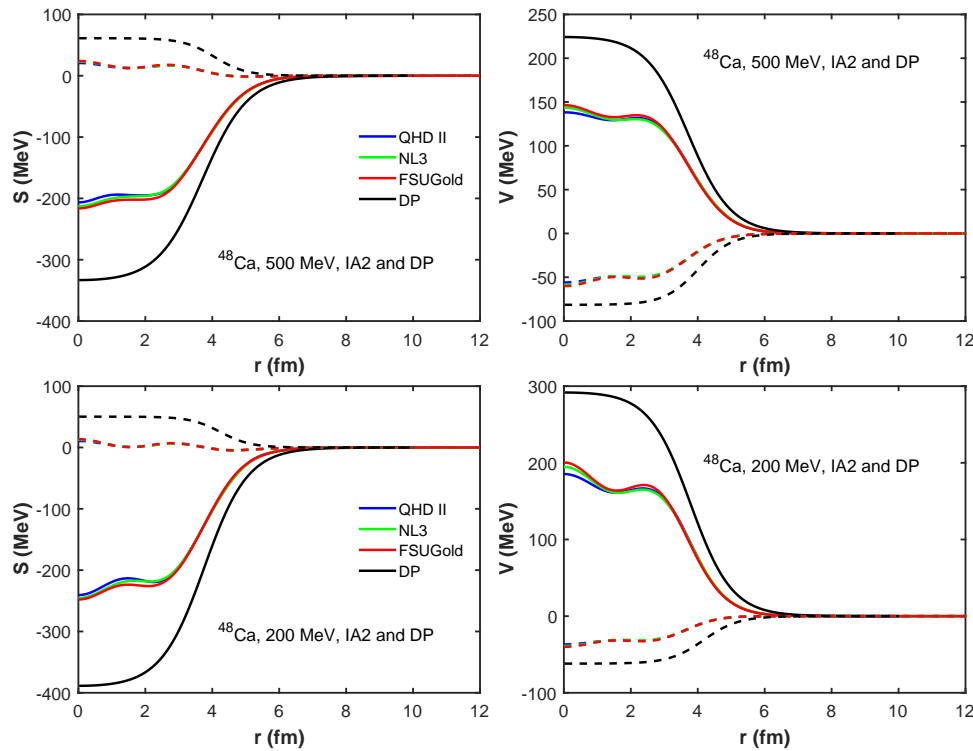


**Figure 3.7:** IA2 scalar and vector optical potentials for  $p+^{48}\text{Ca}$  at  $T_{\text{lab}} = 200$  MeV and 500 MeV for QHD-II, NL3, FSUGold RMF models, and Dirac Phenomenology. The blue line denotes QHD II, green line denotes NL3 and red line denotes FSUGold. The potential calculated using Dirac phenomenology is indicated by black line. The solid lines are the real parts while the dashed lines are the imaginary parts.

In figure 3.9, the plots of the IA2 scalar (S), vector (V), tensor (T), space vector (C), Dirac scalar spin-orbit ( $S_{LS}$ ), and Dirac vector spin-orbit ( $V_{LS}$ ) potentials for  $p+^{48}\text{Ca}$  using the NL3 parameter set are shown for  $T_{\text{lab}} = 200, 500,$  and 800 MeV. The real parts are solid lines while the imaginary parts are dashed lines. Figure 3.10 shows the case for  $p+^{54}\text{Ca}$ . One can observe that the main contributions to the IA2 optical potentials come from scalar (S), vector (V), and space vector (C) potentials. In figure 3.9 and 3.10, the strengths of the real parts of S, V, and C decrease as  $T_{\text{lab}}$  increases; this is also the case for  $p+^{40}\text{Ca}$  as shown in Ref. [33].

### 3.4.2 Schrödinger equivalent potentials

In this subsection, the schrödinger equivalent central and spin-orbit potentials will be obtained. In order to solve the scattering state Dirac equation, equation (3.4.45) is separated into its upper and lower two-component wave functions. The equivalent

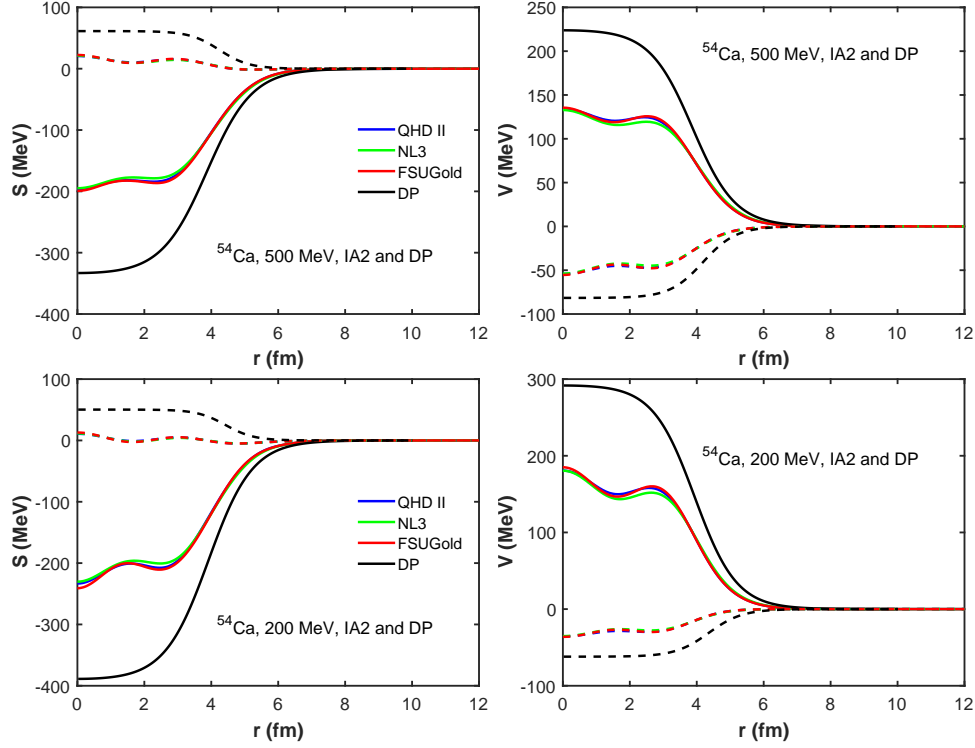


**Figure 3.8:** Same as in figure 3.7 except for  $p+^{54}\text{Ca}$ .

second-order differential equation of state satisfied by  $\psi(r)$  is given by

$$\left[ \frac{-\hbar^2 \nabla^2}{2E} + U_c(r) + U_{so}(r) \boldsymbol{\sigma} \cdot \boldsymbol{\ell} \right] \psi(r) = \frac{\hbar^2 k_{PA}^2}{2E} \psi(r) \quad (3.4.52)$$

where  $k_{PA}$  is the proton-nucleus centre of mass wave number, and

$$E = [\hbar^2 k_{PA}^2 + m^2]^{\frac{1}{2}}. \quad (3.4.53)$$

The effective central and spin-orbit potentials are given, respectively, by

$$\begin{aligned} U_c(r) = \frac{1}{2E} \left\{ 2E\tilde{V}_\kappa + 2m\tilde{S}_\kappa - \tilde{V}_\kappa^2 + \tilde{S}_\kappa^2 - 2V_c\tilde{V}_\kappa \right. \\ \left. + \left( \tilde{T}^2 - \frac{\tilde{T}}{A} \frac{\partial A}{\partial r} + \frac{2\tilde{T}}{r} + \frac{\partial \tilde{T}}{\partial r} \right) \right. \\ \left. + \left( -\frac{1}{2r^2 A} \frac{\partial}{\partial r} \left( r^2 \frac{\partial A}{\partial r} \right) + \frac{3}{4A^2} \left( \frac{\partial A}{\partial r} \right)^2 \right) \right\}, \quad (3.4.54) \end{aligned}$$

and

$$U_{so} = \frac{1}{2E} \left[ -\frac{1}{rA} \left( \frac{\partial A}{\partial r} \right) + \frac{2\tilde{T}}{r} \right]. \quad (3.4.55)$$

Here  $U_c$ ,  $U_{so}$ , and  $V_c$  represent central, spin-orbit, and Coulomb potentials, respectively. The value of  $A$  is obtained using:

$$A = \frac{1}{E + m} \left[ E - \tilde{V}_\kappa + m + \tilde{S}_\kappa - V_c \right], \quad (3.4.56)$$

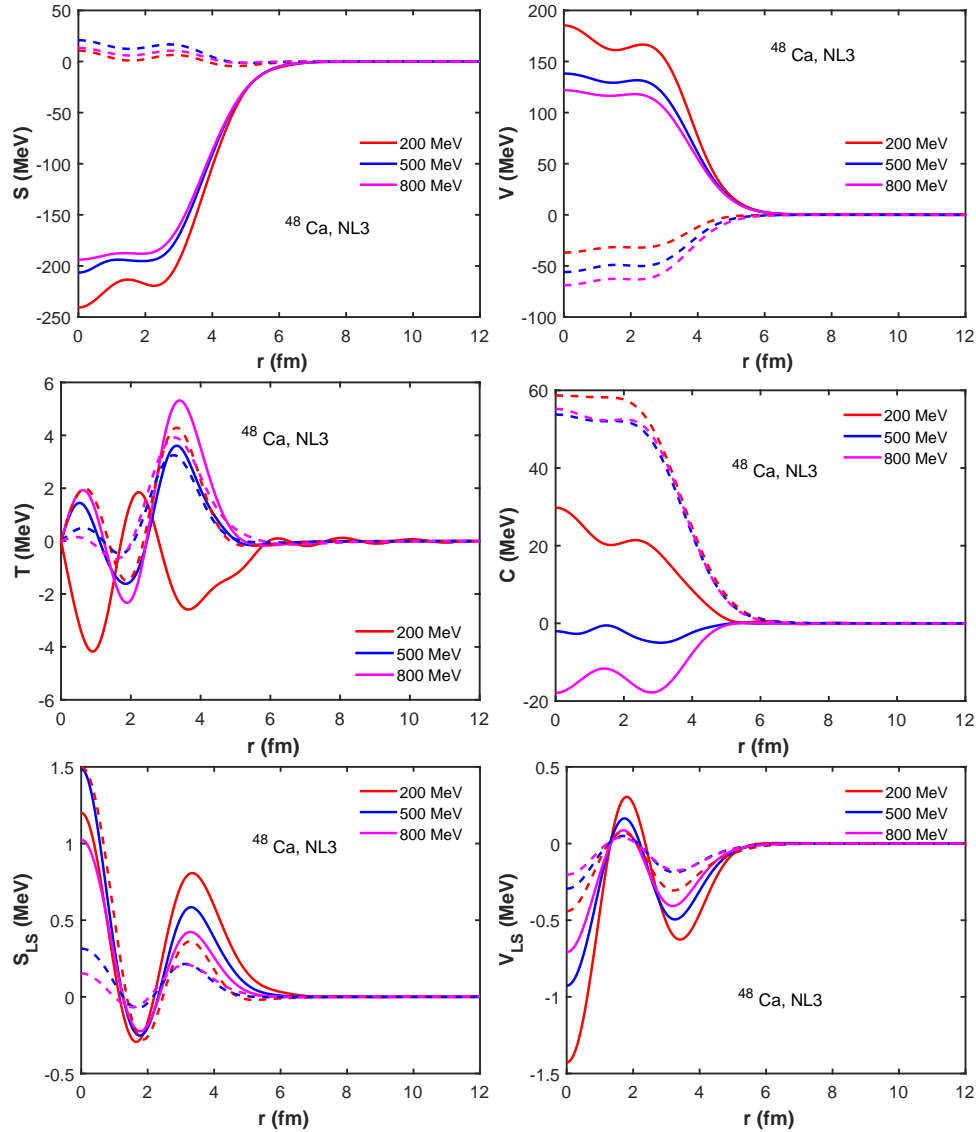


**Figure 3.9:** IA2 scalar ( $S$ ), vector ( $V$ ), tensor ( $T$ ), space vector ( $C$ ), Dirac scalar spin-orbit ( $S_{LS}$ ), and Dirac vector spin-orbit ( $V_{LS}$ ) potentials for  $p+^{48}\text{Ca}$  using the NL3 parameter for  $T_{\text{lab}} = 200, 500, \text{ and } 800$  MeV. The real parts are solid lines while the imaginary parts are dashed lines.

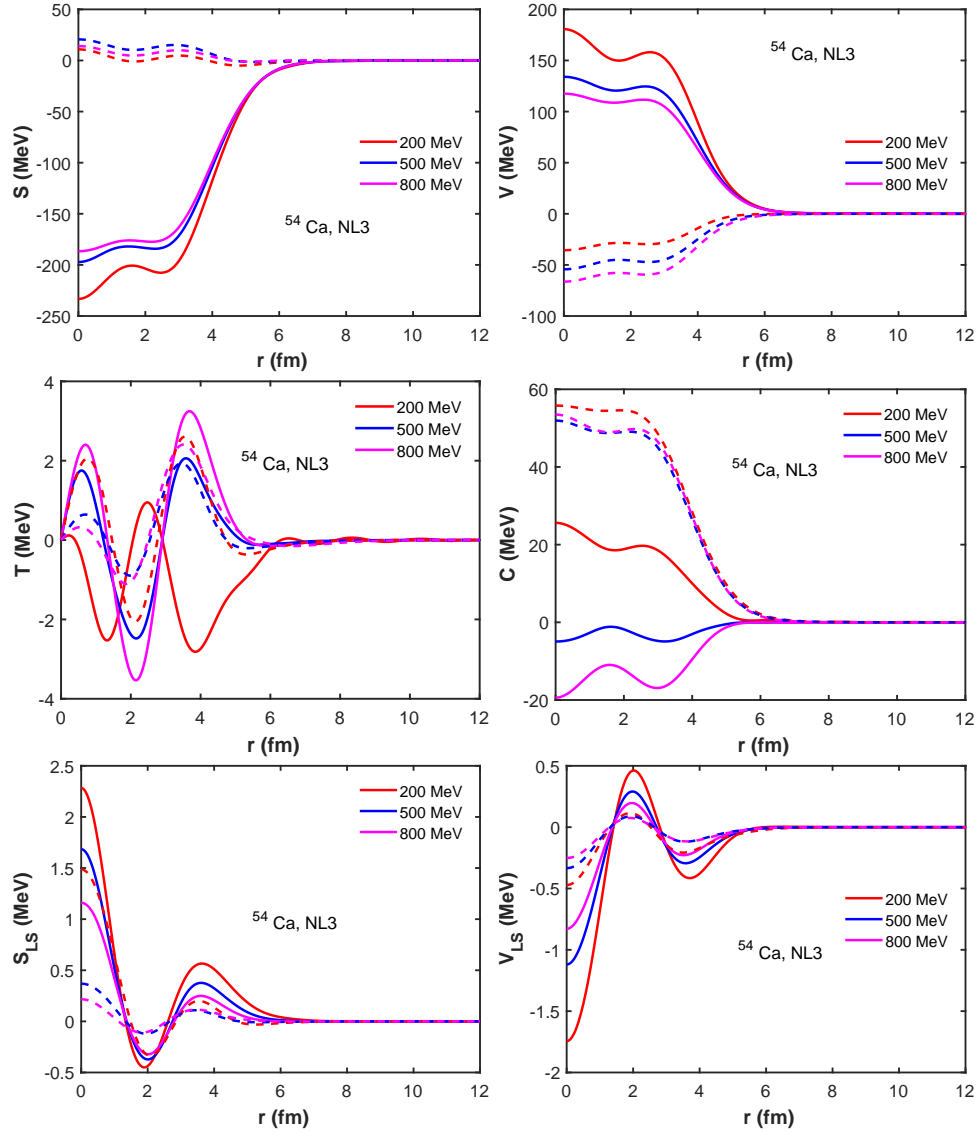


Figure 3.10: Same as in figure 3.9 except for  $p+^{54}\text{Ca}$ .

where

$$\begin{aligned}\tilde{S}_\kappa &= \tilde{S} + \tilde{S}_{LS} + \kappa\tilde{V}_{LS} \\ \tilde{V}_\kappa &= \tilde{V} + \tilde{V}_{LS} + \kappa\tilde{S}_{LS},\end{aligned}\quad (3.4.57)$$

and  $\kappa$  denotes the eigenvalue of  $\boldsymbol{\sigma} \cdot \mathbf{L} + 1$ . It is defined as follows:

$$(\boldsymbol{\sigma} \cdot \mathbf{L} + 1)\tilde{\Psi}_U = -\kappa\tilde{\Psi}_U, \quad (3.4.58)$$

where  $\tilde{\Psi}_U$  denotes an upper component of the Dirac wave function and

$$\kappa = -1 \rightarrow \mathbf{L} = 0. \quad (3.4.59)$$

The Schrödinger equivalent central and spin orbit potentials are shown in figure 3.11 based on the IA2 formalism for  $p+^{48,54}\text{Ca}$  elastic scattering at  $T_{\text{lab}} = 200, 500, 800$

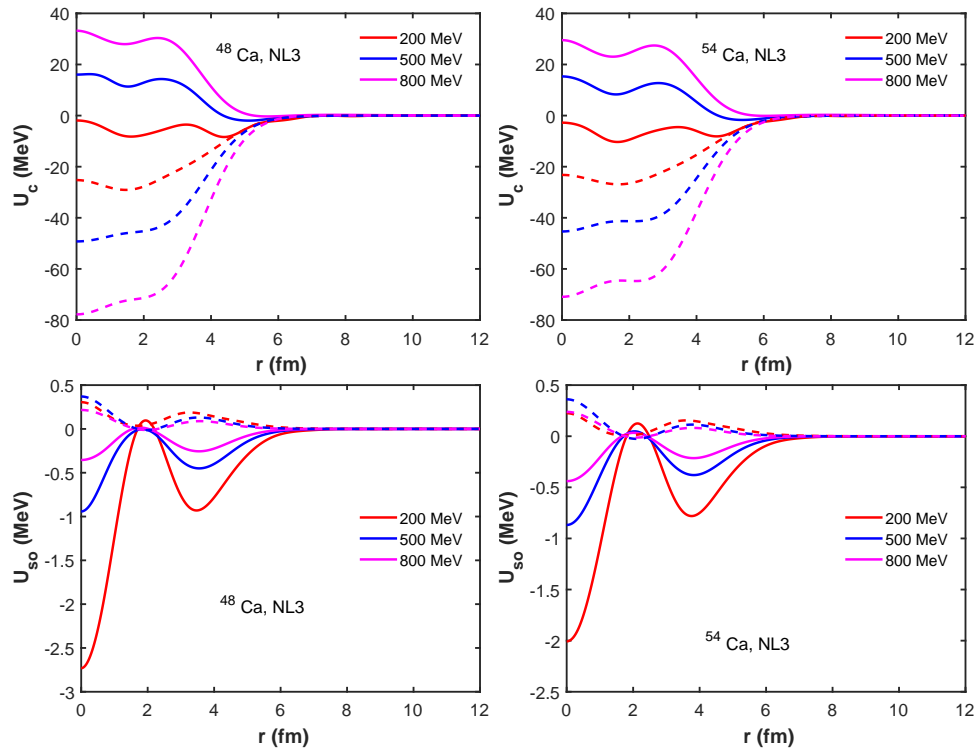


**Figure 3.11:** IA2 Schrödinger equivalent central and spin orbit potentials for  $p+^{48,54}\text{Ca}$ , using the NL3 parameter set, at  $T_{\text{lab}} = 200, 500,$  and  $800$  MeV. The solid lines are real parts while dashed lines denote imaginary parts.

MeV using the NL3 parameter set (for  $\kappa = -1$ , corresponding to  $L = 0$ ). The top left plot contains the central potential for  $p+^{48}\text{Ca}$ , while the right plot contains central potential for  $p+^{54}\text{Ca}$ . The bottom left plot shows the spin-orbit potential for  $p+^{48}\text{Ca}$ , while the bottom right plot shows the spin-orbit potential for  $p+^{54}\text{Ca}$ . The solid lines are real parts while the dashed lines are imaginary parts. It can be observed from the figure that the strengths of the central potentials increase with increase in incident projectile energy for  $p+^{48,54}\text{Ca}$ . The real parts of the spin-orbit potentials decrease as incident projectile energy increases. The Schrödinger equivalent central and spin orbit potentials for proton scattering from unstable nuclei behave in a similar manner to those from stable nuclei.

### 3.4.3 Contributions of sub-classes to IA2 optical potential

In this sub-section, we will look at contributions from different subclasses of the invariant amplitudes to the IA2 optical potential. The subclasses will be grouped into nine. Table 3.4 shows the different sub-classes in each group. Group nine has contributions from all the subclasses, it is the full  $F^{\rho_1\rho_2\rho_1\rho_2}$ .

Figure 3.12 shows the contributions of the different groups to the scalar and vector optical potentials for  $p+^{40}\text{Ca}$  using the QHD II parameter set. The top (bottom) left plot contains the real scalar (vector) potential while the top (bottom) right contains the imaginary scalar (vector) potential. The different sub-classes that contribute to

**Table 3.4:** Table showing contributions of the IA2  $\hat{F}$  sub-classes to the scalar and vector potentials for  $p+^{40}\text{Ca}$  at  $T_{\text{lab}} = 200 \text{ MeV}$ .

Group	$\hat{F}$	Re S	Im S	Re V	Im V
1	$F^{11}$	Yes	Yes	Yes	No
2	$F^{12}$	No	Yes	No	Yes
3	$F^{21}$	Yes	Yes	Yes	Yes
4	$F^{13}$ and $F^{31}$	Yes	Yes	Yes	Yes
5	$F^{14}$ and $F^{41}$	Yes	Yes	Yes	Yes
6	$F^{23}$ and $F^{32}$	Yes	Yes	No	No
7	$F^{22}$ and $F^{33}$	No	Yes	No	No
8	$F^{24}$ and $F^{42}$	Yes	Yes	Yes	Yes
9	$F^{34}$ , $F^{43}$ and $F^{44}$	Yes	Yes	Yes	Yes

the scalar and vector potentials for  $p+^{40}\text{Ca}$  at  $T_{\text{lab}} = 200 \text{ MeV}$  are indicated in table 3.4 with a "yes". A "no" means the group does not contribute to the potential. One can observe from the table that all the groups have contributions to at least the scalar or vector potentials. This means that they are all important.

Figure 3.13 shows the contributions of the different groups to the scalar and vector optical potentials for  $p+^{54}\text{Ca}$  using the NL3 parameter set. The different sub-classes that contribute to the scalar and vector potentials for  $p+^{54}\text{Ca}$  at  $T_{\text{lab}} = 200 \text{ MeV}$  are indicated in table 3.5. Again all the sub-classes contribute to at least either the scalar or vector optical potential. In summary, all the sub-classes of IA2  $\hat{F}$  are important to calculate the optical potentials for both stable and unstable nuclei.

## 3.5 Full folding versus factorised optical potential

In this section, the optical potentials obtained via optimal factorization will be compared with those obtained via full folding. Full folding involves integrating over Fermi momentum; this means including medium effects (Fermi motion) in the target nucleus. We begin with the IA1 formalism.

### 3.5.1 IA1

In the original relativistic impulse approximation (IA1) representation of  $\hat{F}$ , we have

$$\hat{\mathcal{F}}_{\text{IA1}} = F_S (\mathbb{I}_4 \otimes \mathbb{I}_4) + F_P (\gamma^5 \otimes \gamma^5) + F_V (\gamma^\mu \otimes \gamma_\mu) + F_A (\gamma^5 \gamma^\mu \otimes \gamma^5 \gamma_\mu) + F_T (\sigma^{\mu\nu} \otimes \sigma^{\mu\nu}) \quad (3.5.1)$$

or in short form

$$\hat{\mathcal{F}}_{\text{IA1}} = \sum_{L=S}^T \mathcal{F}_L (\lambda^L \otimes \lambda_L) \quad (3.5.2)$$

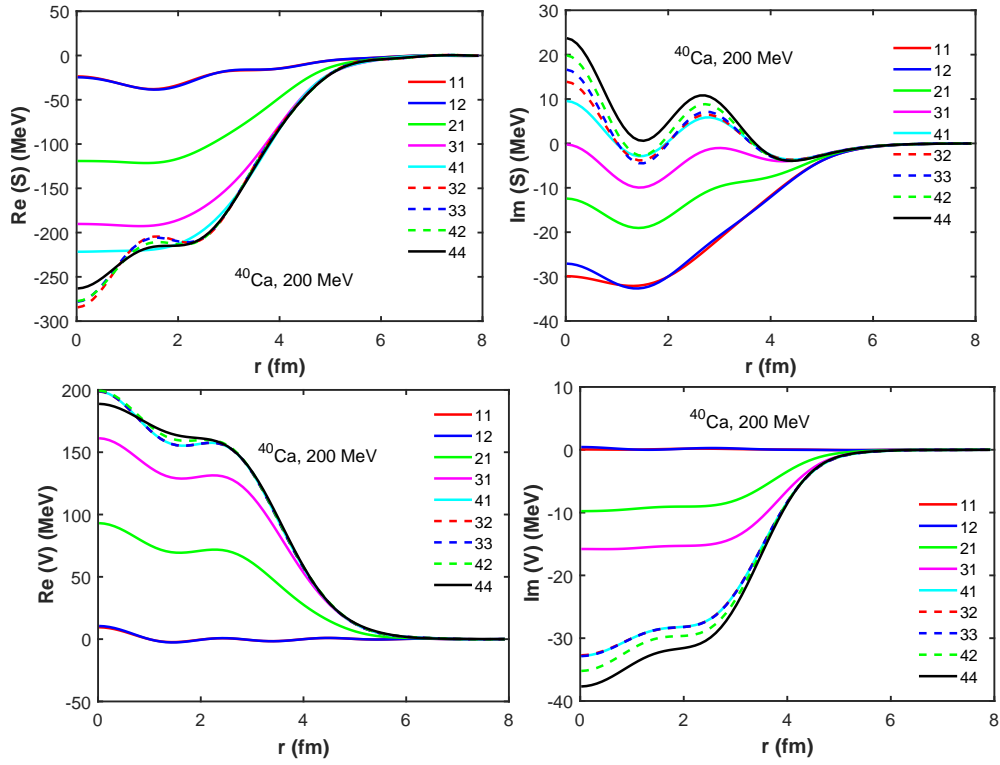


**Figure 3.12:** Contributions of the IA2  $F$  subclasses to  $p+^{40}\text{Ca}$  (QHD II model) at  $T_{\text{lab}} = 200$  MeV.

**Table 3.5:** Table showing contributions of the IA2  $\hat{F}$  sub-classes to the scalar and vector potentials for  $p+^{54}\text{Ca}$  at  $T_{\text{lab}} = 200$  MeV.

Group	$\hat{F}$	Re S	Im S	Re V	Im V
1	$F^{11}$	Yes	Yes	Yes	No
2	$F^{12}$	Yes	Yes	No	Yes
3	$F^{21}$	Yes	Yes	Yes	Yes
4	$F^{13}$ and $F^{31}$	Yes	Yes	Yes	Yes
5	$F^{14}$ and $F^{41}$	Yes	Yes	Yes	Yes
6	$F^{23}$ and $F^{32}$	Yes	Yes	No	No
7	$F^{22}$ and $F^{33}$	Yes	Yes	No	No
8	$F^{24}$ and $F^{42}$	Yes	Yes	Yes	Yes
9	$F^{34}$ , $F^{43}$ and $F^{44}$	Yes	Yes	Yes	Yes

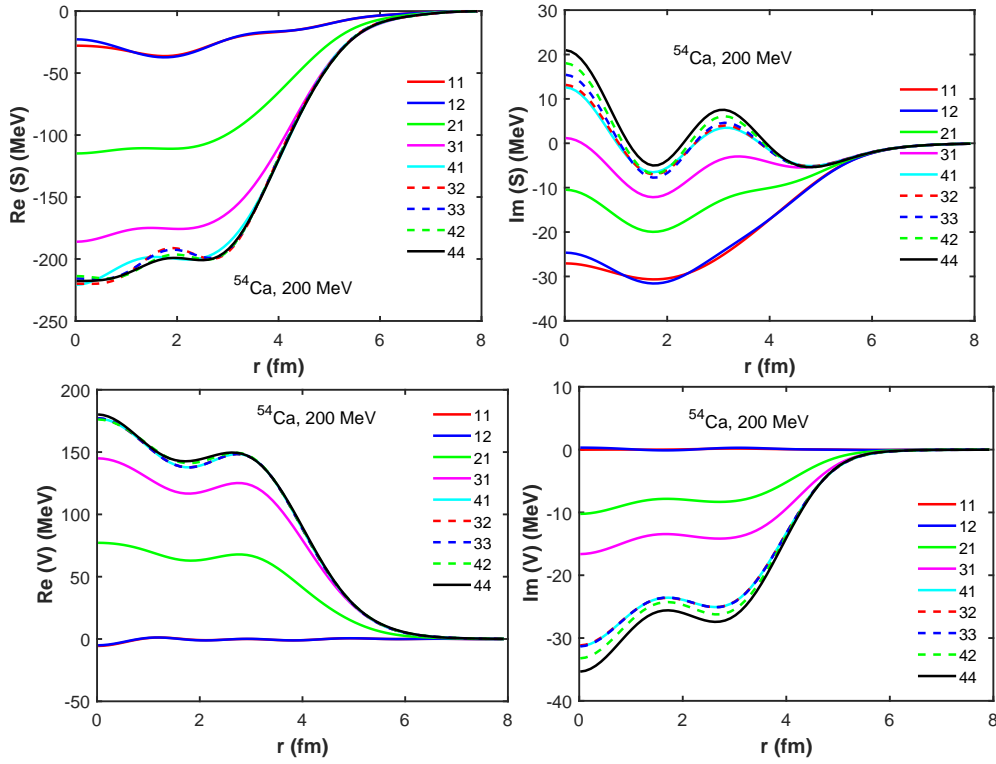


**Figure 3.13:** Contributions of the IA2 F subclasses to  $p+^{54}\text{Ca}$  (NL3 model) at  $T_{\text{lab}} = 200$  MeV.

The optical potential is written as

$$\hat{U}(\mathbf{k}', \mathbf{k}) = \frac{-4\pi i k_{\text{lab}}}{m} \sum_a \int \frac{d^3 P}{(2\pi)^3} \bar{\psi}_a(\mathbf{P} + \frac{1}{2}\mathbf{q}) \hat{\mathcal{F}}(k, P - \frac{1}{2}q; k', P + \frac{1}{2}q) \psi_a(\mathbf{P} - \frac{1}{2}\mathbf{q}). \quad (3.5.3)$$

Since  $\hat{\mathcal{F}}_{\text{IA1}}$  is a  $16 \times 16$  matrix, it means  $\bar{\psi}_\alpha$  should be  $4 \times 16$  matrix and  $\psi_\alpha$  should be  $16 \times 4$  matrix:

$$\bar{\psi}_\alpha = \mathbb{I}_4 \otimes \bar{\phi}_\alpha, \quad \psi_\alpha = \mathbb{I}_4 \otimes \phi_\alpha, \quad (3.5.4)$$

where  $\phi_\alpha$  is the  $4 \times 1$  bound state wave function, and  $\bar{\phi}_\alpha$  is  $1 \times 4$ . This will make the optical potential to be  $4 \times 4$  matrix. We can then write the optical potential as

$$\hat{U}(\mathbf{k}', \mathbf{k}) = \frac{-4\pi i k_{\text{lab}}}{m} \int \frac{d^3 P}{(2\pi)^3} [\mathbb{I}_4 \otimes \bar{\phi}_\alpha(\mathbf{P} + \frac{1}{2}\mathbf{q})] \mathcal{F}_L(\lambda^L \otimes \lambda_L) [\mathbb{I}_4 \otimes \phi_\alpha(\mathbf{P} - \frac{1}{2}\mathbf{q})] \quad (3.5.5)$$

Using the following property of the Kronecker product,

$$(A \otimes B)(C \otimes D) = AC \otimes BD, \quad (3.5.6)$$

we have

$$\begin{aligned} \hat{U}(\mathbf{k}', \mathbf{k}) &= \frac{-4\pi i k_{\text{lab}}}{m} \int \frac{d^3 P}{(2\pi)^3} [\mathbb{I}_4 \lambda^L \otimes \bar{\phi}_\alpha(\mathbf{P} + \frac{1}{2}\mathbf{q}) \lambda_L] [\mathbb{I}_4 \otimes \phi_\alpha(\mathbf{P} - \frac{1}{2}\mathbf{q})] F_L \\ &= \left\{ \frac{-4\pi i k_{\text{lab}}}{m} \int \frac{d^3 P}{(2\pi)^3} [\bar{\phi}_\alpha(\mathbf{P} + \frac{1}{2}\mathbf{q}) \lambda_L \phi_\alpha(\mathbf{P} - \frac{1}{2}\mathbf{q})] F_L \right\} \lambda^L. \end{aligned} \quad (3.5.7)$$

For example, for  $L = S$ , one has

$$U_S = \left\{ \frac{-4\pi i k_{\text{lab}}}{m} \int \frac{d^3 P}{(2\pi)^3} [\bar{\phi}_\alpha(\mathbf{P} + \frac{1}{2}\mathbf{q}) \mathbb{I}_4 \phi_\alpha(\mathbf{P} - \frac{1}{2}\mathbf{q})] F_S \right\} \mathbb{I}_4. \quad (3.5.8)$$

The bound state wave function  $\phi_\alpha$  is given as

$$\phi_\alpha(\mathbf{r}) = \frac{1}{r} \begin{pmatrix} g_{E\ell_j}(r) \mathcal{Y}_{\ell_j m}(\hat{r}) \\ i f_{E\ell_j}(r) \mathcal{Y}_{2j-\ell_j m}(\hat{r}) \end{pmatrix}. \quad (3.5.9)$$

The Fourier transform of the bound state wave function is

$$\phi_\alpha(\mathbf{p}) = 4\pi(-1)^\ell \begin{pmatrix} i^\ell g_{\ell_j}(p) \mathcal{Y}_{\ell_j m}(\hat{p}) \\ i^{2j-\ell+1} f_{2j-\ell_j}(p) \mathcal{Y}_{2j-\ell_j m}(\hat{p}) \end{pmatrix}, \quad (3.5.10)$$

where

$$g_{\ell,j}(p) = \int_0^\infty dr r g_{\ell_j}(r) j_\ell(pr), \quad (3.5.11)$$

$$f_{2j-\ell,j}(p) = \int_0^\infty dr r f_{\ell_j}(r) j_{2j-\ell}(pr), \quad (3.5.12)$$

$$\mathcal{Y}_{\ell_j m}(\hat{p}) = \sum_{s_z=\pm\frac{1}{2}} \left\langle \ell, \frac{1}{2}, m - s_z, s_z \mid jm \right\rangle Y_{\ell, m-s_z}(\hat{p}) \chi_{s_z}. \quad (3.5.13)$$

The expression  $\bar{\phi}_\alpha(\mathbf{P} + \frac{1}{2}\mathbf{q}) \mathbb{I}_4 \phi_\alpha(\mathbf{P} - \frac{1}{2}\mathbf{q}) \equiv \phi_\alpha^\dagger(\mathbf{P} + \frac{1}{2}\mathbf{q}) \gamma^0 \phi_\alpha(\mathbf{P} - \frac{1}{2}\mathbf{q})$  in equation (3.5.8) is simplified into

$$\bar{\phi}_\alpha(\mathbf{P} + \frac{1}{2}\mathbf{q}) \phi_\alpha(\mathbf{P} - \frac{1}{2}\mathbf{q}) = 4\pi \left( j + \frac{1}{2} \right) [g_{\ell_j}(p_+) g_{\ell_j}(p_-) - f_{2j-\ell_j}(p_+) f_{2j-\ell_j}(p_-)], \quad (3.5.14)$$

where  $p_+ = P + \frac{1}{2}q$ ,  $p_- = P - \frac{1}{2}q$ , and the following relation has been used:

$$\sum_{\mu, m, m'} \left\langle \ell m \frac{1}{2} s \mid j \mu \right\rangle \left\langle \ell m' \frac{1}{2} s' \mid j \mu \right\rangle Y_{\ell m}^*(\hat{r}) Y_{\ell m'}(\hat{r}) = \delta_{s, s'} \frac{j + \frac{1}{2}}{4\pi} \quad (3.5.15)$$

Equation (3.5.8) can then be written as

$$U_S(\mathbf{k}', \mathbf{k}) = \left\{ \frac{-4\pi i k_{\text{lab}}}{m} \int \frac{d^3 P}{(2\pi)^3} F_S(k, P - \frac{1}{2}q; k', P + \frac{1}{2}q) \right. \\ \left. \times [g_{\ell_j}(p_+) g_{\ell_j}(p_-) - f_{2j-\ell_j}(p_+) f_{2j-\ell_j}(p_-)] \right\} \mathbb{I}_4. \quad (3.5.16)$$

Following similar procedure, the IA1 vector optical potential gives

$$U_V(\mathbf{k}', \mathbf{k}) = \left\{ \frac{-4\pi i k_{\text{lab}}}{m} \int \frac{d^3 P}{(2\pi)^3} F_V(k, P - \frac{1}{2}q; k', P + \frac{1}{2}q) \right. \\ \left. \times [g_{\ell_j}(p_+) g_{\ell_j}(p_-) + f_{2j-\ell_j}(p_+) f_{2j-\ell_j}(p_-)] \right\} \gamma^0. \quad (3.5.17)$$

### 3.5.2 IA2

In the case of IA2 formalism, we have 16 subclasses of  $\hat{\mathcal{F}}$ . For subclass  $\hat{\mathcal{F}}^{11}$ , only five terms contribute to the amplitude:

$$\hat{\mathcal{F}}^{11} = \hat{\mathcal{F}}_1^{11} + \hat{\mathcal{F}}_2^{11} + \hat{\mathcal{F}}_3^{11} + \hat{\mathcal{F}}_4^{11} + \hat{\mathcal{F}}_5^{11} \equiv \hat{\mathcal{F}}_L^{11}, \quad L = 1 - 5. \quad (3.5.18)$$

The amplitude is written out in full form as

$$\hat{\mathcal{F}}^{11}(k_1, k_2 \rightarrow k'_1, k'_2) = [\Lambda_+(\mathbf{k}_1) \otimes \Lambda_+(\mathbf{k}_2)] F_L^{11} (\lambda^L \otimes \lambda_L) [\Lambda_+(\mathbf{k}'_1) \otimes \Lambda_+(\mathbf{k}'_2)]. \quad (3.5.19)$$

Using the relation in equation (3.5.6), we have

$$\hat{\mathcal{F}}^{11}(k_1, k_2 \rightarrow k'_1, k'_2) = F_L^{11} [\Lambda_+(\mathbf{k}_1) \lambda^L \Lambda_+(\mathbf{k}'_1) \otimes \Lambda_+(\mathbf{k}_2) \lambda_L \Lambda_+(\mathbf{k}'_2)]. \quad (3.5.20)$$

The optical potential for this subclass is then written as

$$\begin{aligned} \hat{U}_{11}(\mathbf{k}', \mathbf{k}) = & \frac{-4\pi i k_{\text{lab}}}{m} \int \frac{d^3 P}{(2\pi)^3} [\mathbb{I}_4 \otimes \bar{\phi}_\alpha(\mathbf{P} + \frac{1}{2}\mathbf{q})] F_L^{11} [\Lambda_+(\mathbf{k}_1) \lambda^L \Lambda_+(\mathbf{k}'_1) \otimes \\ & \Lambda_+(\mathbf{k}_2) \lambda_L \Lambda_+(\mathbf{k}'_2)] [\mathbb{I}_4 \otimes \phi_\alpha(\mathbf{P} - \frac{1}{2}\mathbf{q})] \end{aligned} \quad (3.5.21)$$

Using equation (3.5.6) again, we have

$$\hat{U}_{11}(\mathbf{k}', \mathbf{k}) = \mathcal{M}_L^{11} \int \frac{d^3 P}{(2\pi)^3} [\bar{\phi}_\alpha(\mathbf{P} + \frac{1}{2}\mathbf{q}) \Lambda_+(\mathbf{k}_2) \lambda_L \Lambda_+(\mathbf{k}'_2) \phi_\alpha(\mathbf{P} - \frac{1}{2}\mathbf{q})] [\Lambda_+(\mathbf{k}_1) \lambda^L \Lambda_+(\mathbf{k}'_1)] \quad (3.5.22)$$

where  $\mathcal{M}_L^{11} = \frac{-4\pi i k_{\text{lab}}}{m} F_L^{11}$ . In equation (3.5.21), the first term in square bracket is a complex number, while the second term in square bracket is a  $4 \times 4$  matrix. This path will not be followed, however, because of the complexity involved in the IA2 formalism. Medium effects are incorporated here via the dependence of the NN amplitudes on nuclear matter Fermi momentum. We start from equation (3.4.8):

$$\begin{aligned} \hat{U}(\mathbf{k}', \mathbf{k}) = & -\frac{1}{4} \text{Tr}_2 \left[ \int \frac{d^3 P}{(2\pi)^3} \hat{\mathcal{M}}_{pp}(k, P - \frac{1}{2}q; k', P + \frac{1}{2}q) \hat{\rho}_p(\mathbf{P}, \mathbf{q}) \right] \\ & -\frac{1}{4} \text{Tr}_2 \left[ \int \frac{d^3 P}{(2\pi)^3} \hat{\mathcal{M}}_{pn}(k, P - \frac{1}{2}q; k', P + \frac{1}{2}q) \hat{\rho}_n(\mathbf{P}, \mathbf{q}) \right]. \end{aligned} \quad (3.5.23)$$

The local density approximation is employed to simplify the problem, in which case the density matrices  $\hat{\rho}(\mathbf{P}, \mathbf{q})$  are calculated via [34]:

$$\hat{\rho}(\mathbf{P}, \mathbf{q}) = \int d^3 r e^{i\mathbf{q}\cdot\mathbf{r}} \hat{\rho}[r(P)] \quad (3.5.24)$$

and

$$\hat{\rho}[r(P)] = \rho_s[r(P)] \mathbb{I}_2 + \rho_v[r(P)] \gamma_2^0 - \rho_T[r(P)] \frac{i\boldsymbol{\alpha}_2 \cdot \hat{\mathbf{r}}}{2}. \quad (3.5.25)$$

The following formula shows the relationship between the radius  $r$  and Fermi momentum  $k_F$ :

$$\rho_v(r) = \frac{2k_F^3}{3\pi^2}. \quad (3.5.26)$$

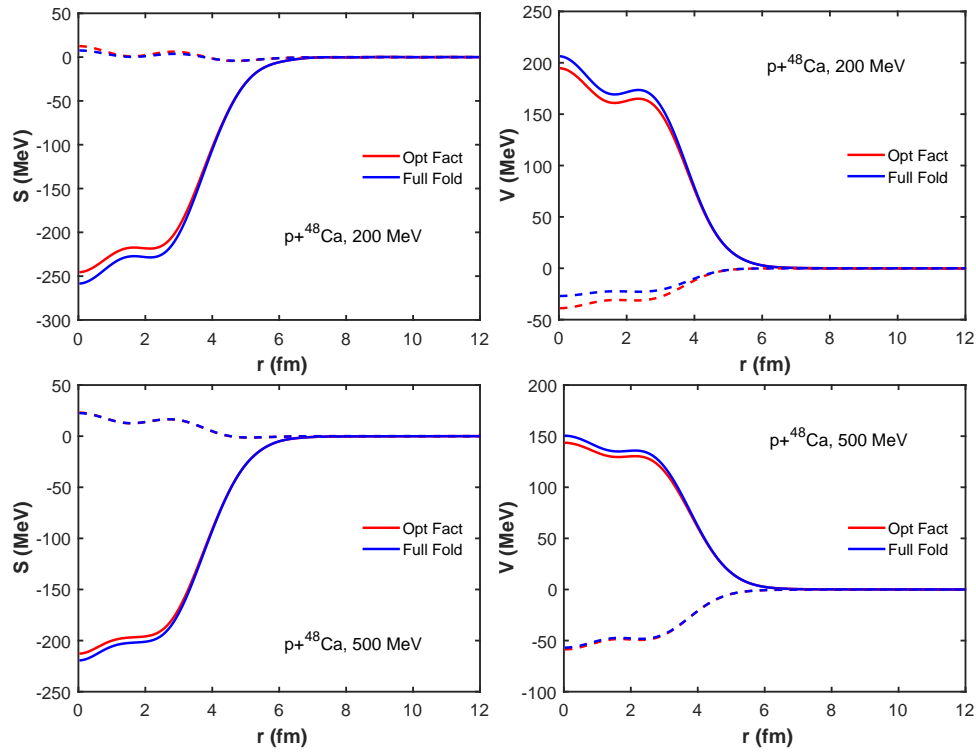


**Figure 3.14:** Full-folding versus factorised scalar and vector optical potentials in the IA2 formalism for elastic scattering of  $p+^{48}\text{Ca}$  (NL3 model) at  $T_{\text{lab}} = 200$  and  $500$  MeV. The localised forms of the optical potentials were used. The real parts are indicated with solid lines while imaginary parts are dashed lines. The full folding ("Full fold") results are shown in blue lines while the optimally factorised ("Opt fact") results are indicated with red lines.

The results of these calculations are shown in Figures 3.14 and 3.15. The Figures show comparisons of the scalar and vector optical potentials in the IA2 formalism calculated using optimal factorisation and full folding. It should be noted that the optical potentials shown in the Figures are all localised. The real optical potentials are indicated with solid lines while the imaginary parts are indicated with dashed lines. The top left plots are scalar potentials at  $T_{\text{lab}} = 200\text{MeV}$ , the top right plots are vector potentials at  $T_{\text{lab}} = 200\text{MeV}$ . The bottom plots are scalar and vector potentials at  $T_{\text{lab}} = 500\text{MeV}$ . One can observe from the Figures that inclusion of medium effects led to increase in real parts of the scalar and vector potentials at  $T_{\text{lab}} = 200\text{MeV}$ . At this incident projectile laboratory energy, there is slight decrease in the imaginary parts of both scalar and vector potentials when medium effects are included. This is the case for both  $^{48,54}\text{Ca}$  targets. At  $T_{\text{lab}} = 500\text{MeV}$ , there is no noticeable difference in the imaginary parts of both scalar and vector potentials. There is slight increase in the real parts of both scalar and vector potentials at this incident energy. In summary, there is not much difference in using optimally factorised optical potentials and full folding optical potentials at  $T_{\text{lab}} = 500\text{MeV}$ . Medium effects are observed at lower energy such as  $T_{\text{lab}} = 200\text{MeV}$ . This will be discussed further in the next chapter.

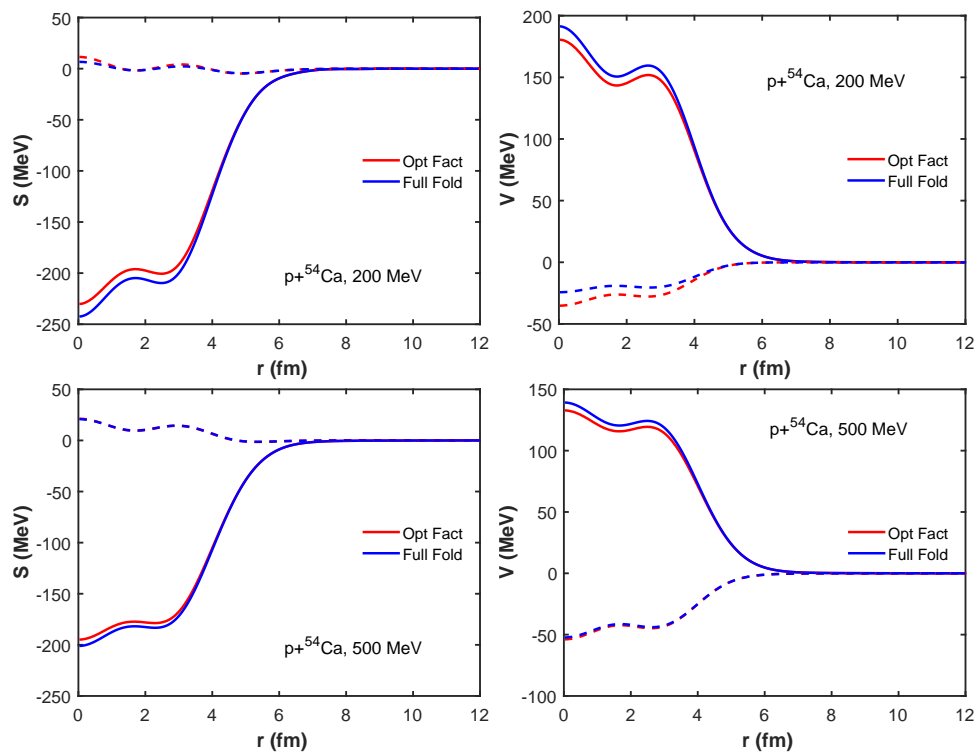


Figure 3.15: Same as in figure 3.14 except for  $p+^{54}\text{Ca}$ .

## Chapter 4

# Solution of the Coordinate Space Dirac Equation

The relativistic optical potentials required to solve the Dirac equation have been calculated in Chapter 3. This chapter contains solutions of the coordinate space Dirac equation with the use of the localised relativistic optical potentials. The solution of the Dirac equation for non-local optical potentials is done naturally in momentum space, and is the topic of Chapter 5. The scattering observables calculated using different RMFT models will be compared; this is done to investigate the sensitivity of the proton-nucleus scattering observables to the different Lagrangian densities. The scattering observables calculated using both IA1 and IA2 optical potentials will also be compared to study the sensitivity of the scattering observables to the two formalisms. The effect of full folding on the scattering observables will then be investigated by comparing with the results calculated using optimally factorised optical potentials.

The Dirac equation for the two component wave function  $u(\mathbf{x})$  is written as

$$(-\nabla^2 + U_c + U_{so}\boldsymbol{\sigma} \cdot \mathbf{L}) u(\mathbf{x}) = (E^2 - m^2) u(\mathbf{x}), \quad (4.0.1)$$

where the central potential  $U_c$  and spin-orbit potential  $U_{so}$  have been given in Chapter 3 for global Dirac phenomenology, IA1, and IA2 optical potentials,  $E$  is the total proton-nucleus centre of mass projectile energy, and  $m$  is the projectile mass. The wave function  $u$  has the same asymptotic behaviour as the wave function at large  $r$ . The boundary condition is imposed by matching  $u$  to the form of a Coulomb scattering solution whose projectile is incident from the  $z$ - direction [29, 120]:

$$u(r) \propto_{r \rightarrow \infty} \left\{ e^{i[kz - \eta \ln 2kr \sin^2 \theta/2]} \left[ 1 - \frac{\eta^2}{2ikr \sin^2 \theta/2} \right] \right\} \chi_{\text{inc}} + \frac{e^{i[kz - \eta \ln 2kr]}}{r} [A(\theta) + B(\theta)\boldsymbol{\sigma} \cdot \hat{n}] \chi_{\text{inc}}, \quad (4.0.2)$$

where  $k = \sqrt{E^2 - m^2}$ ,  $\chi_{\text{inc}}$  is the two-component Pauli spinor,  $\theta$  is the centre of mass scattering angle,  $\hat{n}$  is the normal to the scattering plane,  $\eta \equiv \frac{Ze^2m}{k}$ , and the

nuclear charge is denoted by  $Z$ . A partial wave expansion of equation (4.0.1) yields

$$\left\{ \frac{d^2}{dr^2} + k^2 - \left[ U_c(r) + \binom{\ell}{-\ell-1} U_{\text{so}}(r) \right] - \frac{\ell(\ell+1)}{r^2} \right\} u_\ell^\pm(kr) = 0. \quad (4.0.3)$$

Here,  $\ell$  appears in the equation for  $u_\ell^+(kr)$ ,  $-\ell-1$  appears in the equation for  $u_\ell^-(kr)$ , and  $u_\ell^\pm(kr)$  is equivalent to the Coulomb functions  $F_\ell$  and  $G_\ell$  when there is no nuclear interaction. The initial values for  $u_\ell^\pm(0) = 0$ , and  $u_\ell^\pm(kr)$  is integrated to large  $r$  with the Runge-Kutta/Noumerov algorithm where it is matched to the asymptotic functions via

$$u_\ell^\pm(kr) \sim F_\ell(\eta, kr) + C_\ell^\pm [G_\ell(\eta, kr) + iF_\ell(\eta, kr)], \quad (4.0.4)$$

which reduces to

$$u_\ell^\pm(kr) \cong \sin(kr - \eta \ln 2kr - \ell\pi/2 + \sigma_\ell) + C_\ell^\pm e^{i(kr - \eta \ln 2kr - \ell\pi/2 + \sigma_\ell)}. \quad (4.0.5)$$

This is because the asymptotic expressions for the regular and irregular Coulomb functions are given, respectively, by

$$F_\ell(\eta, kr) \cong \sin(kr - \eta \ln 2kr - \ell\pi/2 + \sigma_\ell) \quad (4.0.6)$$

$$G_\ell(\eta, kr) \cong \cos(kr - \eta \ln 2kr - \ell\pi/2 + \sigma_\ell), \quad (4.0.7)$$

where the Coulomb phase shift

$$\sigma_\ell = \sigma_0 + \sum_{s=1}^{\ell} \tan^{-1} \frac{\eta}{s}, \quad (4.0.8)$$

and  $\sigma_0 = \arg\Gamma(1 + i\eta)$ . Appendix D shows how  $\sigma_\ell$  and the coefficients  $C_\ell^\pm$  are numerically computed. The Coulomb potential is calculated by assuming a constant charge density distribution which has radius  $R = R_0 A^{1/3}$ , where the Coulomb radius constant  $R_0$  is taken to be 1.25 fm. The Coulomb potential is then calculated via:

$$\begin{aligned} V_{\text{coul}} &= \frac{ZZ'e^2}{2R_0} \left( 3 - \frac{r^2}{R_0^2} \right) \quad \text{for } r < R_0 \\ &= \frac{ZZ'e^2}{r} \quad r \geq R_0, \end{aligned} \quad (4.0.9)$$

The Coulomb spin-orbit potential is neglected here; it is known to be negligible except at very high energies.

## 4.1 Scattering observables

The scattering amplitudes  $A(\theta)$  and  $B(\theta)$  are calculated using [29]

$$A(\theta) = f_c(\theta) + \frac{1}{k} \sum_{\ell} e^{2i\sigma_\ell} [(\ell+1)C_\ell^+ + \ell C_\ell^-] P_\ell(\cos \theta), \quad (4.1.1)$$

and

$$B(\theta) = -\frac{i}{k} \sum_{\ell} e^{2i\sigma_\ell} [C_\ell^+ - C_\ell^-] P_\ell^1(\cos \theta), \quad (4.1.2)$$

where the Rutherford scattering amplitude

$$f_c(\theta) = -\frac{\eta}{2k \sin^2 \frac{\theta}{2}} e^{-i\eta \ln\left(\sin^2 \frac{\theta}{2}\right) + 2i\sigma_0}, \quad (4.1.3)$$

$\eta = \frac{mZe^2}{k}$ , and  $P_\ell(\cos \theta)$  and  $P_\ell^1(\cos \theta)$  are the Legendre polynomials and associated Legendre polynomials, respectively. The scattering observables are computed using

$$\frac{d\sigma}{d\Omega} = |A(\theta)|^2 + |B(\theta)|^2, \quad (4.1.4)$$

for the unpolarized differential cross section, which quantifies the intrinsic rate at which the scattered proton can be detected at a given angle,

$$A_y = \frac{2\text{Re}[A^*(\theta)B(\theta)]}{\frac{d\sigma}{d\Omega}}, \quad (4.1.5)$$

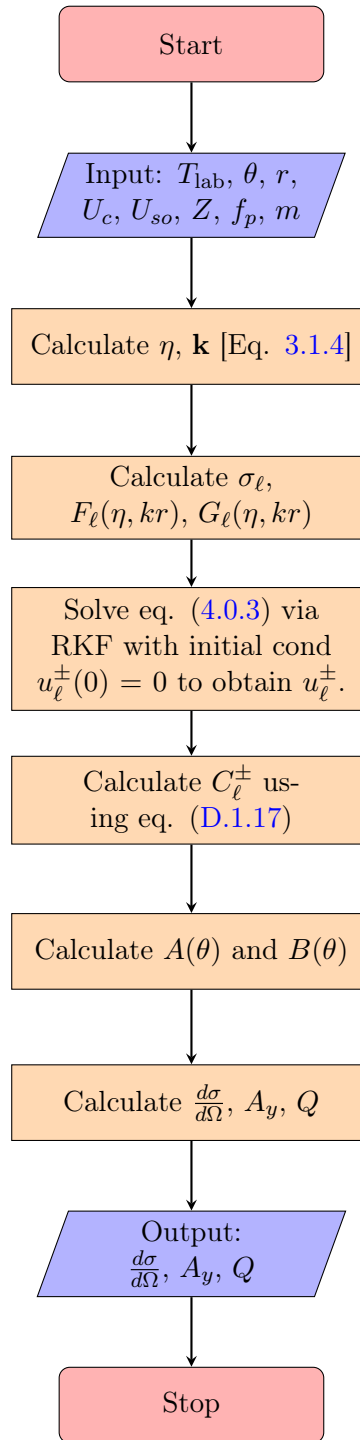
for the analysing power, which measures the effect of changes in the polarization of the beam or target nuclei on scattering cross sections, and

$$Q = \frac{2\text{Im}[A(\theta)B^*(\theta)]}{\frac{d\sigma}{d\Omega}}, \quad (4.1.6)$$

for the spin rotation parameter which is a function of the amount by which the scattering plane component of the scattered proton's polarization vector changes due to the scattering process.

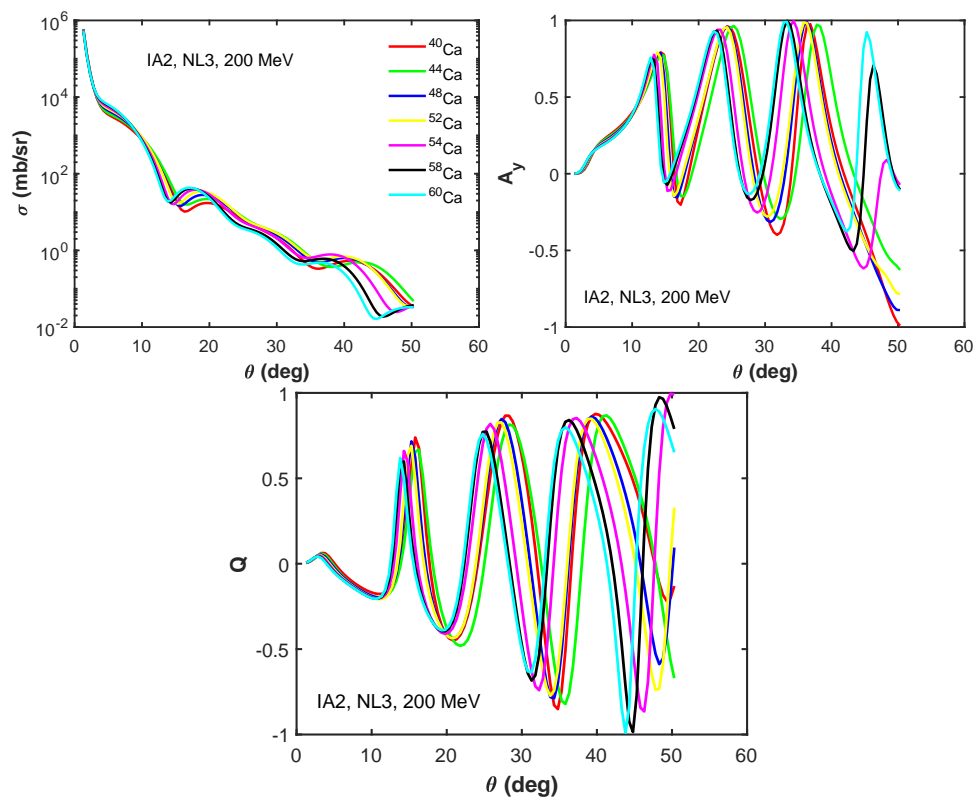
## 4.2 Numerical results and discussions

Figure 4.1 shows the flow chart that illustrates how the scattering observables are computed. The function `SCATOBS` takes as inputs the projectile (proton) incident laboratory energy  $T_{\text{lab}}$ , the central potential  $U_c$ , spin orbit potential  $U_{\text{so}}$ , target charge  $Z$ , radius  $r$ , and the scattering angle  $\theta$ . The scattering angle  $\theta$  is an array that starts with the minimum scattering angle and ends with the maximum scattering angle, with uniform spacing. The required kinematic quantities  $\eta$  and  $\mathbf{k}$  are then calculated, after which the Coulomb phase shift  $\sigma_\ell$ , regular Coulomb functions  $F_\ell(\eta, kr)$ , and irregular Coulomb functions  $G_\ell(\eta, kr)$  are calculated for all partial waves via equations (4.0.8) and (4.0.7). Appendix D describes how these Coulomb functions are numerically calculated. Runge-Kutta-Fehlberg (RKF) algorithm (See Appendix B) is then employed to solve equation (4.0.3) for  $u_\ell^\pm$  using the initial conditions  $u_\ell^\pm(0) = 0$ . The quantities  $C_\ell^\pm$  are calculated using the matching conditions and equation (D.1.17). The Runge-Kutta-Fehlberg (RKF) algorithm has been chosen because it is self starting and gives results that are of very high accuracy. Using the calculated values of  $\sigma_\ell$ ,  $C_\ell^\pm$ , and equation (4.1.3), the quantities  $A(\theta)$  and  $B(\theta)$  are then calculated using equations (4.1.1) and (4.1.2). Finally, the scattering observables  $\frac{d\sigma}{d\Omega}$ ,  $A_y$ , and  $Q$  are computed via equations (4.1.4), (4.1.5), and (4.1.6). In this work, the maximum value of 80 has been used for the partial waves. This is known to be enough for incident laboratory energies less than 1000 MeV [29].



**Figure 4.1:** Flow chart illustrating how the function *SCATOBS* calculates the scattering observables.

The code HOOVER from Ref. [29] has been modified to calculate the scattering observables using IA2 optical potentials, as the code was initially written for only scalar and vector IA1 optical potentials. Similar results have been obtained when compared with the code SCATOBS. The HOOVER code makes use of the Noumerov algorithm. Appendix B gives a description of the Noumerov algorithm.



**Figure 4.2:** Scattering cross section, analysing power, and spin rotation function for the  $^{40,44,48,52,54,58,60}\text{Ca}$  isotopes at  $T_{\text{lab}} = 200$  MeV using the NL3 parameter set and IA2 optical potentials.

In figure 4.2, the plots of the scattering observables (scattering cross section  $\frac{d\sigma}{d\Omega}$  in millibarn per steradian, analysing power  $A_y$ , and spin rotation function  $Q$ ) for elastic proton scattering along calcium isotopic chains at  $T_{\text{lab}} = 200$  MeV using the NL3 parameter set are shown against centre of mass scattering angle  $\theta$  measured in degrees. It can be observed from the scattering cross section plots (shown in top left) that the scattering cross section increases as neutron number increases, and the positions of the diffraction minima are shifted towards smaller centre of mass scattering angles. The plots of the analysing power are shown in the top right panel. As the neutron number increases the values of the maxima and minima decrease, and the maxima and minima are shifted towards smaller scattering angles. This is also the trend in the case of the spin rotation  $Q$ .

### 4.2.1 Comparison of the RMF models

Here, we study the effect of the different forms of the Lagrangian densities on the proton-nucleus scattering observables. Calculations for elastic proton scattering from the stable  $^{48}\text{Ca}$  nucleus are included in order to compare our results with existing experimental data; this will also check the validity and reliability of our calculations.

Figure 4.3 shows scattering cross section calculations for elastic proton scattering from  $^{48,54,58,60}\text{Ca}$  nuclei (at  $T_{\text{lab}} = 200$  MeV) as functions of the centre of mass scattering angle  $\theta$  calculated using the QHD II, NL3, and FSUGold parameter sets with the IA2 relativistic optical potentials. The top left panel shows the results for  $p+^{48}\text{Ca}$ , the top right for  $p+^{54}\text{Ca}$ , bottom left for  $p+^{58}\text{Ca}$  and bottom right for  $p+^{60}\text{Ca}$ . It can be observed from the plots for  $p+^{48}\text{Ca}$  that the three RMF models give very good descriptions of the experimental data (taken from Ref. [20]). There is no conspicuous difference between the RMF models in describing scattering cross section for  $p+^{48}\text{Ca}$  elastic scattering, even at large scattering angle for this projectile energy  $T_{\text{lab}} = 200$  MeV. As expected, global Dirac phenomenology give excellent description of the data. This is because the nucleus  $^{48}\text{Ca}$  is one of the nuclei used to produce the global Dirac phenomenology fits described in Ref. [111]. In the case of proton scattering from  $^{54}\text{Ca}$  shown in top right panel of figure 4.3, the three RMF models also give similar description of the scattering cross section. There are some noticeable differences, however, at large scattering angles  $\theta$ . Our calculations are compared with the theoretical results obtained by Vorabbi in Ref. [97]. There is good agreement between our results at small scattering angles, as the two calculations give the same first minimum, while the global Dirac phenomenology potential gives a slightly higher value of the cross section at the first minimum. At large scattering angles, there is small disagreement between the two results. The plots displayed in bottom left of figure 4.3 show the scattering cross section calculations for  $p+^{58}\text{Ca}$ . The three RMF models give similar description of the elastic scattering cross section except at large scattering angles. The IA2 calculations are compared with the theoretical results obtained by Rashdan in Ref. [64]. Apart from the difference in the first minimum, the results agree well. Rashdan's calculations and global Dirac phenomenology potential give higher scattering cross sections at the first minimum than the IA2 calculations. The scattering cross section calculations for  $p+^{58}\text{Ca}$  are shown in the bottom right plots of figure 4.3. Again the three RMF models give similar description of the scattering cross section except at large scattering angles where there is minute difference in their descriptions. Here, the IA2 calculations are compared with the theoretical calculations presented in Ref. [34] by Kaki. There is a very good agreement between our results and that of Kaki, as the two results give identical values of scattering cross section at the first minimum. It should be noted that the IA2 formalism was also employed by Kaki, but with the use of different Lagrangian densities.

Figure 4.4 shows analysing power calculations for elastic proton scattering from  $^{48,54,58,60}\text{Ca}$  nuclei (at  $T_{\text{lab}} = 200$  MeV) as functions of the centre of mass scattering angle  $\theta$  calculated using the QHD II, NL3, and FSUGold parameter sets with the IA2 optical potentials. The top left panel show plots of the analysing power for  $p+^{48}\text{Ca}$ . As with the case of the scattering cross section, the three RMF models give

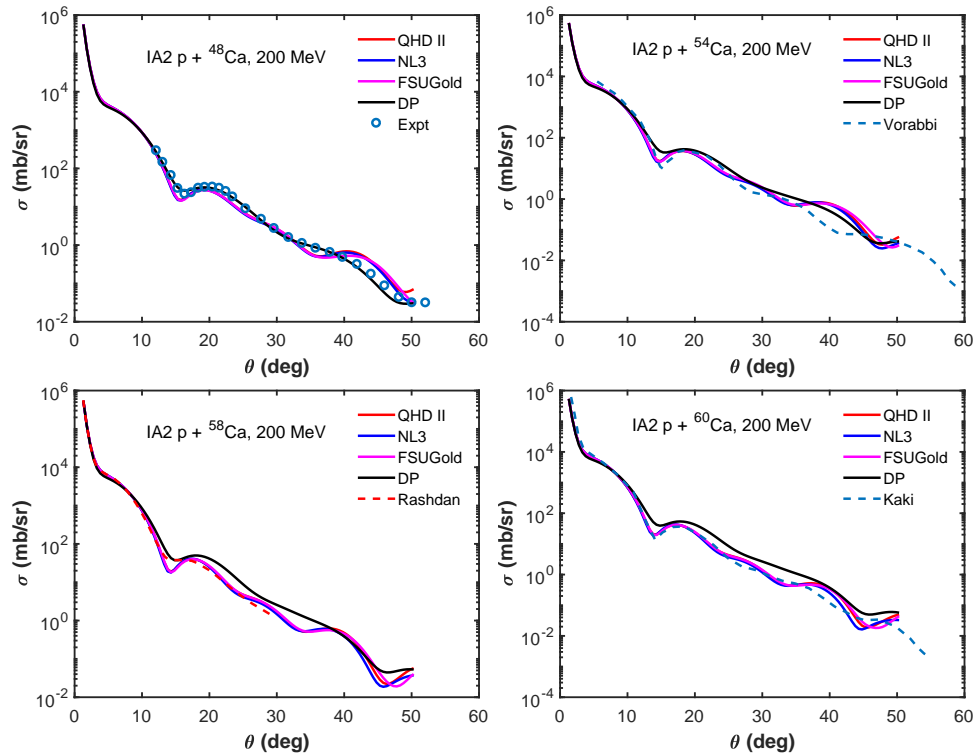


**Figure 4.3:** Scattering cross section calculations showing comparison of the different Lagrangian densities for proton scattering from  $^{48,54,58,60}\text{Ca}$  at  $T_{\text{lab}} = 200$  MeV using IA2 optical potentials.

comparable descriptions of the analysing power for  $^{48}\text{Ca}$  target, and they all give a good description of the analysing power experimental data. The IA2 calculations give a better description of the analysing power data at large scattering angles than the global Dirac phenomenology potential. The top right panel in figure 4.4 shows plots of the analysing power for  $p+^{54}\text{Ca}$ . The three RMF models give comparable descriptions of the analysing power except at large scattering angles. Unlike the scattering cross section case, there is disagreement between the IA2 calculations and the result obtained by Vorabbi in Ref. [97] at small and large scattering angles. The bottom left panel shows the results for  $p+^{58}\text{Ca}$ . There is also similar description by the RMF models, but there is disagreement with the global Dirac phenomenology calculation. The plots shown in bottom right panel are those for  $p+^{60}\text{Ca}$ . There is very good agreement between our calculations and that of Kaki. The difference between the RMF models is again noticed at large scattering angles.

The results for the spin rotation  $Q$  for elastic proton scattering from  $^{48,54,58,60}\text{Ca}$  using the IA2 optical potentials and the three RMF models are shown in figure 4.5 for  $T_{\text{lab}} = 200$  MeV. The top left panel shows the plots for  $^{48}\text{Ca}$  nucleus. The three RMF models give good description of the the analysing power data except at small scattering angle  $\theta \lesssim 13^\circ$ , where the IA2 potentials underestimate the data. The global Dirac phenomenology, however, give good description of the data at small scattering angle, and poor description at large scattering angle. The top right panel in the same figure shows plots for  $^{54}\text{Ca}$  nucleus. There is disagreement between the

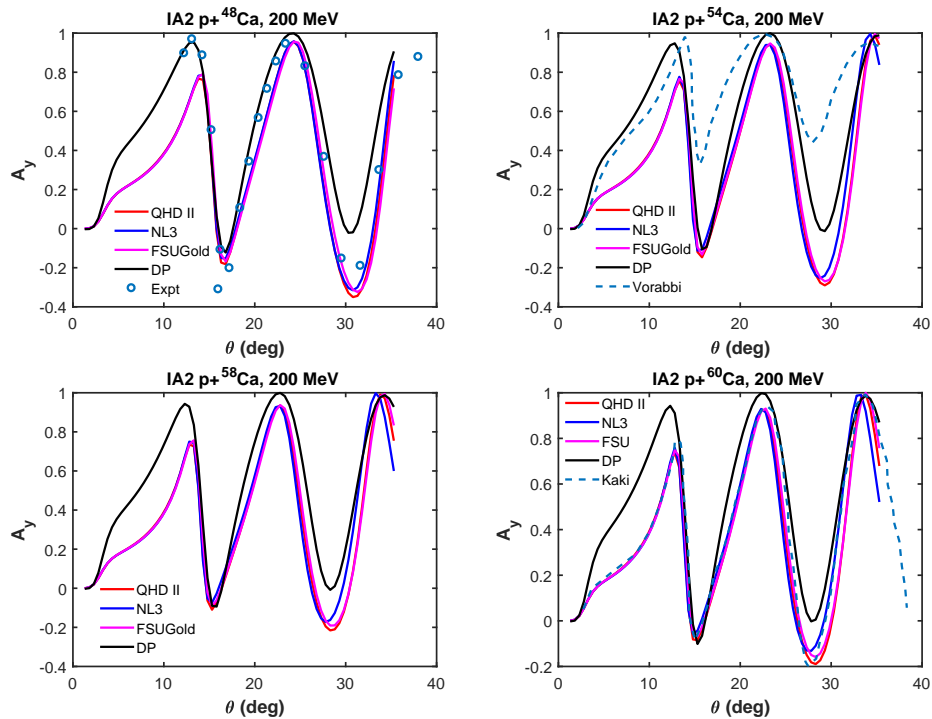


**Figure 4.4:** analysing power calculations showing comparison of the different Lagrangian densities for proton scattering from <sup>48,54,58,60</sup>Ca at  $T_{\text{lab}} = 200$  MeV.

global phenomenology potential, Vorabbi theoretical results, and our calculations. The global phenomenology potential gives higher values at small and large scattering angles compared to our own calculations. The small difference between the RMF models in describing the analysing power is noticed at large scattering angle. The bottom left panel shows the analysing power result for <sup>58</sup>Ca. Again, the difference between the RMF models is noticed at large scattering angles, and the global Dirac phenomenology potential gives higher values of the analysing power compared with the RMF models with IA2 potentials. Similar trends can be observed with the <sup>60</sup>Ca nucleus shown in bottom right panel of the same figure. There is good agreement between our calculations and that of Kaki.

The scattering cross section results are shown in figure 4.6 for <sup>48,54,58,60</sup>Ca targets using the IA2 optical potentials and the three RMF models at  $T_{\text{lab}} = 500$  MeV. There is good agreement between the three RMF models and the global Dirac phenomenology potential for <sup>48</sup>Ca shown in top left panel of the figure and <sup>54</sup>Ca shown in top left panel. The small difference can be seen at large scattering angles. The bottom panels show the results for <sup>58,60</sup>Ca targets. The global Dirac phenomenology potential gives higher values of the scattering cross section than the RMF models. Our calculations and that of Kaki are in very good agreement as shown in the bottom right panel for <sup>60</sup>Ca target.

Figures 4.7 and 4.8 show, respectively, the analysing power and spin rotation results for <sup>48,54,58,60</sup>Ca targets using the IA2 optical potentials and the three RMF models for  $T_{\text{lab}} = 500$  MeV. It can be observed from the two Figures that there is

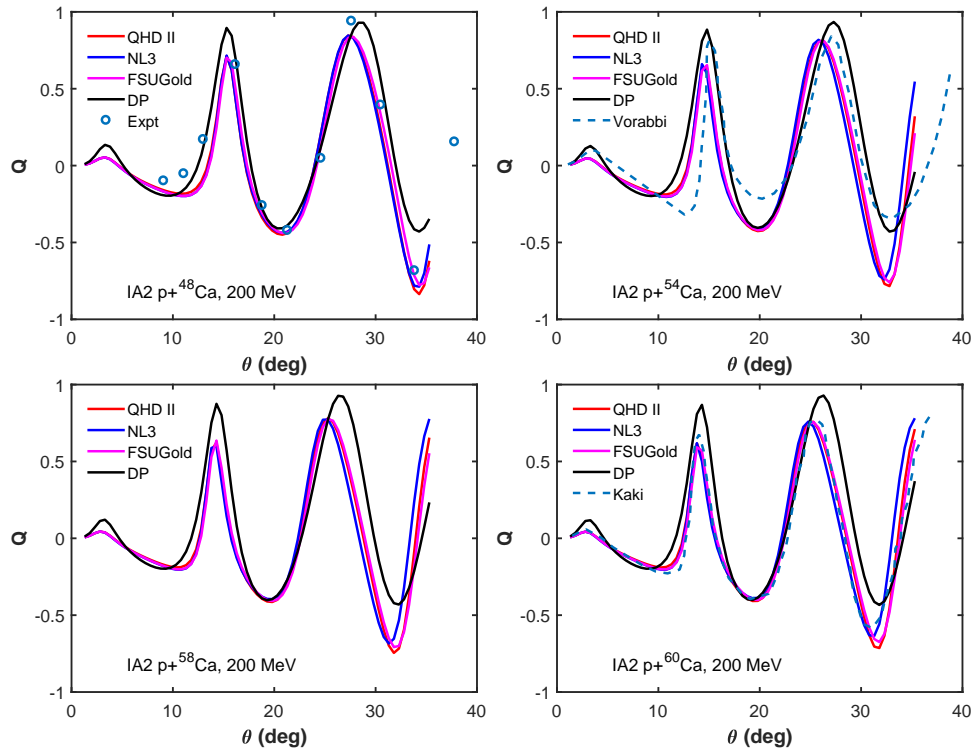


**Figure 4.5:** Spin rotation parameter calculations showing comparison of the different Lagrangian densities for proton scattering from  $^{48,54,58,60}\text{Ca}$  at  $T_{\text{lab}} = 200 \text{ MeV}$ .

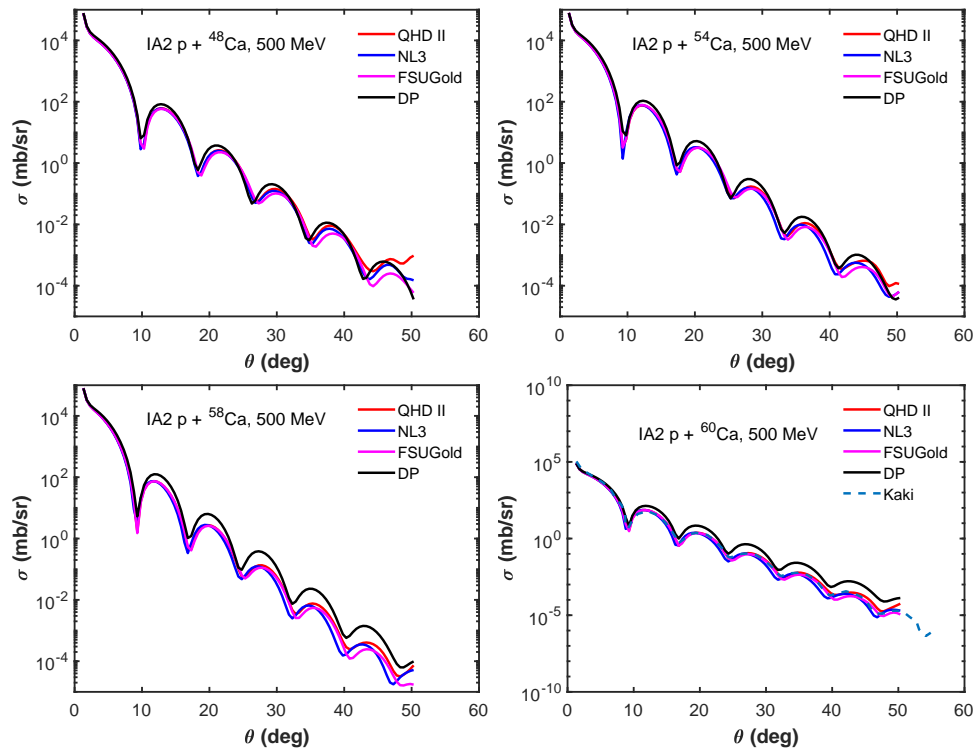


**Figure 4.6:** Scattering cross section calculations showing comparison of the RMF models for  $^{48,54,58,60}\text{Ca}$  at  $T_{\text{lab}} = 500 \text{ MeV}$ .

poor agreement between the RMF models and global Dirac phenomenology potential. The RMF models give comparable descriptions the spin observables except at large scattering angles where the difference between the RMF models becomes conspicuous. There is also good agreement between our calculations and that of Kaki, except at large scattering angles.

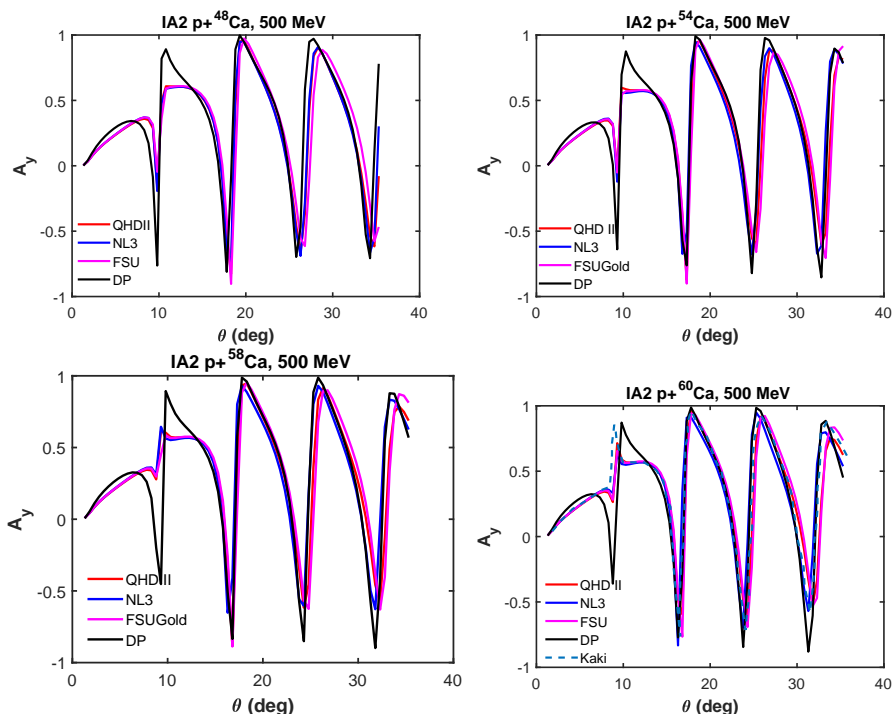


**Figure 4.7:** analysing power calculations showing comparison of the RMF models for  $^{48,54,58,60}\text{Ca}$  at  $T_{\text{lab}} = 500 \text{ MeV}$ .

The scattering observables for elastic proton scattering from  $^{48,54,58,60}\text{Ca}$  targets at  $T_{\text{lab}} = 800 \text{ MeV}$  are shown in Figures 4.9, 4.10, and 4.11 for scattering cross section, analysing power, and spin rotation function, respectively. One can observe that there is agreement between our calculations and experimental data (where available). The difference between the RMF models are seen at large scattering angles. The Dirac phenomenology potential gives higher values of the scattering observables than the IA2 especially for  $^{54,58,60}\text{Ca}$  targets. There is no experimental data for elastic proton scattering from  $^{54,58,60}\text{Ca}$  targets, however, for comparison.

#### 4.2.2 IA1 versus IA2

In this sub-section, the results of the scattering cross section and spin observables obtained using the IA1, IA2, and global Dirac phenomenology will be presented and compared. The calculations have been carried out using the NL3 parameter set in the case of IA1 and IA2.

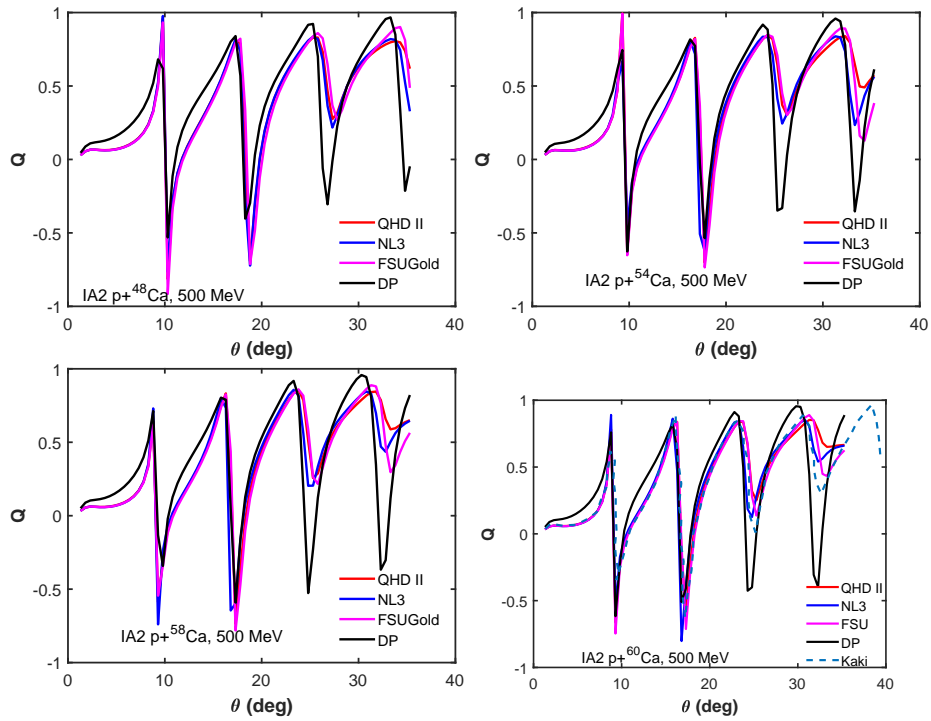


**Figure 4.8:** Spin rotation parameter calculations showing comparison of the RMF models for  $^{48,54,58,60}\text{Ca}$  at  $T_{\text{lab}} = 500 \text{ MeV}$ .

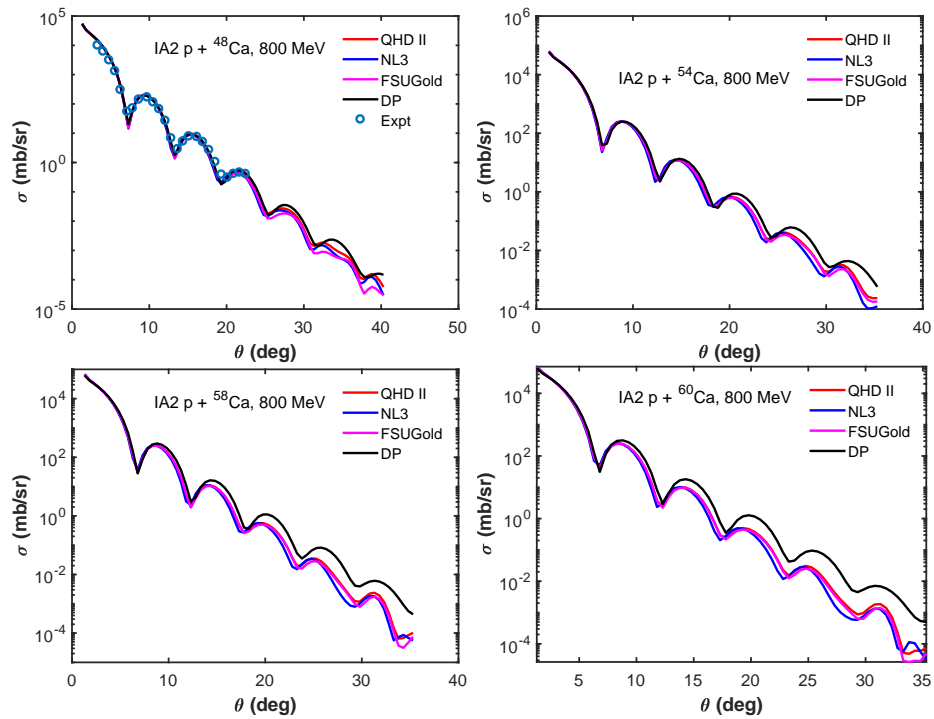


**Figure 4.9:** Scattering cross section calculations showing comparison of the RMF models for  $^{48,54,58,60}\text{Ca}$  at  $T_{\text{lab}} = 800 \text{ MeV}$ .

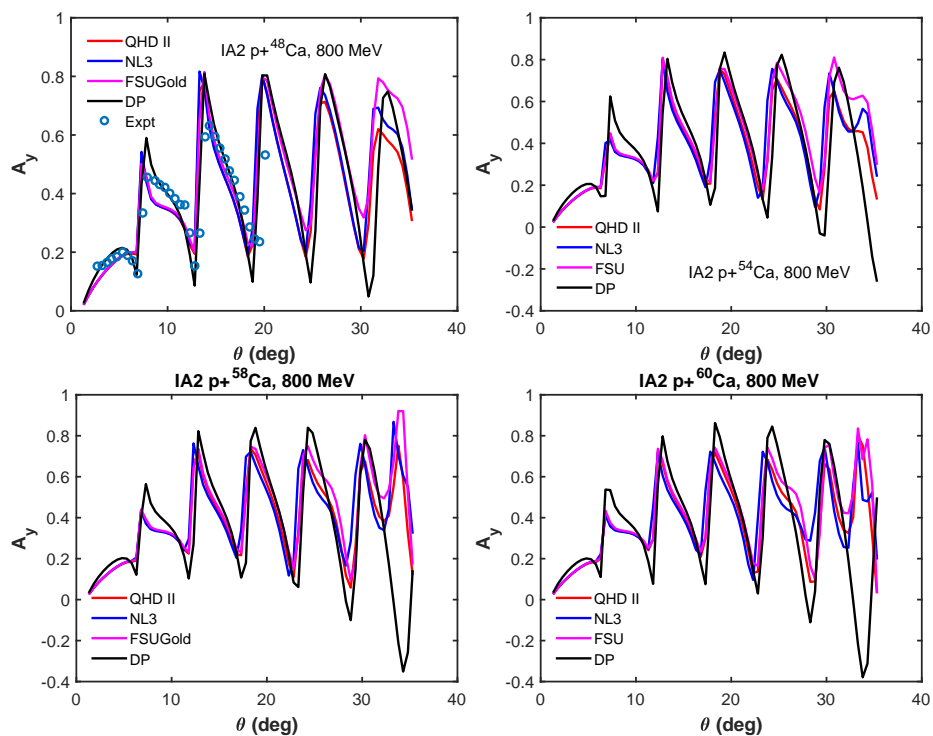


**Figure 4.10:** Analysing power calculations showing comparison of the RMF models for  $^{48,54,58,60}\text{Ca}$  at  $T_{lab} = 800$  MeV.

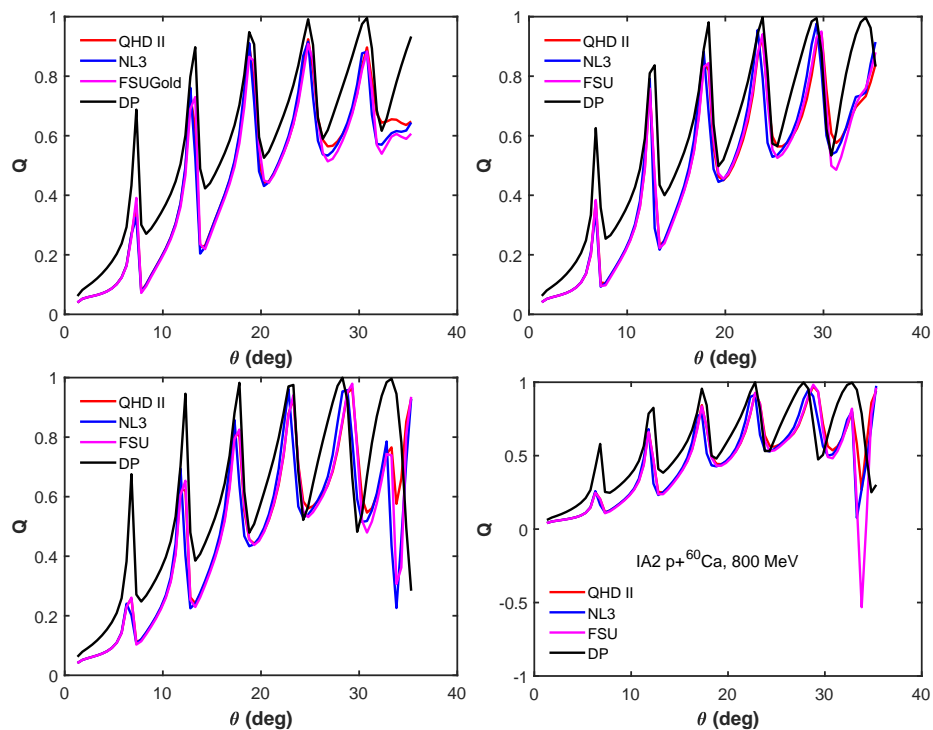


**Figure 4.11:** Spin rotation parameter calculations showing comparison of the RMF models for  $^{48,54,58,60}\text{Ca}$  at  $T_{lab} = 800$  MeV.

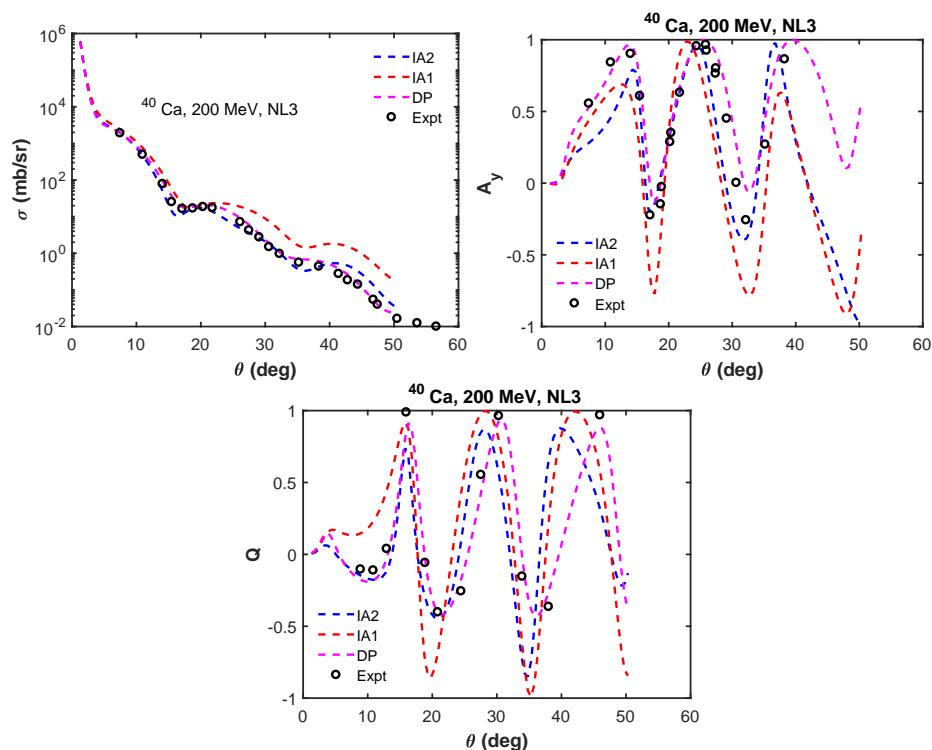


**Figure 4.12:** Comparison of the IA1, IA2, and global Dirac phenomenology scattering observables for  $^{40}\text{Ca}$  target at  $T_{\text{lab}} = 200 \text{ MeV}$ .

Figure 4.12 shows the plots of the scattering cross section, analysing power and spin rotation parameter against centre of mass scattering angle  $\theta$  for elastic proton scattering from  $^{40}\text{Ca}$  at  $T_{\text{lab}} = 200 \text{ MeV}$  using the NL3 parameter set. The figure shows comparison of the IA1, IA2, and Dirac phenomenology with experimental data. The top left panel shows the plots for the scattering cross section, the top right panel for analysing power, and the bottom panel for spin rotation function. The same scattering observables are shown in figure 4.13 for  $T_{\text{lab}} = 500 \text{ MeV}$ , and figure 4.14 for  $T_{\text{lab}} = 800 \text{ MeV}$ . One can observe that at  $T_{\text{lab}} = 500 \text{ MeV}$ , there is competition between IA1, IA2 and Dirac phenomenology in describing the experimental data for the three scattering observables. The difference between the three formalisms is noticed at large scattering angles. At  $T_{\text{lab}} = 800 \text{ MeV}$ , there is competition between these formalisms in describing the scattering cross section data. The IA1 and Dirac phenomenology, however, give better descriptions of the analysing power and spin rotation data. The IA2 formalism underestimates the spin rotation parameter data at this incident projectile laboratory energy. At  $T_{\text{lab}} = 200 \text{ MeV}$ , the IA2 formalism gives a very good description of the scattering observables especially scattering cross section and spin rotation parameter. The IA1 formalism overestimates the scattering cross section, and failed to give correct descriptions of the minima and maxima in the case of the analysing power and spin rotation parameter. This follows from the overly large scalar and vector optical potentials given by the IA1 formalism at this incident projectile laboratory energy. One should note that the IA2 formalism also did not properly describe the analysing power at low scattering angle  $\theta \lesssim 13^\circ$ , but

give proper description at  $\theta \gtrsim 13^\circ$ .

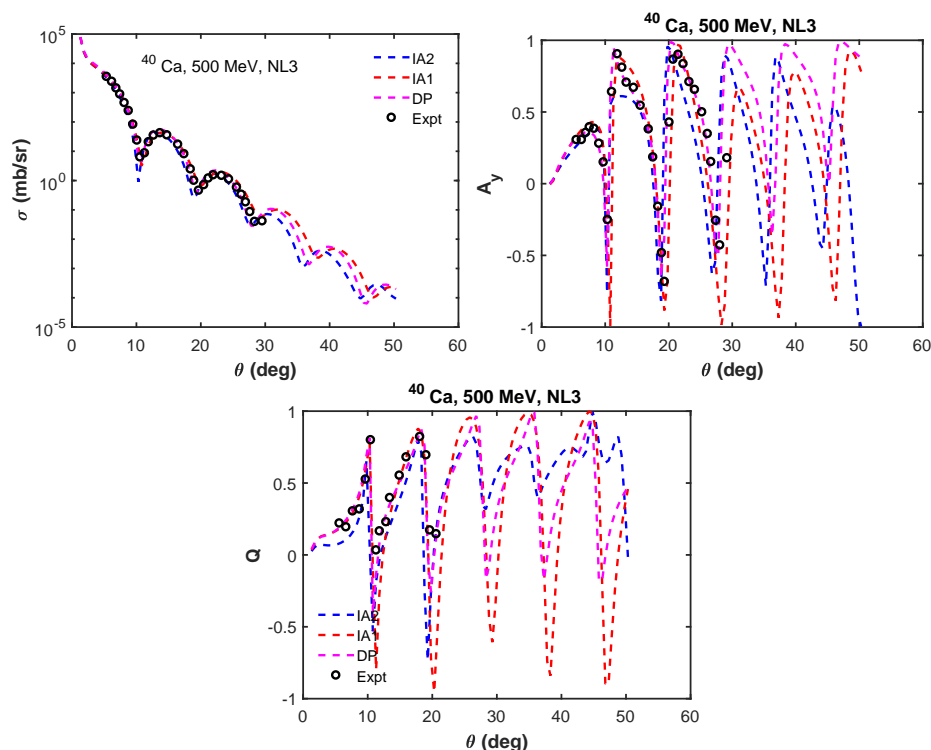


**Figure 4.13:** Comparison of the IA1, IA2, and global Dirac phenomenology scattering observables for  $^{40}\text{Ca}$  target at  $T_{\text{lab}} = 500 \text{ MeV}$ .

In Figures 4.15, 4.16, and 4.17, the plots of the elastic scattering observables are plotted against centre of mass scattering angle for  $p+^{48}\text{Ca}$  at  $T_{\text{lab}} = 200 \text{ MeV}$ ,  $500 \text{ MeV}$ , and  $800 \text{ MeV}$ , respectively. It can be observed that at  $T_{\text{lab}} = 200 \text{ MeV}$ , the IA2 formalism and Dirac phenomenology give very good descriptions of the three scattering observables. The IA1 formalism, apart from giving the correct first minimum, overestimates the scattering cross section data, and did not accurately predict the minima and maxima in analysing power and spin rotation parameter data. The three formalisms give similar descriptions of the scattering observables at  $T_{\text{lab}} = 500 \text{ MeV}$ , but at large scattering angles, one begin to notice the difference between the three formalisms. At  $T_{\text{lab}} = 800 \text{ MeV}$ , the three formalisms give very good descriptions of the scattering cross section and analysing power experimental data. There is no experimental data to compare the results produced for the spin rotation parameter, but the IA2 formalism gives lower values at small scattering angle, and larger values at large scattering angles when compared with the IA1 formalism.

The plots of the elastic proton scattering observables against centre of mass scattering angle for the unstable  $^{54}\text{Ca}$  target at  $T_{\text{lab}} = 200 \text{ MeV}$  and  $500 \text{ MeV}$  are shown in Figures 4.18 and 4.19, respectively. There is no experimental data to compare, so (where available) comparisons are made with other theoretical calculations. From figure 4.18, one observes that apart from the first minimum, the IA1 formalism gives

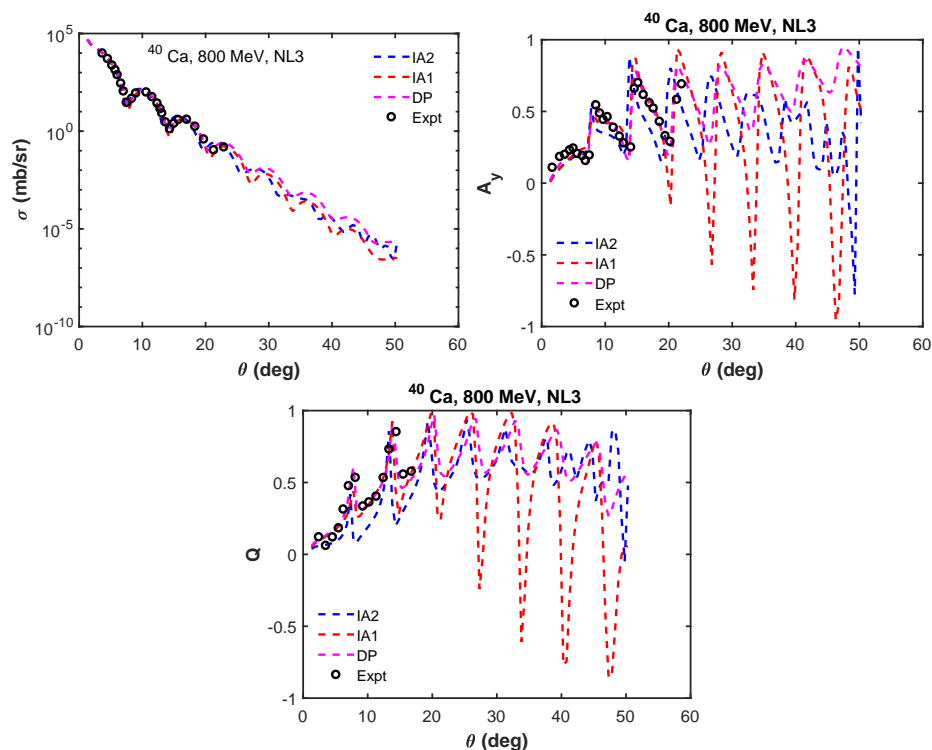


**Figure 4.14:** Comparison of the IA1, IA2, and global Dirac phenomenology scattering observables for  $^{40}\text{Ca}$  target at  $T_{\text{lab}} = 800 \text{ MeV}$ .

larger values of the scattering cross section compared with the other results; this is the trend also for the stable  $^{40,48}$  targets at this incident energy. There is no good agreement between our calculations and the theoretical results obtained by Vorabbi in Ref. [97] in the case of the analysing power and spin rotation parameter. Until there is experimental data to compare, we may not know which is the better calculation. At  $T_{\text{lab}} = 500 \text{ MeV}$ , except at large scattering angles, there is comparable predictions of the three scattering observables by the three formalisms. The IA1 gives deeper minima of analysing power and spin rotation compared to the IA2 formalism at large scattering angle.

Figures 4.20 and 4.21 show the plots of the elastic proton scattering observables against centre of mass scattering angle for the unstable  $^{58}\text{Ca}$  target at  $T_{\text{lab}} = 200 \text{ MeV}$  and  $500 \text{ MeV}$ , respectively. At  $T_{\text{lab}} = 200 \text{ MeV}$ , the IA2 calculation is in good agreement with the calculation of Rashdan in Ref. [64]. As expected, the IA1 calculation gives larger values after the first dip, compared with the IA2 and Dirac phenomenology calculations. Unlike the case of stable nuclei, there is no good agreement between the IA1 and IA2 descriptions of the scattering observables at  $T_{\text{lab}} = 500 \text{ MeV}$ . Apart from the minimum at  $\theta \approx 10^\circ$ , the IA1 gives deeper minima of analysing power and spin rotation and larger scattering cross section compared to the IA2 formalism.

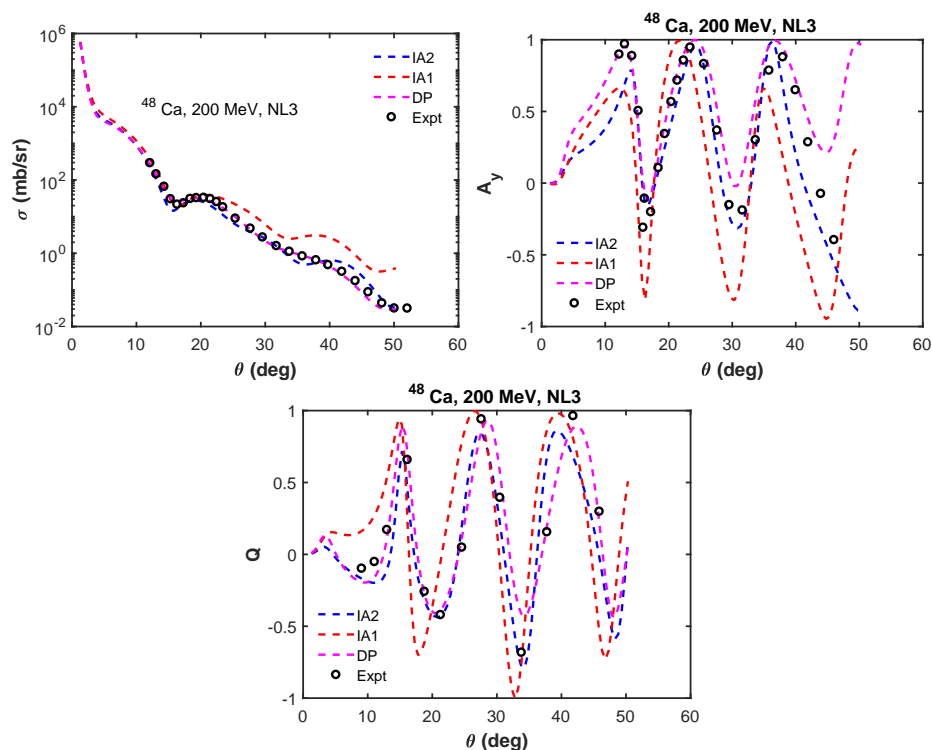


**Figure 4.15:** Comparison of the IA1, IA2, and global Dirac phenomenology scattering observables for  $^{48}\text{Ca}$  target at  $T_{\text{lab}} = 200 \text{ MeV}$ .

### 4.2.3 Effect of full folding versus optimally factorised optical potential on scattering observables

The results of the scattering observables calculated using optimally factorised optical potentials and full folding optical potentials will be presented and compared here; this will show the effect of medium contributions on the scattering observables.

Figures 4.22–4.27 show the scattering cross section, analysing power and spin rotation function for elastic proton scattering from  $^{48,54,58}\text{Ca}$  targets at  $T_{\text{lab}} = 200 \text{ MeV}$  and  $500 \text{ MeV}$ . The calculations obtained using optimally factorised optical potentials are compared with the calculations that incorporate medium effects. In figure 4.22, the scattering observables are shown against scattering angle for  $^{48}\text{Ca}$  at  $T_{\text{lab}} = 200 \text{ MeV}$ . There is not much effect of including medium modifications on the cross section at this incident energy. There is conspicuous effect, however, on the analysing power; the analysing power data at the first maximum is better reproduced. The use of optimally factorised optical potential could not correctly reproduce the first maximum of the analysing power data, as it underestimates it. Medium effect is also seen on the spin rotation function at large scattering angles and first minimum.

In all the three  $^{48,54,58}\text{Ca}$  targets, there is no noticeable contribution of medium effect on the scattering observables at  $T_{\text{lab}} = 500 \text{ MeV}$ . This is observed from Figures 4.23, 4.25, and 4.27. Figures 4.24 and 4.26 show the case for  $^{54,58}\text{Ca}$  at  $T_{\text{lab}} = 200 \text{ MeV}$ . One can observe that there is no contribution of medium effect to the

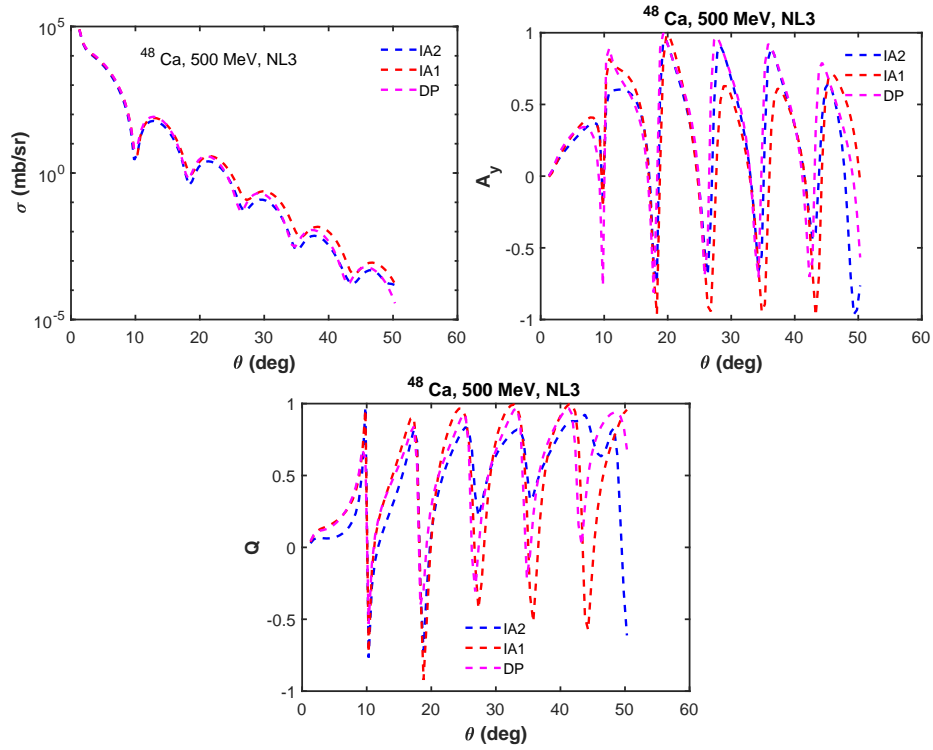


**Figure 4.16:** Comparison of the IA1, IA2, and global Dirac phenomenology scattering observables for  $^{48}\text{Ca}$  target at  $T_{\text{lab}} = 500 \text{ MeV}$ .

scattering cross sections for both nuclei. The contributions are seen in the analysing power and spin rotation function. Medium modification increases the value of the first analysing power maximum and increases the depth of the third minimum. For spin rotation function, medium effect increases the value of the first minimum and maximum, and reduces the depth of the third minimum. In summary, medium effect has contributions at  $T_{\text{lab}} = 200 \text{ MeV}$  and not at  $T_{\text{lab}} = 500 \text{ MeV}$  for the stable and unstable nuclei discussed here.

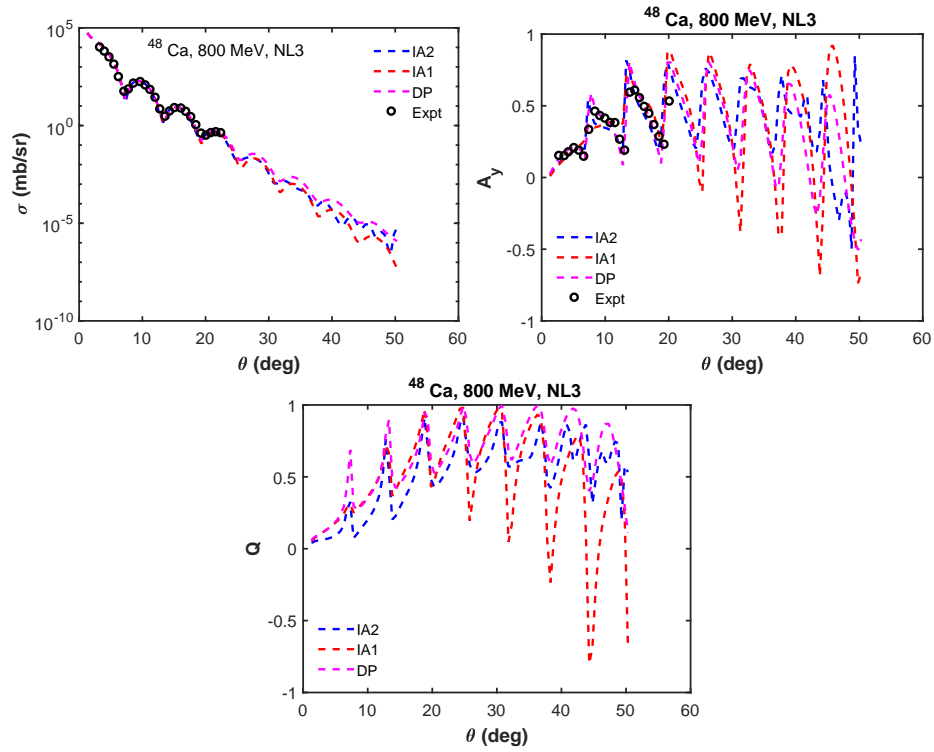


**Figure 4.17:** Comparison of the IA1, IA2, and global Dirac phenomenology scattering observables for  $^{48}\text{Ca}$  target at  $T_{\text{lab}} = 800 \text{ MeV}$ .

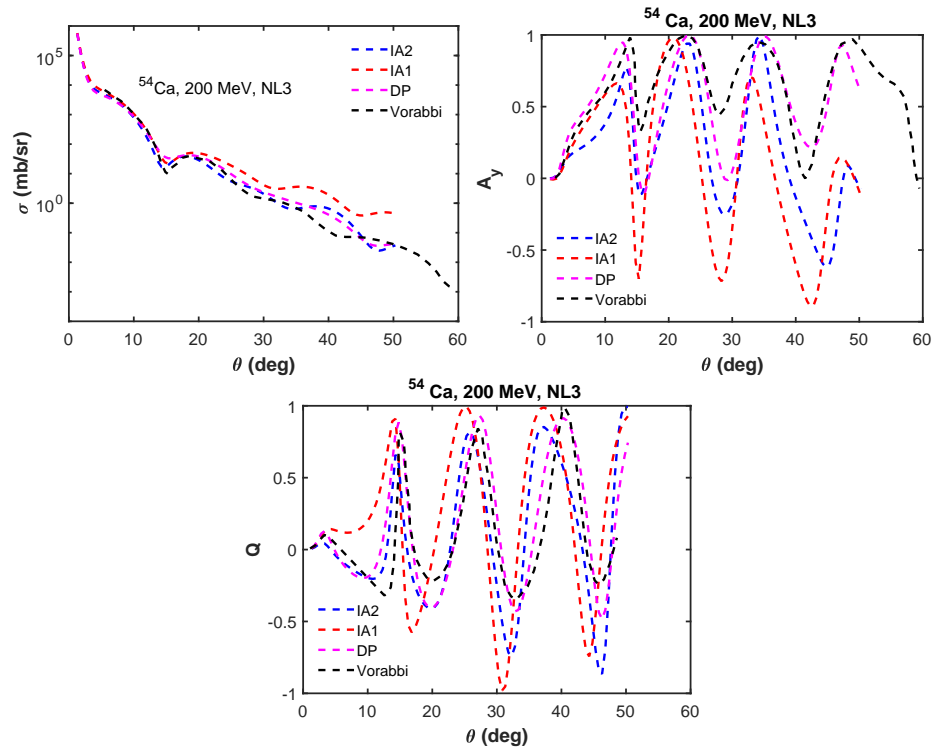


**Figure 4.18:** Comparison of the IA1, IA2, and global Dirac phenomenology scattering observables for  $^{54}\text{Ca}$  target at  $T_{\text{lab}} = 200 \text{ MeV}$ .

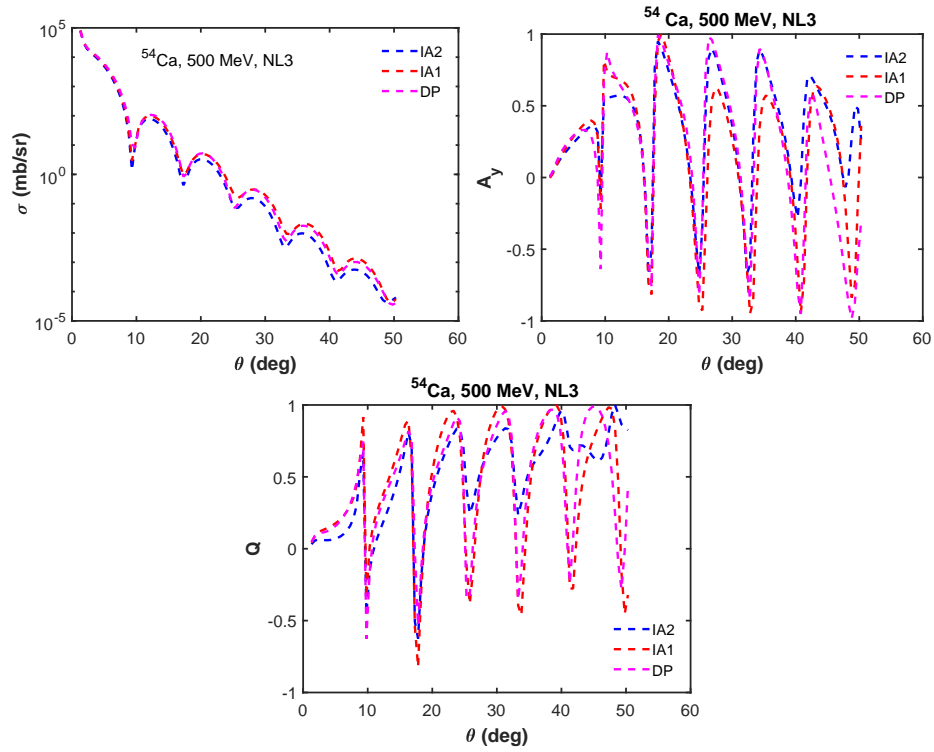


**Figure 4.19:** Comparison of the IA1, IA2, and global Dirac phenomenology scattering observables for  $^{54}\text{Ca}$  target at  $T_{\text{lab}} = 500 \text{ MeV}$ .

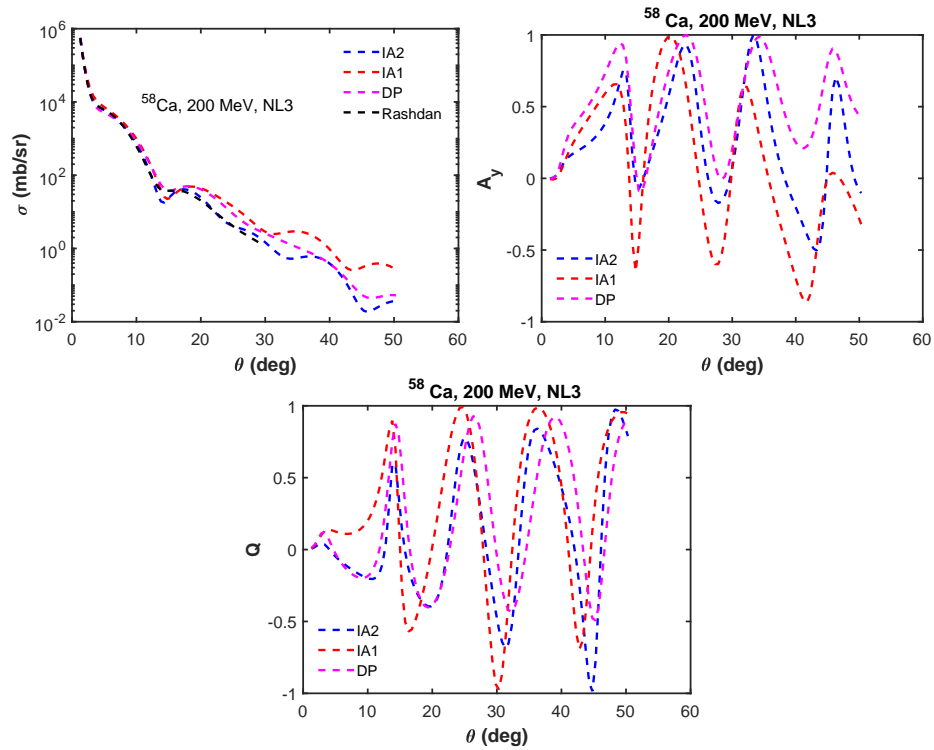


**Figure 4.20:** Comparison of the IA1, IA2, and global Dirac phenomenology scattering observables for  $^{58}\text{Ca}$  target at  $T_{\text{lab}} = 200 \text{ MeV}$ .

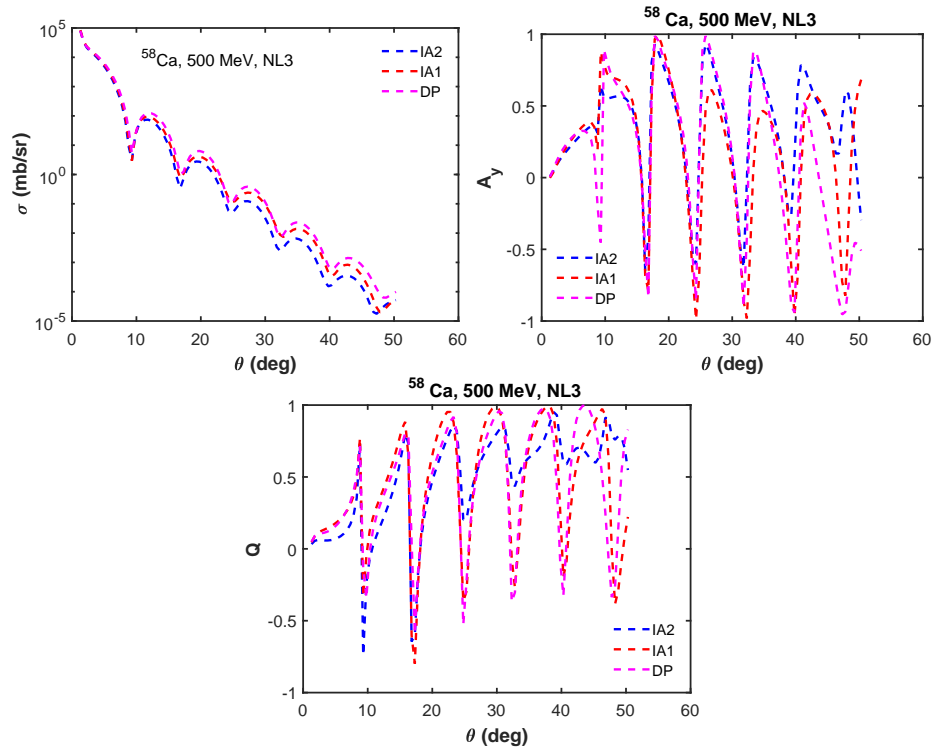


**Figure 4.21:** Comparison of the IA1, IA2, and global Dirac phenomenology scattering observables for  $^{58}\text{Ca}$  target at  $T_{\text{lab}} = 500 \text{ MeV}$ .

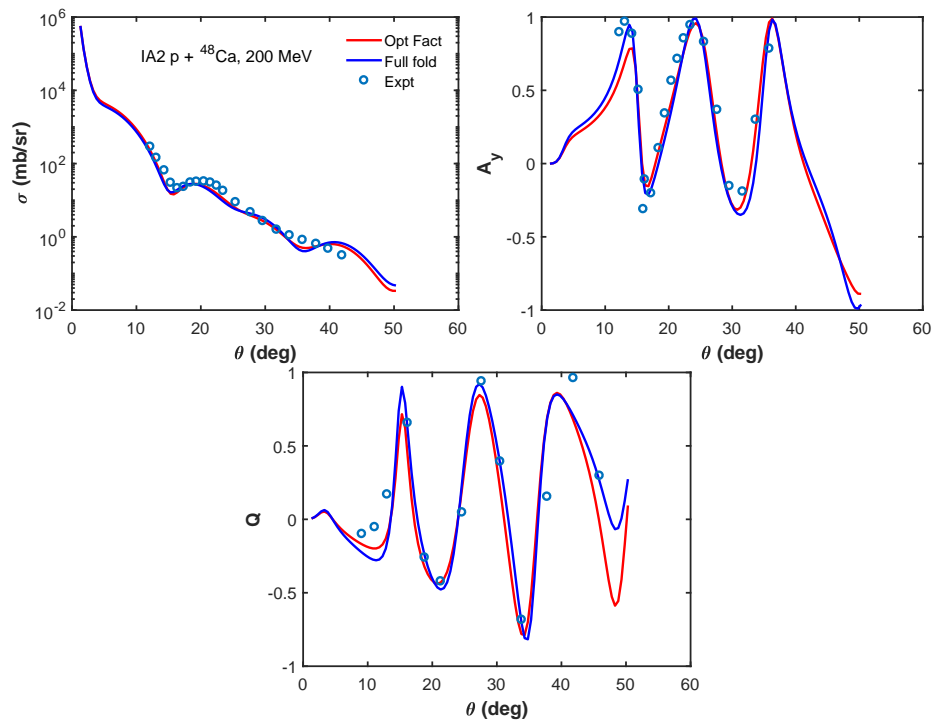


**Figure 4.22:** Effect of full folding versus optimally factorised optical potential on scattering observables for proton scattering from  $^{48}\text{Ca}$  target at  $T_{\text{lab}} = 200 \text{ MeV}$ .

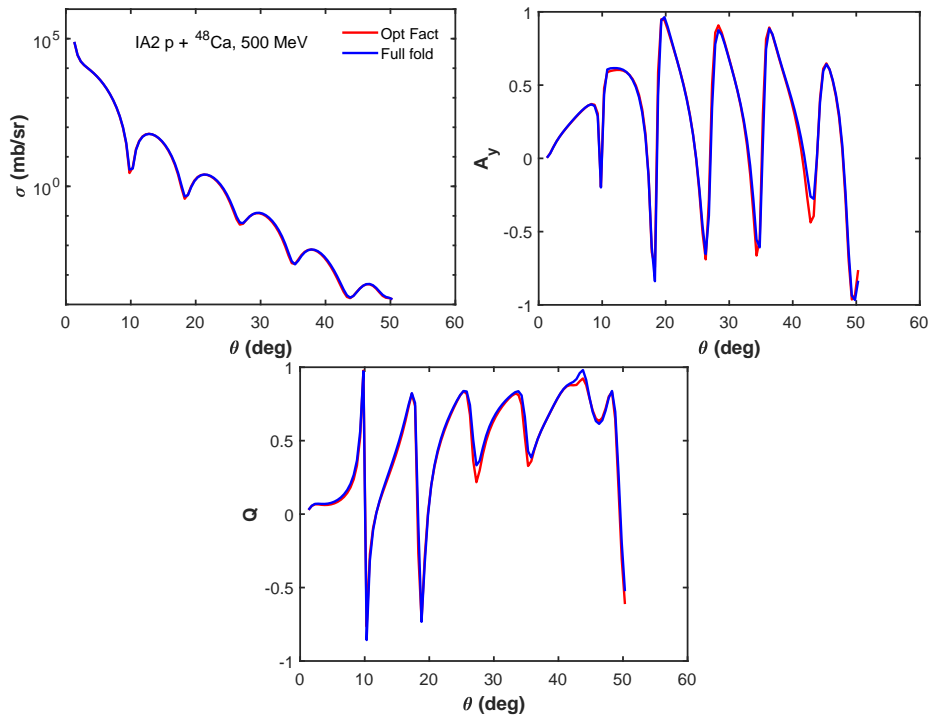


**Figure 4.23:** Effect of full folding versus optimally factorised optical potential on scattering observables for proton scattering from  $^{48}\text{Ca}$  target at  $T_{\text{lab}} = 500$  MeV.

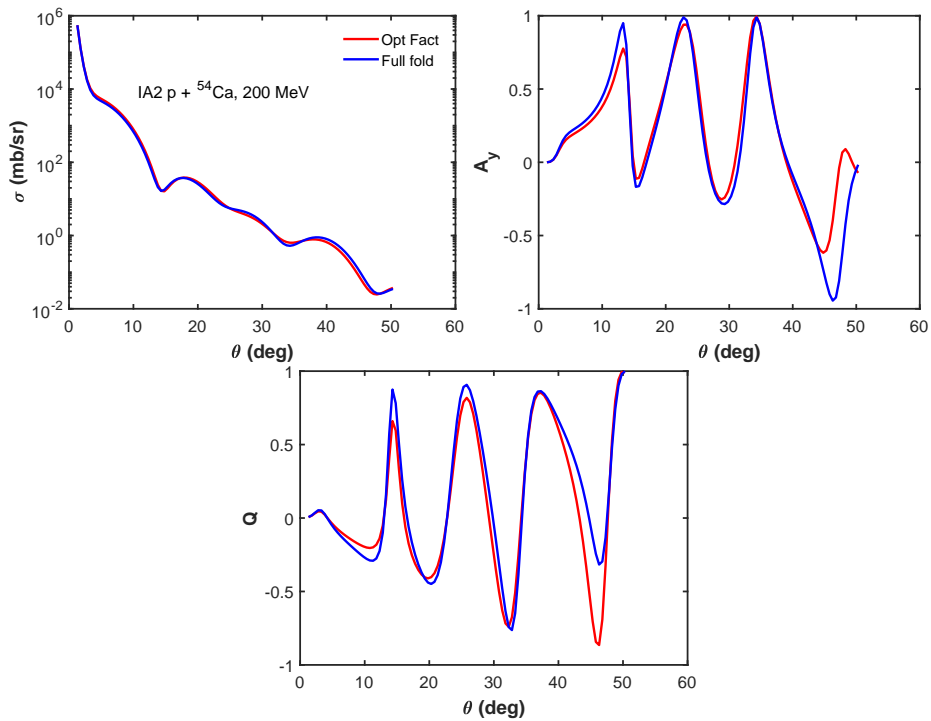


**Figure 4.24:** Effect of full folding versus optimally factorised optical potential on scattering observables for proton scattering from  $^{54}\text{Ca}$  target at  $T_{\text{lab}} = 200$  MeV.

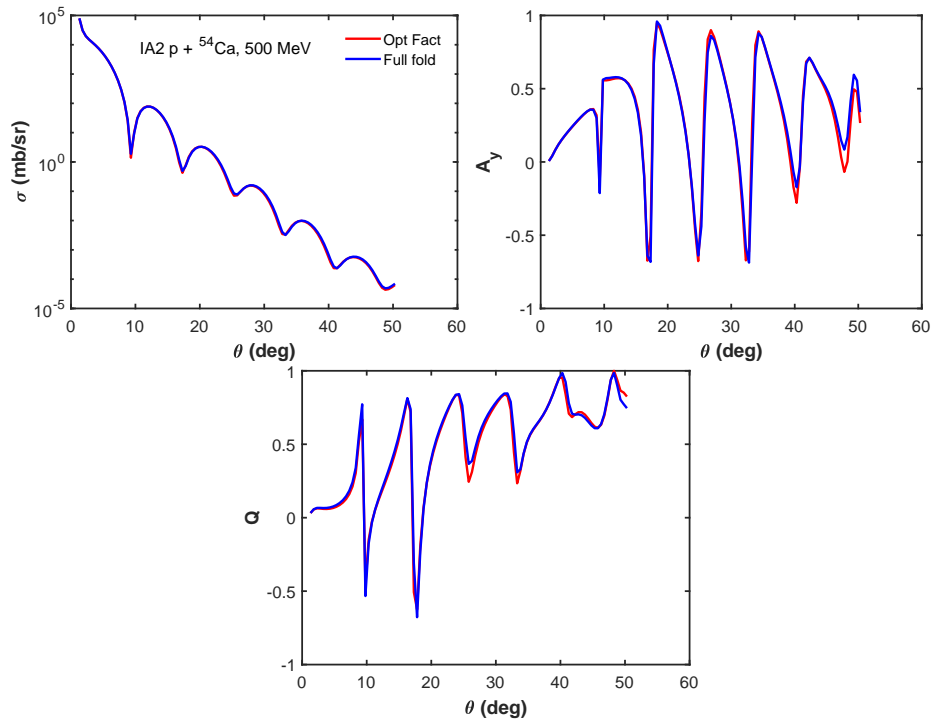


**Figure 4.25:** Effect of full folding versus optimally factorised optical potential on scattering observables for proton scattering from  $^{54}\text{Ca}$  target at  $T_{\text{lab}} = 500$  MeV.

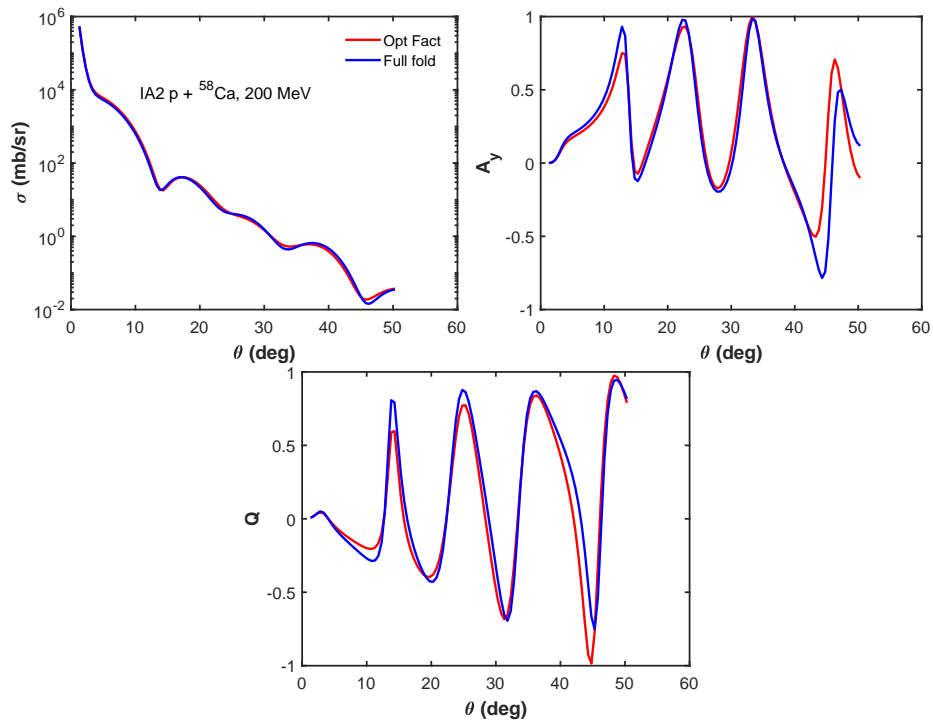


**Figure 4.26:** Effect of full folding versus optimally factorised optical potential on scattering observables for proton scattering from  $^{58}\text{Ca}$  target at  $T_{\text{lab}} = 200$  MeV.

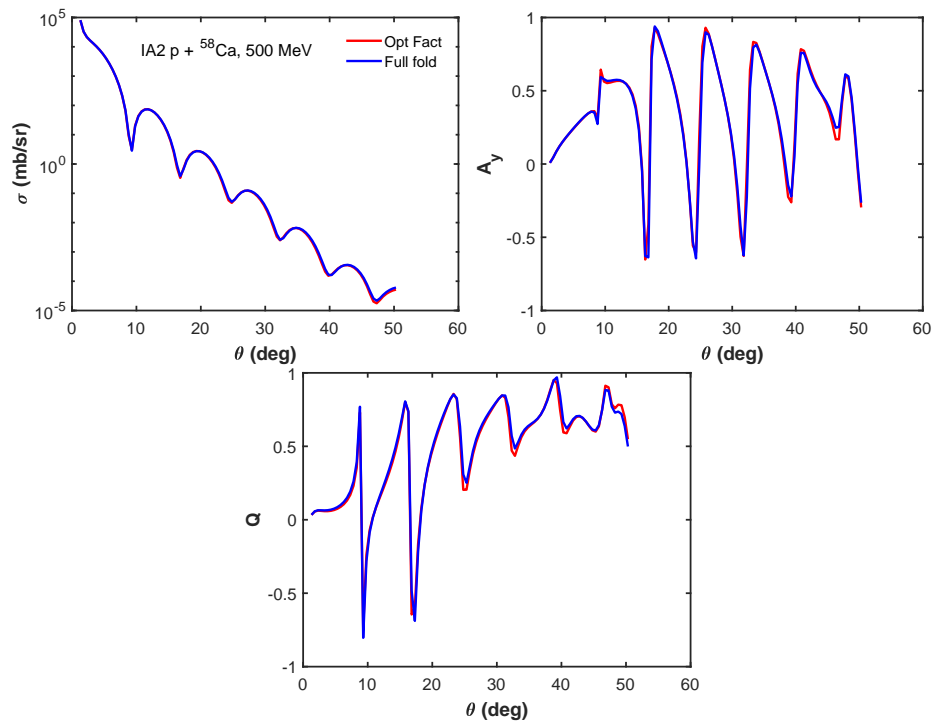


**Figure 4.27:** Effect of full folding versus optimally factorised optical potential on scattering observables for proton scattering from  $^{58}\text{Ca}$  target at  $T_{\text{lab}} = 500 \text{ MeV}$ .

## Chapter 5

# Dirac Equation in Momentum Space

In this chapter, we present the solution of the momentum space Dirac equation using non-local optical potentials. This is to enable us check the validity of using localised optical potentials to calculate elastic scattering observables at intermediate energies. The momentum space Dirac equation is transformed to two coupled Lippmann-Schwinger-like equations in momentum space. The momentum-space integral equation approach to solving scattering problem deals directly with the scattering amplitudes, whose values can be measured experimentally [121]. This method also incorporates the required boundary conditions in scattering problems. The two integral equations are numerically solved to calculate the elastic scattering observables. The results obtained are then compared with those calculated using localised optical potentials presented in Chapter 4.

The stationary-state Dirac equation for the scattering of a particle of mass  $m$  from an external central field  $U$  can be written as

$$(\not{p} - m) |\Psi\rangle = U |\Psi\rangle,$$

$$[E\gamma^0 - \mathbf{k}' \cdot \boldsymbol{\gamma} - m] \Psi(\mathbf{k}') = \int \frac{d^3k}{(2\pi)^3} \hat{U}(\mathbf{k}', \mathbf{k}) \Psi(\mathbf{k}) = 0, \quad (5.0.1)$$

where  $E$  is the on-shell energy calculated in the proton-nucleus centre of mass frame,  $m$  is mass of the projectile, and  $\hat{U}(\mathbf{k}', \mathbf{k})$  is the optical potential. In the static approximation, only three-momentum can be transferred; energy is fixed. The positive energy free state with momentum  $\mathbf{k}$  and rest frame spin projection  $\lambda$  satisfies

$$(\not{p} - m) |\mathbf{k}, \lambda(+)\rangle = 0, \quad (5.0.2)$$

where

$$|\mathbf{k}, \lambda(+)\rangle = u_{\lambda}^{\pm}(\mathbf{k}) |\mathbf{k}\rangle, \quad (5.0.3)$$

and the Dirac spinors (+ superscript for positive energy state and – superscript for negative energy state):

$$u_{\lambda}^{\pm}(\mathbf{k}) = N_k \left( \frac{1}{\frac{\boldsymbol{\sigma} \cdot \mathbf{k}}{E(\mathbf{k}+m)}} \right) \chi_{\lambda}, \quad (\text{positive energy}) \quad (5.0.4)$$

$$u_{\lambda}^{-}(\mathbf{k}) = N_k \begin{pmatrix} \frac{-\boldsymbol{\sigma} \cdot \mathbf{k}}{E(\mathbf{k}+m)} \\ 1 \end{pmatrix} \chi_{\lambda}, \quad (\text{negative energy}) \quad (5.0.5)$$

where 1 is the  $2 \times 2$  identity matrix,  $\boldsymbol{\sigma}$  is the  $2 \times 2$  Pauli matrix, and the normalization factor

$$N_k = \left[ \frac{E(\mathbf{k}) + m}{2E(\mathbf{k})} \right]^{\frac{1}{2}}, \quad E(\mathbf{k}) = (k^2 + m^2)^{\frac{1}{2}}. \quad (5.0.6)$$

Two-component Pauli spinors  $\chi_{\lambda}$  are helicity eigenstates, i.e.,

$$\boldsymbol{\sigma} \cdot \mathbf{k} \chi_{\lambda} = 2 \lambda k \chi_{\lambda}, \quad (5.0.7)$$

where helicity  $\lambda$  has values  $\pm \frac{1}{2}$ ,  $\chi_{+\frac{1}{2}}$  denotes spin up, and  $\chi_{-\frac{1}{2}}$  denotes spin down.

This enables equations (5.0.4) and (5.0.5) to be written as:

$$u_{\lambda}^{+}(\mathbf{k}) = N_k \begin{pmatrix} 1 \\ \frac{2\lambda k}{E(\mathbf{k})+m} \end{pmatrix} \chi_{\lambda}, \quad (5.0.8)$$

and

$$u_{\lambda}^{-}(\mathbf{k}) = N_k \begin{pmatrix} \frac{-2\lambda k}{E(\mathbf{k})+m} \\ 1 \end{pmatrix} \chi_{\lambda}, \quad (5.0.9)$$

The states used here are labelled with the component of the spin along the projectile direction, which may be called helicity  $\lambda$ . Helicity is the component, in the direction of motion, of the particle total angular momentum. It is invariant under rotations which makes it possible to construct states of definite angular momentum  $j$ , where all involved particles have definite helicities [122]. Along the z-direction, Pauli spinors are given as

$$\chi_{+\frac{1}{2}} = \begin{pmatrix} 1 \\ 0 \end{pmatrix}, \quad \chi_{-\frac{1}{2}} = \begin{pmatrix} 0 \\ 1 \end{pmatrix} \quad (5.0.10)$$

and along the direction  $(\theta, \phi)$ , they are given by [123]

$$\chi_{+\frac{1}{2}}(\theta, \phi) = \begin{pmatrix} \cos \frac{\theta}{2} \\ e^{i\phi} \sin \frac{\theta}{2} \end{pmatrix}, \quad \chi_{-\frac{1}{2}}(\theta, \phi) = \begin{pmatrix} -e^{-i\phi} \sin \frac{\theta}{2} \\ \cos \frac{\theta}{2} \end{pmatrix} \quad (5.0.11)$$

The free states positive energy and negative energy relate, respectively, to the particle and antiparticle degrees of freedom. These basis states have the orthonormality relations [124]

$$\langle \mathbf{k}', \lambda'(\pm) | \mathbf{k}, \lambda(\pm) \rangle = \delta_{\lambda' \lambda} \delta(\mathbf{k}' - \mathbf{k}), \quad \langle \mathbf{k}', \lambda'(\pm) | \mathbf{k}, \lambda(\mp) \rangle = 0, \quad (5.0.12)$$

and the Dirac kets  $|\mathbf{k}\rangle$  satisfy

$$\langle \mathbf{k}' | \mathbf{k} \rangle = (2\pi)^3 \delta^3(\mathbf{k}' - \mathbf{k}). \quad (5.0.13)$$

The integral equation equivalent of equation (5.0.1) is

$$|\Psi\rangle = |\mathbf{k}, \lambda(+)\rangle + \frac{1}{\not{p} - m + i\epsilon} U |\Psi\rangle, \quad (5.0.14)$$

where a small positive imaginary term has been added to the energy in order to avoid singularity and to ensure outgoing scattered waves.

The transition operator  $\hat{T}$  is defined as

$$\hat{T} |\mathbf{k}, \lambda(+)\rangle = \hat{U} |\Psi\rangle. \quad (5.0.15)$$

Equation (5.0.14) then leads to the operator integral equation:

$$\hat{T} = \hat{U} + \hat{U} \frac{1}{\not{p} - m + i\epsilon} \hat{T}. \quad (5.0.16)$$

Using the helicity basis, equation (5.0.16) can be reduced to a coupled set of integral equations. For positive energy initial states, the matrix elements of  $\hat{T}$  satisfy [32]

$$\begin{aligned} \langle \mathbf{k}', \lambda', \rho' | \hat{T} | \mathbf{k}, \lambda, + \rangle &= \langle \mathbf{k}', \lambda', \rho' | \hat{U} | \mathbf{k}, \lambda, + \rangle \\ &+ \sum_{\rho'' \lambda''} \int \frac{d^3 l}{(2\pi)^3} \langle \mathbf{k}', \lambda', \rho' | \hat{U} | l, \lambda'', \rho'' \rangle \Gamma^{\rho''}(l) \langle l, \lambda'', \rho'' | \hat{T} | \mathbf{k}, \lambda, + \rangle, \end{aligned} \quad (5.0.17)$$

where

$$\Gamma^\pm(\mathbf{k}) = \frac{1}{E \mp E(\mathbf{k})}, \quad (5.0.18)$$

$$\langle \mathbf{k}', \lambda', \rho' | \hat{U} | \mathbf{k}, \lambda, \rho \rangle = \bar{u}_{\lambda'}^{\rho'}(\mathbf{k}') \hat{U}(\mathbf{k}', \mathbf{k}) u_{\lambda}^{\rho}(\mathbf{k}), \quad (5.0.19)$$

and

$$\langle \mathbf{k}', \lambda', \rho' | \hat{T} | \mathbf{k}, \lambda, \rho \rangle = \bar{u}_{\lambda'}^{\rho'}(\mathbf{k}') \hat{T}(\mathbf{k}', \mathbf{k}) u_{\lambda}^{\rho}(\mathbf{k}). \quad (5.0.20)$$

In equation (5.0.17),  $\rho''$  sums over positive and negative energy states. Negative energy state is present due to coupling to virtual  $N\bar{N}$  pairs. The no-pair analysis discussed in Ref. [32] can be obtained if one only considers  $\rho'' = +$  and  $\rho' = +$ . This means that the projection of the relativistic optical potential is only on the positive-energy states.

## 5.1 Partial-wave analysis of the T-matrix

The following equation shows how the T-matrix is related to helicity amplitudes:

$$\phi_{\lambda, \lambda'}(\mathbf{k}, \mathbf{k}') = -\frac{\mu}{2\pi} \langle \mathbf{k}', \lambda', + | \hat{T} | \mathbf{k}, \lambda, + \rangle, \quad (5.1.1)$$

where the relativistic reduced mass  $\mu$  is given by

$$\mu = \frac{EE_T(\hat{\mathbf{k}})}{E + E_T(\hat{\mathbf{k}})}, \quad (5.1.2)$$

and  $\hat{\mathbf{k}}$  is the nucleon–nucleus centre of mass frame on–shell momentum. The expansion of equation (5.0.17) is done by introducing complete states with total angular momentum  $j$ , projection  $m$ , rho–spin  $\rho$ , and helicity  $\lambda$ :

$$\sum_{j,m,\lambda,\rho} |j, m, \lambda, \rho\rangle \langle j, m, \lambda, \rho| = 1. \quad (5.1.3)$$

For states of definite parity, the required overlaps are

$$\langle j, m, \lambda', \rho' | \Omega_k, \lambda, \rho \rangle = \sqrt{2j+1} \delta_{\rho\rho'} \delta_{\lambda,\lambda'} \mathcal{D}_{m\lambda}^j(\Omega_k), \quad (5.1.4)$$

where  $\mathcal{D}_{m\lambda}^j(\Omega_k)$  represents rotation which specifies the orientation of  $\mathbf{k}$  with respect to a certain system of axes. The partial–wave expansion for the T–matrix is obtained as

$$\langle \mathbf{k}', \lambda', \rho' | \hat{T} | \mathbf{k}, \lambda, \rho \rangle = \sum_{j,m} (2j+1) \mathcal{D}_{m\lambda'}^{j*}(\Omega_{k'}) \langle \lambda', \rho' | T^j(k', k) | \lambda, \rho \rangle \mathcal{D}_{m\lambda}^j(\Omega_k), \quad (5.1.5)$$

where the T–matrix partial–wave is independent of  $m$  due to rotational invariance [32]. As stated before, the initial momentum lies along the z–axis and we obtain the final momentum by a rotation

$$|\mathbf{k}\rangle = R(\phi, \theta, -\phi) |k\hat{z}\rangle. \quad (5.1.6)$$

Thus,

$$\mathcal{D}_{m\lambda}^j(\Omega_k) = \delta_{m,\lambda}, \quad (5.1.7)$$

and

$$\mathcal{D}_{m\lambda}^j(\Omega_{k'}) = e^{i(m-\lambda)\phi} d_{m\lambda}^j(\theta). \quad (5.1.8)$$

The T–matrix partial–wave expansion is then given by

$$\langle \mathbf{k}', \lambda', \rho' | \hat{T} | \mathbf{k}, \lambda, \rho \rangle = \sum_j (2j+1) d_{\lambda\lambda'}^j(\theta) \langle \lambda', \rho' | T^j(k', k) | \lambda, \rho \rangle. \quad (5.1.9)$$

In the same manner, the optical potential partial–wave expansion is given as

$$\langle \mathbf{k}', \lambda', \rho' | \hat{U} | \mathbf{k}, \lambda, \rho \rangle = \sum_j (2j+1) d_{\lambda\lambda'}^j(\theta) \langle \lambda', \rho' | U^j(k', k) | \lambda, \rho \rangle. \quad (5.1.10)$$

## 5.2 Partial–wave analysis of U

The eight term optical potential in the IA2 formalism has already been given in chapter 3:

$$\hat{U}(\mathbf{k}', \mathbf{k}) = \sum_{\nu=1}^8 U_\nu(\mathbf{k}', \mathbf{k}) \hat{\chi}_\nu(\mathbf{q}, 1). \quad (5.2.1)$$

Substituting equation (5.2.1) into equation (5.0.19), we obtain

$$\begin{aligned} \langle \mathbf{k}', \lambda', \rho' | \hat{U} | \mathbf{k}, \lambda, \rho \rangle &= \bar{u}'_{\lambda'}(\mathbf{k}') \left[ U_1 + \gamma^0 U_2 - \frac{\boldsymbol{\alpha} \cdot \mathbf{q}}{m} U_3 + \frac{\boldsymbol{\gamma} \cdot \mathbf{q}}{m} U_4 + \frac{\boldsymbol{\alpha} \cdot \mathbf{k}}{m} U_5 \right. \\ &\quad \left. + \frac{\boldsymbol{\gamma} \cdot \mathbf{k}}{m} U_6 + \frac{(\boldsymbol{\alpha} \cdot \mathbf{k})(\boldsymbol{\alpha} \cdot \mathbf{q})}{m^2} U_7 + \frac{(\boldsymbol{\gamma} \cdot \mathbf{k})(\boldsymbol{\alpha} \cdot \mathbf{q})}{m^2} U_8 \right] u_\lambda^\rho(\mathbf{k}), \end{aligned} \quad (5.2.2)$$

which can also be written as

$$\begin{aligned} \langle \mathbf{k}', \lambda', \rho' | \hat{U} | \mathbf{k}, \lambda, \rho \rangle &= \bar{u}'_{\lambda'}(\mathbf{k}') \left[ U_1 + \gamma^0 U_2 - \gamma^5 \frac{\boldsymbol{\sigma} \cdot \mathbf{q}}{m} U_3 + \gamma^0 \gamma^5 \frac{\boldsymbol{\sigma} \cdot \mathbf{q}}{m} U_4 + \gamma^5 \frac{\boldsymbol{\sigma} \cdot \mathbf{k}}{m} U_5 \right. \\ &\quad \left. + \gamma^0 \gamma^5 \frac{\boldsymbol{\sigma} \cdot \mathbf{k}}{m} U_6 + \frac{(\boldsymbol{\sigma} \cdot \mathbf{k})(\boldsymbol{\sigma} \cdot \mathbf{q})}{m^2} U_7 + \gamma^0 \frac{(\boldsymbol{\sigma} \cdot \mathbf{k})(\boldsymbol{\sigma} \cdot \mathbf{q})}{m^2} U_8 \right] u_\lambda^\rho(\mathbf{k}), \end{aligned} \quad (5.2.3)$$

where the following relations have been used:

$$(\gamma^5)^2 = 1, \quad \boldsymbol{\alpha} \cdot \mathbf{a} \equiv \gamma^5 \boldsymbol{\sigma} \cdot \mathbf{a}, \quad \boldsymbol{\gamma} \cdot \mathbf{a} \equiv \gamma^0 \gamma^5 \boldsymbol{\sigma} \cdot \mathbf{a} \equiv \gamma^0 \boldsymbol{\alpha} \cdot \mathbf{a}. \quad (5.2.4)$$

Using the helicity eigenstates

$$\boldsymbol{\sigma} \cdot \mathbf{k} u_\lambda^\rho(\mathbf{k}) = 2 \lambda k u_\lambda^\rho(\mathbf{k}), \quad (5.2.5)$$

equation (5.2.3) becomes

$$\begin{aligned} \langle \mathbf{k}', \lambda', \rho' | \hat{U} | \mathbf{k}, \lambda, \rho \rangle &= \left[ U_1 S^{\rho' \rho} + U_2 B^{\rho' \rho} + \frac{2 \lambda' k' - 2 \lambda k}{m} (U_3 P^{\rho' \rho} - U_4 R^{\rho' \rho}) \right. \\ &\quad \left. + \frac{2 \lambda k}{m} (U_5 P^{\rho' \rho} - U_6 R^{\rho' \rho}) + \frac{k^2 + 4 \lambda \lambda' k k' - 2 k k' \cos \theta}{m^2} \right. \\ &\quad \left. \times (U_7 S^{\rho' \rho} + U_8 B^{\rho' \rho}) \right] d_{\lambda \lambda'}^{1/2}(\theta), \end{aligned} \quad (5.2.6)$$

where the reduced rotation matrix element (Wigner-d function)  $d_{\lambda \lambda'}^{\frac{1}{2}}(\theta)$  emerges due to overlap of initial and final spinors [32, 125]:

$$\chi_{\lambda'}^\dagger(\theta) \chi_\lambda = d_{\lambda \lambda'}^{1/2}(\theta) = \delta_{\lambda \lambda'} \cos \frac{\theta}{2} + (\lambda' - \lambda) \sin \frac{\theta}{2}. \quad (5.2.7)$$

Here,  $\chi_{\lambda'}(\theta)$  is the rotated Pauli spinor at an angle  $\theta$  to the z axis in the x-z plane. The Wigner-d function has the explicit form [126]

$$\begin{aligned} d_{\lambda \lambda'}^j(\theta) &= (-1)^{j-m'} [(j+m)!(j-m)!(j+m')!(j-m')!]^{\frac{1}{2}} \\ &\quad \times \sum_k \frac{(\cos \frac{\theta}{2})^{m+m'+2k} (\sin \frac{\theta}{2})^{2j-m-m'-2k}}{k!(j-m-k)!(j-m'-k)!(m+m'+k)!} \end{aligned} \quad (5.2.8)$$

where the summation on  $k$  is over all possible values that give non-negative factorial arguments. For this study, the values needed are [127]

$$d_{00}^j(\theta) = P_j(\cos \theta), \quad (5.2.9)$$

$$d_{\frac{1}{2}, \frac{1}{2}}^j(\theta) = d_{-\frac{1}{2}, -\frac{1}{2}}^j(\theta) = \frac{1}{2} \sec \frac{\theta}{2} \left( P_{j-1/2}(\cos \theta) + P_{j+1/2}(\cos \theta) \right), \quad (5.2.10)$$

and

$$d_{-\frac{1}{2}, \frac{1}{2}}^j(\theta) = -d_{\frac{1}{2}, -\frac{1}{2}}^j(\theta) = \frac{1}{2} \csc \frac{\theta}{2} \left( P_{j-1/2}(\cos \theta) - P_{j+1/2}(\cos \theta) \right). \quad (5.2.11)$$

The factors  $S_{\lambda'\lambda}^{\rho'\rho}$ ,  $B_{\lambda'\lambda}^{\rho'\rho}$ ,  $P_{\lambda'\lambda}^{\rho'\rho}$ , and  $R_{\lambda'\lambda}^{\rho'\rho}$  are from overlaps of Dirac spinors. They are defined below.

$$S_{\lambda'\lambda}^{\rho'\rho} = \bar{u}_{\lambda'}^{\rho'}(k') u_{\lambda}^{\rho}(k), \quad (5.2.12)$$

$$B_{\lambda'\lambda}^{\rho'\rho} = \bar{u}_{\lambda'}^{\rho'}(k') \gamma^0 u_{\lambda}^{\rho}(k), \quad (5.2.13)$$

$$P_{\lambda'\lambda}^{\rho'\rho} = \bar{u}_{\lambda'}^{\rho'}(k') \gamma^5 u_{\lambda}^{\rho}(k), \quad (5.2.14)$$

$$R_{\lambda'\lambda}^{\rho'\rho} = \bar{u}_{\lambda'}^{\rho'}(k') \gamma^0 \gamma^5 u_{\lambda}^{\rho}(k), \quad (5.2.15)$$

where

$$\begin{aligned} S_{\lambda'\lambda}^{++} &= -S_{\lambda'\lambda}^{--} = N_{k'} N_k \left[ 1 - \frac{4\lambda\lambda'kk'}{(E(\mathbf{k}) + m)(E(\mathbf{k}') + m)} \right] \\ S_{\lambda'\lambda}^{+-} &= S_{\lambda'\lambda}^{-+} = N_{k'} N_k \left[ -\frac{2\lambda k}{E(\mathbf{k}) + m} - \frac{2\lambda' k'}{E(\mathbf{k}') + m} \right], \end{aligned} \quad (5.2.16)$$

$$\begin{aligned} B_{\lambda'\lambda}^{++} &= B_{\lambda'\lambda}^{--} = N_{k'} N_k \left[ 1 + \frac{4\lambda\lambda'kk'}{(E(\mathbf{k}) + m)(E(\mathbf{k}') + m)} \right] \\ B_{\lambda'\lambda}^{+-} &= -B_{\lambda'\lambda}^{-+} = N_{k'} N_k \left[ \frac{2\lambda' k'}{E(\mathbf{k}') + m} - \frac{2\lambda k}{E(\mathbf{k}) + m} \right], \end{aligned} \quad (5.2.17)$$

$$\begin{aligned} P_{\lambda'\lambda}^{++} &= P_{\lambda'\lambda}^{--} = N_{k'} N_k \left[ \frac{2\lambda k}{E(\mathbf{k}) + m} - \frac{2\lambda' k'}{E(\mathbf{k}') + m} \right] \\ P_{\lambda'\lambda}^{+-} &= -P_{\lambda'\lambda}^{-+} = N_{k'} N_k \left[ 1 + \frac{4\lambda\lambda'kk'}{(E(\mathbf{k}) + m)(E(\mathbf{k}') + m)} \right], \end{aligned} \quad (5.2.18)$$

$$\begin{aligned} R_{\lambda'\lambda}^{++} &= -R_{\lambda'\lambda}^{--} = N_{k'} N_k \left[ \frac{2\lambda k}{E(\mathbf{k}) + m} + \frac{2\lambda' k'}{E(\mathbf{k}') + m} \right] \\ R_{\lambda'\lambda}^{+-} &= R_{\lambda'\lambda}^{-+} = N_{k'} N_k \left[ 1 - \frac{4\lambda\lambda'kk'}{(E(\mathbf{k}) + m)(E(\mathbf{k}') + m)} \right]. \end{aligned} \quad (5.2.19)$$

Note that the definition of  $u^{\rho}(k)$  is equivalent to the definition of  $u_{\lambda}^{\rho}(k)$  given in equation (5.0.8) but without the Pauli spinor  $\chi_{\lambda}$ .

Partial-wave expansion of the eight IA2 optical potentials is given by [32]:

$$U_\nu(\mathbf{k}', \mathbf{k}) = \sum_{\ell} (2\ell + 1) U_{\nu\ell}(k', k) d_{00}^{\ell}(\cos \theta). \quad (5.2.20)$$

where the Wigner function  $d_{00}^{\ell}(\cos \theta) = P_{\ell}(\cos \theta)$ . If we multiply both sides of equation (5.2.20) by  $P_{\ell}(\cos \theta)$ , integrate over  $\cos \theta$  from 0 to  $\pi$ , and use the following orthonormality condition of the Legendre polynomial:

$$\int_{-1}^1 P_n(x) P_m(x) dx = \frac{2\delta_{nm}}{2n + 1}, \quad (5.2.21)$$

the partial-wave terms of the eight optical potentials can be obtained from

$$U_{\nu\ell} = \frac{1}{2} \int_{-1}^1 dx P_{\ell}(x) U_{\nu}(\mathbf{k}', \mathbf{k}), \quad (5.2.22)$$

where  $x$  is the cosine of the angle ( $\theta$ ) between  $\mathbf{k}'$  and  $\mathbf{k}$ , i.e.,  $x = \cos \theta = \hat{\mathbf{k}}' \cdot \hat{\mathbf{k}}$ . The expansion of the full IA2 optical potential is then given by

$$\langle \mathbf{k}', \lambda', \rho' | \hat{U} | \mathbf{k}, \lambda, \rho \rangle = \sum_j (2j + 1) d_{\lambda\lambda'}^j(\theta) \langle \lambda', \rho' | U^j(k', k) | \lambda, \rho \rangle. \quad (5.2.23)$$

By making use of the relation

$$d_{m_1 n_1}^{j_1}(\theta) d_{m_2 n_2}^{j_2}(\theta) = \sum_{|j_1 - j_2|}^{j_1 + j_2} \sum_{mn} C_{j_1 m_1 j_2 m_2}^{jm} d_{mn}^j(\theta) C_{j_1 n_1 j_2 n_2}^{jn}, \quad (5.2.24)$$

to couple  $d_{\lambda\lambda'}^{\frac{1}{2}}(\theta)$  with  $d_{00}^{\ell}(\theta)$  in order to obtain functions of definite  $j$ , we have the partial-wave terms of the optical potential written as

$$\begin{aligned} \langle \lambda', \rho' | U^j(k', k) | \lambda, \rho \rangle &= \sum_{\ell=j-\frac{1}{2}}^{j+\frac{1}{2}} \frac{2\ell + 1}{2j + 1} \langle \ell, \frac{1}{2}, 0, \lambda' | j \lambda' \rangle \langle \ell, \frac{1}{2}, 0, \lambda | j \lambda \rangle \left\{ U_{1,\ell}(k', k) S_{\lambda'\lambda}^{\rho'\rho} \right. \\ &+ U_{2,\ell}(k', k) B_{\lambda'\lambda}^{\rho'\rho} + \frac{2\lambda k' - 2\lambda k}{m} \left[ U_{3,\ell}(k', k) P_{\lambda'\lambda}^{\rho'\rho} - U_{4,\ell}(k', k) R_{\lambda'\lambda}^{\rho'\rho} \right] \\ &+ \frac{2\lambda k}{m} \left[ U_{5,\ell}(k', k) P_{\lambda'\lambda}^{\rho'\rho} - U_{6,\ell}(k', k) R_{\lambda'\lambda}^{\rho'\rho} \right] \\ &+ \left( \frac{k^2 + 4\lambda\lambda'kk'}{m^2} \right) \left[ U_{7,\ell}(k', k) S_{\lambda'\lambda}^{\rho'\rho} + U_{8,\ell}(k', k) B_{\lambda'\lambda}^{\rho'\rho} \right] \\ &- \left( \frac{2kk'}{m^2} \right) \left( \frac{\ell}{2\ell + 1} \right) \left[ U_{7,\ell-1}(k', k) S_{\lambda'\lambda}^{\rho'\rho} + U_{8,\ell-1}(k', k) B_{\lambda'\lambda}^{\rho'\rho} \right] \\ &\left. - \left( \frac{2kk'}{m^2} \right) \left( \frac{\ell + 1}{2\ell + 1} \right) \left[ U_{7,\ell+1}(k', k) S_{\lambda'\lambda}^{\rho'\rho} + U_{8,\ell+1}(k', k) B_{\lambda'\lambda}^{\rho'\rho} \right] \right\}. \end{aligned} \quad (5.2.25)$$

The optical potential in states of definite parity is obtained by using equation (5.2.25) in equation (5.3.7).

### 5.3 Partial-wave analysis of the integral equation

Substituting equations (5.1.9) and (5.1.10) into equation (5.0.17), the following partial-wave integral equation is obtained:

$$\begin{aligned} \langle \lambda', \rho' | T^j(k', k) | \lambda, \rho \rangle &= \langle \lambda', \rho' | U^j(k', k) | \lambda, \rho \rangle + \sum_{\lambda'' \rho''} \int_0^\infty dk'' \frac{k''^2}{2\pi^2} \\ &\times \langle \lambda', \rho' | U^j(k', k'') | \lambda'', \rho'' \rangle \Gamma^{\rho''}(k'') \langle \lambda'', \rho'' | T^j(k'', k) | \lambda, \rho \rangle, \end{aligned} \quad (5.3.1)$$

where the relation

$$\int d\Omega_l (2j+1) \mathcal{D}_{m\lambda''}^{j*}(\Omega_l) \mathcal{D}_{m'\lambda''}^j(\Omega_l) = 4\pi \delta_{jj'} \delta_{mm'} \quad (5.3.2)$$

has been used to carry out integration over the angles of the intermediate state. Equation (5.3.1) is actually coupled integral equations (for particular  $\lambda, \lambda'$ ) because of the sum over  $\lambda''$ , but can be decoupled if we introduce states of definite parity, and use the fact that parity operator  $\hat{P}$  reverses helicity. Also  $\rho = \pm$  states have opposite intrinsic parity, i.e.,

$$\hat{P} |\lambda, \rho\rangle = \rho |-\lambda, \rho\rangle. \quad (5.3.3)$$

Parity eigenstates are given by

$$\hat{P} |r, \lambda, \rho\rangle = r |r, \lambda, \rho\rangle, \quad (5.3.4)$$

where parity eigenvalue  $r = \pm$ . For these states, definite orbital angular momentum  $l$  is related to total angular momentum  $j$  and parity  $r$  by  $l = j \pm \frac{1}{2}$  and  $r = \rho(-1)^l$ , respectively. The states are expressed as

$$|r, \lambda, \rho\rangle \equiv \frac{1}{\sqrt{2}} (|\lambda, \rho\rangle + r\rho |-\lambda, \rho\rangle). \quad (5.3.5)$$

The T-matrix and optical potential matrix elements in states of good parity ( $r = \pm$ ) are then given, respectively, as

$$\langle \lambda', \rho' | T_r^j(k', k) | \lambda, \rho \rangle \equiv \frac{1}{2} [\langle \lambda', \rho' | T^j(k', k) | \lambda, \rho \rangle + r\rho \langle \lambda', \rho' | T^j(k', k) | -\lambda, \rho \rangle], \quad (5.3.6)$$

$$\langle \lambda', \rho' | U_r^j(k', k) | \lambda, \rho \rangle \equiv \frac{1}{2} [\langle \lambda', \rho' | U^j(k', k) | \lambda, \rho \rangle + r\rho \langle \lambda', \rho' | U^j(k', k) | -\lambda, \rho \rangle], \quad (5.3.7)$$

and the decoupled integral equations are given as

$$\begin{aligned} \langle \lambda', \rho' | T_r^j(k', k) | \lambda, \rho \rangle &= \langle \lambda', \rho' | U_r^j(k', k) | \lambda, \rho \rangle + \sum_{\rho''} \int_0^\infty dk'' \frac{k''^2}{2\pi^2} \\ &\times \langle \lambda', \rho' | U_r^j(k', k'') | \lambda', \rho'' \rangle \Gamma^{\rho''}(k'') \langle \lambda', \rho'' | T_r^j(k'', k) | \lambda, \rho \rangle, \end{aligned} \quad (5.3.8)$$

in which there is no more sum over helicities  $\lambda$  (but there is still sum over  $\rho''$ ). If we denote helicity amplitude by  $\langle \lambda' | \phi | \lambda \rangle$ , with incident helicity  $\lambda$  and final helicity  $\lambda'$ , then for elastic proton scattering from a spin-zero nucleus, the two required helicity amplitudes are expanded as follows [32, 125]:

$$\phi_1(\theta) \equiv \langle + | \phi | + \rangle \equiv \phi_{1/2, 1/2}(\mathbf{k}, \mathbf{k}') = \sum_j \frac{2j+1}{2\hat{k}} \phi_1^j d_{1/2, 1/2}^j(\theta), \quad (5.3.9)$$

$$\phi_2(\theta) \equiv \langle + | \phi | - \rangle \equiv \phi_{1/2, -1/2}(\mathbf{k}, \mathbf{k}') = \sum_j \frac{2j+1}{2\hat{k}} \phi_2^j d_{-1/2, 1/2}^j(\theta). \quad (5.3.10)$$

The partial-wave amplitudes  $\phi_1^j$  and  $\phi_2^j$  are obtained from the T-matrix elements in states of definite parity as:

$$\phi_1^j \equiv -\frac{\mu\hat{\mathbf{k}}}{2\pi} \left[ \left\langle \frac{1}{2}, + | T_+^j(\hat{\mathbf{k}}, \hat{\mathbf{k}}) | \frac{1}{2}, + \right\rangle + \left\langle \frac{1}{2}, + | T_-^j(\hat{\mathbf{k}}, \hat{\mathbf{k}}) | \frac{1}{2}, + \right\rangle \right], \quad (5.3.11)$$

$$\phi_2^j \equiv -\frac{\mu\hat{\mathbf{k}}}{2\pi} \left[ \left\langle \frac{1}{2}, + | T_+^j(\hat{\mathbf{k}}, \hat{\mathbf{k}}) | \frac{1}{2}, + \right\rangle - \left\langle \frac{1}{2}, + | T_-^j(\hat{\mathbf{k}}, \hat{\mathbf{k}}) | \frac{1}{2}, + \right\rangle \right]. \quad (5.3.12)$$

The K-matrix formalism is employed to solve the partial-wave integral equations (5.3.8). In this formalism, one separates the delta function and principal-value contributions of the propagator

$$\begin{aligned} \Gamma^+(k'') &= \frac{1}{E - E(k'') + i\epsilon} \\ &= \frac{-i\pi\mu}{\hat{\mathbf{k}}} \delta(k'' - \hat{\mathbf{k}}) + \frac{\mathcal{P}}{E - E(k'')}, \end{aligned} \quad (5.3.13)$$

where  $\mathcal{P}$  denotes the principal-value part.

The nucleon-nucleus T-matrix is related to the K-matrix through the relation

$$-\frac{\mu\hat{\mathbf{k}}}{2\pi} T_r^j(\hat{\mathbf{k}}, \hat{\mathbf{k}}) = \frac{K_r^j(\hat{\mathbf{k}}, \hat{\mathbf{k}})}{1 - iK_r^j(\hat{\mathbf{k}}, \hat{\mathbf{k}})}. \quad (5.3.14)$$

Therefore, for matrix elements that involves one positive energy state and one on-shell momentum, we have the following K-matrix

$$\langle \lambda', \rho' | K_r^j(k', \hat{\mathbf{k}}) | \lambda, + \rangle = \frac{-\mu\hat{\mathbf{k}}}{2\pi} \langle \lambda', \rho' | T_r^j(k', \hat{\mathbf{k}}) | \lambda, + \rangle \left[ 1 - \frac{i\mu\hat{\mathbf{k}}}{2\pi} \langle \lambda, + | T_r^j(\hat{\mathbf{k}}, \hat{\mathbf{k}}) | \lambda, + \rangle \right]^{-1}. \quad (5.3.15)$$

For  $\lambda = \lambda'$ , the K-matrix equation (5.3.15) obeys the principal-value integral equation

$$\begin{aligned} \langle \lambda, \rho' | K_r^j(k', \hat{\mathbf{k}}) | \lambda, + \rangle &= \frac{-\mu\hat{\mathbf{k}}}{2\pi} \langle \lambda, \rho' | U_r^j(k', \hat{\mathbf{k}}) | \lambda, + \rangle + \sum_{\rho''} \mathcal{P} \int_0^\infty dk'' \frac{k''^2}{2\pi^2} \\ &\quad \times \langle \lambda, \rho' | U_r^j(k', k'') | \lambda, \rho'' \rangle \Gamma^{\rho''}(k'') \langle \lambda, \rho'' | K_r^j(k'', \hat{\mathbf{k}}) | \lambda, + \rangle. \end{aligned} \quad (5.3.16)$$

Equation (5.3.16) is solved in states  $\lambda = \frac{1}{2}$  and  $\rho = \rho' = +$  to obtain the phase shifts  $\delta_j^\pm$  for proton–nucleus elastic scattering using the equation

$$\tan \delta_j^\pm = \left\langle \frac{1}{2}, + | K_\pm^j(\hat{\mathbf{k}}, \hat{\mathbf{k}}) | \frac{1}{2}, + \right\rangle. \quad (5.3.17)$$

The partial–wave helicity amplitudes  $\phi_1^j$  and  $\phi_2^j$  are then calculated using the relations:

$$\phi_1^j = \frac{1}{2i} \left( e^{2i\delta_j^+} + e^{2i\delta_j^-} - 2 \right), \quad (5.3.18)$$

$$\phi_2^j = \frac{1}{2i} \left( e^{2i\delta_j^+} - e^{2i\delta_j^-} \right). \quad (5.3.19)$$

The three scattering observables to be calculated are differential cross section ( $\sigma$ ), analysing power ( $A_y$ ), and spin–rotation function ( $Q$ ). For elastic proton–nucleus scattering, these observables are obtained from the helicity amplitudes using the following relations:

$$\sigma = |\phi_1|^2 + |\phi_2|^2, \quad (5.3.20)$$

$$A_y = \frac{2 \operatorname{Im}(\phi_1 \phi_2^*)}{|\phi_1|^2 + |\phi_2|^2}, \quad (5.3.21)$$

$$Q = \frac{\cos(\theta) \operatorname{Re}(\phi_1 \phi_2^*) + \frac{1}{2} \sin(\theta) [|\phi_1|^2 - |\phi_2|^2]}{|\phi_1|^2 + |\phi_2|^2}. \quad (5.3.22)$$

## 5.4 Solution of the integral equations

In this section, we describe how the momentum space integral equations are solved in order to calculate the scattering observables. We discuss the treatment of principal value part of the integral equations, discretisation of the integral equations, inclusion of Coulomb potential, and treatment of high angular momentum states.

### 5.4.1 Dealing with the principal value $\mathcal{P}$

For a spin–half (proton) scattering from a spin zero target, there is a constraint on equation (5.3.16), which is that the equation is solved in states  $\lambda = \frac{1}{2}$  and  $\rho = \rho' = +$ . Equation (5.3.16) is actually two coupled integral equations and it is written more explicitly as

$$\begin{aligned} \left\langle \frac{1}{2}, + | K_r^j(k', \hat{\mathbf{k}}) | \frac{1}{2}, + \right\rangle &= \frac{-\mu \hat{\mathbf{k}}}{2\pi} \left\langle \frac{1}{2}, + | U_r^j(k', \hat{\mathbf{k}}) | \frac{1}{2}, + \right\rangle \\ &+ \mathcal{P} \int_0^\infty dk'' \frac{k''^2}{2\pi^2} \left\langle \frac{1}{2}, + | U_r^j(k', k'') | \frac{1}{2}, + \right\rangle \Gamma^+(k'') \left\langle \frac{1}{2}, + | K_r^j(k'', \hat{\mathbf{k}}) | \frac{1}{2}, + \right\rangle \\ &+ \mathcal{P} \int_0^\infty dk'' \frac{k''^2}{2\pi^2} \left\langle \frac{1}{2}, + | U_r^j(k', k'') | \frac{1}{2}, - \right\rangle \Gamma^-(k'') \left\langle \frac{1}{2}, - | K_r^j(k'', \hat{\mathbf{k}}) | \frac{1}{2}, + \right\rangle \end{aligned} \quad (5.4.1)$$

and

$$\begin{aligned} \left\langle \frac{1}{2}, - |K_r^j(k', \hat{\mathbf{k}})|_{\frac{1}{2}}, + \right\rangle &= \frac{-\mu \hat{\mathbf{k}}}{2\pi} \left\langle \frac{1}{2}, - |U_r^j(k', \hat{\mathbf{k}})|_{\frac{1}{2}}, + \right\rangle \\ &+ \mathcal{P} \int_0^\infty dk'' \frac{k''^2}{2\pi^2} \left\langle \frac{1}{2}, - |U_r^j(k', k'')|_{\frac{1}{2}}, + \right\rangle \Gamma^+(k'') \left\langle \frac{1}{2}, + |K_r^j(k'', \hat{\mathbf{k}})|_{\frac{1}{2}}, + \right\rangle \\ &+ \mathcal{P} \int_0^\infty dk'' \frac{k''^2}{2\pi^2} \left\langle \frac{1}{2}, - |U_r^j(k', k'')|_{\frac{1}{2}}, - \right\rangle \Gamma^-(k'') \left\langle \frac{1}{2}, - |K_r^j(k'', \hat{\mathbf{k}})|_{\frac{1}{2}}, + \right\rangle \end{aligned} \quad (5.4.2)$$

Equations (5.4.1) and (5.4.2) are to be solved as coupled integral equations. From these equations,

$$\Gamma^\pm(k'') = \frac{1}{E(\hat{\mathbf{k}}) \mp E(k'')}, \quad (5.4.3)$$

where

$$E(\hat{\mathbf{k}}) = \sqrt{\hat{\mathbf{k}}^2 + m_P^2} + \sqrt{\hat{\mathbf{k}}^2 + m_T^2}, \quad E(k'') = \sqrt{k''^2 + m_P^2} + \sqrt{k''^2 + m_T^2}, \quad (5.4.4)$$

and

$$\mu(\hat{\mathbf{k}}) = \frac{\sqrt{\hat{\mathbf{k}}^2 + m_P^2} \sqrt{\hat{\mathbf{k}}^2 + m_T^2}}{\sqrt{\hat{\mathbf{k}}^2 + m_P^2} + \sqrt{\hat{\mathbf{k}}^2 + m_T^2}}. \quad (5.4.5)$$

There is a pole present in  $\Gamma^+(k'')$  when  $E(\hat{\mathbf{k}}) = E(k'')$ . If our initial system has  $E(\hat{\mathbf{k}}) > 0$ , then only  $\Gamma^+(k'')$  has a pole at  $E(\hat{\mathbf{k}}) = E(k'')$ , while there will be no pole present in  $\Gamma^-(k'')$ . In this case, there will be physical scattered waves of positive energy that travel beyond the range of the potential but only virtual decaying waves of negative energy within the range of the potential. One way to deal with the pole present in  $\Gamma^+(k'')$  is to use the subtraction technique where we subtract a function that is equal to the integrand at singularity point [128, 129]:

$$\mathcal{P} \int_0^\infty \frac{dk'' f(k'')}{E - E(k'')} = \int_0^\infty dk'' \left[ \frac{f(k'')}{E - E(k'')} - \frac{f(\hat{\mathbf{k}})}{(\hat{\mathbf{k}}^2 - k''^2)/2\mu(\hat{\mathbf{k}})} \right], \quad (5.4.6)$$

where we have used the relation

$$\lim_{k'' \rightarrow \hat{\mathbf{k}}} \frac{k''^2 - \hat{\mathbf{k}}^2}{2\mu(\hat{\mathbf{k}})} = E(k'') - E(\hat{\mathbf{k}}). \quad (5.4.7)$$

The second approach to deal with the principal value integral is the Sloan method, in which case one uses symmetric Gauss points around the pole. This approach uses the fact that since the denominator is antisymmetric for a sufficiently small  $\Delta$ , one has [129]

$$\begin{aligned} \mathcal{P} \int_0^\infty \frac{dk'' f(k'')}{E - E(k'')} &= \int_0^{\hat{\mathbf{k}}-\Delta} \frac{dk'' f(k'')}{E - E(k'')} + \lim_{\delta \rightarrow 0} \left[ \int_{\hat{\mathbf{k}}-\Delta}^{\hat{\mathbf{k}}-\delta} \frac{dk'' f(k'')}{E - E(k'')} \right. \\ &\quad \left. + \int_{\hat{\mathbf{k}}+\delta}^{\hat{\mathbf{k}}+\Delta} \frac{dk'' f(k'')}{E - E(k'')} \right] + \int_{\hat{\mathbf{k}}+\Delta}^{k_{\max}} \frac{dk'' f(k'')}{E - E(k'')} \end{aligned} \quad (5.4.8)$$

In this work, we have used  $\Delta = 1.5$ ,  $\delta = 0.0001$  and  $k_{max} = 60 fm^{-1}$ .

The Gauss points are divided into four regions, and it is compulsory that the second and third regions be symmetric around the pole at  $k_p$  in order to successfully apply the Sloan technique. In this work, 8 points are used in the first region, 12 in the second and third regions, and 28 points in the fourth region.

### 5.4.2 Discretisation of the integral equations

The integral equations (5.4.1) and (5.4.2) are converted into linear equations by approximating the integrals as sums over  $N$  Gaussian quadrature points  $k_j$ ;  $j = 1, N$ , weighted by  $w_j$ . For the sake of simplicity, we use the following notations

$$\langle \lambda, \rho' | K_r^j(k', k'') | \lambda, \rho'' \rangle \equiv K_{r, \rho' \rho''}^J(k', k'') \quad (5.4.9)$$

and

$$\langle \lambda, \rho' | U_r^j(k', k'') | \lambda, \rho'' \rangle \equiv U_{r, \rho' \rho''}^J(k', k'') \quad (5.4.10)$$

so that the discretized forms of equations (5.4.1) and (5.4.2) are written, respectively, as

$$\begin{aligned} K_{r, ++}^J(k_i, k_0) &= \frac{-\mu(k_0)k_0}{2\pi} U_{r, ++}^J(k_i, k_0) + \frac{1}{2\pi^2} \sum_{j=1}^N \frac{k_j^2 U_{r, ++}^J(k_i, k_j) K_{r, ++}^J(k_j, k_0) w_j}{E(k_0) - E(k_j)} \\ &+ \frac{1}{2\pi^2} \sum_{j=1}^N \frac{k_j^2 U_{r, +-}^J(k_i, k_j) K_{r, +-}^J(k_j, k_0) w_j}{E(k_0) - E(k_j)} \end{aligned} \quad (5.4.11)$$

and

$$\begin{aligned} K_{r, -+}^J(k_i, k_0) &= \frac{-\mu(k_0)k_0}{2\pi} U_{r, -+}^J(k_i, k_0) + \frac{1}{2\pi^2} \sum_{j=1}^N \frac{k_j^2 U_{r, -+}^J(k_i, k_j) K_{r, ++}^J(k_j, k_0) w_j}{E(k_0) - E(k_j)} \\ &+ \frac{1}{2\pi^2} \sum_{j=1}^N \frac{k_j^2 U_{r, --}^J(k_i, k_j) K_{r, -+}^J(k_j, k_0) w_j}{E(k_0) - E(k_j)} \end{aligned} \quad (5.4.12)$$

where  $i, j = 1, N$ . By using the following notations in equations (5.4.11) and (5.4.12):

$$D_j^{(1)} = \frac{1}{2\pi^2} \frac{w_j k_j^2}{E(k_0) - E(k_j)}, \quad (5.4.13)$$

$$D_j^{(2)} = \frac{1}{2\pi^2} \frac{w_j k_j^2}{E(k_0) + E(k_j)} \quad (5.4.14)$$

we write the two coupled equations as

$$\begin{aligned} K_i^{++}(k_i, k_0) &= \frac{-\mu(k_0)k_0}{2\pi} U_i^{++}(k_i, k_0) + \sum_{j=1}^N D_j^{(1)} U_{ij}^{++}(k_i, k_j) K_j^{++}(k_j, k_0) \\ &+ \sum_{j=1}^N D_j^{(2)} U_{ij}^{+-}(k_i, k_j) K_j^{-+}(k_j, k_0) \end{aligned} \quad (5.4.15)$$

and

$$\begin{aligned} K_i^{-+}(k_i, k_0) &= \frac{-\mu(k_0)k_0}{2\pi} U_i^{-+}(k_i, k_0) + \sum_{j=1}^N D_j^{(1)} U_{ij}^{-+}(k_i, k_j) K_j^{++}(k_j, k_0) \\ &+ \sum_{j=1}^N D_j^{(2)} U_{ij}^{--}(k_i, k_j) K_j^{-+}(k_j, k_0), \end{aligned} \quad (5.4.16)$$

where the subscript  $r$  and superscript  $J$  have been dropped for convenience. We next write equations (5.4.15) and (5.4.16) as a super matrix equation as follows:

$$\begin{aligned} \begin{bmatrix} K_i^{++}(k_i, k_0) \\ K_i^{-+}(k_i, k_0) \end{bmatrix} &= \begin{bmatrix} \frac{-\mu(k_0)k_0}{2\pi} U_i^{++}(k_i, k_0) \\ \frac{-\mu(k_0)k_0}{2\pi} U_i^{-+}(k_i, k_0) \end{bmatrix} + \begin{bmatrix} D_j^{(1)} U_{ij}^{++}(k_i, k_j) & D_j^{(2)} U_{ij}^{+-}(k_i, k_j) \\ D_j^{(1)} U_{ij}^{-+}(k_i, k_j) & D_j^{(2)} U_{ij}^{--}(k_i, k_j) \end{bmatrix} \\ &\times \begin{bmatrix} K_j^{++}(k_j, k_0) \\ K_j^{-+}(k_j, k_0) \end{bmatrix}. \end{aligned} \quad (5.4.17)$$

Again, for simplicity, we use the following notations:

$$\begin{aligned} K_{i'} &= \begin{bmatrix} K_i^{++}(k_i, k_0) \\ K_i^{-+}(k_i, k_0) \end{bmatrix}, \quad U_{i'} = \begin{bmatrix} \frac{-\mu(k_0)k_0}{2\pi} U_i^{++}(k_i, k_0) \\ \frac{-\mu(k_0)k_0}{2\pi} U_i^{-+}(k_i, k_0) \end{bmatrix}, \\ U_{i'j'} &= \begin{bmatrix} D_j^{(1)} U_{ij}^{++}(k_i, k_j) & D_j^{(2)} U_{ij}^{+-}(k_i, k_j) \\ D_j^{(1)} U_{ij}^{-+}(k_i, k_j) & D_j^{(2)} U_{ij}^{--}(k_i, k_j) \end{bmatrix}, \quad K_{j'} = \begin{bmatrix} K_j^{++}(k_j, k_0) \\ K_j^{-+}(k_j, k_0) \end{bmatrix} \end{aligned} \quad (5.4.18)$$

so that equation (5.4.17) can be written as

$$K_{i'} = U_{i'} + U_{i'j'} K_{j'}, \quad \text{where } i', j' = 1, 2N. \quad (5.4.19)$$

Equation (5.4.19) can also be written as

$$(I - U_{i'j'}) K_{i'} = U_{i'}. \quad (5.4.20)$$

If we call the matrix  $(I - U_{i'j'})$  the wave matrix  $F_{i'j'}$ , we can write equation (5.4.20) as the matrix equation

$$[F_{i'j'}]_{2N \times 2N} [K_{i'}]_{2N} = [U_{i'}]_{2N}. \quad (5.4.21)$$

In equation (5.4.21),  $F_{i'j'}$  is a  $2N \times 2N$  matrix,  $K_{i'}$  and  $U_{i'}$  are  $2N$  column vectors. Equation (5.4.21) is a set of  $2N$  linear algebraic equations in  $2N$  unknowns that can be solved using methods such as LU decomposition, matrix inversion, Gaussian elimination methods and so on. We shall make use of the Gaussian elimination method in this work. The MATLAB function `gauss(F,U)` will solve equation (5.4.21) for  $K_{i'}$  using the Gaussian elimination method. The quadrature points and weights are obtained using the function `[k, w] = lgwt(N, a, b)`, where  $N$  is the quadrature point,  $a$  is the lower limit, and  $b$  is the upper limit of the integral.

### 5.4.3 Inclusion of Coulomb potential

Proper treatment of Coulomb corrections in momentum space is vital. There are quite a few techniques that have been introduced for including Coulomb corrections [32, 130–133]. Here we use the approach presented in Ref. [130].

The inclusion of Coulomb corrections modifies the partial-wave expansions of the helicity amplitudes as follows [32]

$$\begin{aligned}\phi_1(\theta) &= \sum_j \frac{2j+1}{2\hat{k}} \phi_1^j d_{1/2,1/2}^j(\theta) + \phi_1^{ptC}(\theta) \\ \phi_2(\theta) &= \sum_j \frac{2j+1}{2\hat{k}} \phi_2^j d_{-1/2,1/2}^j(\theta) + \phi_2^{ptC}(\theta).\end{aligned}\quad (5.4.22)$$

Here  $\phi_1^{ptC}(\theta)$  and  $\phi_2^{ptC}(\theta)$  are the helicity amplitudes for scattering by a point-Coulomb interaction. The partial wave amplitudes  $\phi_1^j$  and  $\phi_2^j$  given by

$$\begin{aligned}\phi_1^j &= \frac{1}{2i} \left[ \left( e^{2i\bar{\delta}_j^+} - 1 \right) e^{2i\delta_{j,C}^+} + \left( e^{2i\bar{\delta}_j^-} - 1 \right) e^{2i\delta_{j,C}^-} \right], \\ \phi_2^j &= \frac{1}{2i} \left[ \left( e^{2i\bar{\delta}_j^+} - 1 \right) e^{2i\delta_{j,C}^+} - \left( e^{2i\bar{\delta}_j^-} - 1 \right) e^{2i\delta_{j,C}^-} \right]\end{aligned}\quad (5.4.23)$$

now include the point-Coulomb phase shifts  $\delta_{j,C}^\pm$  and the Coulomb modified phase shifts  $\bar{\delta}_j^\pm$ . The phase shifts  $\bar{\delta}_j^\pm$ , which include contributions from the strong nuclear potential and the Coulomb potential, are calculated via [130]

$$\bar{\delta}_j^\pm = \delta_j^\pm \left( \hat{U}(\mathbf{k}', \mathbf{k}) + V_C^{Rcut} \right) - \delta_j^\pm \left( V_{ptC}^{Rcut} \right), \quad (5.4.24)$$

where  $\hat{U}(\mathbf{k}', \mathbf{k})$  is the IA2 eight-term optical potential,  $V_C^{Rcut}$  is the cut-off Coulomb interaction, and  $V_{ptC}^{Rcut}$  is the cut-off point Coulomb interaction. The Coulomb potential will combine with the second term  $U_2$  of the IA2 optical potential. The cut-off point Coulomb interaction  $V_{ptC}^{Rcut}$  and Coulomb interaction  $V_C^{Rcut}$  are calculated using [130]

$$V_{ptC}^{Rcut}(q) = \frac{Ze^2}{2\pi^2 q^2} [1 - \cos(qR_{cut})] \quad (5.4.25)$$

and

$$V_C^{Rcut}(q) = \frac{Ze^2}{2\pi^2 q^2} [\rho(q) - \cos(qR_{cut})], \quad (5.4.26)$$

where  $R_{cut}$  is the cut-off radius beyond which the strong nuclear potential vanishes, typically  $R_{cut} = 8 - 10\text{fm}$  (we have used  $R_{cut} = 10\text{fm}$  in our computation). The form factor  $\rho(q)$  is calculated via

$$\rho(q) = \frac{4\pi}{q} \int \rho_{ch}(r) \sin(qr) r dr, \quad (5.4.27)$$

where  $\rho_{ch}(r)$  is the charge density of the target nucleus calculated from relativistic mean field theory (See Chapter 2). Also  $\rho(0) = 1$ , and  $q = |\mathbf{k}' - \mathbf{k}|$  is the momentum transfer. In summary to calculate the Coulomb modified phase shift, we solve

the Lippmann-Schwinger equations for the case where the optical potential includes Coulomb interaction and the case for only the point cut-off Coulomb interaction. The difference between the two phase shifts gives the Coulomb modified phase shifts  $\bar{\delta}_j^\pm$  for states of positive and negative parities.

#### 5.4.4 Solution at high angular momentum states

The method shown in the previous section to solve the momentum space integral equation made use of the partial wave expansion approach, which transforms the three-dimensional equation to a sum of one-dimensional equations, which are then solved by the usual standard technique. There is no difficulty in using this approach for low energy scattering theory problems, because few angular momenta are required at low energies [134]. At high incident projectile energies (in the intermediate energy and high energy region), large number of angular momenta contribute to the scattering amplitude. This makes it difficult to accurately compute the integral in equation (5.2.22) because of the oscillatory nature of the Legendre polynomials (at high angular momentum states). There are at least three approaches to solve this problem:

1. Three dimensional Born approximation: In this case, one solves the integral equations up to certain angular momentum  $\ell_c$  such that the remaining partial waves are treated in the Born approximations. The chosen value of  $\ell_c$  must be such that the use of Born approximation is justified. This approach has been used in Refs. [32, 124, 129, 133, 135, 136]. The use of this approach modifies the helicity amplitudes as follows:

$$\begin{aligned}\phi_1(\theta) &= \sum_{j=\frac{1}{2}}^{j_{\text{cut}}} \frac{2j+1}{2\mathbf{k}} \phi_1^j d_{1/2,1/2}^j(\theta) + \phi_1^{\text{pt}C} + e^{2i\delta_{j_{\text{cut}}+1}^{\text{pt}C}} \phi_{B1}^>(\theta) \\ \phi_2(\theta) &= \sum_{j=\frac{1}{2}}^{j_{\text{cut}}} \frac{2j+1}{2\mathbf{k}} \phi_2^j d_{-1/2,1/2}^j(\theta) + \phi_2^{\text{pt}C} + e^{2i\delta_{j_{\text{cut}}+1}^{\text{pt}C}} \phi_{B2}^>(\theta),\end{aligned}\quad (5.4.28)$$

where  $\phi_1^j$  and  $\phi_2^j$  are as given in equations (5.4.23), and

$$\begin{aligned}\phi_{B1}^>(\theta) &= \phi_{B1}(\theta) - \sum_{j=\frac{1}{2}}^{j_{\text{cut}}} \frac{2j+1}{2\mathbf{k}} \phi_{B1}^j d_{1/2,1/2}^j(\theta) \\ \phi_{B2}^>(\theta) &= \phi_{B2}(\theta) - \sum_{j=\frac{1}{2}}^{j_{\text{cut}}} \frac{2j+1}{2\mathbf{k}} \phi_{B2}^j d_{-1/2,1/2}^j(\theta).\end{aligned}\quad (5.4.29)$$

In equation (5.4.29),  $\phi_{B1}(\theta)$  and  $\phi_{B2}(\theta)$  are the helicity amplitudes calculated using the Born approximation, without angular momentum projection, and  $\phi_{B1}^j$  and  $\phi_{B2}^j$  are the corresponding partial wave helicity amplitudes calculated up to  $j_{\text{cut}}$ . The helicity amplitudes  $\phi_{B1}^>(\theta)$  and  $\phi_{B2}^>(\theta)$  are computed directly from the optical potential and multiplied by  $-\mu/2\pi$  to produce the normalized helicity amplitude in Fermi units.

2. Solving the three dimensional integral equations: With the advancement in computational power, it is now achievable to directly solve the three dimensional integral equation, resulting from such high energy scattering. In our case though, we need to solve two coupled three dimensional integral equations (equation (5.0.17)). The problem is often reduced to two dimensional integral equations. This technique has been applied in Refs. [121, 123, 134, 137, 138].
3. The third technique, which is what we have adopted here, is to use high-order global adaptive quadrature to numerically solve the oscillatory integrals (encountered at large  $\ell$ ) given in equation (5.2.22). The regular quadrature algorithms failed to accurately calculate the integral at high angular momentum states. For example, we initially made use of the composite Simpson method to perform the integration but encountered problems when  $\ell \gtrsim 15$ . However, with the use of the MATLAB function `quadgk`, the integration was performed satisfactorily, at least for the problems studied here. The draw back with the use of this method is the computation time, as the regular quadrature schemes are almost ten times faster. The algorithm used in this function is described in Ref. [139].

## 5.5 Results and discussions

Results of the differential scattering cross section, analysing power and spin rotation function calculated using the non-local optical potentials in the coupled Lippmann-Schwinger-like equations are presented in this section. The flow chart shown in figure 5.1 illustrates how the function `lippschwinger` calculates the scattering observables. The codes are written in MATLAB.

The function takes as inputs the quadrature points  $k$  and  $k'$ , the optical potentials  $U_\nu$ , and the point Coulomb potential  $V_C^{pt}$ . The calculation of quadrature points and weights have earlier been described. Partial wave optical potentials are calculated and the integral equations are solved to obtain  $\langle \frac{1}{2}, + | K^j(\hat{k}, \hat{k}) | \frac{1}{2}, + \rangle$ , from which the phase shifts are calculated using equation (5.3.17). The helicity amplitudes are computed, and the scattering observables calculated using these amplitudes.

Figures 5.2 and 5.3 show results of the elastic scattering cross section calculated using local (in position space) and non-local (in momentum space) IA2 optical potentials for  $^{40,48,54,58}\text{Ca}$  targets at incident projectile energies of 200 and 500 MeV, respectively. Red dashed lines indicate momentum space calculations using non-local optical potentials while blue dashed lines indicate position space calculations using localised optical potentials. Experimental data are shown in black circles. One observes from figure 5.2 that for  $^{40,48}\text{Ca}$  targets, both local and non-local optical potentials give very good descriptions of the differential cross section data, but the use of non-local optical potentials improve the results at large scattering angles. The non-local optical potentials also give better descriptions of the first angle of dip. The bottom panel in the same figure show the plots for  $^{54,58}\text{Ca}$  targets. One can notice the difference between the two approaches at large scattering angles. Scattering cross-section plots for the same targets are shown in figure (5.3) for incident

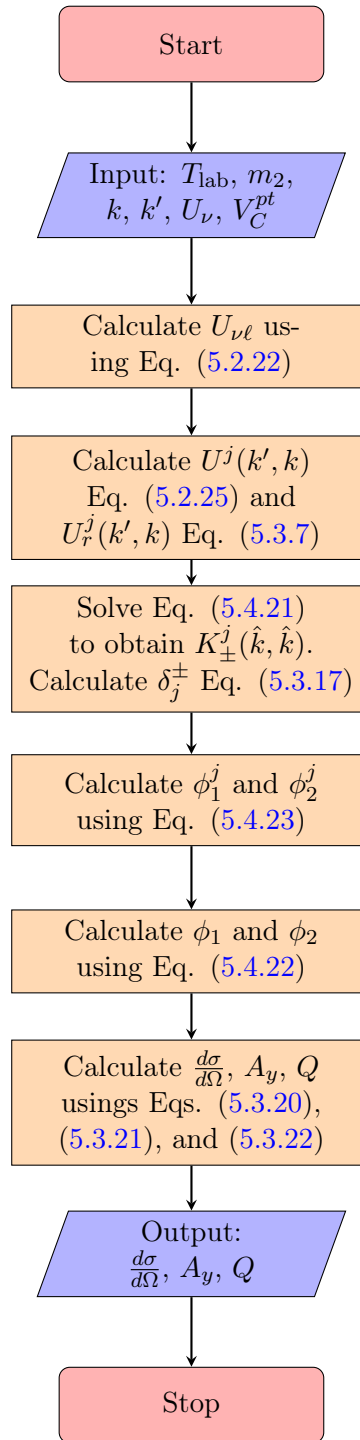


**Figure 5.1:** Flow chart illustrating how the function *Lippschwinger* calculates the scattering observables.

projectile energy of 500 MeV. For  $^{40}\text{Ca}$  target where there is available data, both approaches give competitive descriptions of the scattering cross section data. In all plots, the minor difference between the two approaches is observed at large scattering angles.

Figures 5.4 and 5.5 show plots of the analysing power calculated using local (in position space) and non-local (in momentum space) IA2 optical potentials for  $^{40,48,54,58}\text{Ca}$  targets at incident projectile energies of 200 and 500 MeV, respectively. We observe that the localised optical potentials computed by solving coordinate space Dirac equation gives better descriptions of analysing power data for  $^{40,48}\text{Ca}$  targets. It can not be concluded, however, that the analysing power computed using localised optical potential is better than results obtained using non-local potentials. The poor descriptions of momentum space results may be attributed to the method employed in dealing with the Coulomb potential, because it is known that spin observables, that is analysing power and spin rotation function are very sensitive to the technique used in including Coulomb potential [130]. We believe a better method of treating Coulomb corrections will improve results of the analysing power and spin rotation function especially at incident projectile energy of 200 MeV. The result is better at  $T_{\text{lab}} = 500$  MeV. Similar conclusion can be drawn in figures (5.6) and (5.7) which show plots of spin rotation function at incident projectile energies of 200 and 500 MeV, respectively.

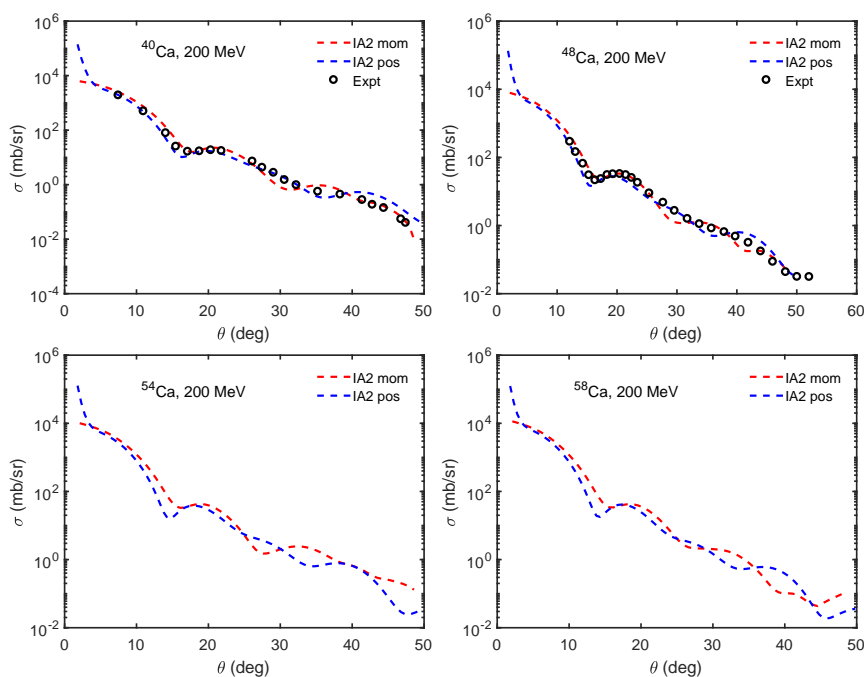


**Figure 5.2:** Scattering cross section calculated in position space and momentum space for  $^{40,48,54,58}\text{Ca}$  targets at  $T_{\text{lab}} = 200$  MeV. Red dashed lines indicate momentum space calculations using non-local potentials while blue dashed lines indicate position space calculations using localised potentials. Experimental data are shown in black circles.

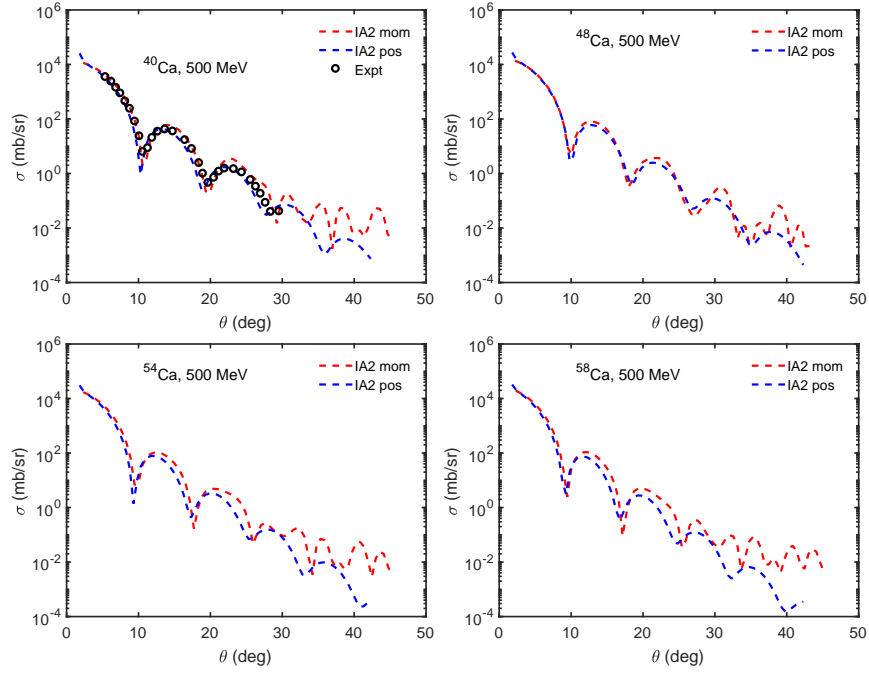


Figure 5.3: Same as in figure 5.2 but for  $T_{\text{lab}} = 500 \text{ MeV}$ .

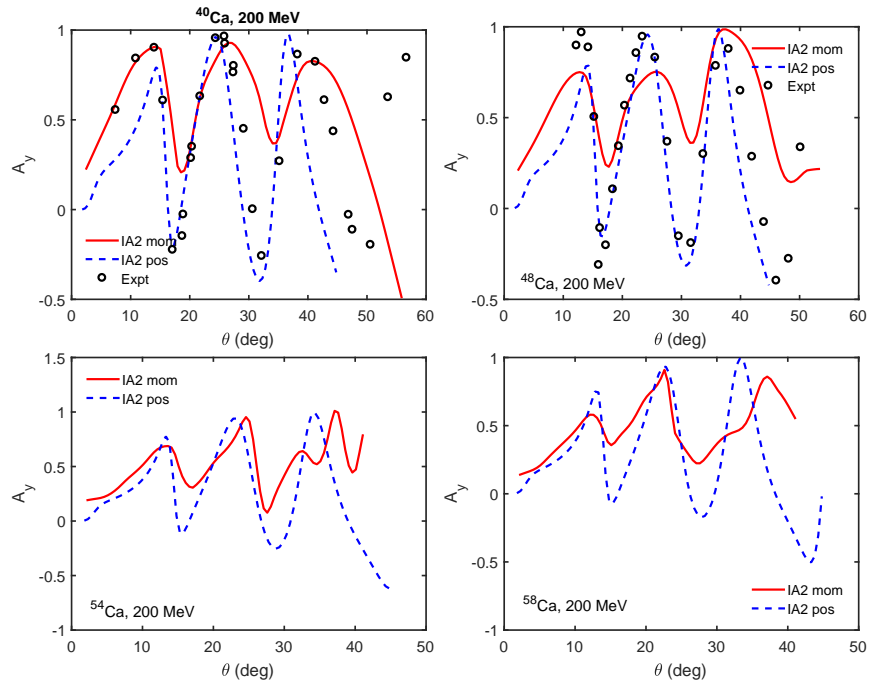
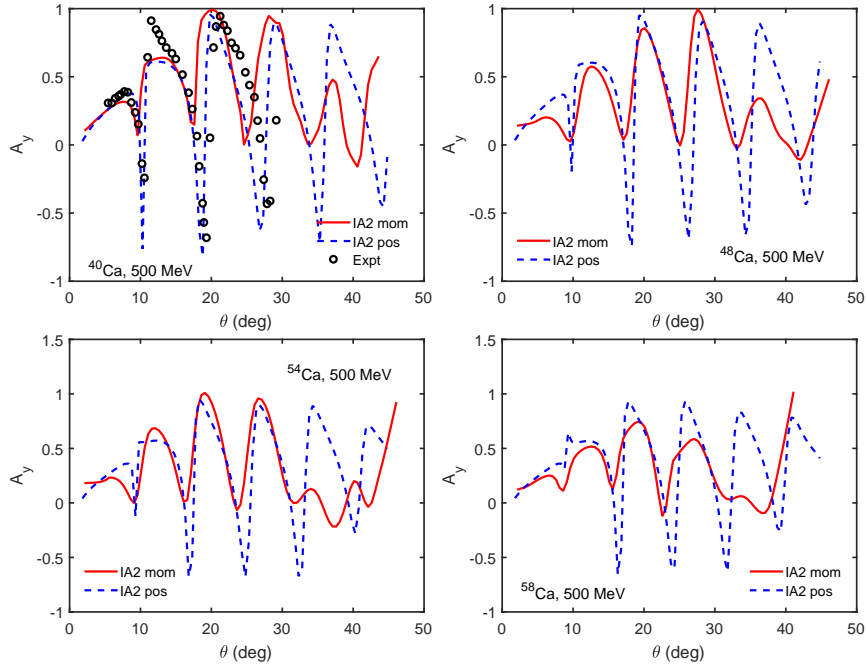


Figure 5.4: Analyzing power calculated in position space and momentum space for  $^{40,48,54,58}\text{Ca}$  targets at  $T_{\text{lab}} = 200 \text{ MeV}$ .

### 5.5.1 Full folding versus optimal factorization in momentum space

Here, we want to examine if use of full-folding optical potentials can give better descriptions of the scattering observables calculated using non-local optical poten-



**Figure 5.5:** Same as in figure 5.4 but for  $T_{\text{lab}} = 500$  MeV.

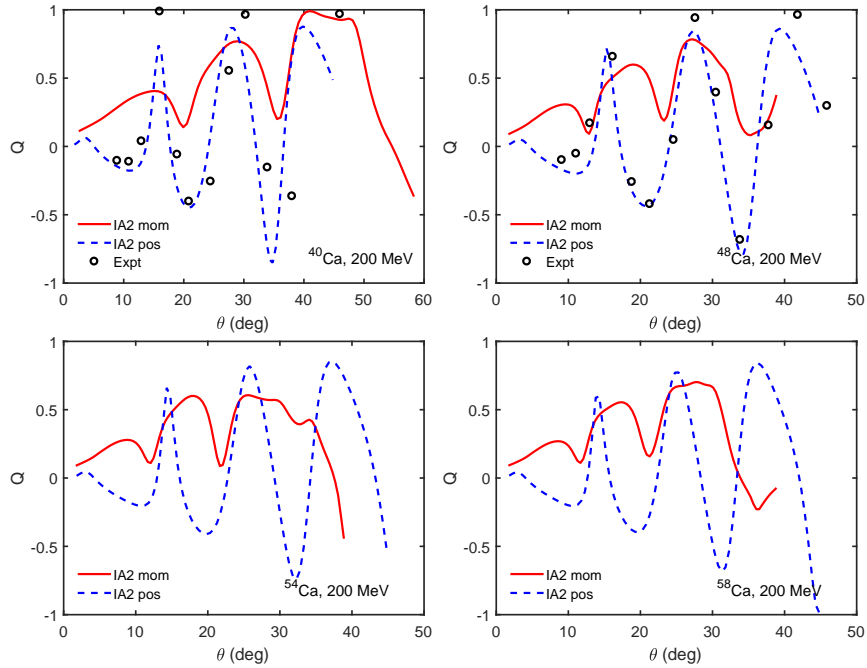


**Figure 5.6:** Spin rotation calculated in position and momentum space for  $^{40,48,54,58}\text{Ca}$  targets at  $T_{\text{lab}} = 200$  MeV.

tials. Figure 5.8 shows results of the scattering observables calculated in momentum space using full-folding optical potential and optimally factorised one for proton scattering on  $^{48}\text{Ca}$  at incident projectile energy of 200 MeV. We observe from the three plots that there is no conspicuous difference between the results obtained us-

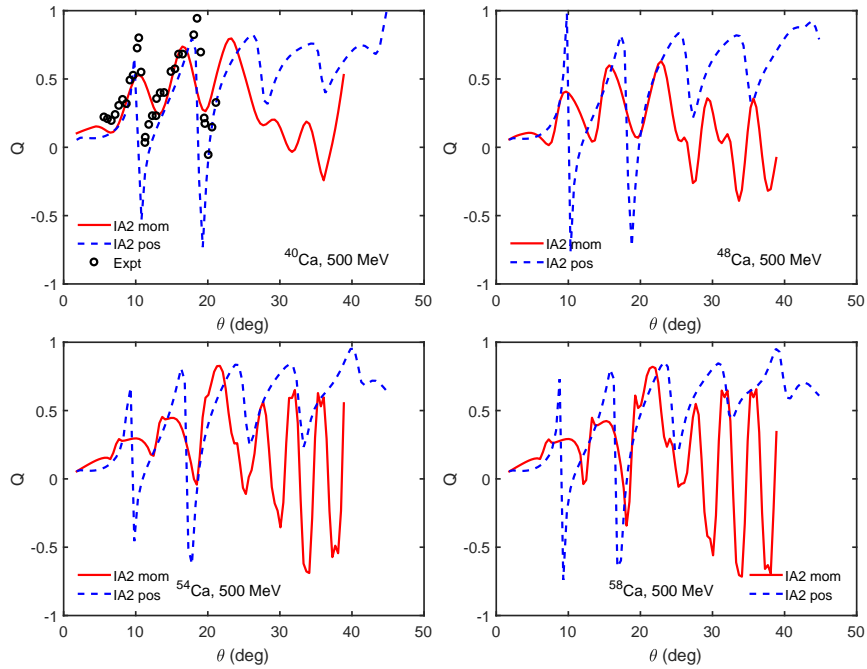


**Figure 5.7:** Same as in figure 5.6 but for  $T_{\text{lab}} = 500$  MeV.

ing full-folding optical potentials and optimally factorised optical potentials. We can therefore conclude that at this incident projectile energy, use of optimally factorised optical potential is sufficient to describe the elastic scattering observables.

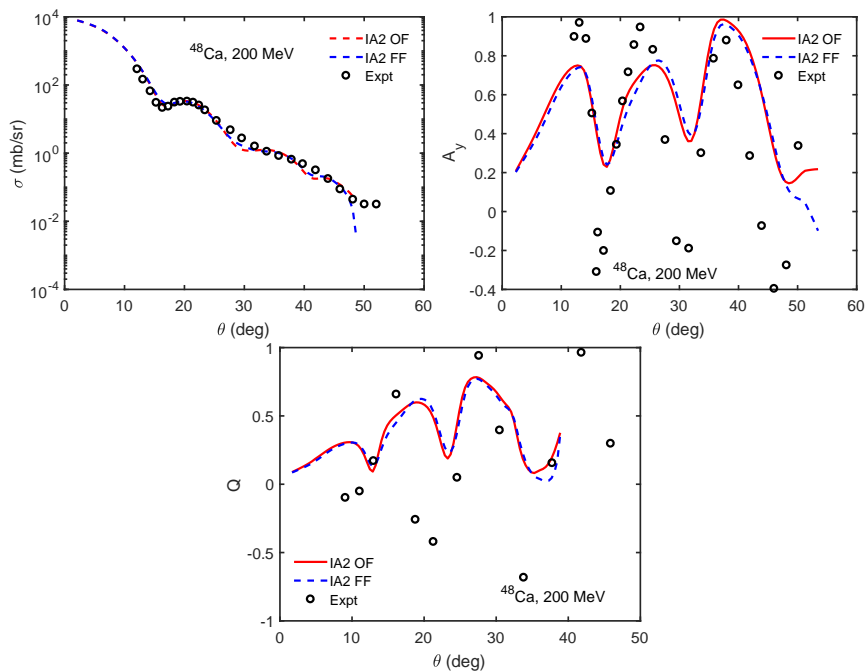


**Figure 5.8:** Elastic scattering observables calculated in momentum space using full-folding optical potential (in blue dashed lines) and optimally factorised one (in red dashed line) for  $p+^{48}\text{Ca}$  target at  $T_{\text{lab}} = 200$  MeV.

### 5.5.2 Effect of using non-local optical potential in IA1 formalism

In chapter 4, we observed that the IA1 formalism did not satisfactorily describe the scattering observable at incident projectile energy of 200 MeV. We have also stated earlier that the relativistic Love-Franey model and IA2 formalism were introduced to solve this problem. Here, we want to study if the use of non-local IA1 optical potentials can improve the results of the elastic scattering observables.

Figure 5.9 shows plots of the scattering observables calculated using the IA1 formalism in both coordinate-space (using localised potentials) and momentum space (using non-local potentials). We observe that the coordinate-space calculation gives better description of the first angle of dip of differential cross section, the momentum space calculation however, give better description at large scattering angles. The two approaches give competitive descriptions of the analysing power and spin rotation function. We can conclude that the use of non-local IA1 optical potential does not solve the problem associated with using the formalism at low energies. The IA2 formalism is recommended to be used at the energies lower than  $\approx 300$  MeV.

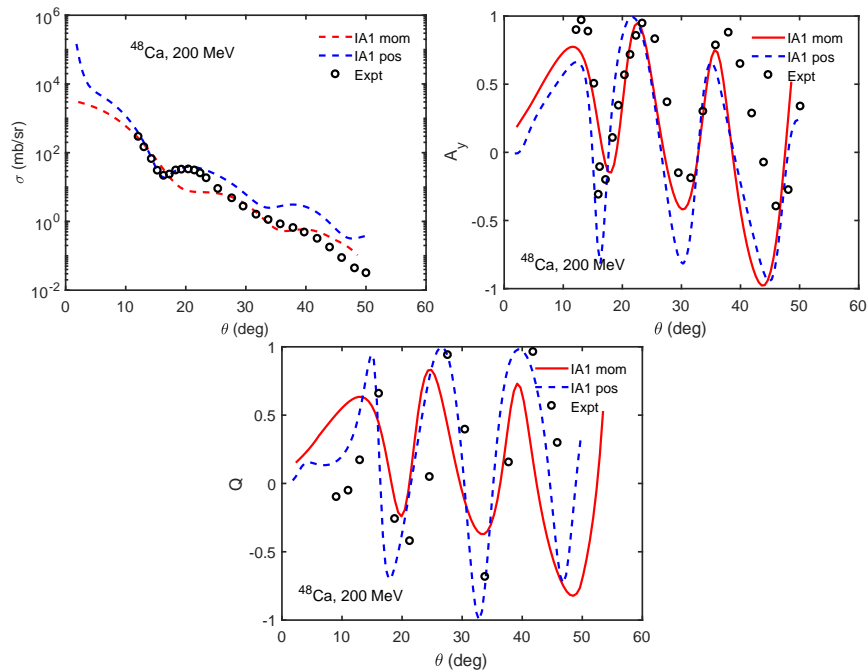


**Figure 5.9:** Elastic scattering observables calculated in momentum space using full-folding optical potential (in blue dashed lines) and optimally factorised one (in red dashed line) for  $p+^{48}\text{Ca}$  target at  $T_{\text{lab}} = 200$  MeV.

## Chapter 6

# Conclusion

We have presented a microscopic study of proton elastic scattering from unstable nuclei using relativistic formalisms. The densities are calculated using bound state wave functions obtained from relativistic mean field theory, employing the QHD I, QHD II, NL3, and FSUGold parameter sets. The different RMF parameter sets give different descriptions of the neutron densities at and close to the interior of the unstable nuclei studied. In the plots of the energy level diagrams, a level inversion was observed with the  $1d_{3/2}$  state coming below the  $2s_{1/2}$  for  $^{48,54}\text{Ca}$  nuclei, a situation that was not observed for  $^{40}\text{Ca}$  isotope. Up to one decimal place, all the RMF models give similar values of the charge densities for calcium isotopes considered here.

The microscopic relativistic optical potentials are calculated using both the IA1 and IA2 formalisms. The optical potentials obtained via global Dirac phenomenology were included to check if the formalism can be applied to the study of unstable nuclei, since the phenomenological potentials were obtained through fits to elastic proton scattering from stable nuclei. As expected, we found that it gives different results with the microscopic formulations for the unstable nuclei. A comparison of the IA1, IA2, and Dirac phenomenology optical potentials shows that the IA2 formalism gives the lowest scalar and vector potential strengths at incident projectile energies of 200 MeV and 500 MeV. At 200 MeV, the IA1 formalism gives potential strengths stronger than Dirac phenomenology for both stable and unstable nuclei. The overly strong scalar and vector optical potentials produced by the IA1 formalism at this low energy (200 MeV) has been attributed to the implicit incorporation of pseudoscalar pion coupling. The optical potentials calculated using optimal factorization are also compared with those obtained with full-folding optical potentials. The effect of using full-folding optical potentials is found at incident projectile energy of 200 MeV, while there is no noticeable difference at 500 MeV and above.

The calculated optical potentials are used as inputs in the Dirac equation. The non-local optical potentials are used in momentum space Dirac equation while the localised optical potentials are employed in coordinate-space Dirac equation. We have decided to use the two approaches to investigate the effect of using non-local optical potentials on the elastic scattering observables for unstable nuclei. After solving the position space Dirac equation, elastic scattering observables were calculated for  $^{40,44,48,52,54,58,60}\text{Ca}$  targets. Plots of the elastic scattering observables for these

calcium isotopes show that the scattering cross section increases as neutron number increases, and the positions of diffraction minima are shifted towards smaller scattering angles. The values of maxima and minima in analysing power are found to decrease as scattering angle increases. Similar behaviour has been observed for the spin rotation function.

In order to check the sensitivity of elastic scattering observables to different RMF densities, we showed plots of the scattering observables with different RMF densities. Except at large scattering angles, all model densities give similar descriptions of the elastic scattering observables for both stable and unstable nuclei considered in this work.

The results of elastic scattering observables computed using IA1 and IA2 formalisms are compared. At incident projectile energy of 500 MeV and 800 MeV, both formalisms give similar descriptions of the elastic scattering observables for both stable and unstable nuclei at low scattering angles, but at large scattering angles, the difference between both formalisms becomes obvious. At incident projectile energy of 200 MeV however, the IA2 gives a better description of the scattering observables for both stable and unstable nuclei. The inability of IA1 formalism to give proper descriptions of the scattering observables at incident projectile energies  $\lesssim 200$  MeV is due to the large scalar and vector optical potentials it gives at low energies.

We also discussed effect of full-folding optical potentials on the scattering observables compared with the calculations using optimally factorised optical potentials. We found that the use of full-folding optical potentials improve the spin observables (analysing power and spin rotation function) at incident projectile energy of 200 MeV, while there is no discernible difference at 500 MeV. However, there is no significant difference between using full-folding optical potential and optimally factorised one in momentum space (using non-local potentials) at incident projectile energy of 200 MeV. Of course, at incident projectile energies greater than 200 MeV, Pauli-blocking effect is known to be negligible.

Finally, we studied elastic scattering observables calculated using non-local optical potentials. To achieve this we substituted the non-local optical potential into momentum space Dirac equation, which is then transformed to two coupled integral equations. The transformation is necessary because the scattering observables are connected to the T-matrix. The treatment of solutions at high angular momentum states is done using high-order global adaptive quadratures to solve the oscillatory integrals encountered at high angular momenta. This approach is sufficient for the nuclei studied in this work and at incident projectile energies  $\lesssim 500$  MeV. Matrix inversion technique was used to solve the coupled integral equations, from which the elastic scattering observables are computed. We observed that results of momentum space calculations using non-local optical potentials give better descriptions of differential cross-section data at incident projectile energy of 200 MeV. There is competitive description of differential cross-section data at incident projectile energy of 500 MeV between the two approaches. No conclusion can be drawn for calculations of analysing power and spin rotation function at  $T_{\text{lab}} = 200$  MeV because our current treatment of Coulomb correction needs to be improved. It is known that

spin observables (analysing power and spin rotation function) are very sensitive to the technique used in including Coulomb potential. We believe a better method of treating Coulomb corrections especially at incident projectile energy of 200 MeV will improve results of the analysing power and spin rotation function calculated in momentum space using non-local optical potentials.

To summarize, we respond to the questions posed in chapter 1.

- *Can reaction studies from unstable nuclei provide a better discriminator in the choice between the IA1 and IA2 representations of the nucleon-nucleon invariant amplitudes?*

IA1 optical potential gives large scalar and vector potential strengths at low energy, which results in poor description of elastic scattering observables for both stable and unstable nuclei, especially at large scattering angles. So to study unstable nuclei at energies lower than  $\approx 200$  MeV, IA2 optical potential is recommended to be used. At energies  $\gtrsim 500$  MeV, both formalisms give similar descriptions of the scattering observables at low scattering angles. The difference between the two approaches is observed at large scattering angles. Experimental data are therefore required at large scattering angles for incident projectile energy of 500 MeV to determine which formalism gives better description of unstable nuclei at this incident energy.

- *What is the effect of using full-folding optical potential compared to the factorised form of the optical potential?*

We found that the use of full-folding optical potentials improve the description of scattering observables, especially analysing power and spin rotation function at incident projectile energy of 200 MeV. We therefore recommend using full-folding optical potentials at  $T_{\text{lab}} \lesssim 200$  MeV. The use of optimally factorised optical potentials at incident projectile energy of 500 MeV and above is sufficient.

- *What is the effect of using non-local form of the optical potential on the scattering observables?*

Scattering cross section results obtained using non-local potentials give better descriptions of experimental data at low energies and large scattering angles than results obtained using localised optical potentials. Use of localised optical potential at incident energies above 500 MeV is sufficient because there is no discernible difference between using non-local potentials and localised potentials at this energy. No conclusion can be drawn yet for analysing power and spin rotation function because the approach used to treat Coulomb contribution here did not give satisfactory results for the spin observables.

- *The effect of the different forms of the Lagrangian density, namely QHDII, NL3 and FSUGold.*

The different Lagrangian densities give similar descriptions of scattering observables at intermediate energies for both stable and unstable nuclei considered here. Minor difference are however, observed at large scattering angles.

# Appendices

# Appendix A

## A.1 Dirac Matrices

$$\alpha_i = \begin{pmatrix} 0 & \sigma_i \\ \sigma_i & 0 \end{pmatrix}, \quad \beta = \begin{pmatrix} 1 & 0 \\ 0 & -1 \end{pmatrix}, \quad (\text{A.1.1})$$

$$\gamma^i = \begin{pmatrix} 0 & \sigma_i \\ -\sigma_i & 0 \end{pmatrix}, \quad \gamma^0 = \begin{pmatrix} 1 & 0 \\ 0 & -1 \end{pmatrix}, \quad \gamma^5 = \begin{pmatrix} 0 & 1 \\ 1 & 0 \end{pmatrix}, \quad (\text{A.1.2})$$

where the 0 and 1 are  $2 \times 2$  matrices, and  $\sigma_i$  are the Pauli matrices shown below.

$$\sigma^{ij} = \begin{pmatrix} \sigma_k & 0 \\ 0 & \sigma_k \end{pmatrix}, \quad \sigma^{0i} = i \begin{pmatrix} 0 & \sigma_i \\ \sigma_i & 0 \end{pmatrix}, \quad \sigma^{0i} = i\alpha_i, \quad (\text{A.1.3})$$

and the Pauli matrices

$$\sigma_1 = \begin{pmatrix} 0 & 1 \\ 1 & 0 \end{pmatrix}, \quad \sigma_2 = \begin{pmatrix} 0 & -i \\ i & 0 \end{pmatrix}, \quad \sigma_3 = \begin{pmatrix} 1 & 0 \\ 0 & -1 \end{pmatrix}. \quad (\text{A.1.4})$$

More explicitly,

$$\gamma^0 = \begin{pmatrix} 1 & 0 & 0 & 0 \\ 0 & 1 & 0 & 0 \\ 0 & 0 & -1 & 0 \\ 0 & 0 & 0 & -1 \end{pmatrix}, \quad \gamma^1 = \begin{pmatrix} 0 & 0 & 0 & 1 \\ 0 & 0 & 1 & 0 \\ 0 & -1 & 0 & 0 \\ -1 & 0 & 0 & 0 \end{pmatrix}, \quad \gamma^2 = \begin{pmatrix} 0 & 0 & 0 & -i \\ 0 & 0 & i & 0 \\ 0 & i & 0 & 0 \\ -i & 0 & 0 & 0 \end{pmatrix}, \quad (\text{A.1.5})$$

$$\gamma^3 = \begin{pmatrix} 0 & 0 & 1 & 0 \\ 0 & 0 & 0 & -1 \\ -1 & 0 & 0 & 0 \\ 0 & 1 & 0 & 0 \end{pmatrix}, \quad \gamma^5 = \begin{pmatrix} 0 & 0 & 1 & 0 \\ 0 & 0 & 0 & 1 \\ 1 & 0 & 0 & 0 \\ 0 & 1 & 0 & 0 \end{pmatrix} \quad (\text{A.1.6})$$

The gamma matrices have the following properties:

$$\gamma^\mu \gamma^\nu + \gamma^\nu \gamma^\mu \stackrel{\text{def}}{=} \{\gamma^\mu, \gamma^\nu\} = 2g^{\mu\nu}, \quad (\text{A.1.7})$$

where the metric tensor

$$g^{\mu\nu} = \begin{pmatrix} 1 & 0 & 0 & 0 \\ 0 & -1 & 0 & 0 \\ 0 & 0 & -1 & 0 \\ 0 & 0 & 0 & -1 \end{pmatrix}. \quad (\text{A.1.8})$$

$$(\gamma^i)^2 = -1, \quad (\gamma^0)^2 = 1, \quad i = 1, 2, 3 \quad (\text{A.1.9})$$

$$\gamma^\dagger = -\gamma, \quad \gamma_0^\dagger = \gamma_0 \quad (\text{A.1.10})$$

# Appendix B

## B.1 Numerical differentiation of data

In this appendix, numerical differentiation and integration of data will be discussed. The first derivative of a function  $f(x)$  with respect to  $x$  is given by [140]

$$f'(x) \equiv \lim_{h \rightarrow 0} \left[ \frac{f(x+h) - f(x)}{h} \right]. \quad (\text{B.1.1})$$

The second derivative is defined by

$$f''(x) \equiv \lim_{h \rightarrow 0} \left[ \frac{f'(x+h) - f'(x)}{h} \right]. \quad (\text{B.1.2})$$

There are quite a few methods that can be used to find the derivative of a function on a computer. Some of them are the forward-difference method, backward difference method, central difference method, and Richardson extrapolation method. Among the techniques listed, Richardson extrapolation gives the most accurate result. The Richardson extrapolation method for first derivative is given by

$$f'_R(x) = \frac{8f(x+h) - 8f(x-h) - f(x+2h) + f(x-2h)}{12h} + O(h^4), \quad (\text{B.1.3})$$

while for second derivative, it is given by

$$f''_R(x) = \frac{-f(x+2h) + 16f(x+h) - 30f(x) + 16f(x-h) - f(x-2h)}{12h^2} + O(h^4). \quad (\text{B.1.4})$$

Equations (B.1.3) and (B.1.4) were used to carry out the first and second numerical differentiation of data in this thesis.

## B.2 Numerical integration of data

To carry out numerical integration, Simpson's rule was employed. Trapezoid rule is another method but of lower accuracy compared to the Simpson's rule. There is a built-in MATLAB function to numerically integrate data using Trapezoid's rule,

called `trapz`. The following formula is used for the Simpson's rule [141]

$$\int_a^b f(x)dx \cong \sum_{m=0}^{N/2-1} \int_{x_{2m}}^{x_{2m+2}} f(x)dx + \frac{h}{3} \{(f_0 + 4f_1 + f_2) + (f_2 + 4f_3 + f_4) + \cdots + (f_{N-2} + 4f_{N-1} + f_N)\}. \quad (\text{B.2.1})$$

Equation (B.2.1) is cast into the MATLAB function `simps(x,f)`, where  $f$  is the function to integrate with respect to  $x$ . There is also the Romberg integration method, but the Simpson's method is adequate for most of this work.

### B.3 Runge–Kutta–Fehlberg method

In solving second-order differential equations arising from Physics problems, the fourth-order Runge–Kutta is the most often used because it has a better convergence, and it is numerically stable compared with other methods such as midpoint integration and Euler methods. An improvement on the fourth-order Runge–Kutta method (error of order  $O(h^4)$ ) is the Runge–Kutta–Fehlberg method, with error of order  $O(h^6)$ . This method is self-starting and the error can be easily computed. For an initial value problem of the form:

$$y' = F(x, y(x)), \quad y(x_0) = y_0, \quad (\text{B.3.1})$$

the solution of the differential equation ( $y(x)$ ) is obtained by iterating the equations:

$$y_{n+1} = y_n + \left( \frac{16k_1}{135} + \frac{6656k_3}{12825} + \frac{28561k_4}{56430} - \frac{9k_5}{50} + \frac{2k_6}{55} \right), \\ x_{n+1} = x_n + h \quad (\text{B.3.2})$$

where  $h$  is the step-size,  $n = 0, 1, 2, \dots$ , and the coefficients  $k_1 - k_6$  are computed using

$$k_1 = hF(x_n, y_n) \\ k_2 = hF\left(x_n + \frac{h}{4}, y_n + \frac{k_1}{4}\right) \\ k_3 = hF\left(x_n + \frac{3h}{8}, y_n + \frac{3k_1}{32} + \frac{9k_2}{32}\right) \\ k_4 = hF\left(x_n + \frac{12h}{13}, y_n + \frac{1932k_1}{2197} - \frac{7200k_2}{2197} + \frac{7296k_3}{2197}\right) \\ k_5 = hF\left(x_n + h, y_n + \frac{439k_1}{216} - 8k_2 + \frac{3680k_3}{513} - \frac{845k_4}{4104}\right) \\ k_6 = hF\left(x_n + \frac{h}{2}, y_n - \frac{8k_1}{27} + 2k_2 - \frac{3544k_3}{2565} + \frac{1859k_4}{4104} - \frac{11k_5}{40}\right). \quad (\text{B.3.3})$$

The error is calculated using

$$error = \frac{1}{360}k_1 - \frac{128}{475}k_3 - \frac{2197}{75240}k_4 + \frac{1}{50}k_5 + \frac{2}{55}k_6 + O(h^6). \quad (\text{B.3.4})$$

In order to solve a second order differential equation, one has to convert the second-order differential equation to two first-order differential equations. For example, to solve a second order differential equation of the form

$$y'' = F(x, y(x), y'(x)), \quad y(x_0) = y_0, \quad y'(x_0) = y'_0. \quad (\text{B.3.5})$$

One converts equation (B.3.5) to two first-order differential equations

$$\begin{aligned} R(x) &= y(x) \\ T(x) &= y'(x) \end{aligned} \quad (\text{B.3.6})$$

The second ODE can now be written as

$$\begin{aligned} \frac{dR(x)}{dx} &= F_1(x, R(x), T(x)) = T(x) \\ \frac{dT(x)}{dx} &= F_2(x, R(x), T(x)) = F(x, R(x), T(x)) \end{aligned} \quad (\text{B.3.7})$$

The RKF method is then written as

$$\begin{aligned} R_{n+1} &= R_n + \left( \frac{16k_1}{135} + \frac{6656k_3}{12825} + \frac{28561k_4}{56430} - \frac{9k_5}{50} + \frac{2k_6}{55} \right), \\ T_{n+1} &= T_n + \left( \frac{16m_1}{135} + \frac{6656m_3}{12825} + \frac{28561m_4}{56430} - \frac{9m_5}{50} + \frac{2m_6}{55} \right), \\ x_{n+1} &= x_n + h, \end{aligned} \quad (\text{B.3.8})$$

where

$$\begin{aligned}
k_1 &= hF_1(x_n, R_n, T_n) \\
k_2 &= hF_1\left(x_n + \frac{h}{4}, R_n + \frac{k_1}{4}, T_n + \frac{m_1}{4}\right) \\
k_3 &= hF_1\left(x_n + \frac{3h}{8}, R_n + \frac{3k_1}{32} + \frac{9k_2}{32}, T_n + \frac{3m_1}{32} + \frac{9m_2}{32}\right) \\
k_4 &= hF_1\left(x_n + \frac{12h}{13}, R_n + \frac{1932k_1}{2197} - \frac{7200k_2}{2197} + \frac{7296k_3}{2197}, T_n + \frac{1932m_1}{2197} - \frac{7200m_2}{2197} + \frac{7296m_3}{2197}\right) \\
k_5 &= hF_1\left(x_n + h, R_n + \frac{439k_1}{216} - 8k_2 + \frac{3680k_3}{513} - \frac{845k_4}{4104}, T_n + \frac{439m_1}{216} - 8m_2 \right. \\
&\quad \left. + \frac{3680m_3}{513} - \frac{845m_4}{4104}\right) \\
k_6 &= hF_1\left(x_n + \frac{h}{2}, R_n - \frac{8k_1}{27} + 2k_2 - \frac{3544k_3}{2565} + \frac{1859k_4}{4104} - \frac{11k_5}{40}, T_n - \frac{8m_1}{27} + 2m_2 \right. \\
&\quad \left. - \frac{3544m_3}{2565} + \frac{1859m_4}{4104} - \frac{11k_5}{40}\right), \\
m_1 &= hF_2(x_n, R_n, T_n) \\
m_2 &= hF_2\left(x_n + \frac{h}{4}, R_n + \frac{k_1}{4}, T_n + \frac{m_1}{4}\right) \\
m_3 &= hF_2\left(x_n + \frac{3h}{8}, R_n + \frac{3k_1}{32} + \frac{9k_2}{32}, T_n + \frac{3m_1}{32} + \frac{9m_2}{32}\right) \\
m_4 &= hF_2\left(x_n + \frac{12h}{13}, R_n + \frac{1932k_1}{2197} - \frac{7200k_2}{2197} + \frac{7296k_3}{2197}, T_n + \frac{1932m_1}{2197} - \frac{7200m_2}{2197} + \frac{7296m_3}{2197}\right) \\
m_5 &= hF_2\left(x_n + h, R_n + \frac{439k_1}{216} - 8k_2 + \frac{3680k_3}{513} - \frac{845k_4}{4104}, T_n + \frac{439m_1}{216} - 8m_2 \right. \\
&\quad \left. + \frac{3680m_3}{513} - \frac{845m_4}{4104}\right) \\
m_6 &= hF_2\left(x_n + \frac{h}{2}, R_n - \frac{8k_1}{27} + 2k_2 - \frac{3544k_3}{2565} + \frac{1859k_4}{4104} - \frac{11k_5}{40}, T_n - \frac{8m_1}{27} + 2m_2 \right. \\
&\quad \left. - \frac{3544m_3}{2565} + \frac{1859m_4}{4104} - \frac{11k_5}{40}\right). \tag{B.3.9}
\end{aligned}$$

One of the advantages of this scheme is that it solves for both  $R_n(x)$  and  $T_n(x)$ , simultaneously.

## B.4 Noumerov algorithm

One of the most widely used method to solve second order differential equation (DE) arising from Physics problems is the Noumerov algorithm. It is an efficient and accurate method used to solve second-order differential equations (without first-order term) of the form:

$$y'' = u(x) + v(x)y. \tag{B.4.1}$$

The centered-difference equation [142]

$$y_{n+1} - 2y_n + y_{n-1} \cong 2 \left( \frac{h^2}{2} y'' + \frac{h^4}{4!} y'''' + O(h^6) \right), \quad (\text{B.4.2})$$

is used to obtain a finite difference scheme. In equation (B.4.2),  $y_n = y(x_n)$  and it is assumed that the  $x_n$  have uniform separation  $h$ . If we denote  $y''$  in equation (B.4.1) by  $Y$ , then equation (B.4.1) can be written as

$$Y = u(x) + v(x)y. \quad (\text{B.4.3})$$

Substituting equation (B.4.3) into equation (B.4.2), gives

$$y_{n+1} = 2y_n - y_{n-1} + h^2 Y_n + \frac{h^4}{12} Y_n'' + O(h^6). \quad (\text{B.4.4})$$

Using the following recurrence relation for the second derivative of  $Y$

$$Y_{n+1} - 2Y_n + Y_{n-1} \cong 2 \left( \frac{h^2}{2} Y'' + \frac{h^4}{4!} Y'''' + O(h^6) \right), \quad (\text{B.4.5})$$

we obtain the Noumerov algorithm as

$$y_{n+1} = \frac{2y_n - y_{n-1} + \frac{h^2}{12} (u_{n+1} + 10Y_n + Y_{n-1})}{1 - h^2 \frac{v_{n+1}}{12}}. \quad (\text{B.4.6})$$

The error in the Noumerov algorithm is of order  $O(h^6)$ . However, unlike the Runge–Kutta–Fehlberg method which is self–starting, the Numerov algorithm requires the knowledge of two previous solutions.

## Appendix C

### C.1 Some constants used in IA2 potential

The nonvanishing values of the scalar coefficients  $C_{nk}^m$  are given below.

$$\begin{aligned}
C_{1,1}^1 &= 1, C_{2,2}^2 = 1, C_{2,4}^4 = 1, C_{3,3}^3 = 1, C_{6,2}^1 = \frac{E(\mathbf{k}) + E(\mathbf{k}')}{2m}, C_{7,1}^2 = \frac{E(\frac{1}{2}\mathbf{q})}{m}, \\
C_{6,4}^1 &= \frac{2\mathbf{q} \cdot \mathbf{k} - \mathbf{q}^2}{2m}, C_{10,1}^2 = \frac{E(\mathbf{k}') + E(\frac{1}{2}\mathbf{q})}{8m}, C_{10,1}^4 = \frac{3}{16}, C_{11,1}^2 = \frac{E(\mathbf{k}) + E(\frac{1}{2}\mathbf{q})}{8m}, \\
C_{10,1}^6 &= -\frac{1}{8}, C_{11,1}^6 = -\frac{1}{8}, C_{11,1}^4 = -\frac{1}{16}, C_{10,2}^5 = -\frac{1}{8}, C_{10,2}^3 = -\frac{3}{16}, \\
C_{11,2}^1 &= \frac{E(\mathbf{k}) + E(\frac{1}{2}\mathbf{q})}{8m}, C_{11,2}^5 = \frac{1}{8}, C_{11,2}^3 = -\frac{1}{16}, C_{10,3}^4 = \frac{E(\mathbf{k}') + E(\frac{1}{2}\mathbf{q})}{8m}, \\
C_{10,3}^2 &= \frac{-2\mathbf{q} \cdot \mathbf{k} + \frac{3}{2}\mathbf{q}^2}{8m^2}, C_{10,3}^8 = \frac{1}{8}, C_{11,3}^4 = \frac{-E(\mathbf{k}) - E(\frac{1}{2}\mathbf{q})}{8m}, \\
C_{11,3}^8 &= \frac{1}{8}, C_{11,3}^2 = \frac{1}{16} \frac{\mathbf{q}^2}{m^2}, C_{10,4}^3 = \frac{E(\mathbf{k}') + E(\frac{1}{2}\mathbf{q})}{8m}, C_{10,4}^7 = -\frac{1}{8}, C_{10,2}^1 = \frac{E(\mathbf{k}') + E(\frac{1}{2}\mathbf{q})}{8m}, \\
C_{10,4}^1 &= \frac{2\mathbf{q} \cdot \mathbf{k} - \frac{3}{2}\mathbf{q}^2}{8m^2}, C_{11,4}^3 = \frac{-E(\mathbf{k}) - E(\frac{1}{2}\mathbf{q})}{8m}, C_{11,4}^7 = \frac{1}{8}, C_{11,4}^1 = \frac{1}{16} \frac{\mathbf{q}^2}{m^2}.
\end{aligned} \tag{C.1.1}$$

Using the rule,

$$\begin{aligned}
C_{12,k}^m &= (-1)^{k+1} C_{10,k}^m, \\
C_{13,k}^m &= (-1)^k C_{11,k}^m,
\end{aligned} \tag{C.1.2}$$

the coefficients  $C_{12,k}^m$  and  $C_{13,k}^m$  are obtained for covariants  $K_{12}$  and  $K_{13}$ . The above equations give the nonvanishing values of  $C_{nk}^m$ . Values not determined from equations (C.1.1) or (C.1.2) are zero.

The values of  $\phi_{ijk}$  needed to evaluate  $D_{m\nu}^{\rho_1\rho_1}$  in equation (3.4.23) are given below.

$$\begin{aligned}
\phi_{i1k} &= \delta_{ik}, \quad i, k = 1 - 8 \\
\phi_{221} &= \phi_{256} = \phi_{265} = \phi_{278} = \phi_{287} = 1, \\
\phi_{324} &= \phi_{357} = \phi_{423} = \phi_{467} = \phi_{728} = \phi_{827} = 1, \\
\phi_{234} &= \phi_{243} = \phi_{368} = \phi_{458} = \phi_{526} = -1, \\
\phi_{537} &= \phi_{548} = \phi_{625} = \phi_{638} = \phi_{657} = -1, \\
\phi_{331} &= \phi_{342} = \phi_{375} = \phi_{485} = \phi_{746} = \phi_{845} = a, \\
\phi_{386} &= \phi_{432} = \phi_{441} = \phi_{476} = \phi_{735} = \phi_{836} = -a, \\
\phi_{362} &= \phi_{373} = \phi_{384} = \phi_{452} = \phi_{474} = \phi_{483} = \phi_{755}c, \\
\phi_{766} &= \phi_{777} = \phi_{788} = \phi_{856} = \phi_{865} = \phi_{878} = \phi_{887} = c, \\
\phi_{351} &= \phi_{461} = -c, \\
\phi_{551} &= \phi_{652} = \phi_{674} = \phi_{683} = \phi_{753} = \phi_{863} = b, \\
\phi_{562} &= \phi_{573} = \phi_{584} = \phi_{661} = \phi_{764} = \phi_{854} = -b, \\
\phi_{771} &= \phi_{784} = \phi_{872} = \phi_{881} = -ab,
\end{aligned} \tag{C.1.3}$$

where

$$\begin{aligned}
a &= \frac{\mathbf{q}^2}{m^2}, \\
b &= \frac{\mathbf{k}^2}{m^2}, \\
c &= \frac{2\mathbf{q}^2 \cdot \mathbf{k}}{m^2}.
\end{aligned} \tag{C.1.4}$$

Values of  $\phi_{ijk}$  not given in equation (C.1.3) are zero.

# Appendix D

## D.1 Coulomb functions

The regular and irregular coulomb functions are given by the following asymptotic formulas which may be used for large values of  $\rho$ :

$$\begin{aligned} F_0 &\sim \sin [Re(\phi_0)] e^{-Im(\phi_0)} \\ F_1 &\sim \sin [Re(\phi_1)] e^{-Im(\phi_1)} \\ G_0 &\sim \cos [Re(\phi_0)] e^{-Im(\phi_0)} \\ G_1 &\sim \cos [Re(\phi_1)] e^{-Im(\phi_1)} \end{aligned} \quad (D.1.1)$$

where

$$\begin{aligned} \phi_0 &= \rho - \eta \ln 2\rho + \sigma_0 + \sum_{k=2}^{\infty} \frac{a_k}{\rho^{k-1}} \left( \frac{1}{1-k} \right) \\ \phi_1 &= \rho - \eta \ln 2\rho + \sigma_1 - \frac{\pi}{2} + \sum_{k=2}^{\infty} \frac{b_k}{\rho^{k-1}} \left( \frac{1}{1-k} \right). \end{aligned} \quad (D.1.2)$$

Here,  $\rho = kr$ , and

$$\begin{aligned} a_1 &= -\eta, \quad a_2 = \frac{-\eta^2}{2} + i\eta \\ b_1 &= -\eta, \quad b_2 = -\frac{2+\eta^2}{2} + \frac{i\eta}{2} \\ a_k &= -\left( \frac{1}{2} \sum_{m=1}^{k-1} a_m a_{k-m} \right) - i \frac{k-1}{2} a_{k-1}. \end{aligned} \quad (D.1.3)$$

The same recurrence relation is valid for  $b_k$ . The coulomb phase shifts for all  $\ell$  are calculated using

$$\sigma_\ell = \sigma_0 + \sum_{s=1}^{\ell} \tan^{-1} \frac{\eta}{s}, \quad (D.1.4)$$

where  $\sigma_0 = \arg\Gamma(1+i\eta)$  is calculated using the approximation

$$\begin{aligned} \sigma_0 &\cong -\eta + \frac{\eta}{2} \ln(\eta^2 + 16) + \frac{7}{2} \tan^{-1} \left( \frac{\eta}{4} \right) - \left[ \tan^{-1} \eta + \tan^{-1} \left( \frac{\eta}{2} \right) + \tan^{-1} \left( \frac{\eta}{3} \right) \right] \\ &\quad - \frac{\eta}{12(\eta^2 + 16)} \left[ 1 + \frac{1}{30} \frac{\eta^2 - 48}{(\eta^2 + 16)^2} + \frac{1}{105} \frac{\eta^4 - 160\eta^2 + 1280}{(\eta^2 + 16)^4} \right]. \end{aligned} \quad (D.1.5)$$

The irregular function  $G_\ell$  for  $\ell > 1$  is computed using forward recurrence relation

$$G_{\ell+1} = \frac{(2\ell + 1) \left[ \eta + \frac{\ell(\ell+1)}{\rho} \right] G_\ell - (\ell + 1) [\ell^2 + \eta^2]^{\frac{1}{2}} G_{\ell-1}}{\ell [(\ell + 1)^2 + \eta^2]^{\frac{1}{2}}}. \quad (\text{D.1.6})$$

To calculate  $F_\ell$  for  $\ell = \ell_{\max} + 1, \dots, 0$ , we let

$$\ell^{(1)} = \ell_{\max} + 10, \quad F_{\ell^{(1)}+1}^{(1)} = 0, \quad \text{and} \quad F_{\ell^{(1)}}^{(1)} = 0.1. \quad (\text{D.1.7})$$

Successive values of  $F_\ell^{(1)}$  are then calculated via the downward recurrence formula:

$$F_{\ell-1}^{(1)} = \frac{(2\ell + 1) \left[ \eta + \frac{\ell(\ell+1)}{\rho} \right] F_\ell^{(1)} - \ell [(\ell + 1)^2 + \eta^2]^{\frac{1}{2}} F_{\ell+1}^{(1)}}{(\ell + 1) [\ell^2 + \eta^2]^{\frac{1}{2}}}. \quad (\text{D.1.8})$$

We obtain  $F_\ell$  using

$$F_\ell = \frac{F_\ell^{(1)}}{\alpha}, \quad \ell = \ell_{\max} + 1, \dots, 0, \quad (\text{D.1.9})$$

where

$$\alpha = \left( F_0^{(1)} G_1 - F_1^{(1)} G_0 \right) (1 + \eta^2)^{\frac{1}{2}}. \quad (\text{D.1.10})$$

The derivatives of the coulomb functions are computed using

$$J'_\ell = \frac{\left[ \frac{(\ell+1)^2}{\rho} + \eta \right] J_\ell - [(\ell + 1)^2 + \eta^2]^{\frac{1}{2}} J_{\ell+1}}{\ell + 1}, \quad (\text{D.1.11})$$

where  $J_\ell$  represents either  $F_\ell$  or  $G_\ell$ . The legendre polynomials are computed by means of the recurrence relations

$$(\ell + 1)P_{\ell+1}(\cos \theta) = (2\ell + 1) \cos \theta P_\ell(\cos \theta) - \ell P_{\ell-1}(\cos \theta), \quad (\text{D.1.12})$$

and

$$P_\ell^{(1)}(\cos \theta) = \frac{\ell + 1}{\sin \theta} \{ \cos \theta P_\ell(\cos \theta) - P_{\ell+1}(\cos \theta) \}, \quad (\text{D.1.13})$$

where

$$P_0(\cos \theta) = 1, \quad P_1(\cos \theta) = \cos \theta. \quad (\text{D.1.14})$$

The phase shifts are computed by matching the logarithmic derivatives of the coulomb functions with those of the numerically integrated functions at large value of  $\rho$ , where the nuclear potential becomes negligible. Matching the logarithmic derivative of the nuclear function  $u_\ell$  with that of its asymptotic form

$$F_\ell + C_\ell (G_\ell + iF_\ell) \quad (\text{D.1.15})$$

yields

$$\frac{u'_\ell}{u_\ell} = \frac{F'_\ell + C_\ell (G'_\ell + iF'_\ell)}{F_\ell + C_\ell (G_\ell + iF_\ell)} \quad (\text{D.1.16})$$

which then leads to

$$C_\ell^\pm = \frac{u_\ell^\pm F'_\ell - u_\ell^{\pm'} F_\ell}{u_\ell^{\pm'} G_\ell - u_\ell^\pm G'_\ell + i(u_\ell^{\pm'} F_\ell - u_\ell^\pm F'_\ell)}, \quad (\text{D.1.17})$$

where  $C_\ell$  is related to the complex phase shifts via

$$C_\ell^\pm = \frac{1}{2i} \left[ e^{2i\delta_\ell^\pm} - 1 \right] \quad (\text{D.1.18})$$

# List of References

- [1] Richard D. Smith and Stephen J. Wallace. Spin observables in quasi-elastic proton-nucleus scattering near 1 GeV. *Phys. Rev. C*, 32:1654–1666, Nov 1985.
- [2] L. Ray and G. W. Hoffmann. Relativistic and nonrelativistic impulse approximation descriptions of 300 – 1000 MeV proton nucleus elastic scattering. *Phys. Rev. C*, 31:538–560, Feb 1985.
- [3] J.C. Caillon and J. Labarsouque. Relativistic RPA response functions for quasielastic electron scattering with a density-dependent NN interaction. *Nuclear Physics A*, 595(2):189 – 208, 1995.
- [4] L. Ray. Neutron isotopic density differences deduced from 0.8 GeV polarized proton elastic scattering. *Phys. Rev. C*, 19:1855–1872, Apr 1979.
- [5] G. W. Hoffmann, L. Ray, M. L. Barlett, R. Ferguson, J. McGill, E. C. Milner, Kamal K. Seth, D. Barlow, M. Bosko, S. Iverson, M. Kaletka, A. Saha, and D. Smith. Elastic scattering of 500–MeV polarized protons from  $^{40,48}\text{Ca}$ ,  $^{90}\text{Zr}$ , and  $^{208}\text{Pb}$ , and breakdown of the impulse approximation at small momentum transfer. *Phys. Rev. Lett.*, 47:1436–1440, Nov 1981.
- [6] M. L. Barlett, G. W. Hoffmann, and L. Ray. *Bull. Am. Phys. Soc*, 27:729, 1982.
- [7] B. C. Clark, Robert L. Mercer, D. G. Ravenhall, and A. M. Saperstein. Optical–model partial-wave analysis of 1 – GeV proton-nucleus elastic scattering. *Phys. Rev. C*, 7:466 – 471, Jan 1973.
- [8] L. G. Arnold, B. C. Clark, E. D. Cooper, H. S. Sherif, D. A. Hutcheon, P. Kitching, J. M. Cameron, R. P. Liljestrand, R. N. MacDonald, W. J. McDonald, C. A. Miller, G. C. Neilson, W. C. Olsen, D. M. Sheppard, G. M. Stinson, D. K. McDaniels, J. R. Tinsley, R. L. Mercer, L. W. Swensen, P. Schwandt, and C. E. Stronach. Energy dependence of the  $p - ^{40}\text{Ca}$  optical potential: A Dirac equation perspective. *Phys. Rev. C*, 25:936–940, Feb 1982.
- [9] L.G. Arnold and B.C. Clark. Relativistic nucleon-nucleus optical model. *Physics Letters B*, 84(1):46 – 50, 1979.
- [10] L. G. Arnold, B. C. Clark, R. L. Mercer, and P. Schwandt. Dirac optical model analysis of  $\vec{p} - ^{40}\text{Ca}$  elastic scattering at 180 MeV and the wine–bottle–bottom shape. *Phys. Rev. C*, 23:1949–1959, May 1981.
- [11] C.J. Horowitz. The imaginary part of the relativistic nucleon–nucleus optical potential at 50 – 200 MeV. *Physics Letters B*, 117(3):153 – 156, 1982.

- [12] L. S. Celenza, B. Goulard, and C. M. Shakin. Quantum field theory and nuclear structure. *Phys. Rev. D*, 24:912–925, Aug 1981.
- [13] L. S. Celenza and C. M. Shakin. Relativistic many-body theory. *Phys. Rev. C*, 24:2704–2714, Dec 1981.
- [14] M. R. Anastasio, L. S. Celenza, and C. M. Shakin. Dirac phenomenology in nuclear structure and reactions. *Phys. Rev. C*, 23:2606–2615, Jun 1981.
- [15] B. C. Clark, S. Hama, R. L. Mercer, L. Ray, and B. D. Serot. Dirac-equation impulse approximation for intermediate-energy nucleon–nucleus scattering. *Phys. Rev. Lett.*, 50:1644–1647, May 1983.
- [16] L. Ray, G.W. Hoffmann, and W.R. Coker. Nonrelativistic and relativistic descriptions of proton-nucleus scattering. *Physics Reports*, 212(5):223 – 328, 1992.
- [17] B. C. Clark, S. Hama, and R. L. Mercer. *The interaction between medium energy nucleons in nuclei*, page 260. American Institute of Physics, 1983.
- [18] L. S. Celenza, M. K. Liou, L. C. Liu, and C. M. Shakin. Multiple-scattering theory and the relativistic optical model. *Phys. Rev. C*, 10:398 – 401, Jul 1974.
- [19] C. J. Horowitz. Relativistic Love–Franey model: Covariant representation of the NN interaction for N–nucleus scattering. *Phys. Rev. C*, 31:1340–1348, Apr 1985.
- [20] D. P. Murdock and C. J. Horowitz. Microscopic relativistic description of proton-nucleus scattering. *Phys. Rev. C*, 35:1442–1462, Apr 1987.
- [21] D. D. van Niekerk. *Application of the relativistic random-phase and distorted wave-impulse approximations to quasielastic proton nucleus scattering*. PhD thesis, Stellenbosch University, 2010.
- [22] A. Rahbar, B. Aas, E. Bleszynski, M. Bleszynski, M. Haji-Saeid, G. J. Igo, F. Irom, G. Pauletta, A. T. M. Wang, J. B. McClelland, J. F. Amann, T. A. Carey, W. D. Cornelius, M. Barlett, G. W. Hoffmann, C. Glashauser, S. Nanda, and M. M. Gazzaly. First measurement of the spin rotation parameter  $Q$  for  $p$ - $^{40}\text{Ca}$  elastic scattering at 500 MeV. *Phys. Rev. Lett.*, 47:1811–1814, Dec 1981.
- [23] J. A. McNeil, L. Ray, and S. J. Wallace. Impulse approximation NN amplitudes for proton-nucleus interactions. *Phys. Rev. C*, 27:2123–2132, May 1983.
- [24] J. R. Shepard, J. A. McNeil, and S. J. Wallace. Relativistic impulse approximation for  $p$ -nucleus elastic scattering. *Phys. Rev. Lett.*, 50:1443–1446, May 1983.
- [25] B. C. Clark, S. Hama, R. L. Mercer, L. Ray, G. W. Hoffmann, and B. D. Serot. Energy dependence of the relativistic impulse approximation for proton–nucleus elastic scattering. *Phys. Rev. C*, 28:1421–1424, Sep 1983.
- [26] M. V. Hynes, A. Picklesimer, P. C. Tandy, and R. M. Thaler. Characteristic Dirac signature in elastic proton scattering at intermediate energies. *Phys. Rev. Lett.*, 52:978–981, Mar 1984.
- [27] J. A. Tjon and S. J. Wallace. Meson theoretical basis for Dirac impulse approximation. *Phys. Rev. C*, 32:267–276, Jul 1985.
- [28] Z. P. Li, G. C. Hillhouse, and J. Meng. Validity of the relativistic impulse approximation for elastic proton-nucleus scattering at energies lower than 200 MeV. *Phys. Rev. C*, 78:014603, 2008.

- [29] C. J. Horowitz, D. P. Murdock, and B. D. Serot. *Computational Nuclear Physics 1: Nuclear Structure*, chapter The Relativistic Impulse Approximation, pages 129 – 151. Springer–Verlag Berlin Heidelberg, 1991.
- [30] J. A. Tjon and S. J. Wallace. Symmetric, Lorentz invariant NN amplitude: Yukawa representation. *Phys. Rev. C*, 35:280–297, Jan 1987.
- [31] J. A. Tjon and S. J. Wallace. Generalized impulse approximation for relativistic proton scattering. *Phys. Rev. C*, 36:1085–1104, Sep 1987.
- [32] N. Ottenstein, E. E. van Faassen, J. A. Tjon, and S. J. Wallace. Off-shell effects in elastic scattering of protons by nuclei. *Phys. Rev. C*, 43:2393–2411, May 1991.
- [33] Kaori Kaki. Multiple scattering contributions to the RIA optical potential. *Nuclear Physics A*, 516(3):603 – 632, 1990.
- [34] K. Kaki. Relativistic impulse approximation analysis of unstable calcium isotopes:  $^{60-74}\text{Ca}$ . *Phys. Rev. C*, 79:064609, Jun 2009.
- [35] Kaori Kaki. Relativistic impulse approximation analysis of elastic proton scattering from He isotopes. *Phys. Rev. C*, 89:014620, Jan 2014.
- [36] K. Kaki. Reaction cross sections of proton scattering from carbon isotopes: 8-22C.
- [37] G. C. Hillhouse and P. R. De Kock. Relativistic effects on polarization transfer observables for quasielastic proton-nucleus scattering. *Phys. Rev. C*, 49:391–400, Jan 1994.
- [38] G. C. Hillhouse and P. R. De Kock. Sensitivity of quasielastic ( $p \rightarrow n$ ) spin-transfer observables to relativistic Dirac effects. *Phys. Rev. C*, 52:2796–2799, Nov 1995.
- [39] G. C. Hillhouse, B. I. S van der Ventel, S. M. Wyngaardt, and P. R. De Kock. Nuclear medium modifications of the NN interaction via quasielastic ( $\vec{p}, \vec{p}'$ ) and ( $\vec{p}, \vec{n}$ ) scattering. *Phys. Rev. C*, 57:448–451, Jan 1998.
- [40] B. I. S. van der Ventel, G. C. Hillhouse, P. R. De Kock, and S. J. Wallace. Polarization transfer observables for quasielastic proton-nucleus scattering in terms of a complete Lorentz invariant representation of the NN scattering matrix. *Phys. Rev. C*, 60:064618, Nov 1999.
- [41] B. I. S. van der Ventel, G. C. Hillhouse, and P. R. De Kock. Relativistic predictions of quasielastic proton-nucleus spin observables based on a complete lorentz invariant representation of the NN scattering matrix. *Phys. Rev. C*, 62:024609, Jul 2000.
- [42] B. I. S. van der Ventel, G. C. Hillhouse, and P. R. De Kock. In T. Noro, H. Sakaguchi, H. Sakai, and T. Wakasa, editors, *Proceedings of RCNP International Symposium on Nuclear Responses and Medium Effects*, page 183. Universal Academy Press Inc, November 1998.
- [43] B. I. S. van der Ventel and G. C. Hillhouse. Sensitivity of exclusive proton knockout spin observables to different Lorentz invariant representations of the NN interaction. *Phys. Rev. C*, 69:024618, Feb 2004.
- [44] C. J. Horowitz and M. J. Iqbal. Relativistic effects on spin observables in quasielastic proton scattering. *Phys. Rev. C*, 33:2059–2069, Jun 1986.

- [45] G. B. Adera. *Relativistic Distorted wave analysis of neutrino-induced strange particle production on nuclei*. PhD thesis, Stellenbosch University, 2014.
- [46] D. D. van Niekerk, B. I. S. van der Ventel, N. P. Titus, and G. C. Hillhouse. Relativistic description of inclusive quasielastic proton–nucleus scattering with relativistic distorted-wave impulse approximation and random-phase approximation. *Phys. Rev. C*, 83:044607, Apr 2011.
- [47] N. Titus. *Relativistic eikonal formalism applied to inclusive quasielastic proton-induced nuclear reactions*. PhD thesis, Stellenbosch University, 2010.
- [48] N. P. Titus, B. I. S. van der Ventel, D. D. van Niekerk, and G. C. Hillhouse. Relativistic distorted–wave analysis of quasielastic proton–nucleus scattering. *Phys. Rev. C*, 83:044616, Apr 2011.
- [49] Y. Ikebata. (p,2p) reaction in zero-range and finite-range relativistic distorted-wave impulse approximation. *Phys. Rev. C*, 52:890, 1995.
- [50] C. J. Horowitz and D. P. Murdock. Quasielastic proton-nucleus scattering in a relativistic plane-wave impulse approximation. *Phys. Rev. C*, 37:2032–2050, 1988.
- [51] Y. Blumenfeld, E. Khan, F. Maréchal, and T. Suomijärvi. Proton scattering from unstable nuclei. *Pramana*, 57(2):493–504, 2001.
- [52] Michael Thoennessen and Bradley Sherrill. From isotopes to the stars. *Nature*, 473:25 – 26, 2011.
- [53] Samuel S. M. Wong. *Introductory Nuclear Physics*. Wiley-VCH Verlag GmbH & Co. KGaA, 2nd edition, 2004.
- [54] Tohru Motobayashi. World new facilities for radioactive isotope beams. *EPJ Web of Conferences*, 66:01013, 2014.
- [55] Björn Jonson. Light dripline nuclei. *Physics Reports*, 389(1):1 – 59, 2004.
- [56] Lindroos. Review of ISOL-type radioactive beam facilities. In *Proceedings of EPAC*, pages 45 – 49, Lucerne, Switzerland, 2004. EPAC.
- [57] Hans Paetz Schieck. *Nuclear Reactions: An Introduction*, volume 882 of *Lecture Notes in Physics*. Springer-Verlag Berlin Heidelberg, 1 edition, 2014.
- [58] Jeroen Büscher. *Beta–decay study of the halo nuclei  ${}^6\text{He}$ ,  ${}^{11}\text{Be}$  and  ${}^{11}\text{Li}$* . PhD thesis, KU Leuven, 2010.
- [59] H Geissel, G Munzenberg, and K Riisager. Secondary exotic nuclear beams. *Annual Review of Nuclear and Particle Science*, 45:163–203, 1995.
- [60] N. Alamanos and A Gillibert. *Selected topics in reaction studies with exotic nuclei*, volume 651 of *Lect. Notes Phys.* Springer-Verlag, Berlin Heidelberg, 2004.
- [61] J. J. Kelly, B. S. Flanders, F. W. Hersman, J. H. Heisenberg, J. Calarco, J. P. Connelly, T. E. Milliman, A. Scott, F. T. Baker, V. Penumetcha, W. P. Jones, G. T. Emery, A. D. Bacher, C. Olmer, M. A. Grimm, and M. L. Whiten. Neutron transition densities from  ${}^{88}\text{Sr}(p,p')$  at  $E_p=200$  MeV. *Phys. Rev. C*, 47:2146–2158, May 1993.
- [62] T Suomijärvi. Proton scattering on unstable nuclei. *Journal of Physics G: Nuclear and Particle Physics*, 25(4):741, 1999.

- [63] E. Khan, T. Suomijärvi, Y. Blumenfeld, Nguyen Van Giai, N. Alamanos, F. Auger, E. Bauge, D. Beaumel, J.P. Delaroche, P. Delbourgo-Salvador, A. Drouart, S. Fortier, N. Frascaria, A. Gillibert, M. Girod, C. Jouanne, K.W. Kemper, A. Lagoyannis, V. Lapoux, A. Lepine-Szily, I. Lhenry, J. Libert, F. Marechal, J.M. Maison, A. Musumarra, S. Ottini-Hustache, P. Piattelli, S. Pita, E.C. Pollacco, P. Roussel-Chomaz, D. Santonocito, J.E. Sauvestre, J.A. Scarpaci, and T. Zerguerras. Proton scattering from the unstable nuclei  $^{30}\text{S}$  and  $^{34}\text{Ar}$ : structural evolution along the sulfur and argon isotopic chains. Experiment performed at the GANIL national facility, Caen, France. *Nuclear Physics A*, 694(1):103 – 131, 2001.
- [64] M Rashdan. Implication of proton-nucleus scattering for density distributions of unstable nuclei. *Eur. Phys. J. A*, 16:371–379, 2003.
- [65] G Gangopadhyay and Subinit Roy. Relativistic mean field study of neutron-rich even-even C and Be isotopes. *Journal of Physics G: Nuclear and Particle Physics*, 31(9):1111, 2005.
- [66] W. Mittig and P. Roussel-Chomaz. Results and techniques of measurements with inverse kinematics. *Nuclear Physics A*, 693(1):495 – 513, 2001. Radioactive Nuclear Beams.
- [67] Y. Matsuda, H. Sakaguchi, H. Takeda, S. Terashima, J. Zenihiro, T. Kobayashi, T. Murakami, Y. Iwao, T. Ichihara, T. Suda, T. Ohnishi, Y. Watanabe, H. Otsu, K. Yoneda, Y. Satou, K. Ozeki, and M. Kanazawa. Elastic scattering of protons from  $^9\text{C}$  with a 290 MeV/nucleon  $^9\text{C}$  beam. *Phys. Rev. C*, 87:034614, Mar 2013.
- [68] P. Egelhof, G.D. Alkhozov, M.N. Andronenko, A. Bauchet, A.V. Dobrovolsky, S. Fritz, G.E. Gavrilov, H. Geissel, C. Gross, A.V. Khanzadeev, G.A. Korolev, G. Kraus, A.A. Lobodenko, G. Münzenberg, M. Mutterer, S.R. Neumaier, T. Schäfer, C. Scheidenberger, D.M. Seliverstov, N.A. Timofeev, A.A. Vorobyov, and V.I. Yatsoura. Nuclear-matter distributions of halo nuclei from elastic proton scattering in inverse kinematics. *The European Physical Journal A - Hadrons and Nuclei*, 15(1):27–33, 2002.
- [69] P Ring. Relativistic mean field theory in finite nuclei. *Prog. Part. Nucl. Phys.*, 37:193–263, 1996.
- [70] G. A. Lalazissis, J. König, and P. Ring. New parametrization for the Lagrangian density of relativistic mean field theory. *Phys. Rev. C*, 55:540–543, Jan 1997.
- [71] Andrea Meucci. Relativistic mean field theory of nuclear structure. Talk given at Department of Theoretical nuclear physics, University of Pavia, Italy, November 2000.
- [72] B. D. Serot and J. D. Walecka. *Advances in nuclear physics*, volume 16. Plenum, New York, 1986.
- [73] Y. K. Gambhir and P. Ring. Relativistic mean-field description of the ground-state nuclear properties. *Pramana*, 32(4):389–404, 1989.
- [74] J.D Walecka. A theory of highly condensed matter. *Annals of Physics*, 83(2):491 – 529, 1974.
- [75] Brian D. Serot and John Dirk Walecka. Recent progress in quantum hadrodynamics. *International Journal of Modern Physics E*, 06(04):515–631, 1997.
- [76] Peter Ring. *The microscopic treatment of the nuclear system*, pages 195–232. Springer Berlin Heidelberg, Berlin, Heidelberg, 2001.

- [77] S. K. Patra and C. R. Praharaaj. Relativistic mean field study of light medium nuclei away from beta stability. *Phys. Rev. C*, 44:2552, 1991.
- [78] J. Boguta and A.R. Bodmer. Relativistic calculation of nuclear matter and the nuclear surface. *Nuclear Physics A*, 292(3):413 – 428, 1977.
- [79] N. K. Glendenning. *Compact stars*. Springer, 2nd edition, 2000.
- [80] P. G. Reinhard, M. Rufa, J. Maruhn, W. Greiner, and J. Friedrich. Nuclear ground-state properties in a relativistic meson-field theory. *Zeitschrift für Physik A Atomic Nuclei*, 323(1):13–25, Mar 1986.
- [81] M.M. Sharma, M.A. Nagarajan, and P. Ring. Rho meson coupling in the relativistic mean field theory and description of exotic nuclei. *Physics Letters B*, 312(4):377 – 381, 1993.
- [82] Y. Sugahara and H. Toki. Relativistic mean field theory for unstable nuclei with non-linear  $\sigma$  and  $\omega$  terms. *Nuclear Physics A*, 579:557–572, 1994.
- [83] Wenhui Long, Jie Meng, Nguyen Van Giai, and Shan-Gui Zhou. New effective interactions in relativistic mean field theory with nonlinear terms and density-dependent meson-nucleon coupling. *Phys. Rev. C*, 69:034319, Mar 2004.
- [84] B. G. Todd-Rutel and J. Piekarewicz. Neutron-rich nuclei and neutron stars: A new accurately calibrated interaction for the study of neutron-rich matter. *Phys. Rev. Lett.*, 95:122501, Sep 2005.
- [85] C. J. Horowitz and J. Piekarewicz. Neutron star structure and the neutron radius of  $^{208}\text{Pb}$ . *Phys. Rev. Lett.*, 86:5647–5650, Jun 2001.
- [86] B. G. Todd and J. Piekarewicz. Relativistic mean-field study of neutron-rich nuclei. *Phys. Rev. C*, 67:044317, Apr 2003.
- [87] J. P. W. Diener. Relativistic mean field theory applied to the study of neutron star properties. Master’s thesis, Stellenbosch University, 2008.
- [88] B. G. Rutel. *Exotic Nuclei and Relativistic Mean-Field Theory*. PhD thesis, Florida State University, 2004.
- [89] BirBikram Singh, S. K. Patra, and Raj K. Gupta. Cluster radioactive decay within the preformed cluster model using relativistic mean-field theory densities. *Phys. Rev. C*, 82:014607, Jul 2010.
- [90] I. Angeli and K.P. Marinova. Table of experimental nuclear ground state charge radii: An update. *Atomic Data and Nuclear Data Tables*, 99(1):69 – 95, 2013.
- [91] R. F. Garcia-Ruiz, M. L. Bissell, K. Blaum, A. Ekström, N. Frömmgen, G. Hagen, M. Hammen, K. Hebeler, J. D. Holt, G. R. Jansen, M. Kowalska, K. Kreim, W. Nazarewicz, R. Neugart, G. Neyens, W. Nörtershäuser, T. Papenbrock, J. Papuga, A. Schwenk, J. Simonis, K. A. Wendt, and D. T. Yordanov. Unexpectedly large charge radii of neutron-rich calcium isotopes. *Nature Physics*, 12:594–599, 2016.
- [92] J. Meng, H. Toki, S. G. Zhou, S. Q. Zhang, W. H. Long, and L. S. Geng. Relativistic continuum Hartree Bogoliubov theory for ground state properties of exotic nuclei. *Progress in particle and nuclear physics*, 57:470–563, 2006.

- [93] H. Kucharek and P. Ring. Relativistic field theory of superfluidity in nuclei. *Zeitschrift für Physik A Hadrons and Nuclei*, 339(1):23–35, Mar 1991.
- [94] J. Meng and P. Ring. Relativistic Hartree-Bogoliubov description of the neutron halo in  $^{11}\text{Li}$ . *Phys. Rev. Lett.*, 77:3963–3966, Nov 1996.
- [95] Jie Meng. Relativistic continuum Hartree-Bogoliubov theory with both zero range and finite range Gogny force and their application. *Nuclear Physics A*, 635(1):3 – 42, 1998.
- [96] P. Ring and P. Schuck. *The nuclear many-body problem*. Springer, Heidelberg, 1980.
- [97] Matteo Vorabbi. *Electron and proton scattering off nuclei with neutron and proton excess*. PhD thesis, Università Degli Studi di Pavia, 2014.
- [98] I. Tanihata, H. Hamagaki, O. Hashimoto, S. Nagamiya, Y. Shida, N. Yoshikawa, O. Yamakawa, K. Sugimoto, T. Kobayashi, D.E. Greiner, N. Takahashi, and Y. Nojiri. Measurements of interaction cross sections and radii of He isotopes. *Physics Letters B*, 160(6):380 – 384, 1985.
- [99] N. Fukunishi, T. Otsuka, and I. Tanihata. Neutron-skin and proton-skin formations in exotic nuclei far from stability. *Phys. Rev. C*, 48:1648–1655, Oct 1993.
- [100] M.T. Yamashita, Lauro Tomio, and T. Frederico. Radii in weakly-bound light halo nuclei. *Nuclear Physics A*, 735(1):40 – 54, 2004.
- [101] A. S. Jensen, K. Riisager, D. V. Fedorov, and E. Garrido. Structure and reactions of quantum halos. *Rev. Mod. Phys.*, 76:215–261, Feb 2004.
- [102] Jim Al-Khalili and Filomena Nunes. Reaction models to probe the structure of light exotic nuclei. *Journal of Physics G: Nuclear and Particle Physics*, 29(11):R89, 2003.
- [103] P G Hansen, A S Jensen, and B Jonson. Nuclear halos. *Annual Review of Nuclear and Particle Science*, 45(1):591–634, 1995.
- [104] P.G. Hansen and J.A. Tostevin. Direct reactions with exotic nuclei. *Annual Review of Nuclear and Particle Science*, 53(1):219–261, 2003.
- [105] Jim Al-Khalili. *An Introduction to Halo Nuclei*, pages 77–112. Springer Berlin Heidelberg, Berlin, Heidelberg, 2004.
- [106] L. G. Arnold, B. C. Clark, and R. L. Mercer. Relativistic optical model analysis of medium energy  $p$ - $^4\text{He}$  elastic scattering experiments. *Phys. Rev. C*, 19:917–922, Mar 1979.
- [107] B. C. Clark. A review of phenomenological Dirac analyses. In H. V. von Geramb, editor, *Medium energy nucleon and antinucleon scattering. Proceedings of the international symposium held at Bad Honnef*, number 243, page 391, Berlin Heidelberg, 1985. Springer-Verlag.
- [108] E. D. Cooper, B. C. Clark, R. Kozack, S. Shim, S. Hama, J. I. Johansson, H. S. Sherif, R. L. Mercer, and B. D. Serot. Global optical potentials for elastic  $p + ^{40}\text{Ca}$  scattering using the Dirac equation. *Phys. Rev. C*, 36:2170–2172, Nov 1987.
- [109] E.D. Cooper, B.C. Clark, S. Hama, and R.L. Mercer. Dirac-global fits to calcium elastic scattering data in the range 21-200 MeV. *Physics Letters B*, 206(4):588 – 591, 1988.

- [110] R. Kozack and D. G. Madland. Dirac optical potentials for nucleon scattering by  $^{208}\text{Pb}$  at intermediate energies. *Phys. Rev. C*, 39:1461–1474, Apr 1989.
- [111] S. Hama, B. C. Clark, E. D. Cooper, H. S. Sherif, and R. L. Mercer. Global Dirac optical potentials for elastic proton scattering from heavy nuclei. *Phys. Rev. C*, 41:2737, 1990.
- [112] E. D. Cooper, S. Hama, B. C. Clark, and R. L. Mercer. Global Dirac phenomenology for proton-nucleus elastic scattering. *Phys. Rev. C*, 47:297, 1993.
- [113] E.D. Cooper and B.K. Jennings. Smooth relativistic two-body propagators. *Nuclear Physics A*, 483(3):601 – 618, 1988.
- [114] R. G. Newton. *Scattering theory of waves and particles*. Springer, New York, 2nd edition, 1982.
- [115] J. A. McNeil, J. R. Shepard, and S. J. Wallace. Impulse–approximation Dirac optical potential. *Phys. Rev. Lett.*, 50:1439–1442, May 1983.
- [116] L. S. Celenza and C. M. Shakin. Relativistic and nonrelativistic models of the nuclear optical potential. *Phys. Rev. C*, 29:1784, 1984.
- [117] Y. Jin and R. W. Finlay. Analysis of total neutron-nucleus cross sections using relativistic impulse approximation. *Phys. Rev. C*, 47:1697, 1993.
- [118] W. R. Coker and L. Ray. Nuclear tensor term in the relativistic impulse approximation for proton-nucleus elastic scattering. *Phys. Rev. C*, 42:2242, 1990.
- [119] J. D. Lumpe and L. Ray. Correlation effects in the relativistic impulse approximation treatment of proton–nucleus elastic scattering. *Phys. Rev. C*, 35:1040–1059, Mar 1987.
- [120] I. E. McCarthy. *Introduction to Nuclear Theory*. Wiley, New York, 1968.
- [121] A S Kadyrov, I Bray, A T Stelbovics, and B Saha. Direct solution of the three–dimensional Lippmann–Schwinger equation. *Journal of Physics B: Atomic, Molecular and Optical Physics*, 38(5):509, 2005.
- [122] M. Jacob and G.C. Wick. On the general theory of collisions for particles with spin. *Annals of Physics*, 7(4):404 – 428, 1959.
- [123] George L. Caia, Vladimir Pascalutsa, and Louis E. Wright. Solving potential scattering equations without partial wave decomposition. *Phys. Rev. C*, 69:034003, Mar 2004.
- [124] M. V. Hynes, A. Picklesimer, P. C. Tandy, and R. M. Thaler. Relativistic (Dirac equation) effects in microscopic elastic scattering calculations. *Phys. Rev. C*, 31:1438–1463, Apr 1985.
- [125] Joseph J. Kubis. Partial–wave analysis of spinor Bethe-Salpeter equations for single–particle exchange. *Phys. Rev. D*, 6:547–564, Jul 1972.
- [126] V K Khersonskii D A Varshalovich, A N Moskalev. *Quantum Theory of Angular Momentum*. World Scientific, Singapore, 1988.
- [127] Roger G Newton. *Scattering theory of waves and particles*. Texts and Monographs in Physics. Springer Berlin Heidelberg, New York, 2nd edition, 1982.
- [128] Rubin H. Landau. *Quantum Mechanics II, a second course in quantum theory*. Wiley-VCH, Verlag, 2nd edition, 2008.

- [129] Stephen P. Weppner. *Microscopic calculations of first order optical potentials for nucleon-nucleus scattering*. PhD thesis, Ohio University, 1997.
- [130] R. Crespo and J. A. Tostevin. Treatment of the Coulomb interaction in momentum space calculations of proton elastic scattering. *Phys. Rev. C*, 41:2615–2619, Jun 1990.
- [131] C. M. Vincent and S. C. Phatak. Accurate momentum-space method for scattering by nuclear and Coulomb potentials. *Phys. Rev. C*, 10:391–394, Jul 1974.
- [132] C Elster, L C Liu, and R M Thaler. A practical calculational method for treating Coulomb scattering in momentum space. *Journal of Physics G: Nuclear and Particle Physics*, 19(12):2123, 1993.
- [133] A. Picklesimer, P. C. Tandy, R. M. Thaler, and D. H. Wolfe. Momentum space approach to microscopic effects in elastic proton scattering. *Phys. Rev. C*, 30:1861–1879, Dec 1984.
- [134] C. Elster, J. H. Thomas, and W. Glöckle. Two-body T-matrices without angular-momentum decomposition: Energy and momentum dependences. *Few-Body Systems*, 24(1):55–79, 1998.
- [135] A. Picklesimer, J. W. Van Orden, and S. J. Wallace. Final state interactions and relativistic effects in the  $(e \rightarrow, e'p)$  reaction. *Phys. Rev. C*, 32:1312–1326, Oct 1985.
- [136] S. P. Weppner, Ch. Elster, and D. Hüber. Off-shell structures of nucleon-nucleon  $t$  matrices and their influence on nucleon-nucleus elastic scattering observables. *Phys. Rev. C*, 57:1378–1385, Mar 1998.
- [137] S. Veerasamy, Ch. Elster, and W. N. Polyzou. Two-nucleon scattering without partial waves using a momentum space Argonne V18 interaction. *Few-Body Systems*, 54(12):2207–2225, Dec 2013.
- [138] I. Fachruddin, Ch. Elster, and W. Glöckle. Nucleon-nucleon scattering in a three dimensional approach. *Phys. Rev. C*, 62:044002, Sep 2000.
- [139] L.F. Shampine. Vectorized adaptive quadrature in MATLAB. *Journal of Computational and Applied Mathematics*, 211(2):131 – 140, 2008.
- [140] William J. Thompson. *Computing for Scientists and Engineers: A Workbook of Analysis, Numerics, and Applications*. John Wiley and Sons, New York, 1992.
- [141] W. Y. Yang, W. Cao, T. S. Chung, and J. Morris. *Applied numerical methods using MATLAB*. John Wiley and Sons, Hoboken, New Jersey, 2005.
- [142] J. L. M. Quiroz González and D. Thompson. Getting started with Numerov’s method. *Comput. Phys.*, 11(5):514–515, September 1998.